

Copyright is owned by the Author of the thesis. Permission is given for a copy to be downloaded by an individual for the purpose of research and private study only. The thesis may not be reproduced elsewhere without the permission of the Author.

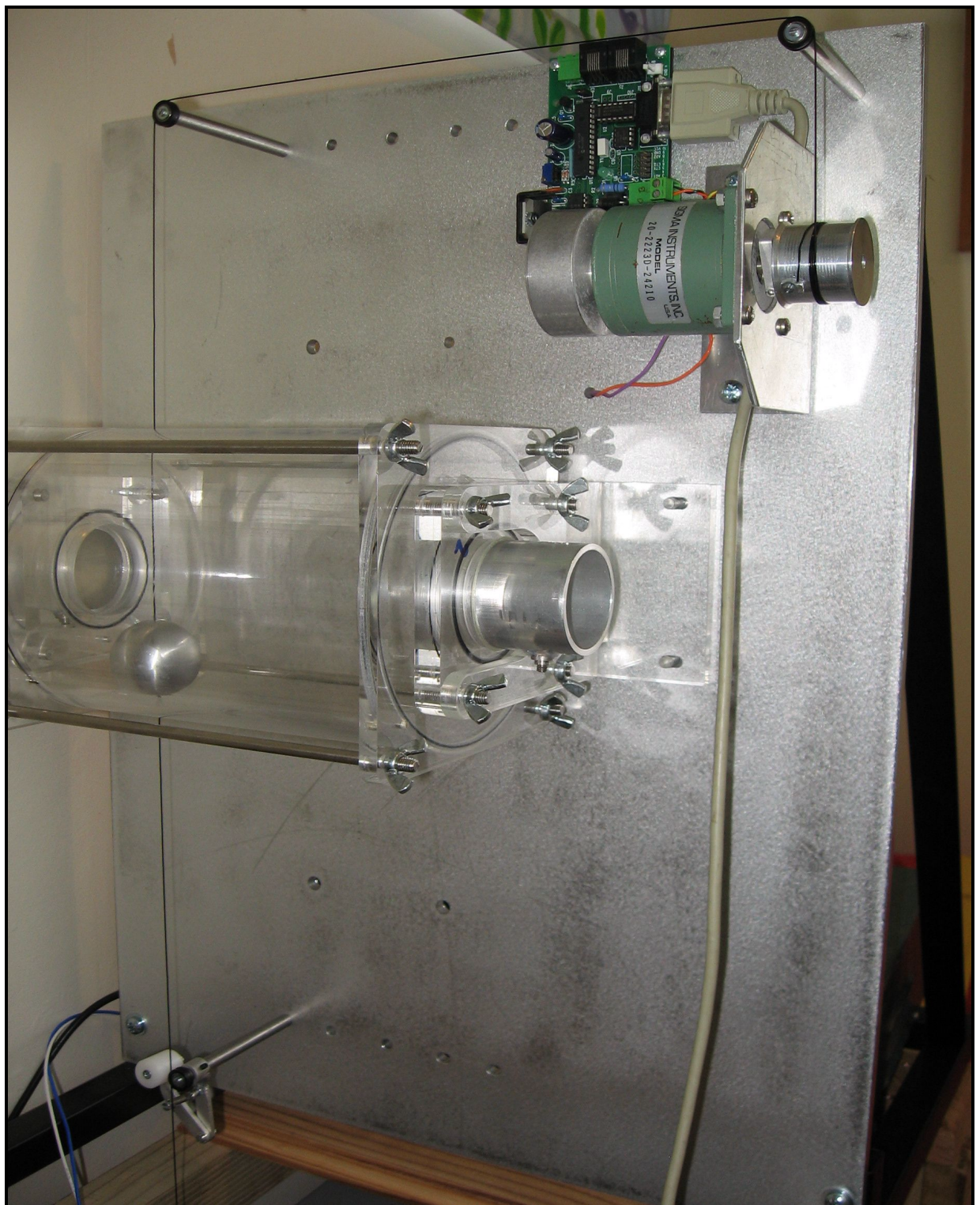
The application of Helmholtz resonance to determination of the volume of solids, liquids and particulate matter

A thesis presented in partial fulfilment of the requirements for the degree of
Doctor of Philosophy
in
Instrumentation and Process Engineering

At Massey University, Palmerston North
New Zealand

Emile Stefan Webster

November
2010



Pulley apparatus set up for mapping the resonant frequency versus sample location in the horizontal configuration

Abstract

The aim of this investigation was the creation of a high precision volume measurement device using the Helmholtz resonator principle, the purpose of which was to measure, without interference, liquids, solids and particulate samples. A previous study by Nishizu *et al.* (2001) suggested they achieved an accuracy of about $\pm 1\%$ of full scale, where full scale is 100% fill of the resonator chamber. Theory suggested that with careful design and measurement accuracy of approximately $\pm 0.1\%$ should be achievable.

A high precision resonator was designed using acoustic theory and drawn using SolidWorksTM computer aided design software. This was then built using a computerised numerical controlled milling machine. The resulting resonator was coupled to a 16-bit high-speed data acquisition system driven by purpose-made LabVIEWTM software. Using a resonant hunting method, repeatability was within $\pm 1\text{mL}$ for a 3L chamber and the accuracy was better than $\pm 3\text{mL}$, which is $\pm 0.1\%$ of full scale for liquid and solid samples.

Testing of particulate material gave results indicating complex behaviour occurring within the resonator. Accuracy of sub-millimetre granular samples was restricted to approximately $\pm 1\%$, and fill factors to about 50%. This reduction in accuracy was caused by a combination of energy absorption and resonant peak broadening. Medium sized particles, between 1mm and 15mm allowed measurement accuracies of approximately $\pm 0.5\%$. Larger samples, greater than 15mm in diameter, gave results with comparable accuracy to water and solids tested.

It was found that most materials required a post measurement curve fit to align predictive volume calculations. All samples were observed to have a predictive deviation curve with coefficients dependent on the material or general shape. This curve appeared to be a function of sample regularity and/or whether the sample has interstitial spaces. To achieve high measurement accuracy temperature compensation was required to negate drifts in sample measurement.

Chamber mapping was conducted using a spherical solid moved to precise locations, then making a three-dimensional frequency map of the inside of a dual port resonator. This showed the length extension term for the moving mass of air in the port penetrates roughly three times further than theory suggests. However, the influence of this extra 'tail' was found to be negligible when calculating sample volumes.

A new method of measuring volume was developed using Q profile shifting and ambient temperature information. Accuracies for this method were comparable to those found using the resonant hunting method. A significant advantage of the new method is a 2-3 second measurement time compared to approximately 40 seconds for the resonant hunting method. The Q profile shifting method allowed volume measurements on samples moving through a dual port resonator at speeds of up to 100mm/s.

Free fall measurements proved unsuccessful using existing methods, but variations in signal data for different sample sizes suggest the need for future investigation.

Follow-up studies may provide new interpretation models and methods for high-speed acquisition and analysis required to solve freefall measurements.

Precise temperature (speed of sound) and flange factor (responsible for port length extension) relationships were evaluated. The correction factor for the speed of sound with temperature was found to be marginally different to established theory using the Helmholtz equation due to temperature secondary effects in the port length extension factor. The flange factor, which determines port length extension, for the configurations used in this investigation was experimentally found to be approximately 5% less than theoretical values.

It was established that the sample to be measured must be within a certain region of the chamber for accurate volume measurements to be made. If the sample were larger than the bounded region the resonant frequency would no longer obey the Helmholtz relationship. This would thereby reduce the accuracy of the measurement. All samples irrespective of cross sectional area were found to alter the resonant frequency when they were over 85% of the chamber height.

An equalisation method termed environmental normalisation curve was developed to prevent environmental and loudspeaker deficiencies from colouring Q profiles used in Q profile shifting procedures. This was undertaken as Q profile shifting relies on consistency in the Q profile. The environmental normalisation curve was able to equalise external factors to within $\pm 0.4\text{dB}$. The environmental normalisation method could be used to post-process data or applied in real time to frequency generation.

The controlled decent Q profile shifting technique was refined further to be used in continuous measurements in a single port resonator. Samples could theoretically be measured up to 15% of full-scale fill before resonant peak predictability would compromise accuracy. Measurement times were from one to three seconds, depending on environmental temperature stability.

An alternative Helmholtz resonator was developed and investigated using an inverted port. This variant has potential applications for a seal-less chamber and port with rapid non-interference chamber access. Q factors for the inverted port resonator were found to be significantly less than tradition Helmholtz resonators. It is believed this is due to a larger boundary layer acoustic resistance occurring in the inverted port.

A variable chamber resonator was designed and built as a further development of the Helmholtz resonator volume measurement system, as the uncertainty of measurement is a function of resonant chamber size. Therefore, using the variable chamber resonator the chamber size could be customised to the sample size. In this way the uncertainty of measurement could be minimised. The variable chamber resonator was used with both the resonant hunting method and the Q profile shifting method.

Volume measurements on produce and minerals using the variable chamber resonator yielded results of similar accuracy to measurements on calibration samples. Each sample type displayed characteristics that would make specific calibration necessary. Both techniques were able to detect hidden void spaces, larger than 2% of the sample volume, and in punctured samples. Therefore, both methods may be viable for rapid sorting of produce and minerals.

Acknowledgements

I would like to thank my supervisor, Professor Clive Davies, for his continued encouragement throughout my course of study, providing opportunities for personal development and assistance in attaining scholarships and funding for this investigation.

I would like to thank my wife, Nadia, for her support in allowing me the time to conduct this thesis and her tireless efforts in proof reading and editing early drafts.

Thanks also to Steve Tallon (PhD), co-supervisor, for his help in reading and critiquing later drafts. Thanks also for help in gaining access to Industrial Research LTD (IRL) anechoic facilities and instruments used for calibration purposes.

Lastly I would like to thank the workshop services at the Massey University Wellington campus, especially Mike Turner for his excellent work in fabricating the various resonator components, pulley apparatus and variable chamber resonator.

Table of contents

Abstract.....	i
Acknowledgements	iii
Table of contents	v
Figures and Tables	ix
Nomenclature	xvii
Basic equations	xix
Glossary	xxi
Chapter 1 Introduction and literature review.....	1
1.1 Introduction.....	3
1.2 Literature Review: Volume measurement.....	7
1.2.1 Experimental volume measurement using a Helmholtz resonator	7
1.2.2 Patent for Helmholtz volume measurement device	9
1.2.3 Experimental Helmholtz resonator with variable chamber size	9
1.2.4 Pycnometers	10
1.2.5 Commercial pycnometers	12
1.2.6 Commercial methods for sorting produce and minerals	12
1.2.7 Spheres in a resonant cavity.....	13
Literature review conclusions	14
Chapter 2 Helmholtz resonator theory	15
2.1Helmholtz resonator theory	17
2.1.1 Traditional Helmholtz resonator theory.....	17
2.1.2 Chirp frequencies	18
2.1.3 Non-ideal behaviour in the port: length extension.....	18
2.1.4 Non-ideal behaviour in the port: radiation resistance	21
2.1.5 Non-ideal behaviour in the port: viscosity and turbulence	22
2.1.6 Non-ideal behaviour in the port: heat conductive losses	23
2.1.7 Non-ideal behaviour in the port: relaxation time.....	24
2.1.8 Non-ideal behaviour in the port: non-linear effects.....	24
2.1.9 Non-ideal behaviour in the port: port placement	25
2.1.10 Non-ideal behaviour in the port: port shape	26
2.1.11 Non-ideal behaviour: chamber and port length	26
2.1.12 Non-ideal behaviour: chamber shape.....	27
2.1.13 Resonator chamber with many apertures.....	28
2.1.14 Analytical transmission and finite element analysis.....	29
2.1.15 Transcendental equations for resonance frequency determination.....	29
Key concepts in Helmholtz resonator design.....	31
Chapter 3 Resonance hunting for volume determination	33
3.1 Introduction and summary	35
3.2 Equipment and samples	37
3.2.1 Resonators.....	37
3.2.2 Microphones	38
3.2.3 Data Acquisition (DAQ) Hardware	39
3.2.4 Temperature sensors	39
3.2.5 Software	39
3.2.6 Pink noise.....	40
3.2.7 Chirps – Frequency sweep	40
3.2.8 Square wave	40
3.2.9 Loudspeaker	41

3.2.10 Pulley apparatus	41
3.2.11 Stepper-motor	43
3.2.12 Solid samples	43
3.2.13 Granular samples	43
3.2.14 Liquid samples	44
3.2.15 Acoustic barrier disks	44
3.3 Methods.....	45
3.3.1 Characterising the fabricated resonators	45
3.3.2 Repeatability of measurements using resonators	45
3.3.3 Temperature effects	45
3.3.4 Calibrating the asymmetric single port resonator	46
3.3.5 Effects of port symmetry	48
3.3.6 Effects of sample irregularities	48
3.3.7 Measurement on granular materials.....	49
3.3.8 Effects of air leaks on resonant frequency and Q factor	50
3.3.9 Effects of sample position on volume measurements.....	51
3.3.10 Controlled decent using a dual-port resonator and resonant hunting	51
3.3.11 Measurement of port flanging effects	52
3.4 Results	53
3.4.1 Characterising the fabricated resonators	53
3.4.2 Repeatability of measurements using resonators	54
3.4.3 Temperature effects	56
3.4.4 Calibrating the asymmetric single port resonator	58
3.4.5 Effects of port symmetry	62
3.4.6 Effects of sample irregularities	62
3.4.7 Measurement on granular materials.....	65
3.4.8 Effects of air leaks on resonant frequency and Q factor	73
3.4.9 Effects of sample position on volume measurements.....	75
3.4.10 Controlled decent using a dual-port resonator and resonant hunting	77
3.4.11 Measurement of port flanging effects	78
3.5 Discussion.....	81
3.5.1 Characterising the fabricated resonators	81
3.5.2 Repeatability of measurements using resonators	81
3.5.3 Temperature effects	83
3.5.4 Calibrating the asymmetric single port resonator	83
3.5.5 Effects of port symmetry	84
3.5.6 Effects of sample irregularities	85
3.5.7 Measurement on granular materials.....	86
3.5.8 Effects of air leaks on resonant frequency and Q factor	88
3.5.9 Effects of sample position on volume measurements.....	89
3.5.10 Controlled decent using a dual-port resonator and resonant hunting	90
3.5.11 Measurement of port flanging effects	90
Chapter 4 New methods in volume determination using Helmholtz resonance .91	
4.1 Introduction and summary	93
4.2 Equipment and samples	95
4.2.1 Variable chamber resonator (VCR)	95
4.2.2 Inverted port resonators	95
4.2.3 Buoyancy rig.....	96
4.2.4 Agricultural produce and mineral samples	96
4.3 Methods.....	99

4.3.1 Phase shift technique.....	99
4.3.2 Q profile shifting – Controlled decent	99
4.3.3 Q profile shifting – Free falling sample	101
4.3.4 Environmental Normalisation Curve (ENC)	102
4.3.5 Continuous Q Profile Shifting technique (QPS).....	102
4.3.6 Inverted port resonators	103
4.3.7 Variable chamber resonator (VCR)	103
4.3.8 Applications – Produce and mineral testing	104
4.4 Results	105
4.4.1 Phase shift technique.....	105
4.4.2 Q profile shifting – Controlled drop	105
4.4.3 Q profile shifting – Free falling sample	108
4.4.4 Environmental normalisation curve (ENC)	109
4.4.5 Continuous Q profile shifting technique.....	112
4.4.6 Inverted port resonators	116
4.4.7 Variable chamber resonator (VCR)	118
4.4.8 Applications – Produce and mineral testing	122
4.5 Discussion.....	127
4.5.1 Phase shift technique.....	127
4.5.2 Q profile shifting – Controlled drop	127
4.5.3 Q profile shifting – Free falling sample	128
4.5.4 Environmental normalisation curve (ENC)	129
4.5.5 Continuous Q profile shifting technique.....	130
4.5.6 Inverted port resonators	131
4.5.7 Variable chamber resonator (VCR)	131
4.5.8 Applications – Produce and mineral testing	132
Chapter 5 Conclusions and recommendations.....	135
5.1 Conclusions.....	137
5.1.1 Characterising the fabricated resonators.....	137
5.1.2 Repeatability of measurements using resonators	137
5.1.3 Temperature effects	138
5.1.4 Calibrating the asymmetric single port resonator	138
5.1.5 Effects of port symmetry	138
5.1.6 Effects of sample irregularities	138
5.1.7 Measurement of granular materials	139
5.1.8 Effects of air leaks on resonant frequency and Q factor	139
5.1.9 Effects of sample position on volume measurements.....	139
5.1.10 Controlled decent and free falling sample using a dual-port resonator	140
5.1.11 Environmental normalisation curve (ENC)	140
5.1.12 Continuous Q profile shifting technique.....	140
5.1.13 Inverted port resonators	141
5.1.14 Variable chamber resonator (VCR)	141
5.1.15 Applications – Produce and mineral testing	141
5.2 Recommendations	143
5.2.1 Energy in resonance, improving the Q factor	143
5.2.2 Thermal heating and temperature inside the resonator	143
5.2.3 Broadband noise from particle reemission of sound.....	143
5.2.4 Effects of particle shape when testing granular materials	143
5.2.5 Phase shifting method of measuring sample volume.....	143
5.2.6 Alternate methods for volume measurements of moving samples	143

5.2.7 Measurement of surface hardness and structure	144
5.2.8 Energy impulse response	144
Appendix A Mathematics of acoustics	145
1. The wave equation	145
2. Solutions to the wave equation for Helmholtz resonator.....	147
3. Mechanical Power and Q factor for a resonator	149
4. Mechanical piston radiator.....	150
5. Directivity of a piston source	153
6. Pressure at the piston source	154
7. Radiation impedance.....	157
8. Flanged and un-flanged ports.....	158
9. Mechanical resistance caused by boundary layer	159
10. Mechanical stiffness caused by an orifice	162
11. Acoustic transmission effects	162
12. Lumped parameters.....	168
13. Diffraction from edge effects.....	169
Appendix B Software descriptions and functional block diagrams	171
1. Resonant hunting	171
2. Broad frequency scanner.....	172
3. Chamber mapping using resonant hunting	173
4. Q profile shifting.....	174
State 1 – Resonant hunting on empty chamber.....	174
State 2 – Generate Q profile.....	175
State 3 – Perform Q profile shifting.....	176
5. Continuous Q profile shifting	177
State 3 – Continuous Q profile shifting	177
6. VCR Q profile shifting.....	178
State 1 – Acquire Q profile	178
State 2 – Dynamic Q profile shifting	179
State 3 and 4 – Create and check an ENC profile.....	180
Appendix C Loudspeaker Parameters.....	181
1. Loudspeaker design considerations	181
2. Loudspeaker enclosure design	181
3. Noise cancellation and echo suppression.....	182
4. Loudspeaker lobes and interference.....	183
Appendix D Calibrations.....	187
1. Density measurements of marbles used in granular testing.....	187
2. Calibration of variable chamber resonator, SMC LXPB200 linear actuator	187
3. Anechoic chamber calibration of microphone and loudspeaker.....	188
4. Buoyancy uncertainty due to balance deflection	193
Appendix E Working drawings and data sheets.....	195
Drawings for primary Helmholtz resonator:.....	197
Speaker enclosure drawings:.....	209
Drawings for variable chamber resonator:.....	212
Drawings for volume buoyancy rig:	222
Data sheets	224
References.....	225

Figures and Tables

Figure 1.1.1	Historical Resonators' from Notre Dame Indiana, http://physics.kenyon.edu (last viewed May 2008)	3
Figure 1.1.2	Cross section of historical resonator with listening orifice at rear of chamber. 4	
Figure 1.2.1	Schematic of automatic continuous volume measurement system, Nishizu <i>et al.</i> (2001).	7
Figure 1.2.2	Schematic of Helmholtz resonator fuel tank designed to be used in micro-gravity conditions, Nakano <i>et al.</i> (2006).	8
Figure 1.2.3	a) Helmholtz resonator designed for measuring a human's volume. b) Super position of whistle frequency onto Helmholtz frequency (Johnson Jr., 1995). 9	
Figure 1.2.4	Variable volume Helmholtz resonator designed and implemented by De Bedout <i>et al.</i> (Left) top view, (right) side view (De Bedout <i>et al.</i> , 1996).	10
Figure 1.2.5	Diagram of a constant-volume gas pycnometer. The sample- chamber and the tank, initially filled with gas at two different pressures, are connected by opening valve 'Z' (from Tamari 2004).	11
Figure 2.1.1	a) Simple ideal resonator showing moving mass of air in port compressing air in chamber volume and springing back due to the increased pressure in the chamber. b) Equivalent mass spring system.	17
Figure 2.1.2	Flange material will alter the virtual or effective port length.	18
Figure 2.1.3	Port placed eccentrically with respect to the chamber centre.	25
Figure 2.1.4	Chamber with tapered conical port.	26
Figure 2.1.5	Sinusoidal representation of pressure within chamber occurring when dimensions of the resonator are a significant fraction of the resonant frequency wavelength.	27
Figure 2.1.6	Three methods for determination of resonant frequency using traditional ($1/kL$), improved traditional ($1/kL - [kL]/3$) and transcendental ($\cot[kL]$). 31	
Figure 3.2.1	a) Photo of standard single asymmetric port resonator with blanking plate on bottom face having a 3L chamber (140mm internal diameter), 170mm long port with an internal radius of 44mm and b) schematic diagram.	37
Figure 3.2.2	A) Single 170mm asymmetric port plate B) 51mm asymmetric port plate C) 170mm symmetric port plate	38
Table 3.2.1	Fourteen possible resonator combinations possible using available chamber sizes, port lengths and port types.	38
Figure 3.2.3	Microphone locations on resonant chamber, able to measure port frequency and chamber frequency independently.	39
Figure 3.2.4	A) Schematic of hardware components used in experimental setup. B) Resonator alignment and distance from speaker.	39
Figure 3.2.5	A) Decaying regular spacing of harmonic frequencies present in square wave. B) Expected amplification of harmonic near Helmholtz resonant frequency.	41
Figure 3.2.6	Vertical arrangement of dual port resonator showing pulleys above and below to locate sample.	42
Figure 3.2.7	Horizontal arrangement of dual port 3L resonator showing pulleys above and below to locate sample. Also shown are placement holes for pulley support posts allowing multiple horizontal placements to be investigated.	42

Table 3.2.2	Bulk density and particle density information for granular materials. ‘*’ indicates approximate only.....	43
Table 3.2.3	Change in water density with temperature (Lide, 1990).....	44
Figure 3.3.1	Photo (left) and diagram (right) of water filling of 3L chamber with 170mm, asymmetric port used for volume calibration.	47
Figure 3.3.2	(a): Flanged internal and un-flanged external port, asymmetric. (b): Un-flanged internal and un-flanged external port, symmetric.....	48
Figure 3.3.3	A) Photograph of one of the six flat disks (20mm diameter) used to isolate surface area effects from volume effects. B) Diagram of resonator housing a disk of variable size and position.	49
Figure 3.3.4	A) Photograph of the adjustable piston within chamber and B) Schematic diagram. C) Photo of embedded magnet within piston used for retaining steel coated disks. D) Photo of ballotini coated disk.	50
Figure 3.3.5	(Left) five positions for a spherical sample moving through the resonator vertically. (Right) horizontally adjusted spherical sample. Both configurations are driven by a stepper motor to create resonant mapping characteristics for the dual port resonator.	51
Figure 3.3.6	Flange material added resonator port. Flange material will alter the virtual or effective port length.	52
Figure 3.4.1	Attenuation in peak amplitude caused by changing experimental environment, where ‘A’ and ‘B’ are door A and B and ‘O’ and ‘C’ are open and closed. 3L chamber with a 170mm long, 22mm radius asymmetric port.....	54
Table 3.4.1	Comparison of predicted Q factors, Equation (No.25), and actual measured Q factors, Equation (No.24), from Basic Equations. Q factors were evaluated for various chamber and port configurations at 20 degrees C.....	55
Figure 3.4.2	Resonant Frequency versus amplitude for increasing water fill level indicating changes in peak sound level. Tests used 3L chamber with 22mm radius, asymmetric, 170mm long port.	56
Figure 3.4.3	Empirical, using the Helmholtz equation, and standard theoretical speed of sound gradient for changes in ambient temperature for 3L chamber with 170mm port.	57
Figure 3.4.4	Changing value of the Helmholtz constants (α) for increasing temperature using a 3L chamber with 170mm port.	57
Figure 3.4.5	Deviation difference in volume for increasing chamber fill between predicted volume using Helmholtz equation with and without temperature compensation. Tests used water, 3L chamber with 22mm radius, asymmetric, 170mm long port.	58
Figure 3.4.6	Calibration plot of water fill volume versus actual and predicted resonant frequency (Res Freq). Tests used 3L chamber with 22mm radius, asymmetric, 170mm long port.	59
Figure 3.4.7	Second order curve fit of predicted volume deviation from actual volume. Tests used water, 3L chamber with 22mm radius, asymmetric, 170mm long port.	59
Figure 3.4.8	High Q factor for water calibration tests up to fill of 2500mL. Tests used 3L chamber with 22mm radius, asymmetric, 170mm long port.	60
Figure 3.4.9	Comparison of vertical and horizontal volume deviation with water filling using 3L chamber with 22mm radius 170mm long asymmetric port.	60
Figure 3.4.10	Parabolic curve fit of predicted volume deviation from actual volume using solid piston. Tests used 3L chamber with 22mm radius, asymmetric, 170mm long port.	61

Figure 3.4.11	Deviation of predicted volume from actual volume using water fill data for various chamber volume sizes. Tests used 1, 2 and 3L chambers with 22mm radius, asymmetric, 170mm long port.	61
Figure 3.4.12	Second order curve fit of predicted volume deviation from actual volume using symmetric port. Tests used water, 3L chamber with 22mm radius, symmetric, 170mm long port.	62
Figure 3.4.13	Curves of predicted volume deviation from actual volume using individual spherical samples and large cubic blocks. Tests used 3L chamber with 22mm radius, asymmetric, 170mm long port.	63
Figure 3.4.14	Curves of predicted volume deviation from actual volume using 1, 2 and 3L chambers with individual spherical samples. Tests used 3L chamber with 22mm radius, asymmetric, 170mm long port.	64
Figure 3.4.15	Frequency deviation plot for various disks having different cross sectional area in 3L chamber with 170mm port.....	64
Figure 3.4.16	Plot showing the maximum height a disk can extend into the chamber based on it's cross sectional area percentage to that of the chamber's cross sectional area.	65
Figure 3.4.17	Comparison of actual volume versus predicted particle volume for granular materials tested. Tests used 3L chamber with 22mm radius, 170mm asymmetric port.	66
Figure 3.4.18	Comparison of actual volume versus predicted volume for plastic pallets agricultural granular materials tested. Tests used 3L chamber with 22mm radius, 170mm asymmetric port.	67
Figure 3.4.19	Q factor with increasing particle fill fraction. Using a 3L chamber, 22mm radius, 170mm asymmetric port.	68
Figure 3.4.20	Attenuation with increasing particle fill level for marbles, ballotini and sand. Using a 3L chamber, 22mm radius, 170mm asymmetric port.....	69
Figure 3.4.21	Broad spectrum frequency sweep as measured in the port with three fill fractions of sand. Using a 3L chamber, 22mm radius, 170mm asymmetric port.	70
Figure 3.4.22	Broad spectrum frequency sweep as measured in the chamber with three fill fractions of sand. Using a 3L chamber, 22mm radius, 170mm asymmetric port.	70
Figure 3.4.23	Change in linear curve fitted slope for changing particle size. Using a variable 3L chamber, 22mm radius, 170mm asymmetric port.	71
Figure 3.4.24	Logarithmic trend of Q factor for changing particle size measured at 25% fill. Using a variable 3L chamber, 22mm radius, 170mm asymmetric port.	71
Figure 3.4.25	Comparative Q factor testing with various granular coated piston surfaces. Using a variable 3L chamber, 22mm radius, 170mm asymmetric port.	72
Figure 3.4.26	Experimental differences in volume predictive deviation due to piston coating materials. Using a variable 3L chamber, 22mm radius, 170mm asymmetric port.	73
Figure 3.4.27	Observed linear increase in resonant frequency due to an increasing number of air leaks in the resonant chamber. Using a 3L chamber, 22mm radius, 170mm asymmetric port.	73
Figure 3.4.28	Data fitted with logarithmic decreasing Q factor due to an increasing number of air leaks in the resonant chamber. Using a 3L chamber, 22mm radius, 170mm asymmetric port.	74

Figure 3.4.29	Data fitted with second order curve for rise in frequency with increasing leak diameter. 3L chamber with 170mm long port having 22mm radius.	74
Figure 3.4.30	Q factor with increasing leak diameter fitted with a second order curve. 3L chamber with 170mm long port having 22mm radius.....	75
Figure 3.4.31	Frequency chamber mapping using a 42mL aluminium sphere moved in the radial direction in 1mm steps at 5 positions along the chamber's length. The frequency has been normalised and temperature corrected. Also shown is the 3L chamber indicating orientation of mapping, width being radial movement and horizontal being chamber length.	76
Figure 3.4.32	Frequency chamber mapping using a 42mL aluminium sphere moved in an axial direction in 1mm steps along the chamber's length. Using a 3L chamber with two 22mm radius, 51mm asymmetric ports.....	77
Figure 3.4.33	Enlargement of 'stable' region in figure 4.32. Plot shows change in mL from a central value of 3168mL at 145mm displacement. Using a 3L chamber with two 22mm radius, 51mm asymmetric ports.....	77
Figure 3.4.34	Effects of various flange sizes on resonant frequency used to evaluate port length extension. Measurements taken with 3L resonator having two different port lengths, 51mm and 170mm.....	78
Figure 4.2.1	Variable chamber resonator, 1.6L – 3.5L with 175mm port. Shown are linear actuator placement and movable floor plate allowing sample insertion....	95
Figure 4.2.2	Inverted port resonator with removable port piece allowing easy access to chamber.....	96
Figure 4.2.3	Buoyancy rig used to either suspend sample or provide forced immersion for samples less dense than water.	96
Table 4.2.1	Various produce and mineral samples used in variable chamber resonator using Q profile shifting.	97
Figure 4.3.1	Software adjustments to the Q profile required to make predictive volume measurements. A is the frequency shift due to temperature change, B the frequency shift associated with a volume change and D the total change in frequency that is used to predict the new resonant frequency. C is the amplitude change proportional to the change in microphone level at the initial resonant frequency.....	100
Figure 4.4.1	Q profiles for four chamber configurations, each using a different sized sphere. Using a 3L chamber with two 22mm radius, 51mm asymmetric ports.	105
Figure 4.4.2	Resonant peak with increasing sample size for Q profile shifting. Tests used a 3L chamber with two 22mm radius, 51mm asymmetric ports.	106
Figure 4.4.3	Reduction in RMS amplitude as samples pass through the chamber at 80mm/s. Transition dips are present as the samples pass through the ports. Using a 3L chamber with two 22mm radius, 51mm asymmetric ports.....	106
Figure 4.4.4	Comparison between spline fit and 5 th order polynomial using an empty chamber. 3L chamber with two 22mm radius, 51mm asymmetric ports.	107
Figure 4.4.5	Changes in descent speed for an aluminium sphere of 42mL. Speeds 1, 5 and 10 are 28mm/s, 50mm/s and 100mm/s respectively. Tests used a 3L chamber with two 22mm radius, 51mm asymmetric ports.....	108
Figure 4.4.6	a) Free fall data for 9mL and 23mL spheres. 9mL sphere measurement at 0.1s and 23mL measurement time at 0.25s b) comparison of slower descent speed at 60mm/s. Tests used a 3L chamber with two 22mm radius, 51mm asymmetric ports.....	109

Figure 4.4.7	Corrected Q factor curve using <i>ENC</i> .	109
Figure 4.4.8	Comparison of Q factor curve dynamically adjusted with <i>ENC</i> data and the same Q factor curve post processed using the <i>ENC</i> data.	110
Figure 4.4.9	Stability and linear shifting of environmental profile with changing temperature between 60Hz-100Hz.	110
Figure 4.4.10	Resonant peak amplitudes for various chamber fill levels and the <i>ENC</i> profile.	111
Figure 4.4.11	Q profiles for increasing fill with <i>ENC</i> corrected curves using a 3L chamber and 51mm port with increasing fill level using water.	112
Figure 4.4.12	Five repeat measurements of the Q profile and the environmental curve at 17.0°C showing negligible variation.	112
Figure 4.4.13	Temperature stability tests at T1 (21.9°C) and T2 (13.6°C) using a 3L chamber with a 51mm port and a 278mL steel sphere sample.	113
Figure 4.4.14	Temperature stability: Sound pressure level deviation for the empty chamber and for a 278mL spherical displacement sample. Resonator has 3L chamber with 51mm long, 44mm diameter port.	113
Figure 4.4.15	Q profile stability profiles taken at constant temperature and using 278mL steel sphere sample showing profile insensitivity to volume change. Also shown is a frequency-shifted profile of the empty chamber to allow direct comparison. The chamber was 3L and port 51mm.	114
Figure 4.4.16	Q profile stability: associated sound pressure level deviation for a 278mL spherical displacement sample. Resonator has 3L chamber with 51mm long, 44mm diameter port.	114
Figure 4.4.17	Volume deviation data and second order polynomial fitted curves for differing sample shape using the continuous <i>QPS</i> method. Resonator has 3L chamber with 51mm long, 44mm diameter port.	115
Figure 4.4.18	Continuous <i>QPS</i> deviation volume from true volume using a generic correction factor on water fill, sphere and cube volume. Resonator has 3L chamber with 51mm long, 44mm diameter port.	116
Figure 4.4.19	Environmentally normalization curve, corrected curve and inverted port resonator Q profiles curves with three port insert plug configurations.	117
Figure 4.4.20	Boundary layer to port area becomes substantial for the inverted port resonator necessitating a large port area.	118
Figure 4.4.21	Deviation volume and second order fitted curves, implemented with <i>VCR</i> using <i>QPS</i> , when calibrating for a piston, spheres and cubes. <i>VCR</i> resonator has 3.5L chamber with 175mm long, 44mm diameter port.	119
Figure 4.4.22	<i>VCR</i> deviation volume from true volume using a generic correction factor on piston, sphere and cube volumes. <i>VCR</i> resonator has 3.5L chamber with 175mm long, 44mm diameter port.	119
Figure 4.4.23	<i>VCR</i> volume deviation from true volume using a specific second order correction on piston, sphere and cube volumes. Resonator has 3.5L chamber with 175mm long, 44mm diameter port.	120
Figure 4.4.24	<i>VCR</i> with dynamic <i>QPS</i> of 133mL sample showing original (empty), predicted and measured Q profiles. Resonator has 3.5L chamber with 175mm long, 44mm diameter port.	121
Figure 4.4.25	Plot of amplitude deviation with changing frequency for 133mL sample, predicted and actual Q profiles. Resonator has 3.5L chamber with 175mm long, 44mm diameter port.	121

Figure 4.4.26	VCR with dynamic <i>QPS</i> of 215mL cube sample showing original (empty), predicted and measured <i>Q</i> profiles. VCR resonator has 3.5L chamber with 175mm long, 44mm diameter port.	122
Figure 4.4.27	Plot of amplitude deviation with changing frequency for 215mL cube sample, predicted and actual <i>Q</i> profiles. VCR resonator has 3.5L chamber with 175mm long, 44mm diameter port.	122
Figure 4.4.28	Produce tests displaying the deviation of the predicted volume from the actual volume. VCR resonator has 3.5L chamber with 175mm long, 44mm diameter port.	123
Figure 4.4.29	Mineral tests displaying parabolic deviation of greywacke and linear deviation of schist samples. VCR resonator has 3.5L chamber with 175mm long, 44mm diameter port.	123
Figure 4.4.30	Comparison of two mineral sample types and two produce sample types as measured in VCR with 3.5L chamber volume.	124
Figure 4.4.31	Greywacke and schist samples as measured in VCR with chamber volume of 2L with low deviation in volume measurement.	125
Figure 4.1	Pressure at distance <i>R</i> from surface element caused by a piston radiator.	152
Figure 5.1	Pressure decay from axial direction extending over <i>x</i> , where <i>x</i> is defined as <i>kasin</i> (θ).	154
Figure 6.1	Piston face occupied by two arbitrary surface elements <i>dS</i> and <i>dS'</i> and their geometric relations	155
Figure 7.1	The Resistive and reactive coefficients for increasing <i>ka</i> and the first four term approximations for the Bessel and Struve functions.....	157
Figure 9.1	Velocity profile from internal port surface boundary. Arrows indicate velocity direction and magnitude. The boundary grows linearly with length. ..	160
Figure 11.1	Sound source driving into impedance <i>Z</i> ₁ which then changes to impedance <i>Z</i> ₂ . The distance <i>d=L-x</i> for considering pressure and velocity as a function of the distance from the impedance change.....	165
Figure 4.1a	Polar plot of sound intensity for an 8" speaker at 100Hz	183
Figure 4.1b	Polar plot of sound intensity for an 8" speaker at 500Hz	183
Figure 4.1c	Polar plot of sound intensity for an 8" speaker at 1kHz	184
Figure 4.1d	Polar plot of sound intensity for an 8" speaker at 5kHz	184
Figure 4.2	Interference caused by reradiating by sharp edges within proximity of sound source (fringing).	185
Figure 2.1	The SMC LXPB200 linear actuator diagram showing where calibration measurements were taken.	187
Figure 2.2	<i>Q</i> factor tests of VCR when dry and with a 50mL thin water film covering the piston.	188
Figure 3.1	Broad frequency sweep of anechoic chamber and two positions used in non-anechoic environment. Measurements made with PCB 103A microphone mounted 30 degree off axis at 0.5m. Position 2 taken atop of VCR resonator with port plug 50 degrees off axis at 0.5m.....	189
Figure 3.2	Broad frequency sweep comparison between PCB 103A microphone, <i>Realistic</i> sound meter and <i>Quest</i> sound meter taken in anechoic chamber. Fast sweep, 2Hz/sec.....	190
Figure 3.3	Broad frequency sweep deviation from the PCB 103A microphone for the <i>Realistic</i> sound meter and <i>Quest</i> sound meter taken in anechoic chamber. Fast sweep, 2Hz/sec	190

Figure 3.4	Narrow frequency sweep comparison between PCB 103A microphone, <i>Realistic</i> sound meter and <i>Quest</i> sound meter taken in anechoic chamber. Slow sweep, 0.2Hz/sec.....	191
Figure 3.5	Narrow frequency sweep deviation comparison between <i>Realistic</i> sound meter and <i>Quest</i> sound meter taken in anechoic chamber. Slow sweep, 0.2Hz/sec.....	191
Figure 3.6	Calibration tests using 1Vpp and 2Vpp signals generated by DAQ, demonstrating a 3dB change in level as measured in the port. Also shown is a corrected output profile using <i>ENC</i> data at -37dB.	192
Figure 3.7	Output from the <i>Realistic</i> sound meter and PCB 103A microphone in experimental environment. Amplitude is referenced to a 90dB level (0dB = 90dB).	192
Figure 3.8	Anechoic chamber <i>VCR</i> volume deviation from true volume using a specific correction factor on piston volumes. Resonator has 3.5L chamber with 175mm long, 44mm diameter port.....	193
Figure 4.1	Scale deflection tests for establishing buoyancy uncertainty due to the immersion stem.	194
	Complete Helmholtz resonator assembly with dual ports and pulley back plate assembly.....	208
	Pinch roller assembly.....	208
	Complete Assembly of variable chamber resonator	221

Nomenclature

a	Primary radius , polynomial coefficient (with subscript)	(m)
BL	Boundary layer	(m)
c	Speed of sound	(m/s)
c_p	Specific heat, constant pressure	(J/kg.K)
c_v	Specific heat, constant volume	(J/kg.K)
c_0	Speed of sound (STP)	(m/s)
d	Diameter	(m)
D	Energy density	(W.s/m ³)
f	Force	(N)
$freq$	Frequency	(Hz)
i	Complex notation	-
I	Intensity	(W/m ²)
k	Wave number	($k = \omega/c$)
L	Length	(m)
l_p	Port length	(m)
l_p'	Total port length	(m)
L_{mfp}	Mean free path length	(m)
Δl	Port length extension	(m)
m	Mass	(kg)
M	Mean molecular weight	(kg)
M_{mol}	Molar mass	(kg)
n	Number of moles	-
N	Number of molecules	-
p	Particular pressure	(Pa)
p_0	Pressure at STP	(Pa)
P_0	Primary pressure	(Pa)
δp	Excess pressure	(Pa)
P_r	Prandtl number	-
Q	Quality factor	-
Q_s	Strength of source	-
r	Primary distance from source	(m)
R	Secondary distance from source, Reflection ()	(m)
R_a	Acoustic resistance	(N.m/s ⁵)
R_m	Mechanical resistance	(N.m/s)
R_r	Radiation resistance	(N.m/s)
$R_{reflect}$	Reflective coefficient	-
R_c	Gas constant	(8.31 J/mol.K)
R_N	Reynolds number	-
S	Surface	(m ²)
s	Cross sectional area	(m ²)
ST	Sweep time	(s)
t	Time	(s)
T	Wave period	(s)
T_{emp}	Temperature	(K)
$T_{transmit}$	Transmission coefficient	(m/s)
U_0	Primary velocity	(m/s)
U_s	Specific velocity	(m/s)
U_v	Volume velocity	(m ³ /s)

V	Volume	(m ³)
w	Sample volume	(m ³)
X_a	Acoustic reactance	(N.m/s ⁵)
X_m	Mechanical reactance	(N.m/s)
X_r	Radiation reactance	(N.m/s)
Y	Thermal conductivity	(W/m.K)
Z	Characteristic impedance	(N.m/s ³)
Z_a	Acoustic impedance	(N.m/s ⁵)
Z_m	Mechanical impedance	(N.m/s)
Z_r	Radiation impedance	(N.m/s)
Z_s	Specific impedance	(N.m/s ³)

Greek symbols

α	Helmholtz equation constant	(Hz/K)
β	Temperature gradient compensation	-
δ	Length extension factor	(m)
γ	Adiabatic gas ratio	(c _p /c _v)
θ	Primary angle	(radians)
λ	Wavelength	(m)
μ	Viscosity	(N.s/m ²)
ρ	Particular air density	(kg/m ³)
ρ_0	Density at STP	(kg/m ³)
$\delta\rho$	Excess density	(kg/m ³)
ς	Power reflective coefficient	-
σ	Secondary radius	(m)
τ	Power transmission coefficient	-
ν	Kinematic viscosity	(m ² /s)
ν_{rms}	Root mean squared velocity	(m/s)
φ	Secondary Angle	(radians)
ψ	Tertiary angle	(radians)
ω	Angular frequency	(radians/s)
Ω	Approximation function	-

Subscripts

$+$	Incident	$-$	Reflected
0	Initial value	$1,2$	Later values, coefficient number
c	Chamber	e	Extension
H	High	i	inner
n	Value in	$inst$	Instantaneous
L	Low	max	Maximum
min	Minimum	o	outer
Out	Value out	p	Port
t	Transmitted	T	Temperature
$Therm$	Thermal	$Visc$	Viscous

Vector quantities are represented by either a cap or in **bold**.

Basic equations

Particular pressure: $p = \rho_0 c U_0$ (1)

Volume velocity: $U_v = S U_s$ (2)

Acoustic impedance: $Z_a = p / U_v = Z_s / s_p$ (3)

Specific impedance: $Z_s = p / U_s$ (4)

Mechanical impedance: $Z_m = f / U_s$ (5)

Radiation impedance: $Z_r = Z_a s_p^2 = Z_s s_p$ (6)

Characteristic impedance: $Z = \rho_0 c$ (7)

Acoustic intensity for a sphere: $I = p^2 / 2 \rho_0 c$ (8)

Acoustic power for a sphere: $W = 4 \pi a^2 I$ (9)

Sound energy density: $D = p^2 / \rho_0 c^2 = p^2 / \rho_0$ (10)

Acoustic intensity level (dB): $Intensity = 10 \log_{10} \left(\frac{I_{out}}{I_{in}} \right)$ (11)

Acoustic power level (dB): $power = 10 \log_{10} \left(\frac{W_{out}^2 \rho_0 c}{\rho_0 c W_{in}^2} \right)$ (12)

Specific resistance derivation: $power = 10 \log_{10} \left(\frac{W_{out}^2 R_s^{in}}{R_s^{out} W_{in}^2} \right)$ (12a)

$$power = 20 \log_{10} \left(\frac{W_{out}}{W_{in}} \right) + 10 \log_{10} \left(\frac{R_s^{in}}{R_s^{out}} \right)$$

Sound pressure level (dB): $power = 20 \log_{10} \left(\frac{p}{p_{ref}} \right)$ (13¹)

Excess pressure: $\delta p = p - p_0$ (14)

¹ P_{ref} is a predefined reference pressure of 2x10⁻⁵Pa for hearing and liquids or 0.1Pa for transducer calibration.

Excess density: $\delta\rho = \rho - \rho_0$ (15)

The specific velocity: $U_s = U_0 e^{i\omega t}$ (16)

The specific pressure: $p = P_0 e^{i\omega t}$ (17)

Strength of spherical Source: $Q_s = 4\pi a^2 U_0$ (18)

Forward travelling wave: $p = ZU_s$ (19)

Backward travelling wave: $p = -ZU_s$ (20)

Standard Helmholtz equation

$$\omega_{res} = 2\pi freq = c \sqrt{\frac{s_p}{(V - w)(l_p + \Delta l)}} \quad (21)$$

Sample volume Helmholtz equation

$$w = V - \frac{s_p}{(l_p + \Delta l) \left(\frac{2\pi freq}{\beta c} \right)^2} \quad (22)$$

Temperature correction for speed of sound

$$c_0 = \sqrt{\gamma \frac{P_0}{\rho_0}} = \sqrt{\frac{\mathcal{R}_c T_{emp}}{M}} \quad (23)$$

Measured Q factor equation $Q = \frac{\omega}{(\omega_H - \omega_L)}$ (24)

Theoretical Q factor for a Helmholtz resonator

$$Q = \frac{\omega m}{R_m} = 2\pi \sqrt{\frac{l_p^3 V}{s_p^3}} \quad (25)$$

Glossary

Attenuation	Difference in sound pressure level between two points
BL	Boundary Layer
BEM	Boundary Element Model
Chamber	Main body of resonator in which sample volume is measured
Characteristic impedance	Measure of acoustic resistance in the far field
Chirp	A narrow frequency sweep
CSA	Cross Sectional Area
dB	Decibels, measure of relative sound level
ENC	Environmental Normalisation Curve
Excess pressure	Differential pressure to the density at STP
Excess density	Differential density to the density at STP
Far field	Distance at which sound level is uniform
Flange factor	Multiplying factor for determining port length extension
FFT	Fast Fourier Transform
FEM	Finite Element Model
Helmholtz resonator	Resonator consisting of chamber and port
Interstitial space	Space between adjacent particles in a granular bed
IIR	Infinite Impulse Response (Digital filter)
Length extension	Extra distance the air in port moves beyond physical port length
Mechanical impedance	Combined mechanical resistance and reactance
Mechanical resistance	Sum of all real resistive components in the resonant system
Mechanical reactance	Sum of all imaginary force components in the resonant system
Near field	Distance where localised effects make sound levels non-uniform
Neck	Alternative name for port
Particular pressure	The instantaneous pressure of an oscillatory pressure wave
Pink noise	Random frequencies having equal power
Port	Tube of smaller CSA than chamber connecting chamber to a secondary impedance region (usually an open environment)
Primary pressure	The maximum pressure in an oscillatory pressure wave
Primary velocity	The maximum velocity in an oscillatory wave
Q factor	Quality factor, quality of resonance
QPS	Q Profile Shifting
Radiation impedance	Combined radiation resistance and reactance
Radiation resistance	Measure of the real resistive losses from the port
Radiation reactance	Measure of the imaginary forces in the port
Reflective coefficient	Reflected component based on the ratio change of two impedance mediums
RMS	Root Mean Squared (geometric average)
RTD	Resistive Temperature Device
Specific velocity	The instantaneous velocity of an oscillatory wave

SPL	Sound Pressure Level (dB)
STP	Standard Temperature and Pressure (15°C, 1.01x10 ⁵ Pa)
SWR	Standing Wave Ratio (maximum over minimum pressure)
Transmission coefficient	Transmitted component based on the ratio change of two impedance mediums
VCR	Variable Chamber Resonator
White noise	Random frequencies having random power

Chapter 1

Introduction and literature review

1.1 Introduction

Most people have experienced the sound of Helmholtz resonators without being aware of their underlying principle. Bottles and stringed instruments are perhaps the most common type of Helmholtz resonator. Bottles have the characteristic small opening into a large chamber. If air is blown across a bottle's neck (port) a resonant frequency is emitted that is proportional to the dimensions of the vessel.

A musical instrument such as a guitar has strings placed over an open cavity, the guitar body. The combination of guitar body and orifice act as a Helmholtz resonator with a low broad Q factor. Q factor is the quality factor of a given resonator and indicates the narrowness in frequency range over which the resonator will oscillate. It also indicates the amount of amplification occurring at resonance (See Basic Equations, No.24). The broad Q profile allows the range of tones generated by the strings to be nearly equally amplified.

Resonators form part of our every day lives. A far larger class includes mufflers for cars, noise suppression in air conditioning systems and acoustic dampening in office workspaces. Most serve the purpose of suppressing an unwanted frequency by absorbing the sound within the resonant cavity rather than amplifying it. Acoustic resonators have been known of since the time of the Romans, and it seems probable they were created in one form or another even earlier. The Romans used small resonators for musical instruments and sound damping in their amphitheatres (Dessy, 2001).

The Helmholtz resonator is named after Herman L. F. von Helmholtz [1821-1894], who discovered its physical and mathematical secrets (Helmholtz, 1877). Early experimental resonators such as the type used by Helmholtz are shown in Figure 1.1.1. These instruments consist of a bulbous chamber, a port on the underside and a small stem, Figure 1.1.2, for the user to press against their ear. When air passes over the port the chamber and port will resonate at a frequency determined by the physical characteristics of the instrument: the chamber volume, port length and port cross sectional area. Also important is the physical medium in the resonator and the speed of sound in that medium.

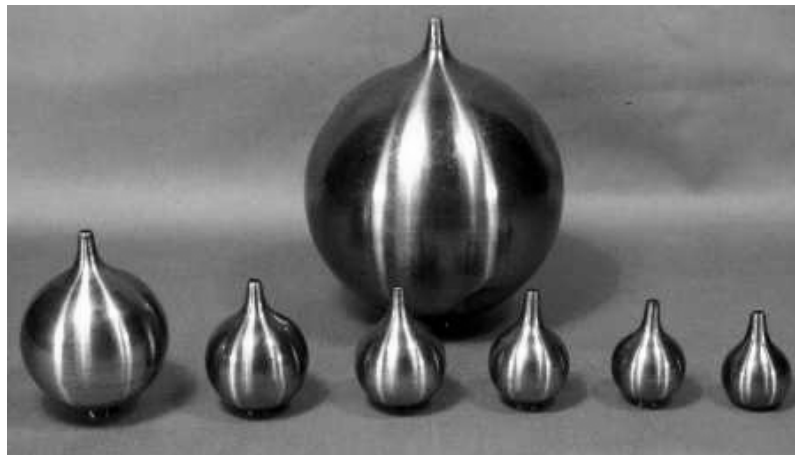


Figure 1.1.1 Historical Resonators' from Notre Dame Indiana, <http://physics.kenyon.edu> (last viewed May 2008)

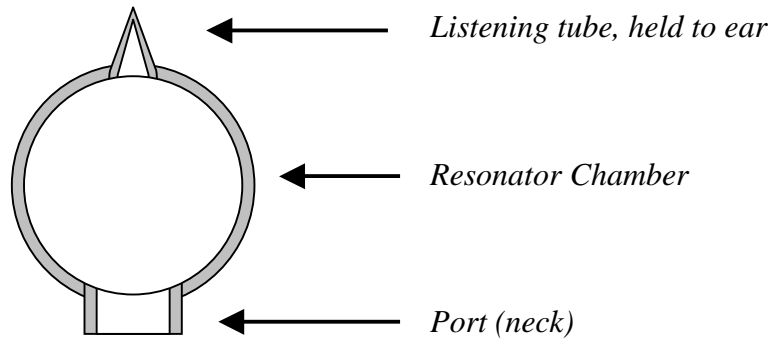


Figure 1.1.2 Cross section of historical resonator with listening orifice at rear of chamber.

The fundamental Helmholtz equation specifies that the resonant frequency is proportional to the square root of the cross sectional area of the port divided by the resonator chamber volume and port length, Equation 1.1.1:

$$freq = \frac{c}{2\pi} \sqrt{\frac{s_p}{V_c l_p}} \quad (1.1.1)$$

where c is velocity of sound, s_p is cross sectional area of throat/opening, V_c is volume of chamber and l_p is length of the port

Helmholtz resonators are a rich area for investigation, despite the fundamental equations of acoustics being put forward by Lord Rayleigh, (1877) almost a hundred years ago. This is due to non-linear effects and developments in new methods for reducing and understanding their complexity.

The purpose of this study has been to investigate the use of Helmholtz resonators as a method for determining the volume of an object. The inclusion of an object into the resonant chamber has the effect of reducing the effective resonator volume. Hence, there is a direct link between the emitted resonant frequency and the volume of the object within the chamber.

The practicalities of such a system allow for non-destructive, deformation free, volume measurements of liquids, solids and granular material within the chamber. Such measurements have historically proved difficult due to the time required for measurement. Classical pycnometers have been the most accurate way of performing interference and degradation free volume measurements. But, pycnometers are very slow devices taking typically between 3 to 5 minutes to make a single measurement. Pycnometers differ slightly in that they can measure skeletal object volumes when gases with appropriately small atomic sizes are used, for example helium and nitrogen.

Using a Helmholtz resonator, a rapid and robust volume measurement system can be created which, in some instances, can be used instead of a pycnometer. Doing so avoids the pycnometer's reliance on lengthy calibration procedures. There is also

potential for far greater reliability with an acoustical system, due to a minimum of moving parts and avoidance of special chamber conditions.

This investigation aimed to rigorously evaluate the variables involved in accurately determining the volume of samples placed within a Helmholtz resonant chamber. A set of methods was developed to better understand the significance and magnitude of the variables likely to affect accuracy. These included chamber dimensions, port dimensions, sample location, sample shape, acoustic barriers, granular samples, dynamic measurements of moving samples and acoustic free-field coupling. Novel approaches in further increasing speed of measurement time were also tested. These included a resonant hunting procedure developed and described in Chapter 3 and three Q profile shifting methods, described in Chapter 4.

1.2 Literature Review: Volume measurement

1.2.1 Experimental volume measurement using a Helmholtz resonator

Nishizu *et al.* (2001) described a method for volume measurements using Helmholtz resonators. They used a three-port resonator driven by a loud speaker in the top port. The system also contained a belt conveyor, which was able to move samples through an inlet port and out an exit port, Figure 1.2.1. A microphone was placed in the loudspeaker port to provide resonant frequency information to a computer.

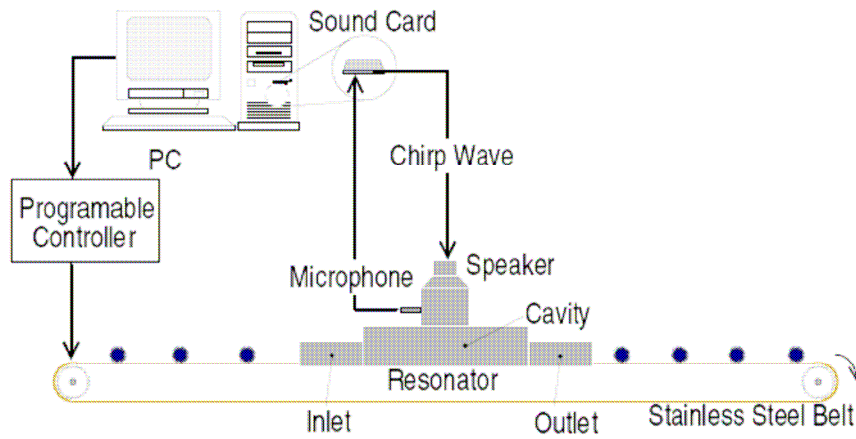


Figure 1.2.1 Schematic of automatic continuous volume measurement system, Nishizu *et al.* (2001).

The analysis for the three-port resonator is similar to that given in Appendix A, Section 12 and results in Equation (1.2.1). The chamber volume for the resonator is variable, changing by an amount determined by the sample volume w . The ports are considered to be equal diameter and length. The length extension term, Equation (1.2.2), is that described by Appendix A, Section 8. Manipulation of Equation (1.2.1) gives Equation (1.2.3), which describes the volume w , of an object placed in the resonant chamber. The resonant frequency is then measured to back-calculate the sample volume.

$$freq = \frac{c}{2\pi} \sqrt{\frac{3s_p}{(V - w)(l_p + \Delta l)}} \quad (1.2.1)$$

where $freq$ is resonant frequency; c is velocity of sound; s_p is cross sectional area of the port; V is volume of chamber; w is the sample volume; l_p is length of the port and where r the radius of the port

$$\Delta l = 0.6r + \frac{8}{3\pi}r \quad (1.2.2)$$

$$w = V - \frac{S_p}{(l_p + \Delta l) \left(\frac{2\pi freq}{c} \right)^2} \quad (1.2.3)$$

The system created by Nishizu *et al.* (2001) was required to make measurements as quickly as possible due to a moving conveyor belt transporting the samples. As a sample moves through the chamber various resonant properties of the chamber will change. A maximum entropy (Bayesian statistics) method of analysing the data was used to reduce the time required to build a frequency spectrum. Precision in the measurement of frequency spectrum usually requires a large number chirps. A chirp is a frequency range over which the sound is incrementally swept through. Chirps are used to pinpoint the resonant frequency. By statistically predicting only the allowable frequencies the resolution of the frequency spectrum was increased. However, the entropic method used by Nishizu *et al.* was not stated.

When the sample enters and leaves a port that port becomes obstructed and the resonant frequency changes in proportion to the available port cross sectional area. Effects such as chamber volume geometry may become significant, as described in Chapter 2, Section 11, when the sample is inside the chamber. These two effects limit the internal region where the Helmholtz equation is valid. Nishizu *et al.* (2001) described this region as the ‘sweet spot’ within the resonator chamber.

A Helmholtz resonator for volume measurements of fuel tanks under micro-gravity is one of the more esoteric uses of the acoustic resonance technique and was developed by Nakano *et al.* (2006). A sealed spherical chamber was used to house the fuel. A stem containing a loudspeaker was connected inside the chamber. The loudspeaker projected sound down this stem and into the cavity in which the fuel was stored, Figure 1.2.2.

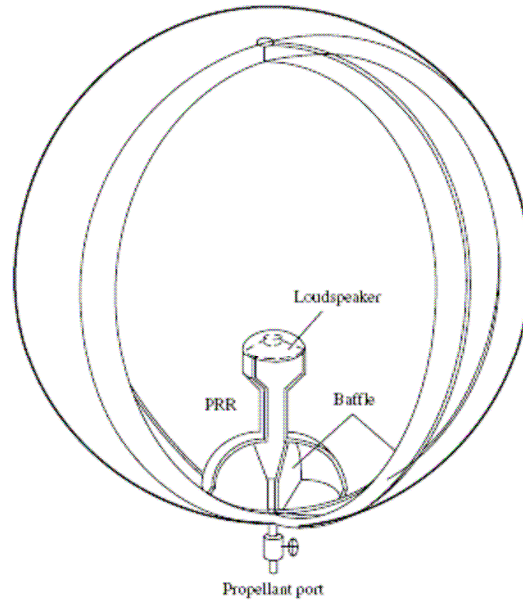


Figure 1.2.2 Schematic of Helmholtz resonator fuel tank designed to be used in micro-gravity conditions, Nakano *et al.* (2006).

The micro-gravity resonator was partially successful with a cautionary note indicating further investigation was required. This may have been due to a variation in the way measurements were taken. In that particular application the speaker was used as the sound source as well as the microphone. The changing impedance of the speaker was used to indicate the resonant frequency. At the point of resonance the impedance will suddenly rise. When using the loudspeaker as a microphone caution is needed to ensure the natural resonance of the loudspeaker does not overlap with the range of resonance caused by the Helmholtz effect.

1.2.2 Patent for Helmholtz volume measurement device

Johnson Jr. (1995) made a US patent application, in which he described a Helmholtz resonator suitable for measuring a human's volume, Figure 1.2.3a. The differences between his technique and others were the method of resonant stimulation and the negation of ambient humidity and temperature effects. The stimulation method relied on blowing air past the resonator port rather than applying a chirp (frequency scan) to isolate the resonant frequency. In principle the resonator is only induced to resonate at its fundamental frequency, which is proportional to the free chamber space.

By incorporating a $\frac{1}{4}$ or $\frac{1}{2}$ wave resonant whistle within the main chamber its frequency will be altered by temperature and humidity at the same rate as the Helmholtz resonator. By superimposing the frequencies of the two resonators the ratio between the two can be used to determine the volume displacement in the main chamber, Figure 1.2.3b. Johnson Jr. claims the accuracy of such a system could be expected to be $\pm 1\%$ of the sample volume and the measurement time only 3 seconds.

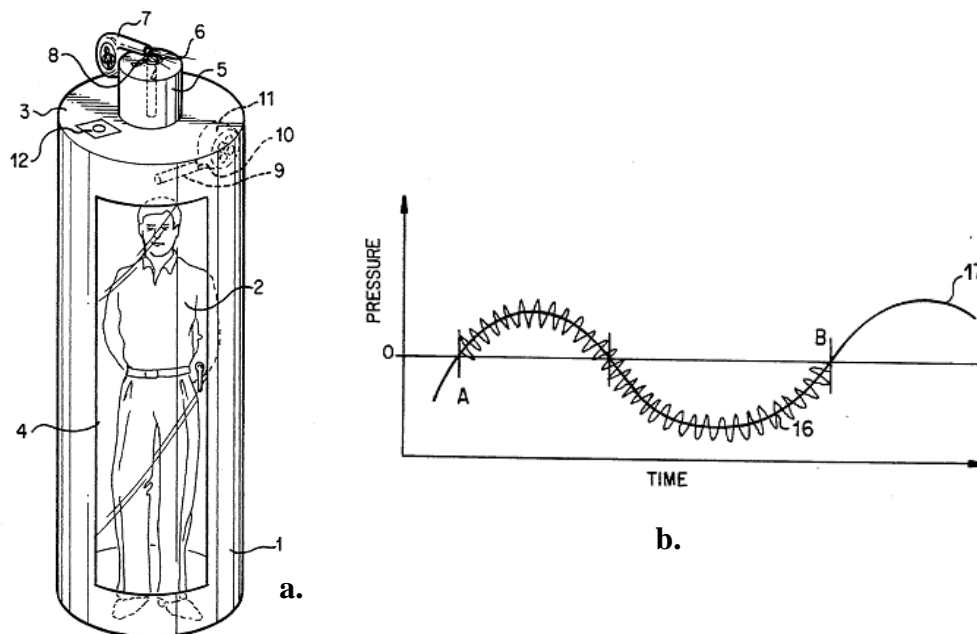


Figure 1.2.3 a) Helmholtz resonator designed for measuring a human's volume. b) Superposition of whistle frequency onto Helmholtz frequency (Johnson Jr., 1995).

1.2.3 Experimental Helmholtz resonator with variable chamber size

De Bedout *et al.* (1996) constructed a variable volume resonator in the hope of developing a system capable of adaptive noise control in ducting systems. They used a hinged wall capable of segmenting off a part of the resonator volume, Figure 1.2.4.

The wall was connected to a motor which was position monitored by a potentiometer. The combination of motor and potentiometer was able to give positional feedback and allow adaptive control.

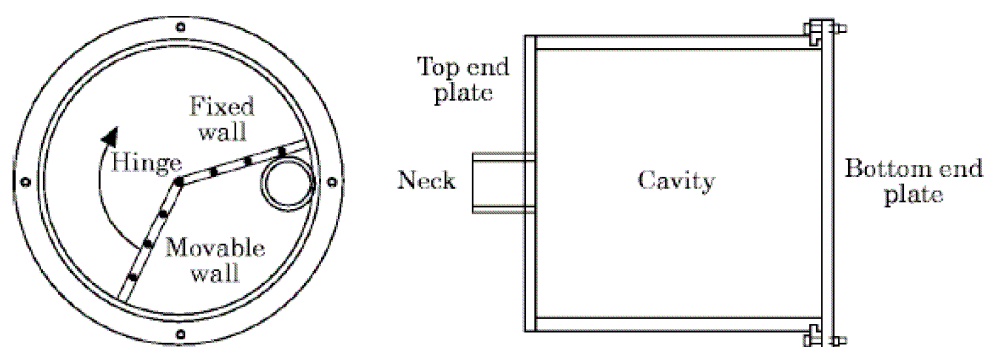


Figure 1.2.4 Variable volume Helmholtz resonator designed and implemented by De Bedout *et al.* (Left) top view, (right) side view (De Bedout *et al.*, 1996)

The system had a number of limitations which included: 1) non-ideal placement of the port and non-ideal internal shape of the resonator leading to significant deviations in resonant frequency prediction 2) the potentiometer was only capable of providing an approximate angle via its resistance 3) there was no temperature speed of sound compensation 4) no attempt to account for discrepancies in signal levels over the frequency range tested 5) the loudspeaker was not suitable for reproducing the low frequency range required of it.

Despite the numerous shortcomings they were able to demonstrate an adaptive resonator could be built that was capable of attenuating the driving frequency up to a maximum value of 30dB, but more typically 20dB. Using acoustical theory a more carefully designed resonator system should be able to give uniform attenuation over the frequency range they intended it for. The addition of temperature compensation would also improve the initial positioning of the wall and allow far quicker closed loop control times.

A determining factor in the development of this adaptive-passive noise control system was the prohibitively expensive digital signal processing systems of the time. This is no longer the case and therefore digital signal processing systems can achieve better results at significantly lower cost (See for example, Texas Instruments, Texas, USA). A digital signal-processing device would inject out of phase sound - active control - into the ducting system to negate unwanted noise.

1.2.4 Pycnometers

The principle of the pycnometer is based on Boyle's ideal gas law. Boyle's law states that pressure, volume, and gas temperature are all related by a simple formula: $P_0 V = n R_c T_{emp}$, where R_c is a gas constant, n is the number of moles and P_0 , V and T_{emp} are pressure, volume and temperature respectively. To measure the volume of a sample, pressure is applied to a sealed vessel at constant temperature. If the volume of the vessel (V_1) is accurately known before the sample is inserted then the pressure change should be proportional to the vessel volume minus the sample volume (V_2). This can be expressed as $V_2 = P_1 V_1 / P_2$.

Pycnometry has many benefits over the traditional Archimedes principle, which involves submerging the sample in a liquid. A disadvantage of the Archimedes principle is the possibility of water damage to the sample. Another disadvantage is the potential for air to be trapped in pores of the sample leading to a false volume measurement.

An accurate pycnometer requires a well-sealed vessel and a very accurate pressure gauge. For non-skeletal volumes air can be used to pressurise the vessel instead of Helium. A difficulty with performing pycnometry is maintaining a constant vessel temperature since the pressure of the vessel is directly related to its temperature. A constant heat source might be required depending on how long it takes to measure the sample volume.

When using a pycnometer the more space occupied by the sample in the chamber the greater the accuracy. This is apparent from the theory of operation, $PV=nRT$, as the pressure difference between empty and occupied space will be greater. This ensures a reading that approaches full scale for the pressure-measuring device. Theoretical calculations by Tamari (2004) suggest a practical range for chamber filling of between 0.4 and 0.7.

For constant volume systems the accuracy is dependent on tank chamber and sample chamber size ratios, Figure 1.2.5. Tamari (2004) notes that the size of the tank chamber should be about $\frac{2}{3}$ the size of the sample chamber. By using a smaller tank the initial pressure can be high and the final pressure significantly lower when compared with having them the same size. This will maximise the pressure step and allow for increased resolution. The uncertainty in the pressure measurement device will play an increasing role as the final pressure reduces. Hence, there are two conflicting requirements, achieve a large pressure step and maintain a high pressure within the sample chamber.

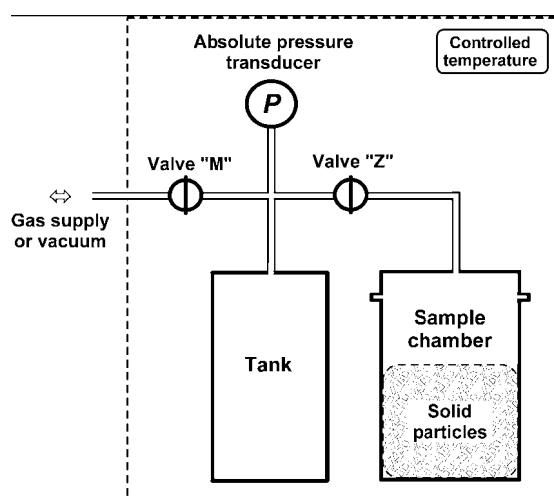


Figure 1.2.5 Diagram of a constant-volume gas pycnometer. The sample-chamber and the tank, initially filled with gas at two different pressures, are connected by opening valve 'Z' (from Tamari 2004).

When the valve 'Z' from Figure 1.2.5 is opened it will cause a sudden pressurisation of the sample chamber, which in turn will cause a rapid temperature rise. This

temperature step must be allowed to dissipate through the walls of the chamber before an accurate pressure reading can be achieved.

Precision in pressure measurement is the biggest uncertainty that pycnometry faces, as noted by both Oppenheimer *et al.* (1997) and Tamari (2004). Oppenheimer observed that a 1% inaccuracy in pressure measurement leads to an approximate 4% uncertainty of the sample volume. According to Tamari 0.0006% to 0.00175% is the ultimate accuracy that could be achieved using a well-designed pycnometer. This is a theoretical calculation. But, the values he derives are based on 'off the shelf' high precision components.

1.2.5 Commercial pycnometers

Readily available commercial pycnometers, such as the AccuPyc 1330 (Made by Micrometrics, USA), typically have very small chambers (providing increased accuracy), use helium gas and can take anywhere between three to thirty minutes per measurement, dependant on required accuracy. This type of pycnometer is suited to laboratories for measuring small complex shapes, powders or chemical samples. Agnew *et al.* (2003) created a much larger and more robust pycnometer for measuring biomass. However, the apparatus had a much-reduced accuracy due to poor filling ratios, a non-ideal tank to chamber ratio and gauge uncertainties.

The Julius Kruttschnitt Mineral Research Centre (JKMRC) has developed a rapid commercial pycnometer for mineral sorting. Commercialisation and manufacture has since been licensed to UltraSort LTD, Australia. The *JK pycnometer* was designed to replace existing technologies for mineral sorting based on buoyancy measurements using heavy toxic liquids. As density is the variable of interest the *JK pycnometer* was equipped with a weighing device to allow densities to be calculated. The *JK pycnometer* is claimed to have an accuracy of $\pm 5\%$ of sample volume and $\pm 4\%$ of sample density. However, measurement times are not specified.

1.2.6 Commercial methods for sorting produce and minerals

The ability to sort fruit is a current problem in industries where fruit density is often associated with ripeness or sugar content. Several methods are frequently used to ascertain the fruit firmness, which can be correlated to density. These include low mass impact, acoustic firmness tests and drop impact tests. These tests usually attempt to measure the propagation speed of sound through the fruit and the impact parameters used to derive a firmness index (Shmulevich *et al.*, 2003).

The impact parameters are a function of peak amplitude after impact and the rise/fall time of the impact. However, impact tests do not give consistent results for firmness for most fruit as the shape of the fruit significantly affects the firmness parameters. Also, non-uniformities in density through the fruit affect these values (Sugiyama *et al.*, 2005). Companies such as Toyoseiki in Japan and Aweta in Holland produce firmness testers.

Optical scanning techniques are the usual non-destructive method for measuring fruit size (volume) in commercial installations. The individual fruit is rotated on a plinth as it is optically scanned. A computer program then assembles the images to give an approximate volume. This method is not sufficiently accurate to sort fruit by density

(having been weighed first). It is however able to size grade fruit and sort by colour. Aweta of Holland produces machines of this type.

Buoyancy methods are currently used for mineral density measurements in mining applications. A mineral sample is immersed in progressively denser liquid until the sample is neutrally buoyant. This method is in the process of being phased out in Australia due to the high toxicity of the heavy liquids used. The *JK pycnometer* was created as an alternative and may eventually replace immersion methods.

1.2.7 Spheres in a resonant cavity.

A number of studies have been conducted on spheres in a resonant cavity, principally Barmatz *et al.* (1983), Leung *et al.* (1982) and Cordero and Mujica (2007). However, all have concentrated on closed cavities, described as a half wave resonator. Their models and measurements focused on a sphere's position in relation to cavity length and how this changes the different modes of resonance (Eigen frequencies). Sometimes this was extended to include the influence of sphere radius to cavity radius ratios. All derive various solutions to the wave equation in attempts to better predict the change in resonant frequency for a given configuration.

Leung *et al.* (1982) performed tests using rigid disks and differing sample materials for the solid spheres. Barmatz *et al.* (1983) also performed preliminary tests on spheres of different material. Both groups noticed no appreciable differences in acoustic behaviour for the different materials. The difference in acoustic impedance between dissimilar solids is generally tens of Megarayles, where 1rayl is $1\text{kg/m}^2\text{s}$. Aluminium and hard plastics are typically around 17×10^6 rayls and steel 47×10^6 rayls. However, the impedance of air is a mere 415 rayls. Therefore, impedance coupling is very poor between a solid and air, with most of the acoustic energy reflected by scattering.

Leung *et al.* (1982) found the behaviour of a disk in a resonant cavity tended to lower the resonant frequency in the vicinity of maximum amplitude velocity. The effect of a disk caused acoustic scattering without inducing a frequency shift caused by a volume change. In this way scattering effects could be isolated from volume effects.

The Helmholtz resonator is significantly different from closed cavities given that the Helmholtz primary resonator frequency is independent of internal chamber dimensions. The exception to this is at higher frequencies where standing wave properties emerge due to half and quarter wave resonant activity. The chamber volume, port dimensions and the speed of sound determine the fundamental frequency of the resonator. Transcendental equations utilise chamber diameter and length for excessively long or wide chambers (See Chapter 2, Section 15). The Helmholtz equation assumes a lumped parameter analysis of the chamber and port, which is true if the pressures in both are equal. For a combined chamber and port length of less than $1/16$ the resonant wavelength the lumped parameter method has been found to be valid (Panton and Miller, 1975).

Literature review conclusions

- There is little existing information on the use of Helmholtz resonators for volume measurements.
- Generally pycnometers capable of high accuracy volume measurements are not robust or suitable for industrial applications. Those that are have tended to be inaccurate and slow.
- Existing methods for measuring produce samples are not very accurate and are either prone to incorrect scanning (optical systems) or inconsistencies caused by non-uniformity in density (acoustic response tests).
- Current methods for mineral density measurements (based on volume) involve highly toxic liquid chemicals.
- Solids in a $\frac{1}{4}$ wave resonant cavity will cause frequency shifts in proportion to their location, their volume and the amount of scatter based on surface geometry. It is expected similar trends should be seen in a Helmholtz resonator, but to a lesser degree.

Chapter 2

Helmholtz resonator theory

2.1 Helmholtz resonator theory

2.1.1 Traditional Helmholtz resonator theory

The ideal resonator equation behaves like a mass spring system with defining constants such as stiffness, mass and an angular frequency, Equation (2.1.1). For most situations this simplification proves adequate to describe the Helmholtz resonator oscillatory system. The mass is the mass of air in the port, $\rho_0 s_p l_p$, and the spring stiffness is the compliance of the air in the port calculated in Appendix A, Section 10 to be $(\rho_0 c^2 s_p^2)/V$, where ρ_0 is the nominal air density, s_p is the port surface area, l_p is the port length, c is the speed of sound and V the volume of the chamber. Placing these into Equation (2.1.1) and cancelling gives the traditional Helmholtz resonator equation.

$$\omega = \sqrt{\frac{\text{stiffness}}{\text{mass}}} = c \sqrt{\frac{s_p}{V l_p}} \quad (2.1.1)$$

This is an idealisation as the length l_p should refer to the moving mass of air in the port only. But in reality this length is about 0.6 longer (See Appendix A, Section 8). Figure 2.1.1 shows simplified diagrams, comparing the physics of the resonator and a mass spring arrangement. This method is often referred to as the lumped parameter method in which the air in the port is considered incompressible (See Appendix A, Section 12).

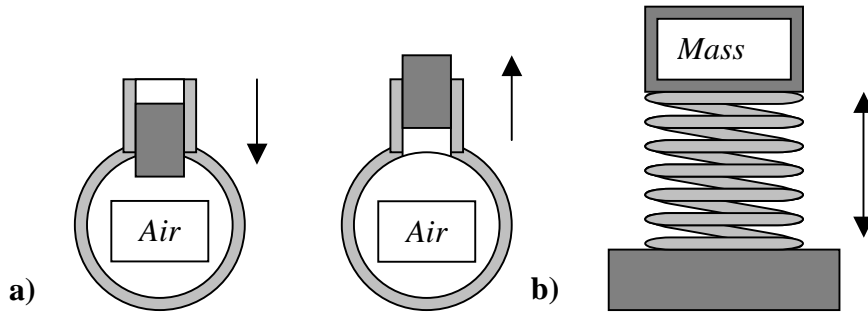


Figure 2.1.1 a) Simple ideal resonator showing moving mass of air in port compressing air in chamber volume and springing back due to the increased pressure in the chamber. b) Equivalent mass spring system.

Making the substitutions, $\omega = 2\pi \text{freq}$, allowing for a port length extension term, Δl , to allow for the non-ideal behaviour of the port and adding a sample displacement volume (w). Equation (2.1.1) can be rewritten as Equation (2.1.2) for a sample volume inserted into the resonant chamber.

$$\text{freq} = \frac{c}{2\pi} \sqrt{\frac{s_p}{(V - w)(l_p + \Delta l)}} \quad (2.1.2)$$

Equation (2.1.2) can be rearranged, Equation (2.1.3), allowing determination of w . This requires the chamber volume to be accurately measured and the resonant frequency of the empty chamber found.

$$w = V - \frac{s_p}{\left(\frac{2\pi freq}{c}\right)^2 (l_p + \Delta l)} \quad (2.1.3)$$

For a resonator of fixed dimensions the main variable is the frequency. If the frequency can be accurately measured it should be possible to calculate the size of the object in the chamber. This assumes a constant velocity of sound (c), which can be evaluated from the temperature, the ideal gas law and the ratio of molar specific heats (γ). Application of a narrow frequency sweep, chirp, will allow localisation of the resonant frequency.

2.1.2 Chirp frequencies

The time for one complete cycle of a given frequency decreases with increasing frequency. If a linear chirp was used the number of cycles produced with increasing frequencies would increase proportionately also. For this reason a logarithmic chirp is required to ensure even weighting to all frequencies being swept through.

The time to complete one cycle (T) is the reciprocal of the frequency, $T=1/freq$. Therefore the sweep time (ST) for the frequencies being chirped through will be the integral of $1/freq$, Equation 2.1.4.

$$ST = \int_{freq_{min}}^{freq_{max}} \frac{1}{freq} = \ln \left| \frac{freq_{max}}{freq_{min}} \right| \quad (2.1.4)$$

The rate of change in the in sweep will be the first derivative of $1/freq$, Equation (2.1.5), which shows the rapid decline in time required for a complete cycle with increasing frequency. The rate of frequency change is an inverse parabola. To avoid the need for logarithmic chirps, narrow frequency scanning is preferable. This can be achieved with a roughing technique like that described in Chapter 3, Section 3.2.6.

$$\frac{dT}{dfreq} = \frac{d}{dfreq} \left(\frac{1}{freq} \right) = -\frac{1}{freq^2} \quad (2.1.5)$$

2.1.3 Non-ideal behaviour in the port: length extension

Work by Lord Rayleigh (1896), Chanaud (1993) and others have shown Equation (2.1.1) to be an idealisation. The port length is in reality extended by a factor determined by the port radius and the quantity of port flange material at each end of the port, Figure 2.1.2.

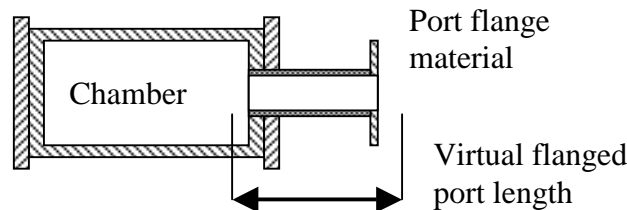


Figure 2.1.2 Flange material will alter the virtual or effective port length.

The pressure within the resonator chamber is not equal at all locations, but is a function of the resonant frequency wavelength. Therefore, in a sufficiently long chamber it is possible to have both low and high-pressure zones co-existing. Non-homogeneous pressure within the resonator chamber invalidates the lumped parameter assumptions used to generate Equation (2.1.1).

Ingard (1953) stated that port end corrections, which is air moving beyond the physical port ends, are not as simple as those derived from the standard method of a piston in a planar surface. They are intimately related to the constraints occurring at the end of the port, the solutions to which are difficult to solve due to the required *a priori* knowledge of the pressure distribution in the port. Part of the problem also stems from the small signal approximations used in generating the wave equation (See Appendix A, Section 2). These lead to singularities at point sources or edges. Ingard (1953) recommended using the non-linear terms that are normally omitted to eliminate this problem.

Most standard texts, such as Blackstock (2000) and Kinsler and Frey (1962), derive a value of $8a/3\pi$, where a is the radius of the port, for the length extension effects caused by an ideal piston in a plane surface. This can be equated with a moving mass of air in a flanged port. In reality the piston is seldom ideal and the flange at the port's entrance is far from being an infinite plane. Coupled to this are the diffraction effects causing scattering and turbulence at the internal and external port ends.

Typical Helmholtz resonators require two different end corrections to be used, one for the internal port and one for the external. Ingard (1953) warns that non-adherence to the end correction factors can lead to considerable error in calculating the resonant frequency. Ingard reports very good agreement between experiment and theory using standard end correction factors, despite the assumptions about non-ideal secondary effects.

End corrections are required and valid for all cavity-like configurations and can be applied to $1/4$ wavelength and $1/2$ wavelength organ tubes (Panton and Miller, 1975). In illustration of the significance of end corrections, consider a simple port chamber configuration with an internal flange. If the port length is 170mm with an internal radius of 22mm, a length correction Δl of 30mm is required. This is calculated based on the end correction is for an internal flanged and external un-flanged port. Hence, the effective length for the port is 200mm, almost 20% more than the physical length.

To better understand the length extension term Silva *et al.* (2008) have derived a number of equations and methods to try and align the Hermitian and causality conditions to length extension calculations. Instead of relying on static values often used to approximate the length extension term. Silva *et al.* (2008) state the Hermitian condition requires the reflection function (R) of a negative frequency must be equal to its complex conjugate, $R(-\omega)=R^*(\omega)$, where R^* is the complex conjugate reflection function and ω the angular frequency. The causal condition given specifies impulse responses must be causally closed.

Existing derivations do not obey these conditions in attempts to give readily usable values. The sacrifice is values that are only true for the system as the angular frequency approaches zero or ka is sufficiently small, less than 1, where k is the wave

number and a the port radius. The result is physically impossible values for large ka values. Despite this, Silva *et al.* (2008) acknowledge it is impossible to derive closed form solutions as the time domain solutions require knowledge of impedance values for the full range of frequencies (See Appendix A, Section 13).

Results of Silva *et al.* (2008) for prediction and experimental values for the length extension were within 8% ($ka < 2$) when the Hermitian and causality conditions were satisfied. This improved to better than 2% ($ka < 3$) when the causality condition was ignored. The significant improvement in not applying closed conditions indicates length extension terms for a port still pose a difficulty in accurately defining the parameters determining the Helmholtz resonator.

Kang and Ji (2007) conducted a numerical study into length correction of ducts in a cylindrical chamber, as occur between the Helmholtz resonator port and the chamber. They used 3D finite element models (FEM) and 2D analytical calculations to better understand the length correction term with regards to the resonator's chamber dimensions and the port dimensions. From the 2D analysis they were able to derive an approximation expression. This expression could be used to calculate the length extension factor so as to be incorporated in the traditional 1D analysis model, Traditional Helmholtz equation, Equation (2.1.1). The derived expression has variables that include the chamber diameter (d_c), the port diameter (d_p) and the quantity of port extension into the chamber (L_e), Equation (2.1.6), where δ is the length extension factor and a the port radius.

$$\frac{\delta}{a} = 0.6165 - 0.7046 \left(\frac{d_p}{d_c} \right) + 0.2051 \exp \left(-3.4453 \frac{L_e}{d_p} \right) - 0.3749 \frac{d_p}{d_c} \exp \left(-2.6023 \frac{L_e}{d_p} \right) \quad (2.1.6)$$

Analysis of the chamber length to chamber diameter ratio by Kang and Ji (2007) suggested this ratio did not influential the length correction term unless the ratio was less than 0.3. This would make for a very long thin resonator in which non-linearities in the pressure wave distributions would be much more significant, and would therefore violate the lumped parameter assumptions (See Appendix A, Section 12).

Numerically, Kang and Ji (2007) found very good agreement between their FEM method and the 2D analytical model, within 1% for the values they considered. It was unfortunate that they did not conduct any experimental work to confirm their numerical results. It is therefore unknown as to how successful their models are in predicting length extension.

The inclusion of one or more perforations in the port has been found to significantly alter the port length extension term, Peat (2008). Resonators with port perforations have been well known for many years and the benefits implemented successfully in muffler systems, mufflers being a type of Helmholtz resonator. However, the effect of the perforations in terms of mathematical analysis has been lacking. Traditionally the design of resonators with port perforations has been trial and error.

Peat (2008) performed a finite element analysis in combination with standard analytical impedance calculations to derive solutions based on the percentage of perforation per unit length and the total length containing perforations. The significance of Peat's research has implications for leaks that may be present in the port of a resonant system. These can occur at the chamber port junction or in microphone fixtures on the exterior of the port. Peat found the port length correction factor was increased to 1.6 from 1.4 for an un-flanged resonator when a single hole making up only 5% of the circumference area was added. This represents a significant alteration to frequency prediction accuracy using the Helmholtz equation. Generally, the acoustic energy is very rapidly dissipated in a pipe containing any perforations.

2.1.4 Non-ideal behaviour in the port: radiation resistance

Lord Rayleigh (1896) discovered that the moving mass of air in the resonator port continues past the physical open ends by an amount determined by the cross sectional area (See Figure 2.1.1). Ingard (1953) repeated this work. The effective inertia of the moving mass of air, acting as an oscillating pneumatic slug, extends the port-air-mass beyond the ports physical boundaries. As noted by Kinsler and Frey (1962), a moving air mass has associated losses, which appear as acoustic radiation and frictional coupling with internal port surface (See Appendix A, Section 9).

When ka is small, boundary layer losses are more prominent than the acoustical radiation energy losses from the external end of the port. They are an order of magnitude larger than the radiation resistance associated with the moving mass of air in the port (Kinsler and Frey, 1962). The exposed port acts as a hemispherical oscillator that has an acoustical coupling co-efficient related to the frequency. At low frequencies ($ka \ll 1$) the port behaves like a point source emanating sound in a hemisphere. As the frequency increases the sound is projected more like a planar source with low divergence (Blackstock, 2000).

The assumptions used in deriving the radiation resistance are only valid for the transmission of sound into a semi-infinite medium, i.e. the constricted port into the unobstructed environment. Equations derived in Appendix A will need appropriate adjustments to account for incident, transmitted and reflected components if the sound is not radiated into free space. An important example of this is a closed tube; most of the energy is reflected minus the frictional viscous losses (See Appendix A, Section 11). Hence radiation losses are minimal in such circumstances.

In a study by Ganghua *et al.* (2008), the coupling efficiency of a small enclosure containing a Helmholtz resonator was investigated. The purpose was to gain a better understanding of energy reduction using various damping membranes in the port of the resonator. By selecting the appropriate acoustically resistive material, broad frequency energy attenuation could be achieved.

Ganghua *et al.* (2008) found that a high energy absorbing membrane prevented effective coupling between the enclosure and the resonator. The resonator was not able to induce sufficient resonance to reduce the energy in the system it was mounted in. Using analytical solutions for the velocity and pressure distributions they were able to show there is an optimum damping coefficient for a given resonator and environmental coupling configuration.

The calculations of Ganghua *et al.* (2008) were designed to maximise the energy reduction to the enclosure housing the resonator. The resonator was designed to have a high Q factor and energy dissipation factor. The high Q factor allows energy to be extracted from the enclosure into the resonator and then dissipated in the port membrane. To calculate the optimal attributes of the resonator the coupling between enclosure and resonator must be analysed.

Calculations and experiments by Ganghua *et al.* were able to show that for an undamped resonator most of the energy loss, in the form of acoustic resistance, is from acoustic radiation resistance and not viscous losses in the port. Hence, most of the energy is reradiated back into the enclosure. This is an important consideration for uncoupled resonators with small internal port areas having remote stimulation.

In a brief study by Iwase (2007) the velocity profile emanating from the port of a Helmholtz resonator was investigated using a velocity probe. He found the velocity profile was uniform right up to the edge of the port surface when measured at the port opening. As the velocity probe was moved upward and outward it showed rapid velocity dispersion, confirming the planar wave rapidly diverges into a hemispherical wave, as predicted by theory (See Appendix A, Section 4).

Additionally, Iwase (2007) was able to map the length extension effect as the velocity profile decays with distance from the port opening. Results suggest smaller length extension effects of the port extended up to 50% of the port length. Standard acoustical theory (Blackstock, 2000) predicts for Iwase's system, the bulk movement should be occurring at lengths less than 12% of the port length. In the study by Iwase, the effect of flanging material at the port opening was also confirmed. The addition of port flanging material was shown to significantly increase the coupling coefficient between the port and the environment.

2.1.5 Non-ideal behaviour in the port: viscosity and turbulence

In accordance with continuum mechanics (Fung, 1994) the mass of air moving within the port must have an air velocity of zero where the air meets the port surface, the no-slip condition. This layer is a frictional loss of energy to the resonator. Despite this the velocity profile is nearly even across the port's area and appears very much as a plane wave, Kinsler and Frey (1962), Blackstock (2000). The boundary condition where matching velocity at the port surface occurs is at the millimetre range (See Appendix A, Section 9).

Kinsler and Frey (1962) suggest any port over 1cm diameter will not be significantly affected by this internal viscous frictional coupling. In theoretical calculations by Ingard (1953) on a Helmholtz resonator he calculated a boundary layer thickness of 0.6mm for a resonator having a resonant frequency of 150Hz. This value is consistent with alternative methods used in Appendix A, Section 9. Exceptions can occur with large sound pressures where the air velocities can be very large.

To some extent, the surface texture of the port plays a part in the viscous losses to the resonant system. The surface still appears as a smooth boundary so long as the coarseness of the surface is not a significant proportion of the cross sectional area. This is primarily due to the low viscosity of air. Ingard (1953) made use of porous materials within the port to add mechanical damping. Damping within the resonator is

common for noise suppression systems such as mufflers and air conditioning ducting. The effect of which is to lower and broaden the overall Q factor of the resonator (see also Section 2.1.4). Q factor being the quality of resonance (See Appendix A, Section 3)

Because Helmholtz resonators are often used in sound damping systems, a broad resonant peak having a low Q is required with high mechanical resistance over the frequency range for which it is intended. Resolvability in frequency requires a high Q factor to be achieved. For an un-damped resonator Q factors of between 30 and 40 are easily obtainable (Ingard, 1953).

Ingard (1953) has stated that within the resonant system the power lost to viscous forces is to be derived from the integral of the friction caused by the port surface and the tangential wave velocity. The surface resistance is the product of the air viscosity density and the angular frequency. For this integral to be valid the surface must appear flat to the wave travelling across its surface. As the boundary layer has been shown to be much smaller than the dimensions of the port this assumption can be considered true. It is not true for small diameter ports, less than 1cm, or small port lengths such as a hole punched plate. There will also be some acoustic losses around the port ends. High friction losses also occur at the port edges, these all contribute to non-linearity in port behaviour.

2.1.6 Non-ideal behaviour in the port: heat conductive losses

Blackstock (2000) and Kinsler and Frey (1962) suggest the heat losses from a propagating wave in a free medium are of a similar magnitude to those caused by viscosity. As a sound wave propagates through the given medium a localised rise in temperature occurs with the rise in pressure. The converse is also true and during the rarefaction, a temperature decrease occurs.

For a given system, the viscous losses experienced by moving air molecules will be small if the boundaries of that system are large compared to the wavelength. The losses associated with heat transfer in the form of non-ideal adiabatic effects will also be small and of a similar magnitude. In the case of a bounded system where the dimensions are small compared to the wavelength the effect of the viscous boundary layer will play a larger part in the dissipation of energy. This is not to say that the losses from either are large, but the relative magnitude of viscous to heat conduction will vary according to the system under investigation.

The resonator is not a free and open system, and therefore does not mimic results for such open systems. Ingard (1953) has suggested the need for careful analysis of waves travelling in a finite system. He classifies two important subcategories, waves in an infinite tube and waves in a finite tube. Application of conservation of energy equations will vary in each case due to the phase relationships between pressure and particle velocity within the finite system. Thus, the velocity is far more significant than the pressure due to the boundary layer effects. As the wave velocity increases so does the boundary layer. Consequently at high sound pressure levels or very high frequencies the port appears more constricted than at low sound pressure levels (See Appendix A, Section 9).

2.1.7 Non-ideal behaviour in the port: relaxation time

Relaxation time is the small instant in which the density change in a fluid is not equal to the pressure change. For example, a very rapid change in piston position will cause the air molecules to experience a sudden rise in density that is out of phase with the related pressure step. This represents a time lag, linked to the transients in which the system is able to bring itself back into equilibrium.

The effect of the relaxation time is a non-linear speed of sound relationship. The speed of sound asymptotically increases proportional to an additional viscosity force, caused by the air's time to reach molecular equilibrium. This applies to poly-atomic gases like air, (Kinsler and Frey, 1962). The sudden burst of energy into the gas is taken up by the modes in which the gas can absorb energy (translational, rotational and vibrational).

The relaxation time for air is about 1.7×10^{-10} seconds. For this study the rate of rise of pressure is orders of magnitude slower than the relaxation time for air and hence relaxation times are not considered significant. Only at very high frequencies or extreme pressure amplitudes is the relaxation time important and is necessary to include it in theoretical calculations.

2.1.8 Non-ideal behaviour in the port: non-linear effects

Ingard (1953) has reported the presence of significant non-linear effects in the port of a resonator under certain conditions. The principle reason for this non-linearity is turbulence caused by particle displacement amplitudes to port length ratios. The ratio of these two variables determines how the onset of turbulence occurs, what proportion of the cross section will be laminar and whether jets occur at the port ends. The transition between different port behaviours occurs at when the port length and particle displacement distance are the same. 'Particle' in this instance refers to air particles not those described later in Chapter 3 for granular materials.

At low sound pressure levels the port flow remains predominantly laminar even with increasing frequency. As the frequency and particle displacement grow, the onset of turbulence starts. If the frequency and amplitude is further increased acoustic jetting starts. This analysis can be contrasted with the normal Reynolds number approach for boundary layer determination (See Appendix A, Section 9). The oscillatory behaviour plays a significant role at large sound pressure levels and at high frequencies.

Associated with non-linear resistance effects is non-linear reactance; the two are intimately related. The resistance caused by turbulence and/or acoustical jetting is energy taken from the mass reactance of the port. The oscillating mass of air in the port connected with the acoustic reactance is required to drive the turbulent effects, and is thus an additional loss to the resonator. This loss can be added to those of viscosity for the resonator.

In this investigation the port lengths are large compared to the particle displacement and the frequencies low. Therefore, air movements within the port are in the linear region and non-linear effects caused by the onset of turbulence or acoustical jetting need not be considered.

2.1.9 Non-ideal behaviour in the port: port placement

The port placement can affect the resonant frequency in two ways. The first is the inclusion and/or protrusion of the port from the resonator chamber. The second is the physical location of the port in terms of chamber symmetry, i.e. the proximity of the port to the chamber wall.

Inclusion and protrusion effects have been extensively analysed and examined by Selamet and Lee (2003). They found that the resonant frequency decreases slightly as the port is shifted from a symmetric orientation, where the port length internal to the chamber is the same as that external, to an asymmetric one, where there is a difference in internal to external port length extension.

Ingard (1953) and Chanaud (1993, 1997) reported on the effects of port placement in terms of its proximity to the chamber wall. As the port is moved closer to the wall the viscosity 'felt' by the mass of air varies at the port entrance and exit. This variation has a significant effect on the resonant frequency.

The port centre displacement was analysed by Ingard (1953) with regard to the port's eccentricity factor, the ratio of the port centre over the radius of the chamber (a/R), Figure 2.1.3, up to the theoretical maximum of 1. The ratio of unity is impossible due to the port having its own radius (r) which restricts the upper limit of a to $R-r$. Therefore, the maximum ratio of eccentricity is $1-r/R$. Ingard's investigation focused on how eccentricity affects port length extension. He noticed that Δl (length extension) was a maximum when this ratio of a/R was zero and minimal when the port was hard up against the chamber wall. A port close to the chamber wall will have a lower effective length hence a higher resonant frequency and vice versa.

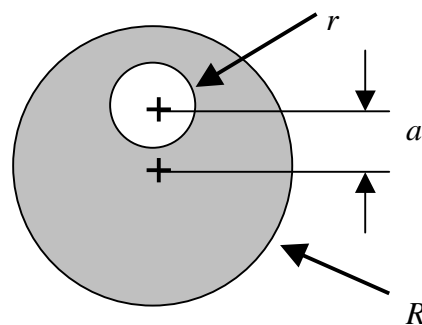


Figure 2.1.3 Port placed eccentrically with respect to the chamber centre.

Chanard (1997) furthered his previous work studying port location effects; the 1993 investigation only included a few cursory calculations. Chanaud's experimental and theoretical results were similar to those of Ingard (1953) using a cylindrical chamber with an eccentrically placed port. Chanaud's results showed the classical Helmholtz equation was unable to predict variations in port placement. Chanaud also demonstrated by experiment, with an irregular rectangular chamber, the inability of the transcendental equations to predict resonant frequencies when the port location is eccentrically placed in the chamber.

2.1.10 Non-ideal behaviour in the port: port shape

Tang (2003) and Selamet and Lee (2003) conducted two types of investigation into port shape, principally the effects of varying the port cross-section with height with conical ports. Ingard (1953) and Chanaud (1993) studied the relationships between port cross sectional shape and the effect these have on the resonant frequency.

Tang's development of the Helmholtz equation, $(\nabla^2 + k)A = 0$, for tapered conical ports and experimental evidence has shown an increase in the resonant frequency is predicted and observed. Tang's analysis and experimental work includes only the cases where r_i is smaller than r_o , Figure 2.1.4. An increase in the resonant gain was also observed in Tang's study, indicating a reduction in the acoustic impedance in the port.

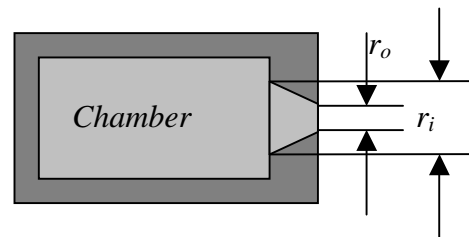


Figure 2.1.4 Chamber with tapered conical port.

Selamet and Lee (2003) also found that an r_i value smaller than the r_o value increased the resonant frequency. In addition they tested the case where r_i is larger than r_o , with again an increase in resonant frequency. In both cases increases in the resonant frequency and its resonant gain value occurred, compared with the standard un-tapered port.

Chanaud (1993) and Ingard (1953) noted port cross sectional shape has little effect on the resonant frequency. This is likely due to the port cross section being large enough, for the pressure wave travelling in the port, to be almost unaffected by the viscosity losses occurring at the port surface. In extreme situations where the port area is narrowed, the boundary layer will become significant and encroach on the bulk laminar flow. The other extreme is where a port dimension becomes a significant proportion of the wavelength; in such cases the lumped parameter approach is violated and no longer valid.

2.1.11 Non-ideal behaviour: chamber and port length

The pressure can be predicted at various chamber heights as shown in Figure 2.1.5, by considering the length of the chamber as occupied by a sinusoidal pressure wave at an instant in time. The dimensions are chosen such that the resonant wavelength is proportional to the length of the chamber. This situation is to be avoided in using the lumped parameter analysis of the Helmholtz resonator, which assumes equal pressure throughout the chamber and port.

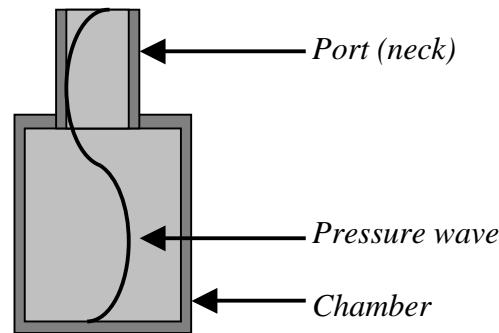


Figure 2.1.5 Sinusoidal representation of pressure within chamber occurring when dimensions of the resonator are a significant fraction of the resonant frequency wavelength.

Panton and Miller (1975) have shown that the deviation caused by the wavelength (λ) induced pressure difference can be significant in predicting precise resonant frequencies. They suggest the length of the chamber should be kept to within $1/16\lambda$ rather than the more traditionally accepted value of $1/4\lambda$, if the lumped parameters assumptions of Equation (2.1.1) are to be valid. Chanaud also found this to be true in his 1993 study. See also Section 2.1.15 for analytical details of Panton and Miller (1975) study.

Selamet, Dickey and Novak (1995) conducted a number of tests, extending the length of chambers to gauge the significance of wavelength to chamber dimensional effects. In their investigation Selamet *et al.* used the chamber length to chamber diameter ratio (l/d) to test non-ideal behaviour. In all cases the chamber volume was kept constant. They found in all non-classical transmission loss analysis, the resonant frequency decreases with increasing l/d . The maximum ratio of l and d tested was 23.92. At extreme ratios secondary $1/4$ wave resonator behaviour was observed in the port in addition to that caused by Helmholtz resonance.

The classical Helmholtz equation was observed to be valid for l/d ratios of less than 1.5 by Selamet *et al.* (1995). At larger ratios transcendental equations derived from transmission theory were needed to accurately predict resonant frequencies (See Section 2.1.15 and Appendix A, Section 11). Computational numerical methods were also used by Selamet *et al.*, but only yielded accurate results when the grid size was small and only for extreme l/d ratios.

In contrast to Panton and Miller (1975), Selamet *et al.* (1995) used a transmission loss apparatus in which the resonator was mounted at right angles midway along a non-reflective duct (anechoic termination). Panton and Miller used a freestanding resonator and applied a sound source to the port entrance at a distance of approximately 1m.

2.1.12 Non-ideal behaviour: chamber shape

Alster (1972) conducted a thorough mathematical analysis of variations in chamber shape. The aim was to improve calculations of resonant frequencies for Helmholtz resonators having unusual chambers. In his paper he studied a range of chamber shapes including spheres, prisms, toroids and cylinders. A secondary purpose was to link mathematical descriptions of the Helmholtz resonator to those of the $1/4$ wave

resonator. Alsters inspiration for this investigation was discrepancies in the observations made by early acoustical pioneers such as Liscovius and Sondhauss, (cited by Alster, 1972).

Liscovius and Sondhauss alleged that a resonator partially filled with water gave the same resonant frequency when the resonator was inclined at various angles. In contrast, modern replications of this experiment give variations of up to 30%, (Alster, 1972). Therefore, it is argued, the classical resonator equation, Equation (2.1.1), is too simple to accurately describe the processes causing resonance. Alster then reasoned the chamber shape must affect the gas inside the chamber, as the water-filled resonator changed its frequency at changing chamber angle with all other variables held constant.

Alster's investigations have explicated the use of form factors for describing the velocity and force profiles within the chamber. If the chamber is sufficiently regular to allow description by a function, then a detailed procedural equation can be generated to describe the end effect of the internal port. Hence, the end correction factor, required for frequency prediction, can be applied where $l_p = l_p' + l_c + l_o$. The physical length of the port is l_p , the length extension due to chamber effect is l_c , and the length extension due to the port's external opening is l_o .

It should be noted that Alster's derivation assumed dimensions of chamber and port not greater than $\frac{1}{4}\lambda$ of resonance and omits viscous forces. This is in keeping with general assumptions used in calculating resonant frequencies. With these cautions Alster was able to achieve accuracies of better than 1% when comparing predicted values with observation.

2.1.13 Resonator chamber with many apertures

The Helmholtz resonator need not consist of a single port. The theory describing the behaviour of a given resonator can be equally applied to the multi-port resonator. The lumped parameter conditions must still apply for validity of predicted frequencies. Ingard (1953) used two different multi-port configurations. The first consisted of a single rectangular port replaced with four smaller rectangular ports amounting to the same overall cross sectional area. The second was a single round port split into two smaller round ports of equal cross sectional area. In these instances the multiple ports were all in the same face. They were also close enough to have their inertial components, which extend beyond the port exit, interfered with each other. The effect of which was a considerable rising of the primary resonant frequency, mainly due to the end effects overlapping into neighbouring ports. The interference between the ports affected the length correction factor for each. Ingard (1953) provides a detailed mathematical analysis of this effect.

In instances where the ports are remote from each other the resonant frequency would be expected to be the same as that for the single port, with the equivalent cross sectional area. Because the length correction is a function of port radius the multi-port resonator's resonant frequency would be expected to be larger by a factor determined by the port size difference. To illustrate this, compare the standard Helmholtz resonator Equation (2.1.7) with the multi-port Equation (2.1.8) in which $s_{p1} = s_{p2}$ and $l_{p1} = l_{p2}$. The denominator for the multi-port resonator is purely a function of the averaged port radius. The effect of which is to raise the resonant frequency, as Δl for

the multi-port resonator will be considerably less than Δl for the single port resonator. The cross sectional area for s_p is the same as that of $2s_{p1}$.

$$freq = \frac{c}{2\pi} \sqrt{\frac{s_p}{V_c(l_p + \Delta l)}} \quad (2.1.7)$$

$$freq = \frac{c}{2\pi} \sqrt{\left(\frac{s_{p1}}{V_c(l_{p1} + \Delta l_1)}\right) + \left(\frac{s_{p2}}{V_c(l_{p2} + \Delta l_2)}\right)} = \frac{c}{2\pi} \sqrt{\frac{2s_{p1}}{V_c(l_{p1} + \Delta l_1)}} \quad (2.1.8)$$

Ingard (1953) also states that the expected Q factor for a multi-port resonator will be considerably less than that for a single port. By considering Equation (2.1.9) it can be seen that the expression for the Q factor is dependant on the length correction factor in the numerator (See Appendix A, Section 3). Therefore, as the length correction factor decreases with reductions in cross sectional area of the port, the Q factor is expected to decrease accordingly.

$$Q = \frac{2\pi c(l_p + \Delta l)}{\omega s_p} = 2\pi \sqrt{\frac{(l_p + \Delta l)^3 V}{s_p^3}} \quad (2.1.9)$$

2.1.14 Analytical transmission and finite element analysis

Boundary value and finite element analysis, also referred to as *BEM* – Boundary Element Method (Selamet and Lee, 2003), are two methods of gaining insight into the behaviour of the Helmholtz resonator. Selamet and Lee have employed both methods to better understand the complex interaction of pressure and velocity at three distinct regions within the resonator. These consist of the port volume, the region immediately surrounding the port in the chamber and the region in the chamber free of the port. Selamet and Lee used a symmetrical port configuration in which half the port protrudes into the chamber and half extends out of it.

Using analytical methods Selamet and Lee (2003) solved the resonator problem using transmission theory for the three regions in both the one-dimensional axial and two-dimensional analytical methods. They found the classical and one dimension axial methods gave poor predictive results, while the two dimensional and finite element analysis gave very good results.

Selamet and Lee (2003) also found the finite element method was able to predict accurately the resonant frequency for tapered port configurations. Tapered port calculations become extremely unwieldy using transmission equations due to the progressive change in volume and surface area. Tang (2003) has attempted a simplified variation of this process with partial success (See Section 2.1.10).

2.1.15 Transcendental equations for resonance frequency determination

The classical Helmholtz resonator formula, Equation (2.1.1), is derived from the damped wave equation with an applied perturbation or forcing function (See Appendix A, Section 2). This equation typically gives results to within 5% with cautious use of both chamber and port lengths and avoidance of extreme asymmetry

in design. The advantage of the classical formula is a continuum of calculable frequencies for a range of resonator dimensions, but it does not allow for the chamber width to length ratio as discussed earlier. Lord Rayleigh (1896) further developed the transcendental resonator formula, Equation (2.1.10), in which intersections of two functions must be numerically resolved in order to determine appropriate frequencies at which the chamber resonates.

$$\cot(kL_c) = \frac{s_c l_p}{L_c s_p} kL_c \quad (2.1.10)$$

where k is the wave number ($k=\omega/c$, c is the speed of sound), L_c is the chamber height, s_c is the cross sectional area of the chamber, l_p is the length corrected port, and s_p is cross sectional area of the port.

The transcendental equation is developed from wave transmission theory. The closed chamber end represents an infinite impedance and the port a reactive load (See Appendix A, Section 11). Because the transcendental equation makes use of the chamber length and cross sectional area, its use can be extended to $1/4$ wave open tube resonators. A natural limit is formed as the port cross sectional area approaches the chamber cross sectional area. By observing the limit as the port cross sectional area approaches zero the equation can also be used for closed tube resonators. Panton and Miller (1975) used these techniques to form a general set of solutions to acoustical resonators. Panton and Miller also derived the classical equation from the transcendental form by expanding out the first three $\cot(kL_c)$ terms, Equation (2.1.11).

$$\cot(kL_c) = \frac{1}{kL_c} - \frac{1}{3} kL_c - \frac{1}{45} (kL_c)^2 \quad (2.1.11)$$

In Equation (2.1.11) the third term is almost negligible compared to the first two terms. If the first term in the expansion is substituted into Equation (2.1.10) the traditional Helmholtz formula results, noting that $L_c s_c$ is equal to the chamber volume V_c . By using the first two terms in the expansion, Equation (2.1.12) is acquired.

$$\frac{s_c l_p}{L_c s_p} kL_c = \frac{1}{kL_c} - \frac{1}{3} kL_c \quad (2.1.12)$$

Cancelling, simplifying and using $k=2\pi freq/c$ gives a new and more accurate classical formulae, Equation (2.1.13), that does not require numerical methods to solve. Equation (2.1.13) is suited to resonators in which the chamber dimensions are greater than $1/16$ of the wavelength.

$$freq = \frac{c}{2\pi} \sqrt{\frac{s_p}{(V_c l_p + \frac{1}{3} s_p L_c^2)}} \quad (2.1.13)$$

An advantage of the transcendental equation is its ability to predict higher order resonant conditions caused by the interior dimensions of the chamber. Figure 2.1.6 is

included to illustrate the deviation caused by taking the first term, traditional, then the first and second term, improved traditional, and lastly the transcendental. The first two are unable to predict higher order harmonic terms due to their monotonic decay, but they show the classical and improved classical aptness for low values of kL_c ($kL_c < 1$).

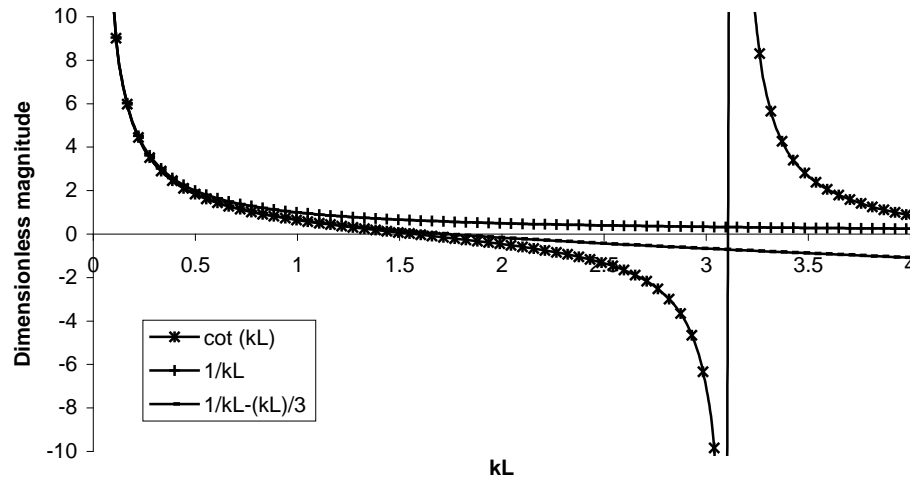


Figure 2.1.6 Three methods for determination of resonant frequency using traditional ($1/kL$), improved traditional ($1/kL - [kL]/3$) and transcendental ($\cot[kL]$).

Key concepts in Helmholtz resonator design

- Frequency increment times can be kept linear for small frequency sweeps.
- Port length extension is very difficult to calculate using theoretical techniques and is better found using empirical techniques.
- Ensure low values of ka (wave number multiplied by port radius) to prevent excessive radiation resistance from the port.
- Q factor can be improved by minimising internal friction resistance in the port and chamber.
- Compromises are necessary to balance port surface area to Q factor. High surface areas increase boundary layer losses whereas high Q factors require long narrow ports.
- Keep sound pressure levels and frequencies low to avoid turbulence and jetting in the port.
- Keep the port centred in the chamber (non-eccentric) to allow predictable flange factor effects.
- Chamber and port lengths should be kept under $1/16$ of the resonant wavelength to avoid lumped parameter violations.
- Chamber shape should be kept regular to prevent changing internal impedance with length.
- Multiple ports should be avoided where possible as extra ports decrease Q factor and increase boundary layer losses in the port.
- When using port and chamber lengths longer than $1/16$ of the resonant wavelength either transcendental or improved Helmholtz equations should be used.

Chapter 3

Resonance hunting for volume determination

3.1 Introduction and summary

The focus of this investigation was the use of a Helmholtz resonator for volume determination. It was not to repeat research into fundamental properties of Helmholtz resonators. Ingard (1953), Chanaud (1993) and others have previously conducted much research on Helmholtz resonator geometries as described in Chapter two. Most acoustical work involves modelling using various idealisations. Inaccuracies and inconsistencies are still present even in models using small, finite element analysis of a well defined system, such as those conducted by Selamet and Lee (2003). Therefore, the focus in the methods developed has been empirical rather than theoretical.

To date only a small number of studies have used resonators to measure volume. Therefore, a comprehensive method was required to investigate how resonance is affected by the inclusion of solid, liquid or granular material within the resonant chamber. Previous studies, such as Nishizu *et al.* (2001), used limited acoustical excitation methods and focused on a narrow configuration, in which accuracy was compromised to measurements of approximately $\pm 1\%$.

An apparatus for testing factors affecting volume measurements using Helmholtz resonance was designed and built based on a thorough investigation of existing Helmholtz resonator literature and the mathematics describing acoustical systems. Of principle interest was creating resonators with a very high Q factor (Quality factor). The higher the Q factor the better the resolvability of frequency and hence determination of sample volume via the Helmholtz equation. To allow rapid determination of frequency, various resonant hunting methods were employed to reduce the scanning time.

Accuracy and speed of measurement for a given system will depend on the method of application of an acoustic source. For this reason several novel approaches were used to ascertain their suitability for this investigation. When speed of measurement is an important factor there is insufficient time to sweep through a broad frequency range to isolate the resonant frequency. Methods involved exposing the resonant system to an array of frequencies either in succession, simultaneously or at a single frequency.

Initial stages of the investigation were concerned with characterising the fundamental resonators in terms of repeatability, effects of the sound source, temperature and environmental considerations. Variations in resonator configurations were also tested to isolate factors contributing to resonator performance. These included symmetric and asymmetric ports, flange material at the port mouth and dual port resonators.

The accuracy of volume measurement depends on temperature since the speed of sound changes significantly with temperature. Therefore, all frequency measurements were associated with a temperature, at the time of measurement. An appropriate temperature factor was used in calculated volumes to ensure accuracy under varying temperature conditions. Effects of air pressure and density tend to counteract each other in regard to effects on the speed of sound (Kinsler and Frey, 1962).

Resonant volume measurements progressed to liquids, solids and granular materials after careful development of a resonant hunting procedure and detailed analysis of

contributing factors in resonator performance. Further investigative work was conducted on chamber mapping a dual port resonator with a spherical sample. This extends early work by Leung *et al.* (1981) and Barmatz *et al.* (1982) on chambers containing a rigid sphere. Nishizu *et al.* (2001) in their pioneering work describe a 'sweet spot' measurement region in a Helmholtz resonator where port interference effects are negligible.

In the interests of completeness, a number of experiments were developed to investigate air leaks on a resonant system. The Q factor is highly dependant on a sealed chamber. Any small air leak will cause significant acoustic resistance to the oscillatory pressure in the chamber. In a commercial application of this method it would be useful to identify such air leaks by their known effects on the resonant system.

3.2 Equipment and samples

Software algorithms and functional block diagrams are given in Appendix B. Full mechanical drawings of all experimental apparatus are in Appendix E.

3.2.1 Resonators

A set of general purpose resonator components were manufactured to investigate resonant volume measurements. By designing interchangeable resonator end-plates and port-plates a wide variety of configurations could be tested. These included variable chamber volume sizes 1L, 2L and 3L, by substituting in different chamber tube lengths, variable port lengths by switching port plates (51mm and 170mm) and the dual port configurations by adding a second port plate, Figure 3.2.1.

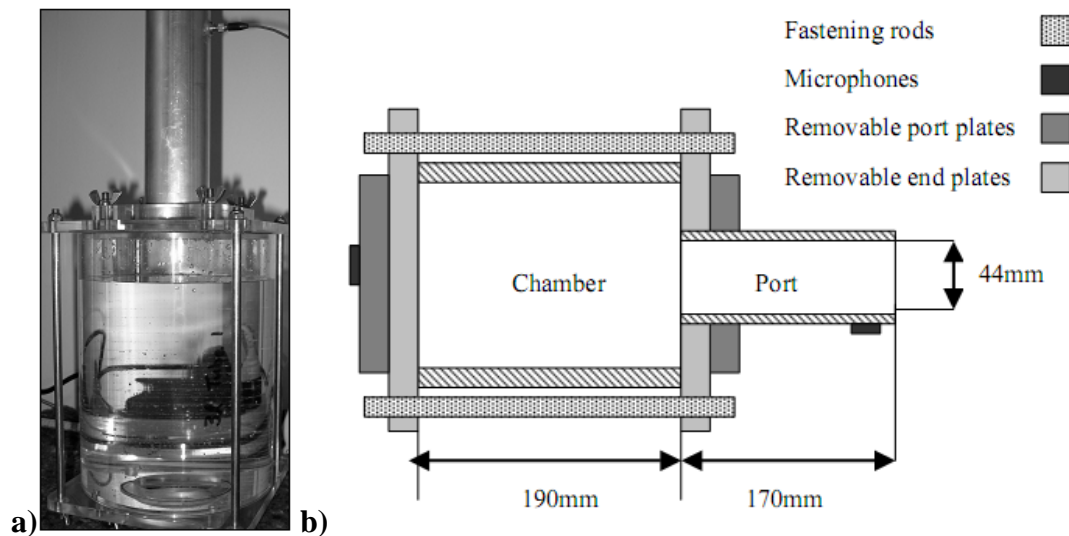


Figure 3.2.1 a) Photo of standard single asymmetric port resonator with blanking plate on bottom face having a 3L chamber (140mm internal diameter), 170mm long port with an internal radius of 44mm and b) schematic diagram.

Chamber end plates were O-ringed to seal against the chamber tube as well as the port plates. Any air leaks between these components would cause variability in the resonant frequency. Port plates and chamber end plates were fastened using a combination of threaded rod and threaded studs secured with wing nuts. The advantage of this system was rapid and easy switching of chamber sizes and port configurations.

All parts were made of clear PerspexTM (150mm diameter, 5mm thick walled tube and 12.5mm thick flats for end plates) to allow easy machining and visibility of samples within the chamber. Ports were made of extruded 50mm aluminium tube with a 3mm wall thickness giving an internal port diameter of 44mm. Chamber lengths were 63mm, 127mm and 190mm to give chamber volumes of 1L, 2L and 3L respectively. An uncertainty analysis was undertaken in Section 3.4.1 to ascertain machining and part tolerances.

Single port configurations were used to test a large range of sample types described in Sections 3.2.12 to 3.2.14. In these instances the sample was not required to pass through the port. Samples included granular material, liquids and solids of varying

shapes and surface textures. The single port chambers were also tested with symmetric and asymmetric port mountings, Figure 3.2.2, and two port lengths.

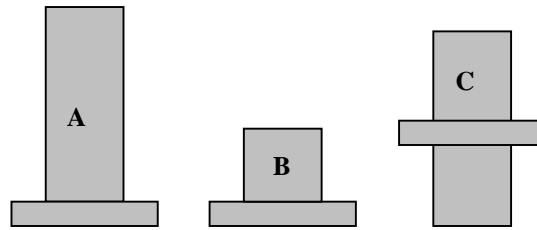


Figure 3.2.2 A) Single 170mm asymmetric port plate B) 51mm asymmetric port plate C) 170mm symmetric port plate

The dual port resonator could be assembled and used to investigate sample location effects within the chamber. A dual port resonator configuration with two short 51mm ports will keep the resonant frequency in the same range as the 170mm single port variation. The addition of an extra port will cause an effective increase in cross sectional area of the port. The main disadvantage of an increase in cross sectional area is a reduction in the Q factor of the resonator. Table 3.2.1 is presented to indicate possible assembly combinations for both single and dual port configurations. Q factors were calculated via Equation (No.25), Basic Equations.

Chamber size (L)	Port length (mm)	Port type	Predicted Q
3	170	asymmetric	527
3	170	symmetric	505
3	51	asymmetric	139
3	Dual 51	asymmetric	59
3	Dual 170&51	asymmetric	149
2	170	asymmetric	430
2	170	symmetric	412
2	51	asymmetric	113
2	Dual 51	asymmetric	40
2	Dual 170&51	asymmetric	122
1	170	asymmetric	304
1	51	asymmetric	80
1	Dual 51	asymmetric	28
1	Dual 170&51	asymmetric	86

Table 3.2.1 Fourteen possible resonator combinations possible using available chamber sizes, port lengths and port types.

3.2.2 Microphones

PCB103A piezoelectric microphones were used in all experimental work. In single port configurations with a 0.17m port two microphones were used, the first spaced 20mm from the port opening, and the second was centre-mounted in the chamber base, Figure 3.2.3. In dual port configurations the second microphone was placed in the same position in the second port, 20mm from the mouth of the port. This allowed comparison of both ports when an object was moving through the chamber. Data sheets for the PCB103A microphones are presented in Appendix E.

The PCB microphone outputs were calculated using the measured voltage signals from the PCB microphones referenced to a 1-volt source. This gave signals in dB

using Equation (No.13), Basic Equations. This differs from Chapter 4 results, which are referenced to a calibrated source as described in Appendix D, giving microphone signals at standard dB levels.

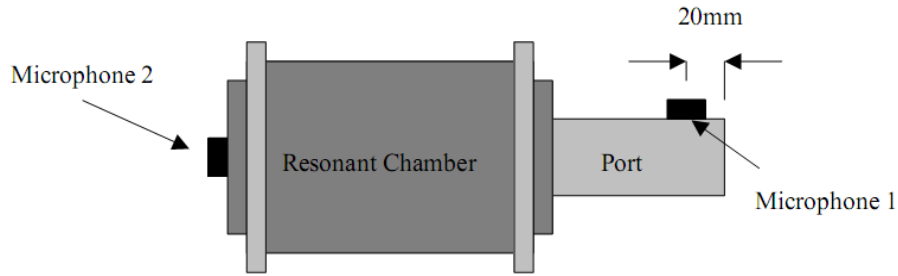


Figure 3.2.3 Microphone locations on resonant chamber, able to measure port frequency and chamber frequency independently.

3.2.3 Data Acquisition (DAQ) Hardware

A National Instruments PCI 6221 M series *DAQ* card was used for the signal generation and analysis from microphones and temperature sensors. It was also used to generate both white and pink noise used in broad-spectrum signal generation, Figure 3.2.4. The speaker was located 400mm from the resonator with the microphone opposite the speaker.

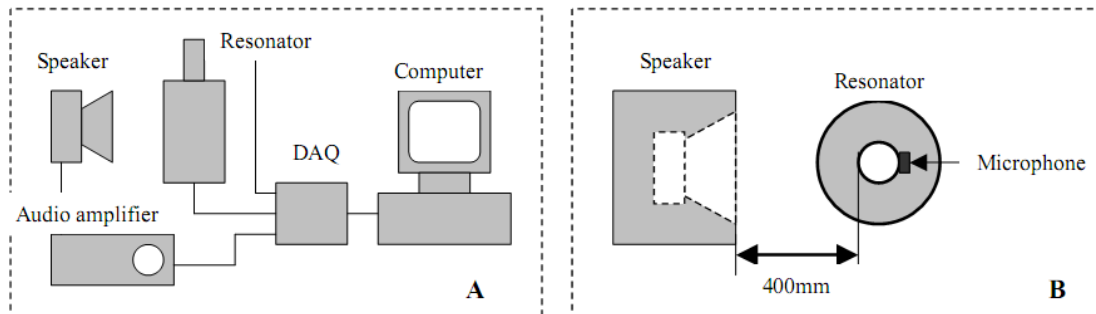


Figure 3.2.4 A) Schematic of hardware components used in experimental setup. B) Resonator alignment and distance from speaker.

3.2.4 Temperature sensors

Speed of sound temperature compensation was provided by an inbuilt resistive temperature device (*RTD*) in the NI BNC-2120 connector block. The *RTD* was able to give linear temperature measurements to a precision of 0.1°C. Calibration of the temperature sensor was via a calibrated Hart Scientific *RTD* temperature meter model 1502A.

3.2.5 Software

Software was specifically designed using National Instruments LabVIEW™ and used extensively in this investigation to generate and acquire frequency data. LabVIEW™ contains tools specifically for time dependent logging of frequency information (Fast Fourier Transforms - FFT) as well as detailed analytical tools for post processing results. Full details of software algorithms are give in Appendix B.

In procedures requiring an accurate resonant frequency determination a three-stage-hunting algorithm was developed. First pink noise was applied to the resonator to establish an approximate resonant frequency. Once determined, a 2Hz frequency

sweep was used to further isolate the resonant peak. Lastly, a very narrow 0.1Hz sweep was applied to detect the resonant frequency to a precision of 0.005Hz.

Software was also developed to control a STP100 Stepper motor controller from PONTECH (San Dimas, California, USA) for the precise positioning of a sample in the dual-port resonator.

3.2.6 Pink noise

A method employed extensively by Chanuad (1997), to quickly locate the approximate resonant frequency, was to use broadband (pink) noise. Pink noise consists of random frequencies of equal power. It is different from white noise, which consists of random frequencies of random power. This method of using broadband noise was also used, but to a lesser extent, by Selamet, Dickey and Novak (1995) for rapidly analysing resonant frequencies.

The advantage of using pink noise is equal power at any given frequency. Therefore, the frequency domain output looks roughly like a step function, equal power at all frequencies. Any resonance should then be observed as a peak in the frequency domain.

3.2.7 Chirps – Frequency sweep

The chirp, or frequency sweep, is a way of measuring the resonator's response to a changing driving frequency or forcing function. This method is limited by the time required for the frequency determination, generally the longer the period of frequency stability the greater the accuracy of the measurement. Therefore, the speed at which the frequency is ramped from an initial frequency to the final frequency must be determined by the required frequency resolution. Frequency measurements are made using a Fast Fourier Transforms (FFT) algorithm.

To avoid excessively long sweep times the sweep range must be kept to a minimum. If the rough size of the object can be determined by other means then the frequency range required to sweep is greatly reduced. For this reason, square wave and pink/white noise methods were used to rapidly gauge the approximate resonant frequency. A repeated 'chirp' over a successively narrow range was then applied to further improve the accuracy (resonant hunting).

The time taken for a complete cycle at a given frequency is a function of the frequency itself. Therefore, the time spent at any given instant producing a frequency needs to be reduced with increasing frequency. For example, at 100 Hz one cycle takes 0.01 seconds, but at 1KHz it takes 0.001 second.

3.2.8 Square wave

One possibility for isolating the approximate volume was to apply a square wave containing odd harmonics of the fundamental. The fundamental frequency will determine the spacing between the harmonics. By inspecting the Fast Fourier Transform (FFT) a disturbance in the decaying peaks appears near the resonant frequency. Everywhere else the harmonics should be in a predictable regular decay pattern with increasing frequency. A perturbation in the square wave harmonic decay may be evident even when a small acquisition time is used to inspect the harmonics, Figure 3.2.5.

It is expected the harmonic peaks in the frequency spectrum will broaden as the acquisition time is decreased. This broadening should not alter the frequency peak location, only its resolvability. So long as the harmonics are sufficiently separated in frequency, the peaks need not be resolved to high precision.

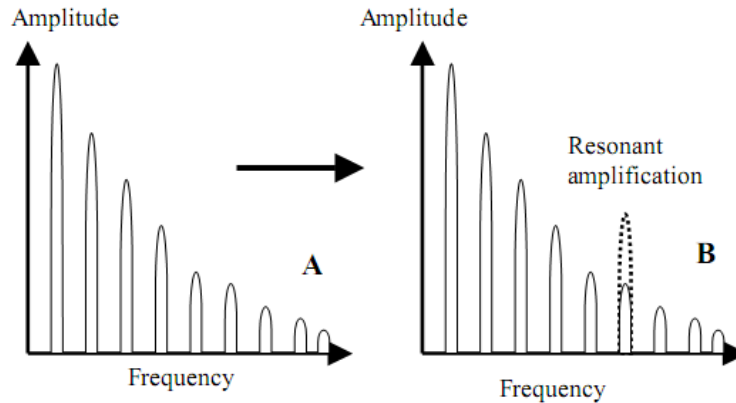


Figure 3.2.5 A) Decaying regular spacing of harmonic frequencies present in square wave. B) Expected amplification of harmonic near Helmholtz resonant frequency.

3.2.9 Loudspeaker

The primary sound source for this investigation was a full range, eight-inch, polycarbonate cone driver in an infinite baffle enclosure. The enclosure was optimally designed using Thiele (1971) and Small (1972) design parameters (See Appendix C). This ensured a reasonably flat response over the range of frequencies used, typically between 60Hz and 500Hz. The distance from the sound source to the resonator was kept to 0.4m. This is the distance at which the sound source behaves like a point source. The distance of equal intensity is proportional to $ka\sin\theta$, where k is wave number (m^{-1}), ' a ' is the speaker diameter (m) and θ the angle (radians) from the centre. Frequency and linearity response for the loudspeaker used are given in Appendix D.

The enclosure was lined with sound absorbent polyester material and made from 25mm thick medium density fibreboard. All joints were rebated to give maximum strength. Corners on all faces were rounded to eliminate secondary fringing effect that can cause interference patterns with the primary sound source. The loudspeaker was flush mounted with the face panel for the same reasons.

3.2.10 Pulley apparatus

A stepper-motor driven pulley system was designed to facilitate the moving of an object through the dual port resonator. The pulley system would allow the investigation of resonance as a function of sample position, both in the radial and axial orientations. The pulley apparatus was made with adjustable feet to allow easy levelling of the height. In addition the support arms at the rear of the mounting plate were made adjustable to facilitate correct angle between plate and base.

Figure 3.2.6 shows the vertical orientation of the dual port resonator with pulleys above and below for correct sample alignment. Also shown is the pulley pinch roller assembly designed to maintain sample position during stepper transitions. The main

supporting back plate is approximately 500mm high and 400mm wide. The over all length of the dual port resonator is 300mm.

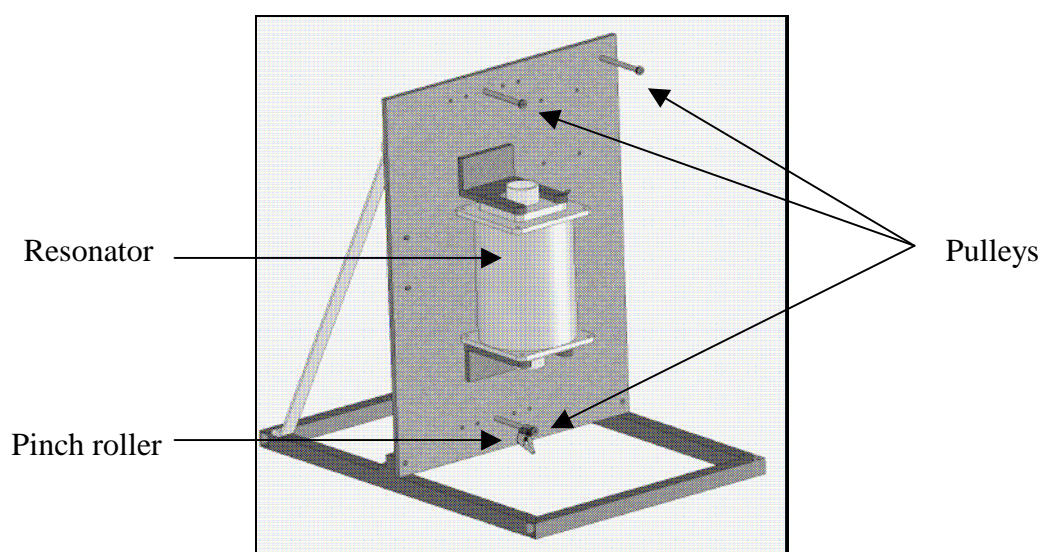


Figure 3.2.6 Vertical arrangement of dual port resonator showing pulleys above and below to locate sample.

A second function of the pulley system was to enable the investigation of off-centre effects of a sample at different radial distances as seen in Figure 3.2.7. The sample was stepped from the top of the chamber wall to the bottom at different horizontal locations. The chamber has small holes drilled into the sides (not shown in figure) to allow a fine steel cord to pass through. Other holes for alternative positions were blocked off.

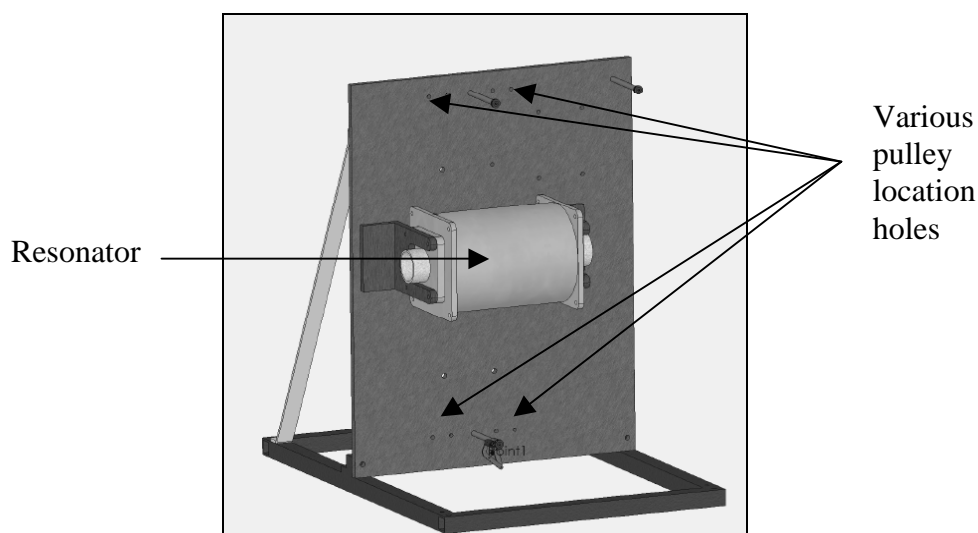


Figure 3.2.7 Horizontal arrangement of dual port 3L resonator showing pulleys above and below to locate sample. Also shown are placement holes for pulley support posts allowing multiple horizontal placements to be investigated.

The combination of vertical and horizontal measurements allowed a three dimensional map to be generated of object location effects within the chamber. Only radial and axial planes were investigated due to chamber symmetry.

3.2.11 Stepper-motor

The stepper-motor is of type Sigma Industries Model 20-2223D-24210 taken from an XY plotter and driven by a STP100 stepper-motor controller (San Dimas, California, USA), connected serially to the controlling computer. The stepper-motor is capable of 400 steps per revolution. A total sample displacement of 250mm was required, which equates to 2.7 turns on a spindle 30mm in diameter. This results in step intervals of 1mm.

3.2.12 Solid samples

Solid sample consisted of spherical and cube samples of varying size. All are given in their water equivalent displacements. Spherical sample sizes by volume were 1mL, 2mL, 7mL, 9mL, 23mL, 42mL, 46mL, 118mL, and 278mL. The diameters of these spheres were 23.85mm, 25.40mm, 35.50mm, 41.63mm, 44.45mm, 60.85mm, and 80.97mm respectively. Cube volumes were 2mL 18mL, 133mL, 215mL, 430mL, 645mL and 860mL. By assembling combinations of the 215mL cubes the last three cube sizes could be acquired.

Volume analysis of spheres and cubes was performed by weight rather than measured dimensions with the exception of chrome steel ball bearings, which were sufficiently regular to allow direct calliper measurement. Small cube samples (2mL to 133mL) were made of aluminium (density, 2699kg/m³), large cube samples (215mL to 860mL) mild steel (density, 7874kg/m³). Spheres were a combination of chromed ball bearings (measured by diameter not density), glass marbles (density, 2520kg/m³), machined aluminium and mild steel. Spherical sample 1mL, 46mL, 118mL were chrome steel; spheres of 2mL, 9mL, 23mL were glass, the 42mL sphere was machined aluminium and the 278mL sphere was mild steel. Aluminium and Steel density sourced from Halliday *et al.*, 1997. The glass marble density was measured using the buoyancy apparatus described in Chapter 4, Section 4.3.3.

3.2.13 Granular samples

Table 3.2.2 provides details on granular material bulk density, particle density and mean sizes. As seed and the plastic pallet varied considerably their values are given as approximate only.

Sample type	Bulk density kg/m ³	Particle density kg/m ³	Mean diameter mm
Sand	1283	2540	0.166
Small ballotini	1449	2473	0.261
Large ballotini	1454	2489	0.713
Panicum seed	688	1720*	1.5*
Rape seed	662	1260*	2*
Plastic pellets	592	1120*	3*
Small marbles	-	2520	15.83
Large marbles	-	2520	24.81

Table 3.2.2 Bulk density and particle density information for granular materials. ‘*’ indicates approximate only.

3.2.14 Liquid samples

Tap water was used as an example for liquid measurements due to it being readily available and having well defined characteristics. It is known to change in density with temperature by a small amount. This could cause errors when using it as a calibration medium. During various calibration conducted in Chapter 3 the temperature range was 10°C to 15°C. Water for calibration was allowed to equilibrate with respect to temperature and de-gassed for two hours prior to use for calibration. Table 3.2.3 gives typical values for water density. For a temperature of 15°C this could lead to a maximum uncertainty of +2mL at a chamber fill of 2L. Quantities of water were measured by weight using asset of Mettler PE6000 scales (± 0.1 g).

Temperature °C	Density kg/m ³
10	999.7
15	999.1
20	998.2
25	997.1

Table 3.2.3 **Change in water density with temperature (Lide, 1990)**

By using an O-ring sealed solid piston barrier the differences between a liquid surface and a solid surface could be analysed. The height of the solid piston could be manually adjusted to reproduce water fill heights. Therefore, the effect of surface of the water could be directly assessed.

3.2.15 Acoustic barrier disks

Steel flat (0.6mm) disks of varying diameter were used as acoustic barriers. They ranged in diameter from 20mm to 120mm (20mm, 40mm, 60mm, 80mm, 100mm and 120mm). A 1mm diameter stem was used to support the disks in the resonant chamber. The stem had an interference fit and was inserted through a specific blank port plate mounted on the resonator base.

3.3 Methods

3.3.1 Characterising the fabricated resonators

A number of tests were needed to find the optimum resonator location with respect to the loudspeaker location. Base measurements of the resonant frequency for each port/chamber configuration were also taken, with no internal sample. The optimum location for the sound source is one where the port is not located in an interference lobe of acoustical loci caused by intrinsic characteristics of the loudspeaker used and/or the chosen frequency. Lobes are regions of equal sound intensity that radiate away from the loudspeaker (See Appendix C, Section 4).

A number of tests were conducted using a broad frequency sweep with different environmental configurations. This was necessary, as the sound source is not coupled directly to the resonator. The environment in which testing was conducted can have secondary resonant properties that change with an open door or similar.

The sound intensity attenuates at a rate proportional to $1/r^2$, where r is the distance from the sound source; hence even at short distances attenuation can be considerable. Other variables such as surrounding fixtures and surfaces provided moderate acoustic absorption and were maintained, where possible, throughout testing. Ambient sound levels for experiments were measured using a Realistic Sound Level Meter model 42-3019 on the dB-C setting (Typical sound levels were between 80dB to 90dB). dB-C is a flat filter response to frequency, 50Hz to 10kHz, that indicates true sound level not perceived sound level such as dB-A and dB-B.

The various resonator configurations were tested to ascertain how closely they matched theoretical calculations using the standard Helmholtz equation. These experimental values were then used as the standard values against which subsequent experimental work was checked.

3.3.2 Repeatability of measurements using resonators

Repeatability of base measurements needed to be established, as accuracy was important factor of this investigation. After finding the optimal sound source location, repeatability tests were carried out by assembling and disassembling the equipment in all possible experimental combinations to be used.

Repeatability was extended further to include a number of calibration samples having well defined geometry (See Section 3.2.12). These consisted of large cubic steel blocks that could be arranged in combinations from 216mL to 864mL. Repeatability was also checked using spherical steel and glass balls of sizes; 1.07mL, 7.06mL, 22.45mL, 42.05mL, 45.83mL and a 278mL (See Section 3.2.10). Samples were placed in the centre of the chamber to maintain symmetry between the sample and the chamber.

3.3.3 Temperature effects

Temperature changes the speed of sound as described by Equation (3.3.1) (See also Appendix A, Section 1). To test whether this equation could be used directly with the existing Helmholtz equation a number of measurements of frequency and temperature were made over a range of steady state temperatures with an unchanged chamber and port.

$$c_0 = \sqrt{\gamma \frac{p_0}{\rho_0}} = \sqrt{\frac{\gamma R_c T_{emp}}{M}} \quad (3.3.1)$$

where c_0 is the speed of sound at a specific temperature, γ is the ratio of molar specific heats, p_0 is the primary pressure, ρ_0 is the primary density, R_c is the universal gas constant, T_{emp} is the temperature in Kelvin and M the molar mass of air.

From Equation (3.3.1) it can be seen that the speed of sound will be proportional to the square root of temperature in Kelvin. For convenience and ease of use in software algorithms the effect of temperature on the speed of sound can be approximated to a high degree of accuracy using the linear form $331.73 + 0.587T_{emp}$ for temperature ranges between 8°C to 24°C. Therefore, a gradient $0.587T_{emp}$ would be expected for changes in the speed of sound occurring within the port as measured by the PCB microphone. These measurements would allow comparison of theoretical and experimental temperature gradients using the Helmholtz resonator Equation (No.21) from Basic Equations.

3.3.4 Calibrating the asymmetric single port resonator

Calibration was conducted using the 3L resonator with a 170mm long asymmetric port (all port material external to the resonator). This configuration was the primary resonator used in the majority of experimental work that followed due to its large chamber size and high Q factor (Quality of resonance). The large chamber size allowed a bigger range of sample volumes to be studied and the high Q factor allowed measurements of resonance behaviour of samples having high sound absorption.

Fill fractions and calibration were investigated by progressively filling the chamber with water (Figure 3.3.1). The water had the same ambient temperature as the experimental equipment and was allowed to equilibrate and degas for 2 hours prior to use. This was to minimise temperature differentials and to allow dissolved gases to escape. The calibration temperature was 15°C indicating there should be less than 3mL uncertainty due to changes in water density with two litres of fill.

Using a Mettler PE6000 set of precision scales, 100mL amounts of water were added to the chamber and the resonant frequencies and temperature recorded. A fill fraction versus detected resonant frequency curve could then be plotted and compared to theory. Successful calibration results would allow theoretical back-calculation of a sample's volume, when placed in the resonators chamber. See Basic Equations, Equation (No.22).

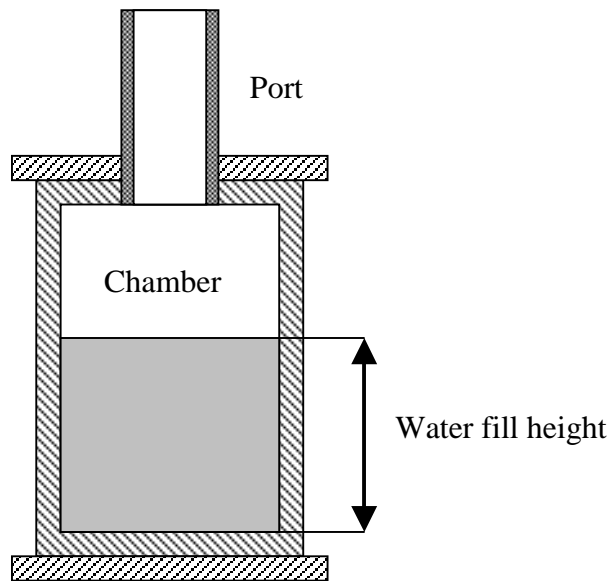
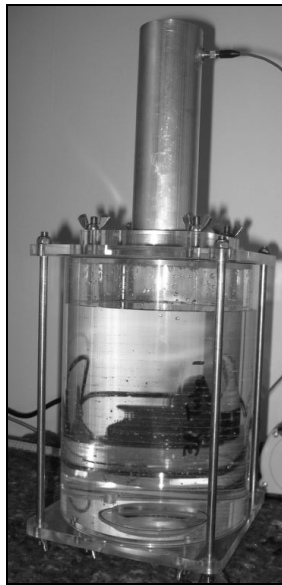


Figure 3.3.1 Photo (left) and diagram (right) of water filling of 3L chamber with 170mm, asymmetric port used for volume calibration.

A second testing method was carried out with the resonator in the horizontal position. Again water was used in filling the chamber in 100mL amounts. Being horizontal the fill level rapidly approached the port and limited the maximum volume to 1000mL. This test would reveal how obstruction of the internal flange affected the Helmholtz equation for calculating chamber displacement. These tests would also be used to assess the suitability of making measurements when the resonator is in the horizontal configuration.

With the resonator again in the vertical orientation precision-machined angular steel blocks, two cubes of 216mL and one rectangular 432mL were used to provide linear volume increases. Sample volumes were made up from 0mL, 216mL, 432mL, 648mL and 864mL cubes. Sample volumes are given as their equivalent water displacement. Resonant frequencies and temperatures were measured and compared with theoretical calculations using the Helmholtz equation. The tests on these samples were repeated in reverse size order and resonant values compared with the first test data.

With large solid objects, relative to the chamber size, the objects under test quickly approach the internal port entrance. This will cause the resonator to behave in a non-linear fashion if samples are within the end correction length (See Appendix A, Section 8). This occurs when the moving mass of air in the port entrance becomes restricted.

To validate water as a suitable calibration medium a solid Perspex piston was created that could be used to adjust the volume of the resonator chamber. This piston was adjusted to various heights and the volume compared with the data collected for the water calibration. If the water absorbed significant amounts of energy or produced significant quantities of water vapour within the chamber during resonance this test should reveal noticeable differences. However, the piston could not be moved with enough precision to allow millilitre comparisons, but would enable volume deviation trends to be compared.

3.3.5 Effects of port symmetry

The end of the port causes an increase in the effective port length by a factor determined by the port diameter and its termination type. If the internal port is flush with the chamber as in figure 3.3.2a, then the effective length should increase by approximately $8/3\pi$ times the port radius (Kinsler and Frey, 1962). In contrast, for an un-flanged port there ought to be an increase in effective length of about 0.6 times the port radius (Figure 3.3.2b).

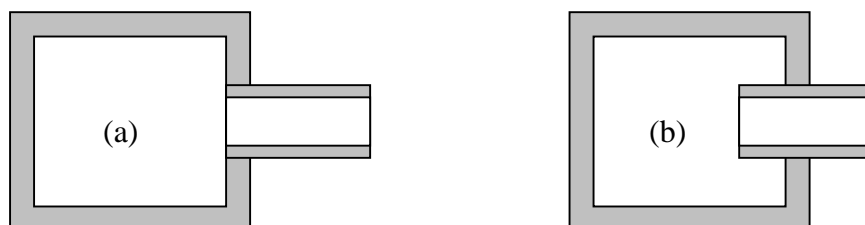


Figure 3.3.2 (a): Flanged internal and un-flanged external port, asymmetric. (b): Un-flanged internal and un-flanged external port, symmetric.

The aim was to confirm the flanging effects of port configuration by comparing both internally flanged and un-flanged ports of 170mm in a 3L chamber with a 44mm port radius. This would complement experimental work by Chanaud (1993) and Selamet and Lee (2003) who investigated port geometries and port symmetries respectively.

When using water for chamber filling, data were gathered on the resonant frequencies at various water heights using the symmetric and asymmetric port placements. Because of the port intrusion for the symmetric configuration only limited filling could be achieved before the water height approached the internal port.

3.3.6 Effects of sample irregularities

Kinsler and Frey (1962) suggested that resonance should not be a function of chamber cavity shape except at higher harmonic frequencies well above those tested for. To test this assumption a simple comparison of spherical and angular samples was conducted (See Section 3.2.12). Data gathered from measuring the volume of cubic steel calibration samples was compared to those using similar spherical volumes.

To test the effects of an acoustic barrier six thin (0.6mm) flat disks of varying diameter, 14% to 86% of the chamber diameter (20mm to 120mm), were used in the resonant chamber and the change in resonant frequency recorded (Figure 3.3.3). To further investigate barrier effects, the resonant frequency was also monitored for each disk at eight heights ranging from 20mm above the chamber floor to 20mm from the interior port opening. In this way the affect of an acoustic barrier was analysed free from a volume induced frequency change. Measurements were made at constant temperature to further isolate only barrier effects. The resonator configuration consisted of a 3L chamber and a 170mm port with a diameter of 44mm.

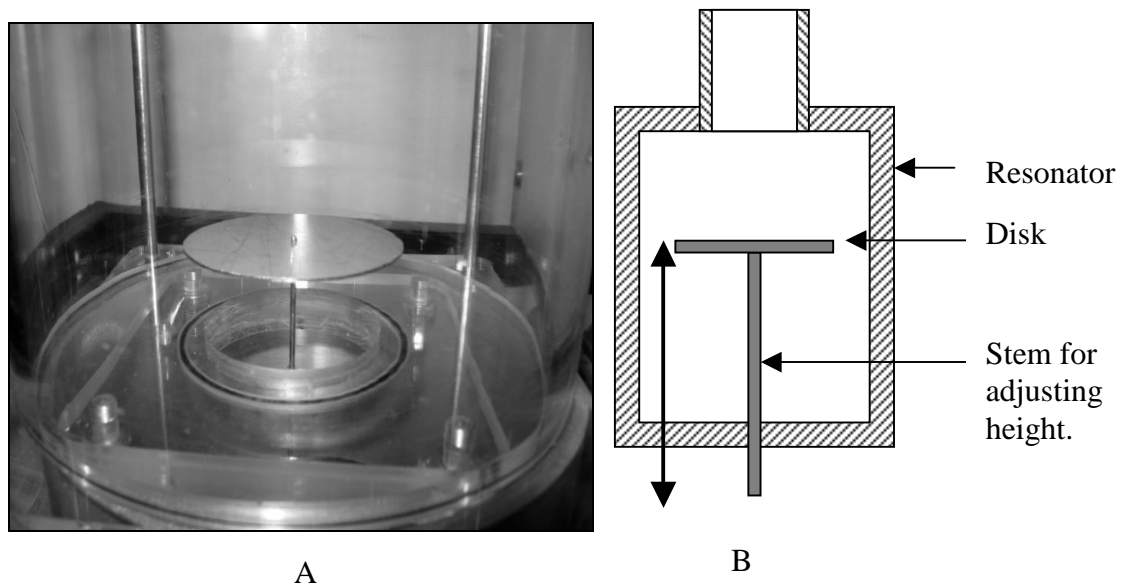


Figure 3.3.3 A) Photograph of one of the six flat disks (20mm diameter) used to isolate surface area effects from volume effects. B) Diagram of resonator housing a disk of variable size and position.

3.3.7 Measurement on granular materials

It was unknown how granular materials in the chamber would affect the overall measurement accuracy. Nisizu's (2001) study mentions the use of rice as a test material but gives little details of its effect on resonance. A number of granular materials were tested using the single 170mm long asymmetrical port and 3L chamber. These included sand (166 μ m mean size), rape seed (2mm mean size), panicum seed (1.5mm mean size), plastic pellets (3mm mean size), glass marbles (mean size 15mm and 24mm) and ballotini (mean size 261 μ m and 713 μ m). The plastic pellets were disk shaped, 3mm in diameter by 1.8mm high, but are expected to behave similarly to 3mm spheres.

The quantity of attenuation/mm depth for each sample material can be calculated by comparing the port/chamber microphone levels. This would indicate how far the sound penetrates into the granular material. By using a large range of particle sizes it was hoped trends might be observed that would allow a lower limit of particle size to be predicted. Sound absorption and retransmission in granular material is an extremely complex phenomenon and it was not the aim of this investigation to conduct extensive research into these effects, merely to gauge the effect of acoustical penetration and suitability for resonant measurements.

Steel disks, the diameter of the chamber, were coated in the previously mentioned granular materials and were attached to the top face of the Perspex piston used for variable chamber volume testing. The coatings were one layer thick to prevent any depth attenuation. A water-based glue (poly vinyl acetate, PVA) was used to adhere the materials to the disk. The purpose of these tests was the separation of granular surface effect from those of acoustic attenuation with granular bed depth. Three magnets within the piston allowed the coated metal disks to adhere to the piston surface. The piston was moved to a range of heights thereby replicating granular materials fill heights, Figure 3.3.4.

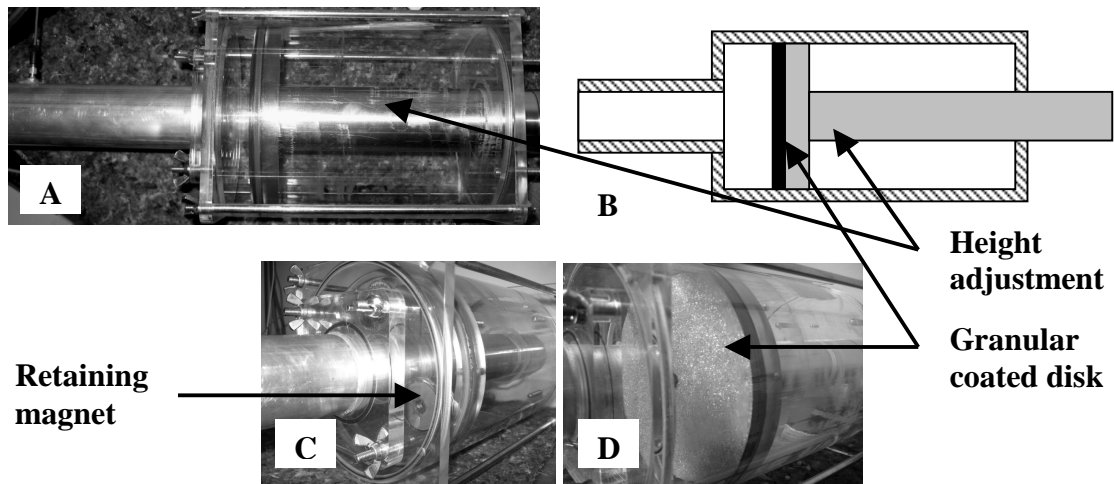


Figure 3.3.4 A) Photograph of the adjustable piston within chamber and B) Schematic diagram. C) Photo of embedded magnet within piston used for retaining steel coated disks. D) Photo of ballotini coated disk.

The coated piston may then allow accurate volume measurements of small amounts of rapeseed, panicum and plastic pellets in the 1L resonator, independent of attenuation caused by the depth of the granular bed material. Using the 1L resonator achieves the best filling ratio for the small sample size. The particle volumes and density for these materials are unknown and only rough values can be gathered through manual measurements of a large number of individual particles. If a small volume of bulk particles could be measured and weighed, a more accurate volume and density may be determined for each.

To this end 50mL of these three granular samples were placed in the 1L resonator with a 170mm asymmetric port. Using the smallest chamber would result in the highest accuracy for the small quantities of these materials. It was observed this quantity was sufficient to coat the base of the chamber without causing any bed depth attenuation.

3.3.8 Effects of air leaks on resonant frequency and Q factor

Air leaks were tested for using the 3L chamber and a 170mm asymmetric port having a 22mm internal radius. Ten 0.8mm diameter holes were drilled in the chamber walls, five on each side to function as air leaks. The holes were spaced at the centre, 32mm above and below the centre and 64mm either side of the centre. These locations would allow experimental testing of holes at different heights and interference between holes on opposing sides, Figure 3.3.5.

Testing started with no air leaks and progressed from one to ten air leaks by adding additional air leaks on opposite sides starting at the top and moving downward. Q factor was recorded to aid in gauging the effect of air leaks on accuracy. A broadening resonant peak would lower the achievable accuracy.

The holed 3L chamber was initially created to allow a thin steel cord to pass through that was used to support the ball in resonant chamber mapping. Air leak testing would determine whether it was necessary to block adjacent holes when testing was conducted in the 'radial sample location experiments' in Section 3.3.9.

To gauge the effects air leaks can have on a Helmholtz resonator, a resonator adaptor plate was made so the air leak hole size could be varied from 2mm diameter to 10mm diameter (2mm, 3mm, 4mm, 5mm, 6mm, 7mm, 8mm and 10mm). An adjustable disk allowed the unused holes to be blocked. As the adapter plate is 12mm thick, boundary layer effects are expected to be significant for the smaller air-leak sizes of 2mm to 5mm (See Appendix A, Section 9).

3.3.9 Effects of sample position on volume measurements

A number of experiments were conducted to create a resonant frequency map of sample location within the chamber, using the pulley apparatus and the 3L dual 51mm port resonator. Static measurements at fixed locations would allow better understanding of dynamic volume measurements.

A spherical aluminium ball sample of 41.63mL (43mm diameter) was adjusted in both the radial (one location at a time) and the axial direction through the chamber using the pulley apparatus and the 3L dual port resonator, Figure 3.3.5. The feed spindle diameter was chosen to give steps of 1mm for one step of the stepper motor (± 0.12 mm total uncertainty for any given position). Doing so allowed investigation of resonant trends with varying sample positions.

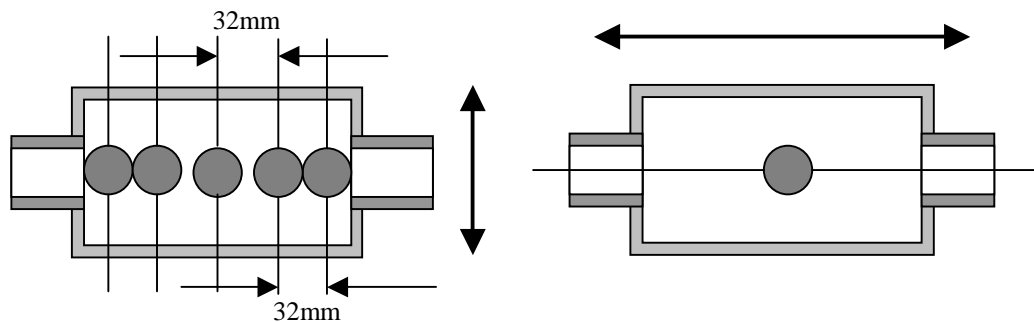


Figure 3.3.5 (Left) five positions for a spherical sample moving through the resonator vertically. (Right) horizontally adjusted spherical sample. Both configurations are driven by a stepper motor to create resonant mapping characteristics for the dual port resonator.

Of principal interest was the effect of object location on accuracy. Changes of the resonant frequency when compared to its value in the central position would indicate a non-ideal measurement location. A location calibration procedure was performed at the start of each test so the repeatability of sample placement could be confirmed. This would negate any cable stretch and stepper motor slippage, which could cause possible uncertainty in sample location. At the end of each test the sample position was then rechecked at the initial position.

The optimum measurement region within the chamber is the area where sample location does not change the resonant frequency. This virtual ‘bubble’ within the chamber also represents the largest object that can be measured.

3.3.10 Controlled decent using a dual-port resonator and resonant hunting

Initial free falling sample measurement experiments started with a controlled decent of the 41.63mL aluminium ball sample moving vertically through the dual 51mm port

3L chamber resonator at 1mm/s. Decent speeds were increased up to a controlled maximum of 100mm/s. Finally, complete free fall tests were conducted.

The three step resonant hunting method was applied to the resonator to gauge how effective it was determining the sample volume, both in terms of accuracy and speed. Free fall response was then tested by allowing a 7.1mL (23.85mm diameter) steel ball bearing to free fall through the chamber while continuous measurements of frequency were taken utilising narrow band chirps.

3.3.11 Measurement of port flanging effects

An early study by Ingard (1953) indicated the need to determine precise values for length extension factors for the ports used. This was necessary to allow accurate calculation of the sample volume using the standard Helmholtz equation with length correction, Equation (No.22), Basic Equations. Flange material was added to the external port to vary the port length extension factor, Figure 3.3.6. A graphical mapping of port length extension to flange ratio was acquired by holding the environmental temperature constant and using flange to port diameter ratios ranging from 0.136 to 6.818. Port lengths of 51mm and 170mm were used to ascertain two different rates of change in length extension for varying flange diameters.

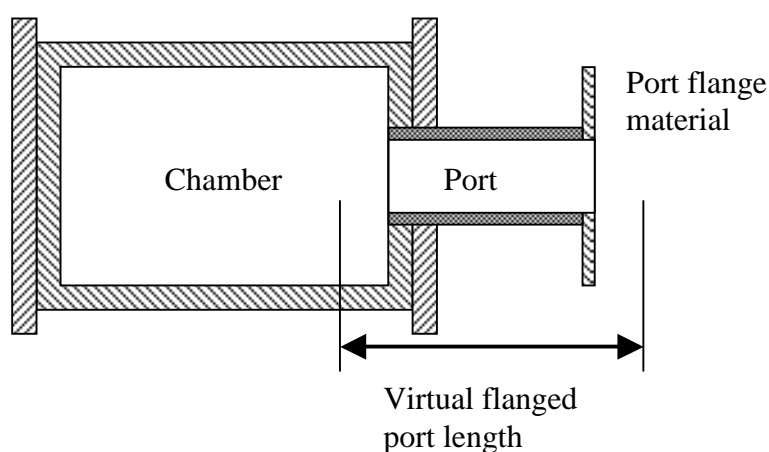


Figure 3.3.6 Flange material added resonator port. Flange material will alter the virtual or effective port length.

3.4 Results

3.4.1 Characterising the fabricated resonators

Early testing using square wave signals to locate the approximate resonant frequency proved unsuccessful as the odd harmonics regularly coincided with second and third harmonics caused by the chamber's physical geometry and artefacts associated with the environment. This resulted in unusual dips and peaks occurring in the square wave harmonics. These were often larger in effect than the primary resonant frequency of the resonator. Therefore, this roughing method of locating the resonant frequency was abandoned in favour of the pink noise method.

An uncertainty analysis of the 3L resonator components was undertaken (Figure 3.2.1). The extruded tube diameter of the port had a variation of less than 0.1mm. The port length uncertainty was less than 0.1mm. Other manufactured Perspex components were created in a computerised numerical controller (CNC) lathe, which was able to machine details to a tolerance of better than 0.05mm. O-ring compression and chamber flexing were the main factors in repeatability discrepancies. The Perspex tube used for the chamber was 5mm, with ± 0.5 mm in wall thickness and 140mm nominal internal diameter. The Perspex tube required significant flexing to fit it to the machined round end plates. O-ring compression in the end plates was not complete when assembled and resulted in ± 0.5 mm height variation. This gives a worst-case volume uncertainty of ± 29 mL or ± 0.42 Hz for a 3L chamber. Measured uncertainty and repeatability results are included in Section 3.4.2.

Ambient conditions played an important part in setting a base line from which results were collected. A number of early tests revealed changes in the resonator's environment changed its response sufficiently to warrant careful replication of the environment for future measurements. The dimensions of the room used were 2.4m, 3.3m and 2.4m, for width, length and height respectively. Results for changes made to the two doors within the room, open (*O*) and closed (*C*), are shown in Figure 3.4.1. Door *A* is 0.76m by 2m and door *B* is 0.72m by 2m. Results are presented at a constant temperature of 15°C. An invalid measurement region exists between 90-95Hz where signal levels are too low to be measured.

A significant attenuation change occurred as measured in the resonator port caused by having a closed room to that of an open one, Figure 3.4.1. Environmental effects can be over-come with an anechoic terminated coupled resonator and sound source configuration. But these all require additions that can create undesirable secondary effects such as unusual port coupling effects encountered by Selamet, Dickey and Novak (1995). It is to be noted that only a change in amplitude occurred with an environment change, not a change in the resonant frequency. But for consistency of measurement the same environmental configuration was used throughout all experimental work that followed. Accounting for environmental factors led to the development of environmental normalisation curves presented in Chapter 4.

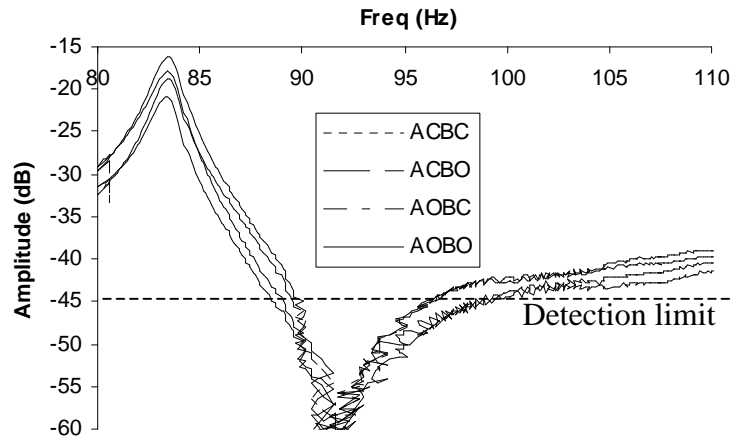


Figure 3.4.1 Attenuation in peak amplitude caused by changing experimental environment, where 'A' and 'B' are door A and B and 'O' and 'C' are open and closed. 3L chamber with a 170mm long, 22mm radius asymmetric port

Frequency results were checked for a number of different resonator placements: 1) upright, 2) on its side, 3) port facing the loudspeaker and 4) the port 90 degrees from the loudspeaker. There was no significant difference in resonant behaviour between the resonator in the upright position and the horizontal position with the port at 90 Degrees from the sound source. When the port was facing into the sound source a small reduction in the resonant frequency was observed. This reduction was typically about 0.1Hz less than the other configurations.

Further tests with the resonator in the upright position showed that the resonator could be moved between 200mm and 600mm from the sound source with no detectable change in the resonant frequency. Additionally, changes in the ambient sound level incident at the port, from 74dB-C to 86dB-C, had no noticeable effect on the resonant frequency. This behaviour is consistent with the resonator located in the main acoustical lobe of the loudspeaker (See Appendix C, Section 4).

Changes in microphone placement orientation with regard to sound source location showed no noticeable changes in either resonant frequency or its corresponding amplitude. These tests were at four rotational angles, 0, 90, 180 and 270 degrees, referenced to the loudspeaker at horizontal and with a port to loudspeaker distance of 400mm.

3.4.2 Repeatability of measurements using resonators

Using the 3L chamber, ten assembly/disassembly tests were undertaken and the predicted volume with temperature compensation compared. These results gave a maximum variation of 3mL between the highest and lowest value. Ten repeat measurements were then taken of the empty chamber with a 1mL variation occurring. These measurements indicate better than predicted consistency between separate measurements and measurements involving disassembly of the resonator.

A number of tests implemented with different chamber configurations revealed the highest Q factors were those using the 2L and 3L chambers. These experiments also

gave information on the suitability of using a combination of two different port lengths. It was observed the 2L and 3L dual port resonators with different port lengths had lower Q factors than the 1L variation.

Theoretical Q factor determination method detailed in Appendix A, Section 3, gave results an order of magnitude higher than those recorded through experiment. A Q factor of 527 is predicted for the first chamber in Table 3.4.1, but in experiment is found to be only 63.3. Similar non-agreement was true for the other variations tested. This is in contrast to the very good agreement of predicted resonant frequency with experimentally measured frequencies. The discrepancies in Q factor are most likely due to omissions in standard theory to include viscous acoustic resistive losses.

Chamber size (l)	Port length (mm)	Port type	Measured Q factor	Predicted Q factor
3	170	asymmetric	63.3	527
3	170	symmetric	62.2	505
3	51	asymmetric	53.0	139
3	Dual 51	asymmetric	47.0	59
3	Dual 170&51	asymmetric	41.3	149
2	170	asymmetric	67.6	430
2	170	symmetric	64.1	412
2	51	asymmetric	41.0	113
2	Dual 51	asymmetric	31.6	40
2	Dual 170&51	asymmetric	40.8	122
1	170	asymmetric	58.1	304
1	51	asymmetric	38.8	80
1	Dual 51	asymmetric	30.3	28
1	Dual 170&51	asymmetric	49.5	86

Table 3.4.1 Comparison of predicted Q factors, Equation (No.25), and actual measured Q factors, Equation (No.24), from Basic Equations. Q factors were evaluated for various chamber and port configurations at 20 degrees C

Repeat tests on individual solid samples showed little variation between measurements. Spherical samples ranging in size from approximately 1mL to 280mL were each measured consecutively five times with only a 1mL variation. Rapid successive measurements ensured marginal temperature drift and allowed direct testing of the sound generation and acquisition system. Similar results were gathered using angular cubic samples ranging from 216mL to 864mL.

There was a variation of approximately 7dB resonant peak amplitude over the range of different fill levels using water calibration data, Figure 3.4.2. The resonant peak amplitude is the signal strength as measured at the port at the systems resonant frequency. The resonant peak differs from the Q factor as the Q factor is derived from the two -3dB frequencies either side of the resonant peak frequency. Therefore, a change in resonant gain does not necessarily adversely affect the precision in determining the resonant frequency.

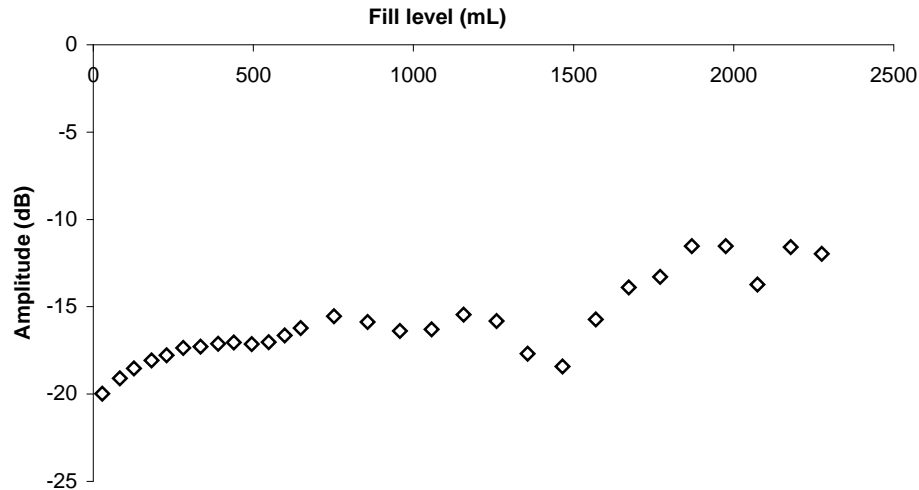


Figure 3.4.2 Resonant Frequency versus amplitude for increasing water fill level indicating changes in peak sound level. Tests used 3L chamber with 22mm radius, asymmetric, 170mm long port.

3.4.3 Temperature effects

Increases in air temperature cause an increase in the speed of sound, and therefore, will change the volume determined by the Helmholtz equation. The volume calculated using the Helmholtz equation, Equation (No.22), with correction via the temperature speed of sound Equations (No.23), is expected to remain constant with increasing temperature. If this assumption were true, other factors within the Helmholtz equation would be temperature insensitive.

The temperature factor for the speed of sound, based on a linear fit, will determine how the resonator volume is calculated for a given temperature change. This is essential if temperature stability is to be incorporated in the software algorithms. A linear gradient of $0.587\text{m/s/}^{\circ}\text{C}$ can be determined over the narrow range of 8°C to 24°C taking the first value of a Taylor expansion from the standard speed of sound temperature Equation (No.23). But, when measured indirectly from the Helmholtz equation a value of $0.534\text{m/s/}^{\circ}\text{C}$ was found. This assumed a constant port length correction with changing temperature, which may not be true. Over the temperature range of 8°C to 24°C an error of 14mL will result by using at temperature compensation gradient of $0.587\text{m/s/}^{\circ}\text{C}$ rather than the experimentally found value of $0.534\text{m/s/}^{\circ}\text{C}$.

By taking measurements of the resonant frequency over a number of days at stable temperatures a plot of temperature versus speed of sound was made, Figure 3.4.3. This showed that calculating the speed of sound indirectly from experiment, using the Helmholtz equation, changes in proportion to $0.534\text{m/s/}^{\circ}\text{C}$. Also presented are the standard values over this temperature range given by Equation (No.23), Basic Equations. The value $0.534\text{m/s/}^{\circ}\text{C}$ was used as an empirical temperature compensation value rather than the established value of $0.587\text{m/s/}^{\circ}\text{C}$. The temperature correction being the product of an additional variable β times c . The beta term, 0.91, is responsible for other temperature sensitive variables in the Helmholtz equation. These results were gained using a 3L chamber with 170mm long port. Similar results were gathered using the 51mm long port.

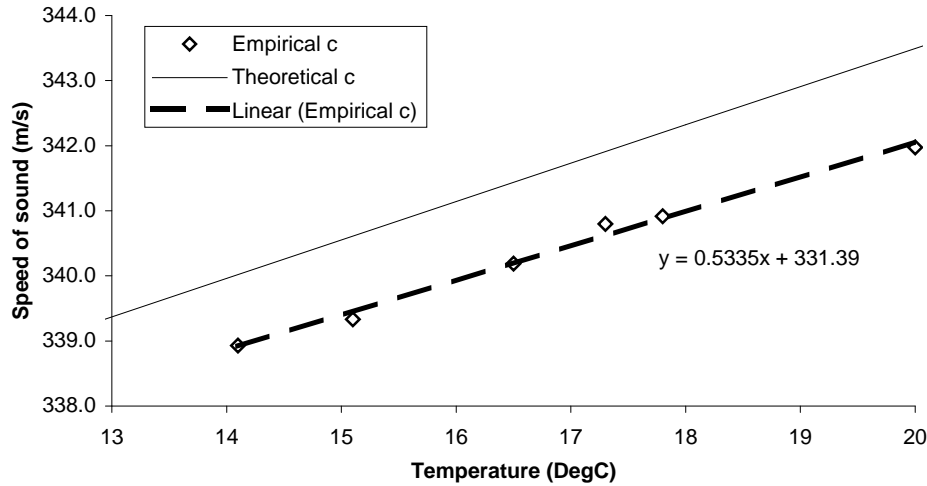


Figure 3.4.3 Empirical, using the Helmholtz equation, and standard theoretical speed of sound gradient for changes in ambient temperature for 3L chamber with 170mm port.

The collection of combined constants given by Equation (3.4.1), derived from Helmholtz equation, defined as alpha (α), should be constant with increasing temperature. Temperature dependence in α can be checked by plotting the measured resonant frequency over the speed of sound, as defined by Equation (No.23) from Basic equations, against temperature, Figure 3.4.4, which should also be equal to α . If α is not dependent on temperature the result is expected to be a horizontal plot. The slight negative gradient of α shows this may not be true. Hence, there may be a minor temperature dependence in α that can be compensated for in using a temperature gradient not consistent with the theoretical value derived from Equation (No.23). The difference is likely to be caused by temperature dependence in the port length correction term Δl . The value of 0.534 m/s/°C was used rather than 0.587 m/s/°C to allow for this subtle difference.

$$\alpha = \frac{1}{2\pi} \sqrt{\frac{s_p}{V(\Delta l + l_p)}} \quad (3.4.1)$$

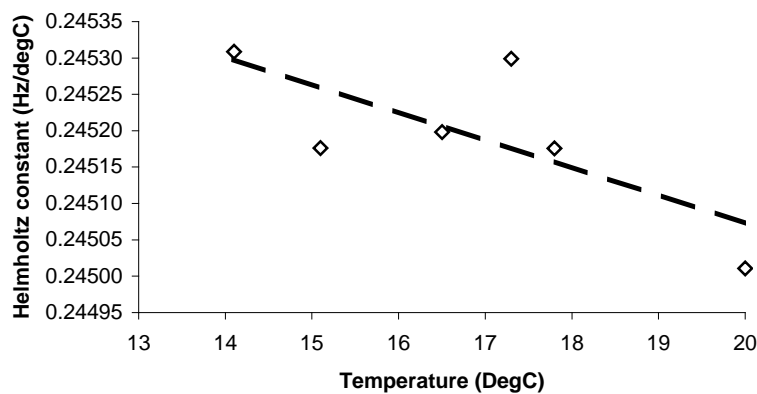


Figure 3.4.4 Changing value of the Helmholtz constants (α) for increasing temperature using a 3L chamber with 170mm port.

Another temperature effect on volume is the thermal expansion of the Perspex resonator. Typical reference values for Perspex's thermal expansion coefficient are between $5 \times 10^{-5}/^{\circ}\text{C}$ and $10 \times 10^{-5}/^{\circ}\text{C}$. For the temperature changes of 8 to 16°C this represents a worst-case volume expansion of 1.45mL for a 3L chamber, far less than the uncertainties calculated for O-rings and chamber cylinder non-uniformity (See Section 3.4.1).

Deviation volumes were plotted for the difference between volume measurements made with temperature compensation and ones without, Figure 3.4.5. Data collected in producing Figure 3.4.5 had a temperature variation of between $+0.1^{\circ}\text{C}$ to $+0.3^{\circ}\text{C}$. By combining the Helmholtz equation and speed of sound equation the expected volume change is expected to be 1mL for every 0.1°C change in temperature. This was calculated using a 3L resonant chamber with 170mm long, 44mm diameter port and Equations (No.22) and (No.23).

Therefore, from an initial zeroing at the start of testing, the values should range between approximately 1 to 3mL from that of non-temperature compensated measurements. This increase can be seen in the un-compensated difference deviation data shown in Figure 3.4.5, despite limitations in volume determination of $\pm 3\text{mL}$. This illustrates the need for precise temperature measurements if temperature drift in volume measurements is to be avoided. A 0.3°C change in temperature represents doubling of the uncertainty from $\pm 0.1\%$ to $\pm 0.2\%$ of the chamber volume, and a halving of the potential accuracy.

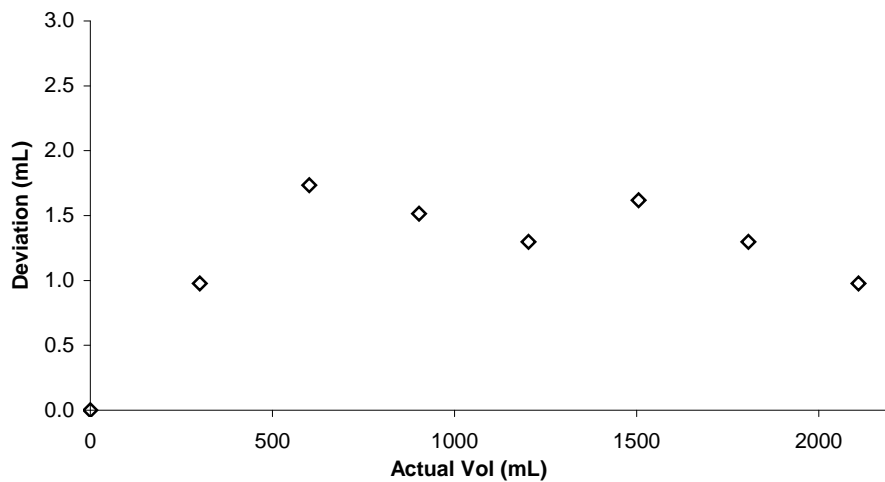


Figure 3.4.5 Deviation difference in volume for increasing chamber fill between predicted volume using Helmholtz equation with and without temperature compensation. Tests used water, 3L chamber with 22mm radius, asymmetric, 170mm long port.

3.4.4 Calibrating the asymmetric single port resonator

Calibration using water to various chamber fill levels gave measured resonant frequency results close to those predicted using the Helmholtz equation with temperature compensation, Figure 3.4.6. Results for the water calibration showed they could be represented with a second order curve fit having a coefficient of

determination of 0.9979. Using a second order curve fit, Figure 3.4.7, overlaid on the experimental results allowed subsequent measurements to be made within 3mL of the actual values when measuring water. This represents an accuracy of better than $\pm 0.1\%$ of full-scale fill (3L).

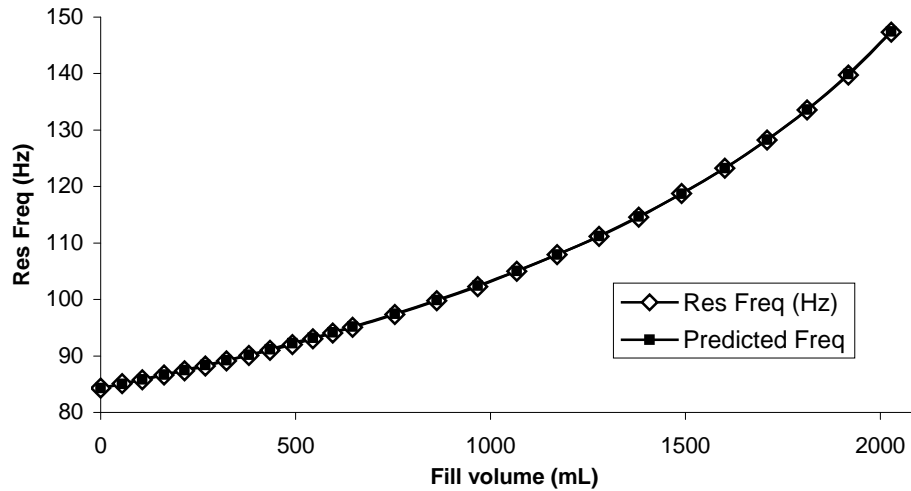


Figure 3.4.6 Calibration plot of water fill volume versus actual and predicted resonant frequency (Res Freq). Tests used 3L chamber with 22mm radius, asymmetric, 170mm long port.

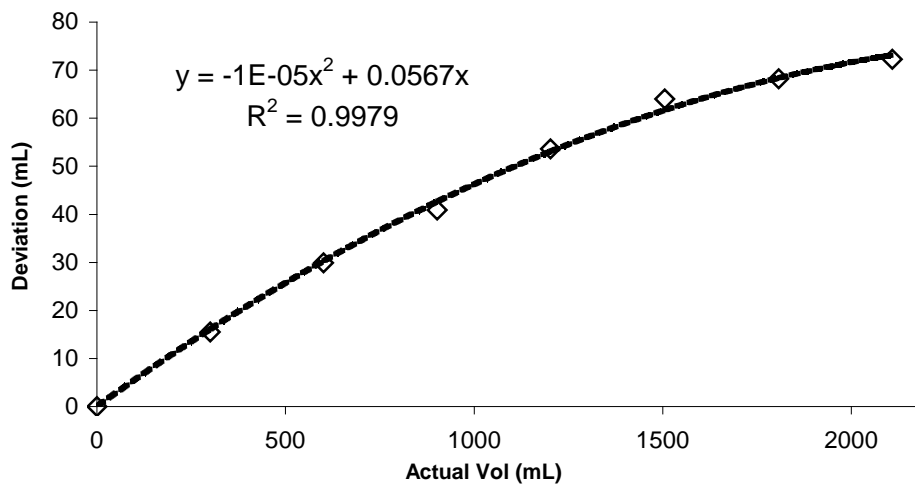


Figure 3.4.7 Second order curve fit of predicted volume deviation from actual volume. Tests used water, 3L chamber with 22mm radius, asymmetric, 170mm long port.

Q factor is an important indicator of resonant strength. It was observed that the Q factor remained steady at approximately 60, Figure 3.4.8, up to a fill of 2.5L in a 3L chamber. The high Q factor provided additional evidence the water absorbed very little energy over the range of fills. A slight rise in the Q factor at ~ 2500 mL may need further investigation as to its cause.

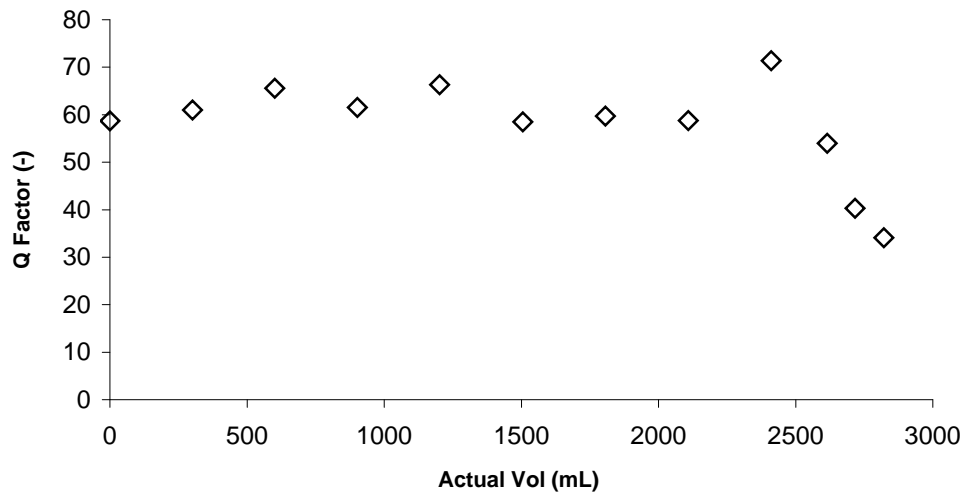


Figure 3.4.8 High Q factor for water calibration tests up to fill of 2500mL. Tests used 3L chamber with 22mm radius, asymmetric, 170mm long port.

The asymmetric 170mm long, 44mm diameter port with 3L chamber configuration was implemented horizontally and 100ml amounts of water cumulatively added (measured by weight on a set of Mettler PE6000 scales). The horizontal tests revealed linear results up to 500mL, at which point there was a distinctive trend towards under prediction, Figure 3.4.9. This can be contrasted to results gained for a vertical chamber, which showed second order over prediction. At 800mL the level of the water was near the interior mouth of the port and it is likely that the assumptions made about an interior flange correction for the resonator were no longer valid. At 1000mL the water was level with the port mouth and no further filling could be tested.

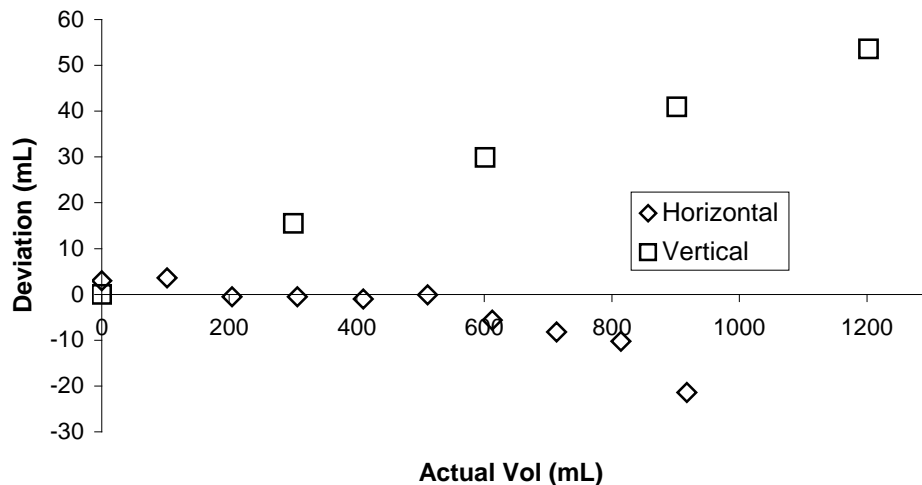


Figure 3.4.9 Comparison of vertical and horizontal volume deviation with water filling using 3L chamber with 22mm radius 170mm long asymmetric port.

A solid piston was used to simulate the water calibration tests with increasing chamber displacement. The piston was moved through a range of chamber heights from 25mm to 150mm at 25mm intervals. The uncertainty in height was $\pm 0.5\text{mm}$, which equated to a volume uncertainty of $\pm 7.5\text{mL}$. The large uncertainty made measurements approximate, but revealed very similar results to those obtained with

water. This verified the suitability using water as a volume calibration method. Volume deviation for the solid piston, Figure 3.4.10, showed almost identical second order behaviour as that for the water calibration data, Figure 3.4.7.

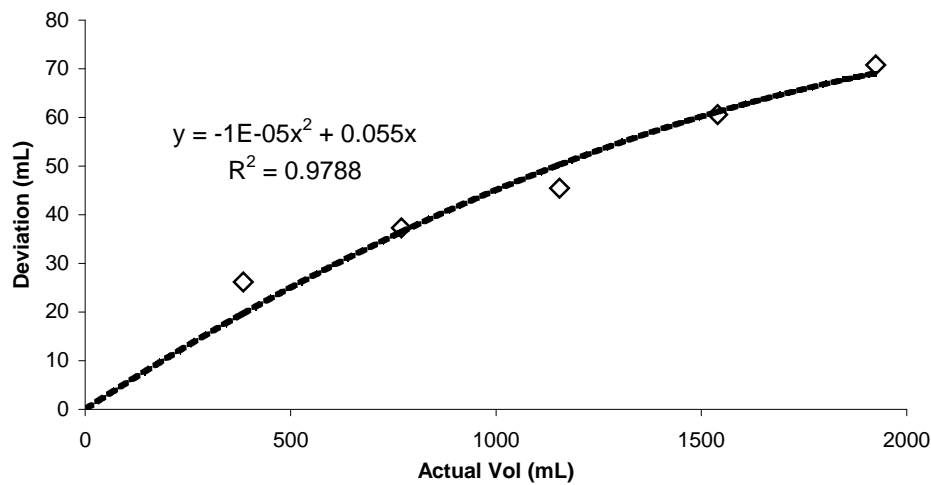


Figure 3.4.10 Parabolic curve fit of predicted volume deviation from actual volume using solid piston. Tests used 3L chamber with 22mm radius, asymmetric, 170mm long port.

Q factor for the solid piston, like the water tests, also revealed an almost flat value of 60 for fill values up to 2L at which point the Q factor rapidly declined, as was observed for the water calibration tests, Figure 3.4.8. The cause of the Q factor drop-off at 2L is due to port interference effects as the chamber floor encroaches into the virtual port extension length (See Figure 3.3.6, Methods).

Data gathered using 1L and 2L chambers with water filling behaved in a similar fashion to deviations in volume using the 3L chamber, Figure 3.4.11. As the water level approached the port all chamber volumes show a characteristic reduction in the deviation volume. This similarity in behaviour suggests there was very little absorption of sound by the water.

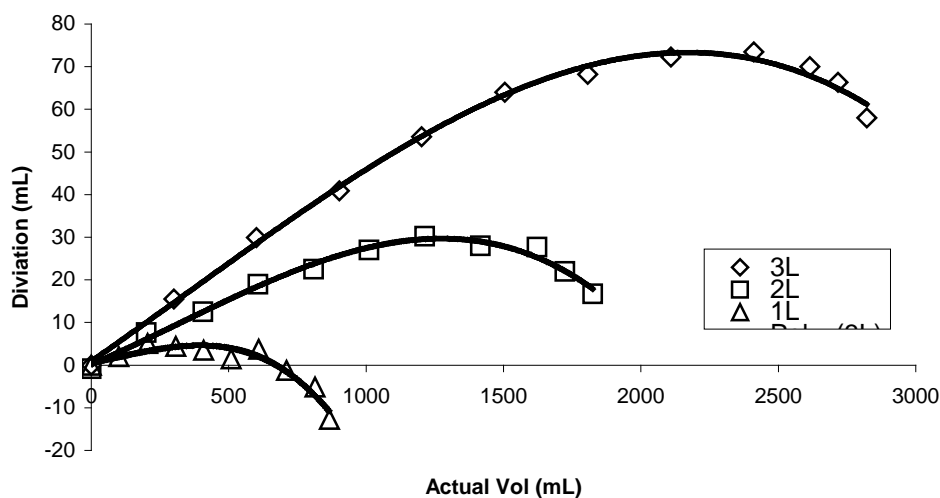


Figure 3.4.11 Deviation of predicted volume from actual volume using water fill data for various chamber volume sizes. Tests used 1, 2 and 3L chambers with 22mm radius, asymmetric, 170mm long port.

3.4.5 Effects of port symmetry

Water calibration using a symmetric 170mm long, 22mm radius port and a 3L resonator gave similar results to those using an asymmetric port. The deviation of predicted volume from the actual volume, Figure 3.4.12, showed a similar second order trend to that seen in the asymmetric port data. However, there was a greater scattering of the results and the parabolic trend showed a lesser maximum for the symmetric port (See Figure 3.3.2). The volume deviation maximum for the asymmetric port was about 70mL compared to only 20mL for the symmetric configuration. The cause is likely to be complex port flanging effects associated with non-linear internal flange behaviour. The acoustic coupling between an internally protruding port and chamber is more complex than a port that is flush with the internal chamber (See for example Kang and Ji, 2008).

A scatter variation of $\pm 2.5\text{mL}$ over a 2.1L fill from an applied second order curve fit was observed using an asymmetric port. In comparison the symmetric port had a $\pm 3.5\text{mL}$ variation over 1.6L of fill. The symmetric configuration could only be filled to approximately 1.6L due to the protrusion of the port into the chamber, which limited the maximum fill. However, results show a larger influence of unpredictable elements for the symmetric port configuration than the asymmetric port. Port intrusion into the chamber and unacceptable scatter in frequency make the symmetric port unsuitable for accurate volume measurement.

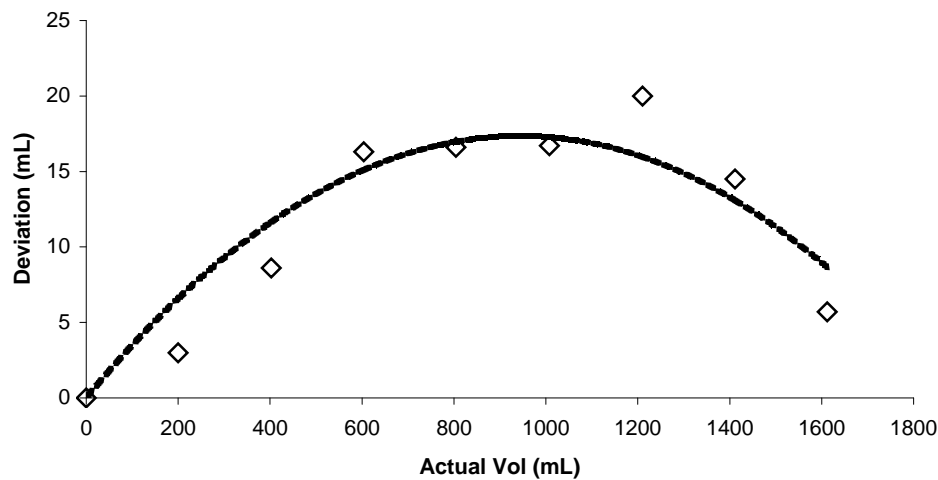


Figure 3.4.12 Second order curve fit of predicted volume deviation from actual volume using symmetric port. Tests used water, 3L chamber with 22mm radius, symmetric, 170mm long port.

3.4.6 Effects of sample irregularities

Cubic blocks and spheres displayed differences in their effect on the resonant frequency, independent of their equivalent volume displacement. Both initially have a near flat volume deviation, which rises with increasing sample volume. The sphere measurements show almost flat volume prediction up to $\sim 100\text{mL}$ at which point a marked increase in over prediction occurs. The same behaviour was observed in the cubic block samples, except significant over prediction appeared at $\sim 400\text{mL}$, Figure 3.4.13.

Volume prediction behaviour for these two sample types is distinctively different from that observed in the water calibration tests. Water tests showed volume deviation could be represented by a second order curve, Figure 3.4.7, whereas individual samples show an almost exponential rise in over prediction at a threshold determined by their surface regularity. This data suggests that the volume displacement type significantly affects the resonant frequency. The three distinct sample types change how the sound propagates in the chamber and hence the transmission properties of the chamber.

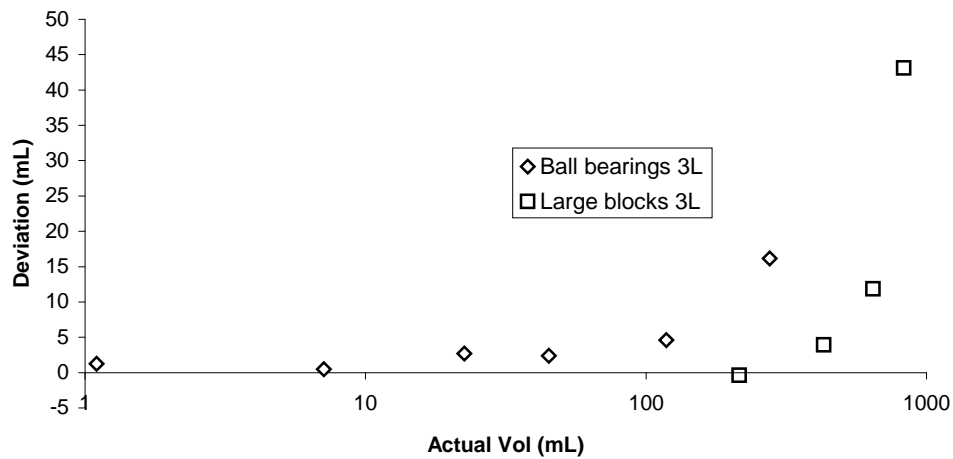


Figure 3.4.13 Curves of predicted volume deviation from actual volume using individual spherical samples and large cubic blocks. Tests used 3L chamber with 22mm radius, asymmetric, 170mm long port.

A comparison was made of data from 1L, 2L and 3L chambers using various spherical samples, Figure 3.4.14. There was a visible difference in the volume deviation between the three chamber sizes used. As noted earlier the 3L chamber showed a rapid increase in over prediction of the sample volume for the largest sample tested. In contrast the 2L chamber showed good agreement between predicted volumes and the actual volumes. A local maximum in over prediction is evident, but this may not be significant as the uncertainty in measurement for the 2L configuration is $\pm 2\text{mL}$. These uncertainties were found using water calibration for 1L and 2L configurations, Figure 3.4.11. The 1L chamber predicted volume data was also very close to the actual volumes of the samples measured, within 1mL. Restriction due to the chamber height limited the largest spherical sample that could be tested to 45mL for the 1L configuration.

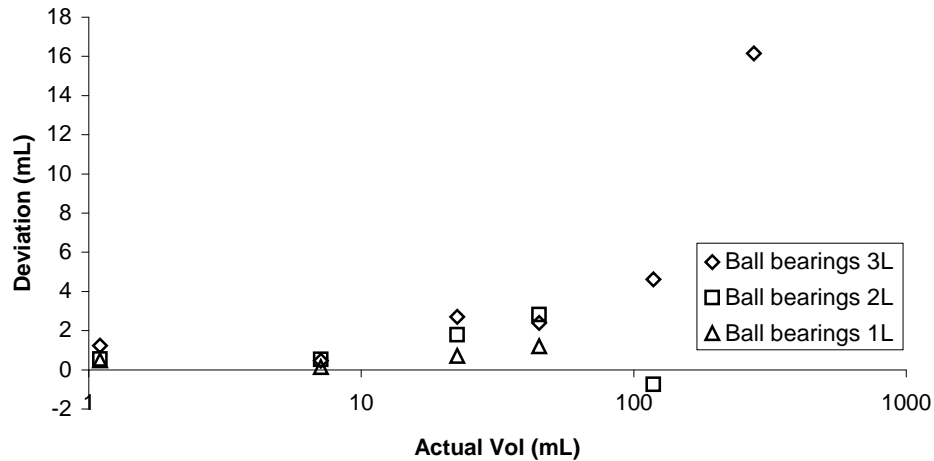


Figure 3.4.14 Curves of predicted volume deviation from actual volume using 1, 2 and 3L chambers with individual spherical samples. Tests used 3L chamber with 22mm radius, asymmetric, 170mm long port.

To test the effects of an acoustic barrier within the chamber a number of thin flat disks were tested at various heights to observe how the resonant frequency changed with their location, Figure 3.4.15. A distinct pattern emerged as the disk diameter was increased. Evidently all disks affected the resonant frequency, lowering it, as they approached the interior port.

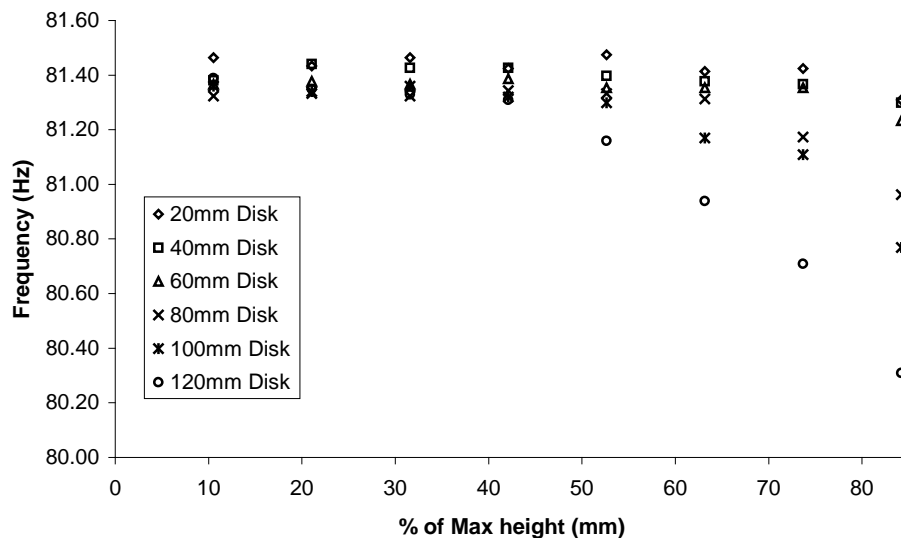


Figure 3.4.15 Frequency deviation plot for various disks having different cross sectional area in 3L chamber with 170mm port.

The height at which a disk adversely affected the resonant frequency is also associated with the disk's size. Where adversely affected is taken to mean – changes the frequency by more than the uncertainty of measurement ($\pm 0.1\%$), derived from water calibration tests in Section 3.4.4. A plot of the maximum disk height, before a change in resonant frequency starts to occur was made, Figure 3.4.16. This suggests the cross sectional area of a disk becomes significant when the disk cross sectional

area exceeds 20% of the chamber cross sectional area. This assumes an upper height limit for the disk of approximately 85% of the chamber height. At which point all disks show interference with the port irrespective of it's cross sectional area. The disks of 0% (disk free chamber) and 100% (segmented chamber) cross sectional area are also included to indicate theoretical limits.

The effect of an acoustic barrier can be compared to the solids and water calibration data from Figures 3.4.13 and 3.4.7 respectively. The cubic block frequency deviation is less than the sphere deviation and the sphere deviation is less than the water. The increased planar surface area of the cubic blocks reduces the resonant frequency as might be expected from the disk data. The principal difference between the disks and the solids is the impedance each imparts on the system. The disk causes an impedance change by partitioning the chamber and creating a secondary cavity behind the disk, whereas the solid samples induce an impedance change, but not a secondary cavity.

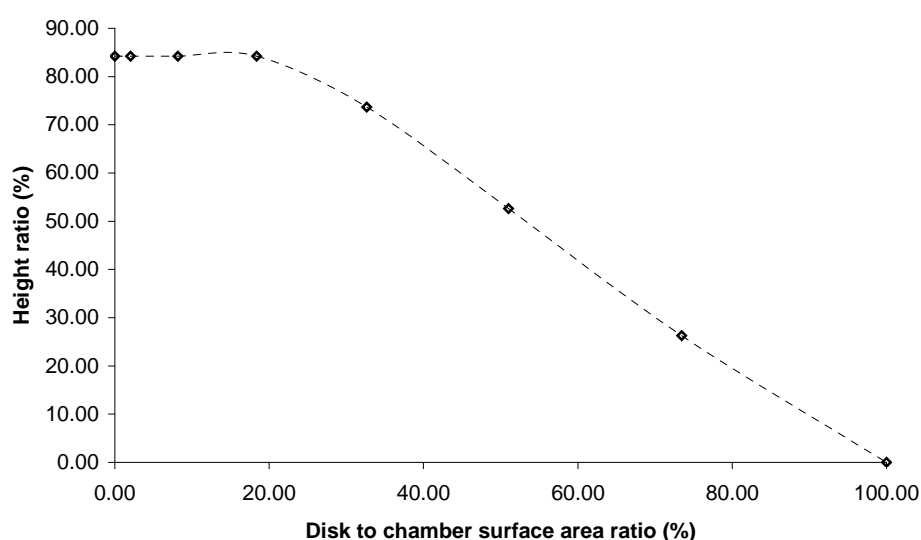


Figure 3.4.16 Plot showing the maximum height a disk can extend into the chamber based on it's cross sectional area percentage to that of the chamber's cross sectional area.

3.4.7 Measurement on granular materials

Behavioural differences were apparent in the various granular materials tested using the asymmetrical, 170mm long, 22mm radius single port, 3L resonator. Experiments showed a marked difference between the larger particles, greater than 1mm and the smaller particles, less than 1mm. The interstitial porosity of a granular sample affected the overall accuracy in volume measurement and hence bulk density determination, Figure 3.4.17. The parity line is included to show the ideal 1:1 relationship between predicted, using the Helmholtz equation, and measured volume.

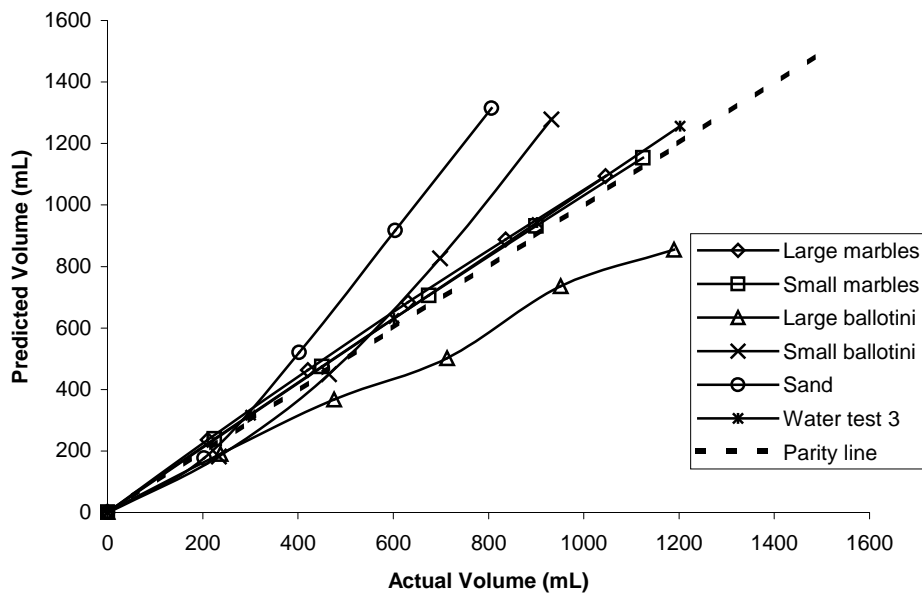


Figure 3.4.17 Comparison of actual volume versus predicted particle volume for granular materials tested. Tests used 3L chamber with 22mm radius, 170mm asymmetric port.

The plotted lines of predicted particle volume and actual particle volume of the marble samples had a direct linear correlation as was observed for the water calibration. However, the ballotini and sand samples showed significant deviation from predicted values. Predicted volume data also shows there is a significant difference between the small ballotini and the large. The volume for the large ballotini is under predicted and the small over predicted. Under prediction was also evident in results for rapeseed, plastic pellets and panicum using the particle density values derived when using the 1L resonator.

Using the 1L resonator, an attempt at accurate volume measurements was made on small quantities of plastic pellets, rapeseed and panicum. This was performed by measuring a thin layer of each sample, having minimal interstitial spaces, on the chamber base (50ml of each, bulk volume). From which, particle density values for the plastic pellets, rapeseed and panicum were found to be 1.12g/cm^3 , 1.26g/cm^3 and 1.72g/cm^3 respectively.

The sand and the small ballotini show a decrease in the predicted volume for the highest fill factor. These final readings do not represent true resonant behaviour, as the Q factor is so low at these fill factors that just about all the incident energy is absorbed in the material. The detected frequencies are merely a complex interplay of the bed material and the chamber, not the chamber and the port.

Volume measurements of the plastic pellets, rapeseed and panicum were all under their true volume, Figure 3.4.18, as was observed when measuring the large ballotini. The size of the particles determines the amount of measurement error. Larger particles showing less and smaller one more, down to a particle diameter limit of approximately 0.7mm (large ballotini). At particle sizes smaller than 1mm acoustic

interstitial viscous effects should have a significant affect on sound penetration into the bed material (See Appendix A, Section 9). Hence, there is expected to be a marked difference in volume measurement capabilities for the smaller diameter granular materials. The rapeseed, plastic pellets and large ballotini all display non-linear trends at 66% fill. This represents an upper fill level where attenuation in the bed interferes with resonant behaviour preventing determination of the resonant frequency.

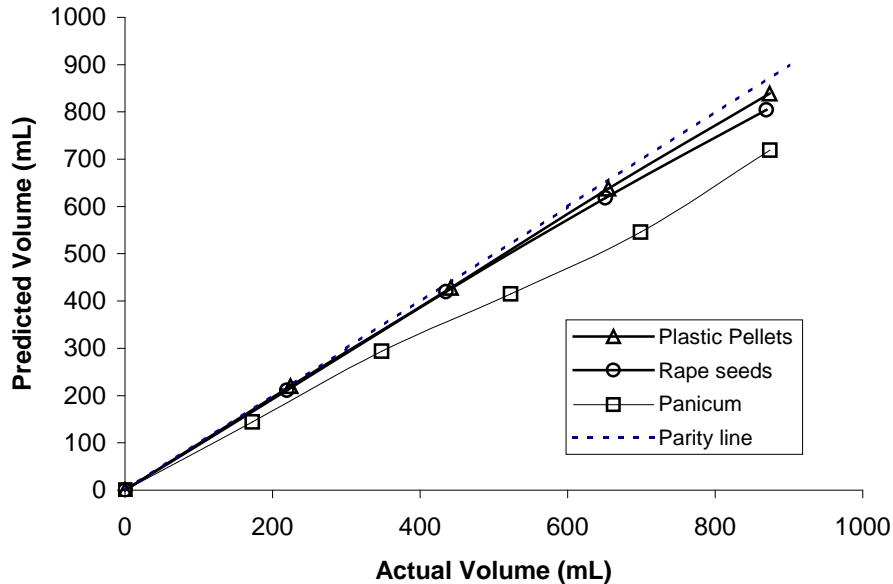


Figure 3.4.18 Comparison of actual volume versus predicted volume for plastic pellets agricultural granular materials tested. Tests used 3L chamber with 22mm radius, 170mm asymmetric port.

The Q factor for both large and small marbles remained high even up to fills of 80%, 1L absolute, Figure 3.4.19. A consistently high Q factor throughout measurements made determination of resonant frequency possible and resulted in good agreement between predicted and actual volume. Accuracy could be maintained at or close to $\pm 0.1\%$ for samples containing particles larger than 16mm in diameter using appropriate curve fitting.

In sharp contrast, the ballotini and sand samples show very rapid decline in Q factor at fills of only 30% by height, 400mL absolute. Q factors of less than ten are usually indicative of resonant behaviour no longer associated with just the chamber and port. Secondary resonance effects are most prominent in the sand and small ballotini samples and can be seen more readily in broad frequency sweep data, Figures 3.4.21 and 3.4.22. Secondary resonant effects may be caused by complex coupling effects between the fill material and the chamber.

Measurement accuracy is reduced in the sand and small ballotini samples due to high sound absorption and resonant peak broadening. Accuracy is dependant on locating the resonant frequency and as Q factor decreases the resonant peak broadens. Volume measurement accuracy is reduced to about $\pm 1\%$ of full-scale fill because of the limited available filling, approximately 30%, and rapid reduction in Q factor. These

results may indicate bulk volume and not true particle volume as sound is effectively dispersed rather than being available to excite the chamber into resonance.

Complete Q factor measurements were not made for panicum, rapeseed or the plastic pellets. Preliminary testing showed results that were midway between large ballotini and small marbles. A steady decline in Q factor occurs from approximately 60 reducing to 10 at fills approaching 80% for these three granular samples. Tenable measurements of volume are still possible even with Q factor broadening, but reducing the measurement accuracy for these samples to about $\pm 0.5\%$ of the chamber volume.

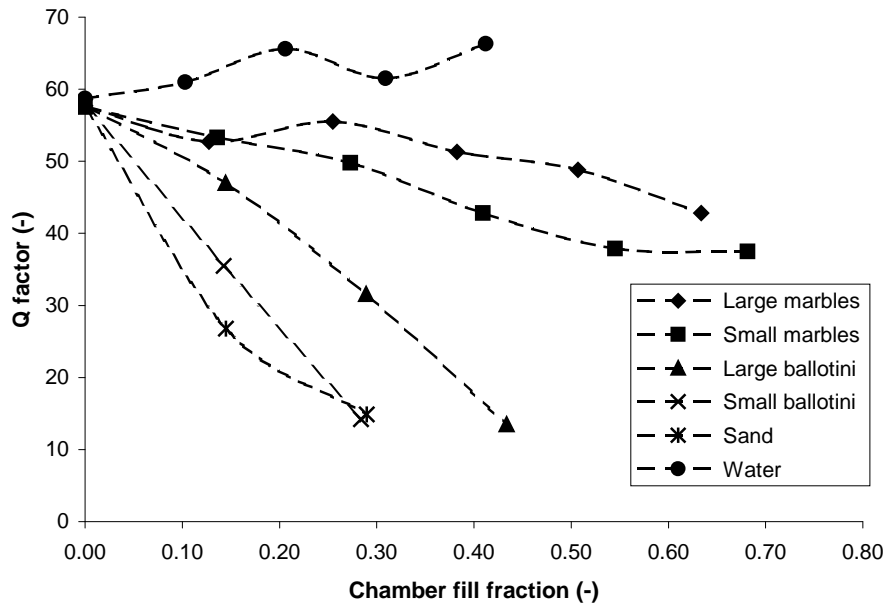


Figure 3.4.19 Q factor with increasing particle fill fraction. Using a 3L chamber, 22mm radius, 170mm asymmetric port.

The attenuation through the granular samples, measured as the microphone differential between port and chamber, increased significantly as the particle size was decreased to less than 1mm. The large ballotini represents a threshold size at which the attenuation becomes large enough to make accurate volume measurements impossible. Figure 3.4.20 shows this marked increase in attenuation for the small ballotini and the sand samples.

Attenuation for panicum, rapeseed and the plastic pellets fell in the region between the marbles and the large ballotini. These samples had only moderate attenuation with depth; as such they have low acoustic energy absorption. This makes them suitable for resonant measurements, as the chamber port interaction will tend to dominate maintaining a high Q factor.

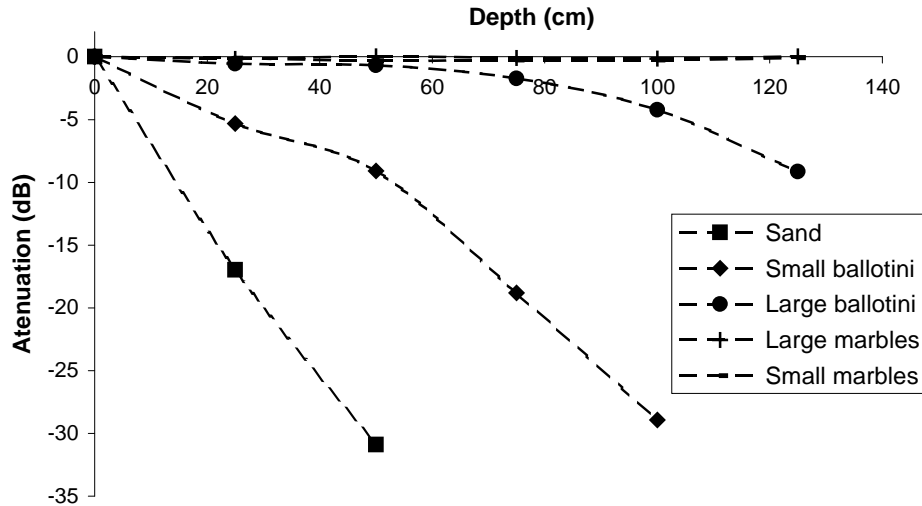


Figure 3.4.20 Attenuation with increasing particle fill level for marbles, ballotini and sand. Using a 3L chamber, 22mm radius, 170mm asymmetric port.

Sand at various fills was tested using a broad-spectrum frequency sweep to test for deviation in expected resonance behaviour. Resonance in the port is still prominent at a fills of over 25%, 416mL absolute volume, but is nonexistent at a 66% fill, 1086mL absolute volume, Figure 3.4.21.

Measurements under the sand in the chamber, Figure 3.4.22, reveal resonance is severely reduced even at the first fill of 12%, absolute volume 208mL. By the time the fill fraction approaches 66% there is no resonant behaviour occurring beneath the sand. Incoming frequencies are converted to broadband noise with increasing fill in both the port and chamber. This is most likely due to frequency scattering and absorption effects caused by the sand.

Broad-spectrum resonance tests were also carried out on ballotini, panicum, rapeseed and plastic pellets. These tests indicated active resonant behaviour at fills of 80% for all but the sand and small ballotini. It appears that the minimum interstitial space for useful resonance measurements is approximately 0.5mm for this particular resonator combination. For resonance to occur, sound waves must have a surface to reflect off. If this is not present the energy incident in the chamber is not available for sustained oscillation.

The minimum interstitial space will be a function of the resonant frequency, approximately 70Hz in this instance, and sound pressure level. It is expected lower frequencies, less than 50Hz, will penetrate finer bed materials more readily. However viscous effects and boundary layer turbulence will need to be considered (See Appendix A, Section 9).

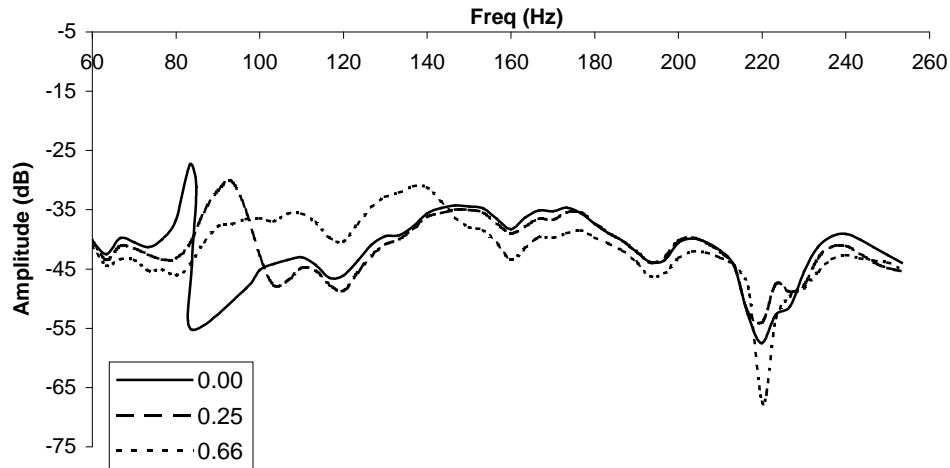


Figure 3.4.21 Broad spectrum frequency sweep as measured in the port with three fill fractions of sand. Using a 3L chamber, 22mm radius, 170mm asymmetric port.

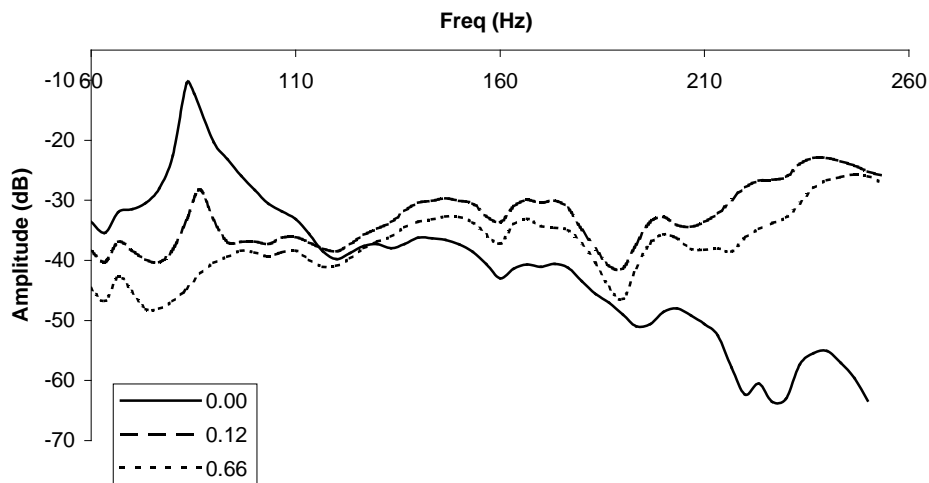


Figure 3.4.22 Broad spectrum frequency sweep as measured in the chamber with three fill fractions of sand. Using a 3L chamber, 22mm radius, 170mm asymmetric port.

Complex interactions take place in the resonator when granular samples are introduced. The acoustic resistance for a given granular material alters the resonant behaviour in a number of ways. This has an associated effect on Q factor and attenuation. Different materials will differ in the way they reflect and transmit sound energy due to their surface geometries and material properties such as density and elastic modulus. These attributes will ultimately decide the final accuracy of a given measurement.

A plot of particle size versus gradient was undertaken, Figure 3.4.23, using the data gathered from linear curve fits of Figures 3.4.17 and 3.4.18. This plot shows good agreement between predicted volume and actual particle volume down to particles of 2mm diameter. A transition into a different regime then takes place with a local minimum occurring at just less than 1mm. At particle sizes smaller than about 0.7mm a rapid increase in the volume over prediction occurs which can be associated with a large rise in acoustic absorption and the onset of a boundary depth beyond which

almost no sound penetrates. These observations suggest volume measurements may be transitioning from particle volume into bulk volume. The depth at which this is expected to occur will be determined by a crossing of the parity line as seen for the small ballotini and sand in Figure 3.4.17. The parity line indicates one to one mapping between prediction and actual particle volume. At a particular depth the sound energy in the bed material plays no part in the resonant behaviour of the chamber due to attenuation. This behaviour is observed in the small ballotini at fills of about 25% and 12% for sand.

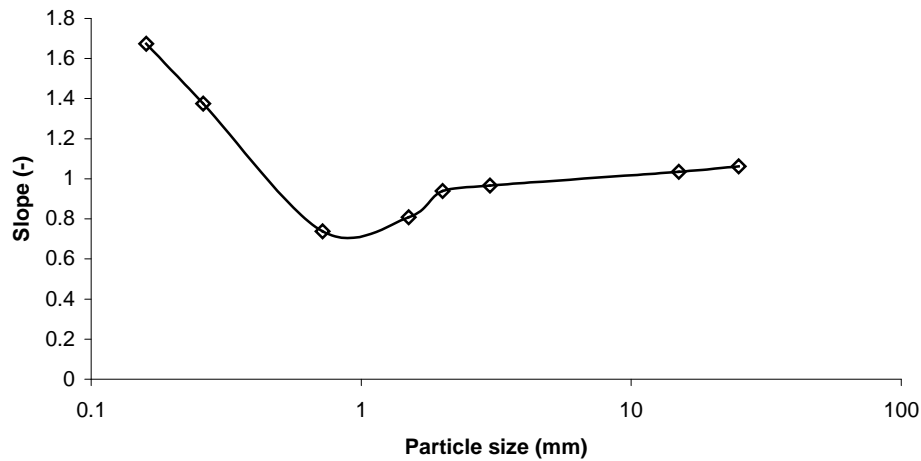


Figure 3.4.23 Change in linear curve fitted slope for changing particle size. Using a variable 3L chamber, 22mm radius, 170mm asymmetric port.

By plotting Q factor as a function of particle size a logarithmic trend was observed, Figure 3.4.24. This data was collected at a fill of 25% using two marble sizes, both ballotini sizes and sand. Figure 3.4.24 shows how resonant peak broadening is related to accuracy. As the resonant peak broadens it becomes more difficult to isolate the resonant frequency. Q factors of between 50 and 60 can yield results of $\pm 0.1\%$ full scale fill, those between 30 and 50 an accuracy of approximately $\pm 0.5\%$ full scale fill and Q factors of less than 30 no better than about $\pm 1\%$ full scale fill. As the Q factor decreases there is a distinct broadening of the resonant peak. This broadening makes precise frequency determination increasingly more difficult, hence the reduction in accuracy.

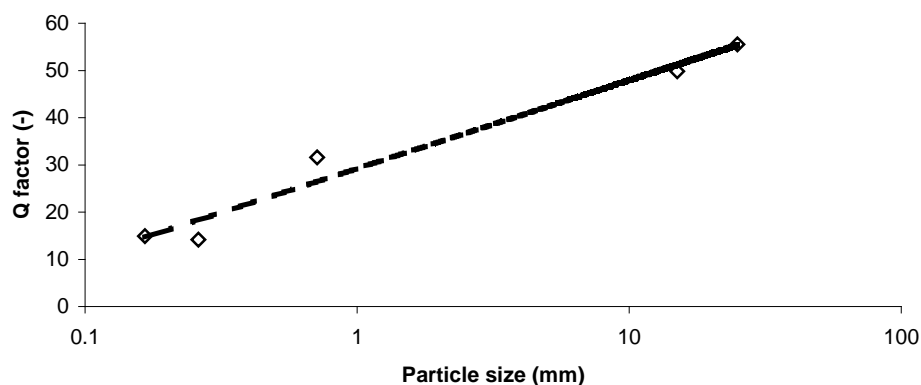


Figure 3.4.24 Logarithmic trend of Q factor for changing particle size measured at 25% fill. Using a variable 3L chamber, 22mm radius, 170mm asymmetric port.

Comparative testing of Q factor and predictive deviation was undertaken using a Perspex piston and granular coated steel disks. Q factors remained high, about 60, for all coating materials including the bare piston, Figure 3.4.25. As the piston was driven into the chamber the Q factor remained in the 50 to 60 range, indicating strong resonant behaviour with very little acoustic absorption from the coating material. These results demonstrate acoustic resistance for granular materials is a product of granular material depth and not surface texture.

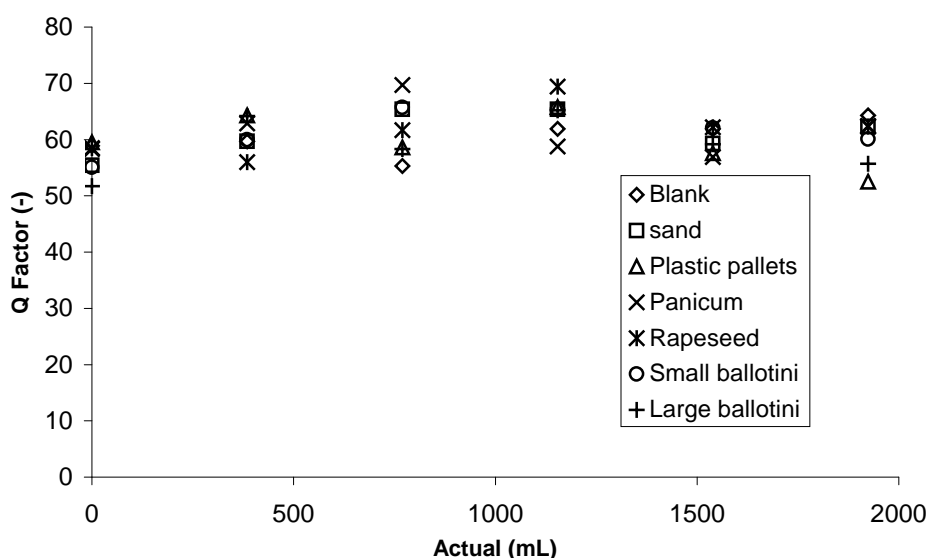


Figure 3.4.25 Comparative Q factor testing with various granular coated piston surfaces. Using a variable 3L chamber, 22mm radius, 170mm asymmetric port.

A marked difference between the granular coated pistons was seen in the volume deviation data gained by comparing actual volume versus predictive volume. The uncoated blank piston had the greatest deviation and the plastic pellets the smallest, Figure 3.4.26. These results show the surface of the piston affects the predictive capabilities for the resonant volume system. The effect on volume deviation due to particle size is not consistent as samples such as panicum and rapeseed exhibit quite different volume deviation trends despite having very similar particle size. The cause of this effect is expected to be differences in seed geometry, density and elastic modulus.

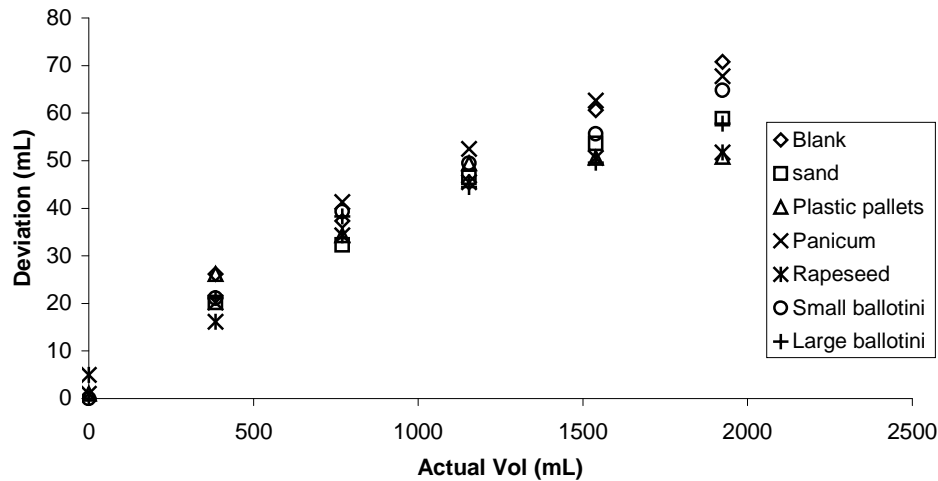


Figure 3.4.26 Experimental differences in volume predictive deviation due to piston coating materials. Using a variable 3L chamber, 22mm radius, 170mm asymmetric port.

3.4.8 Effects of air leaks on resonant frequency and Q factor

The addition of one or more small air leaks in a Helmholtz resonator significantly affects both the resonant frequency and the Q factor. A distinct linear trend was seen as the number of air leaks was increased from zero to ten, Figure 3.4.27. The resonant frequency increased by roughly 0.2Hz/leak, each air leak being 0.8mm in diameter and 5mm in depth. The increase in frequency for the smallest detectable change in volume is 0.01Hz (± 3 mL for the 3L chamber used in these tests with 170mm asymmetric port). Therefore, each leak is equivalent to an error in sample volume of 60mL, twenty times the achievable accuracy of an air leak free chamber.

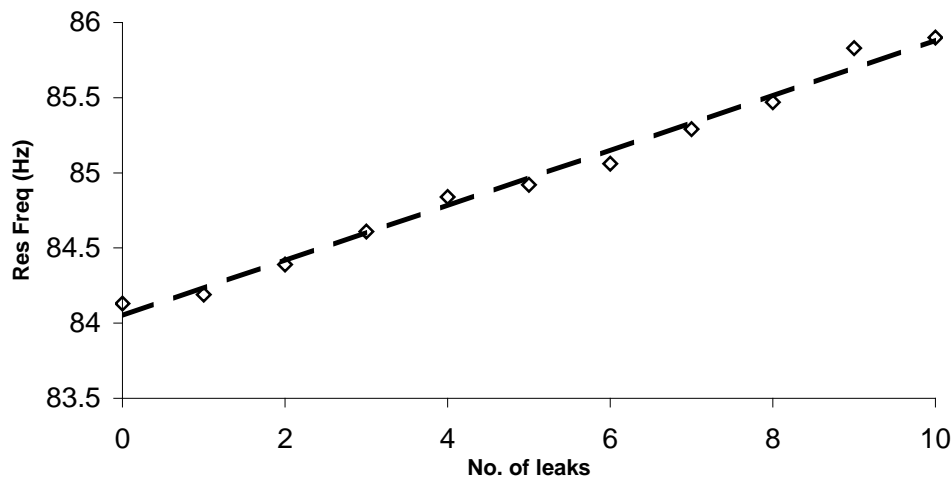


Figure 3.4.27 Observed linear increase in resonant frequency due to an increasing number of air leaks in the resonant chamber. Using a 3L chamber, 22mm radius, 170mm asymmetric port.

A similar trend was also seen in the Q factor, which decreased logarithmically with an increasing number of air leaks, Figure 3.4.28. The decrease was proportional to $-14\text{Log}(n)$, where n is the number of leaks. The rapid decline in Q factor demonstrated the importance of a well-sealed chamber. Even a slight air leak represents a large

acoustic resistive loss to the system. The rapid decrease in Q factor also causes an associated loss in volume prediction capability, lessening the accuracy of any subsequent resonant measurements.

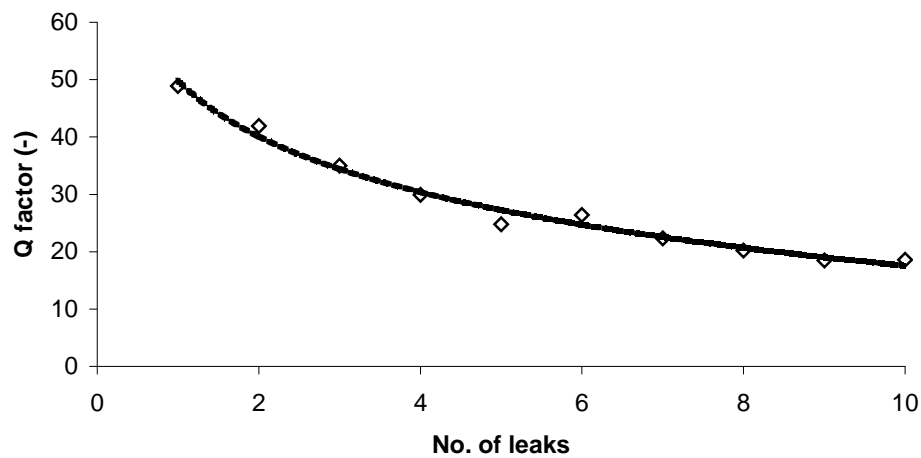


Figure 3.4.28 Data fitted with logarithmic decreasing Q factor due to an increasing number of air leaks in the resonant chamber. Using a 3L chamber, 22mm radius, 170mm asymmetric port.

When the single air leak diameter was increased a rapid increase in the resonant frequency occurred that was more pronounced than that seen with the multiple smaller leaks, Figure 3.4.29. A second order rise in frequency indicated a discernible correlation between the leak diameter and resonant frequency. A correlation coefficient of 0.995 suggests extrapolation to large leak sizes should be possible. The regular frequency behaviour also suggests the resonant frequency should be predictable for systems containing known leaks sizes.

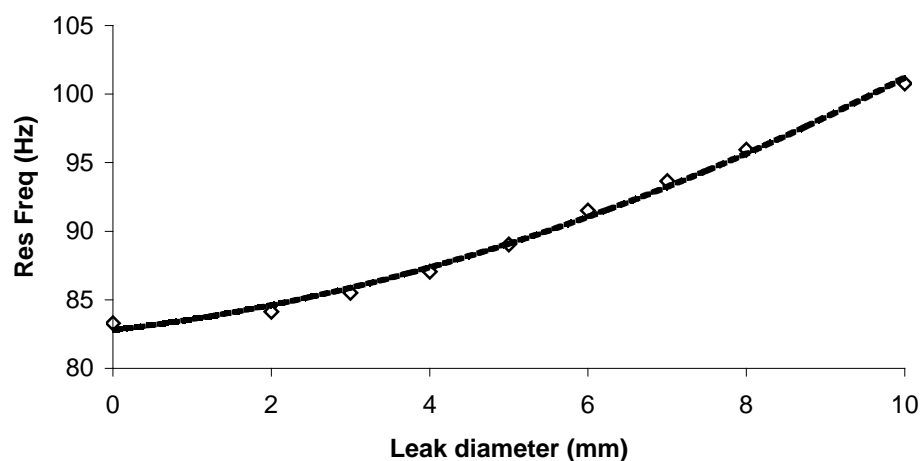


Figure 3.4.29 Data fitted with second order curve for rise in frequency with increasing leak diameter. 3L chamber with 170mm long port having 22mm radius.

Changes in Q factor also could be fitted with a second order trend with increasing leak diameter, Figure 3.4.30, with a noticeable minimum occurring at the air leak

diameter of 6mm. A change in the pinch off region due to a boundary layer should occur after a threshold air leak size. It is expected at this size a secondary port effect should dominate rather than an acoustic loss associated with an air leak. This can only occur when the cross sectional area of the leak is large enough to allow a flow velocity consistent with the resonant frequency flow velocity present in the main port. This was tested and confirmed with the use of a 50mm leak diameter. However, the height of the 50mm diameter hole was inconsistent with the other heights, and is therefore not included in the data of Figure 3.4.30.

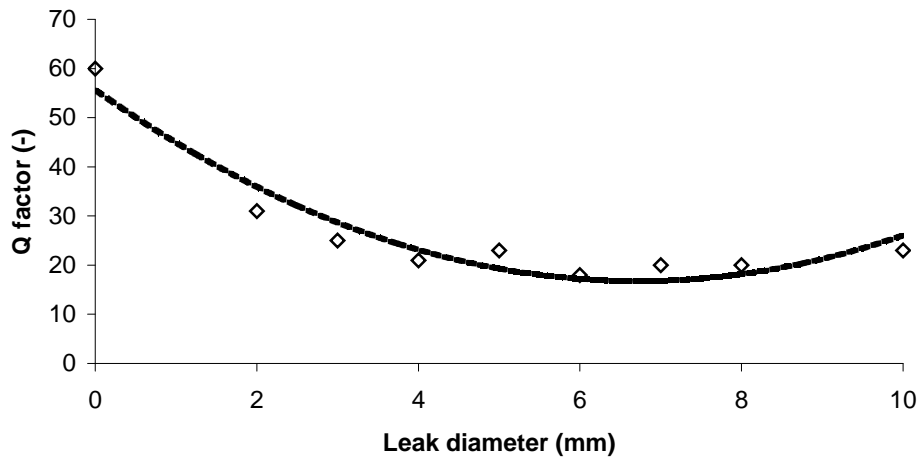


Figure 3.4.30 Q factor with increasing leak diameter fitted with a second order curve. 3L chamber with 170mm long port having 22mm radius.

3.4.9 Effects of sample position on volume measurements

With the 3L dual port resonator in the horizontal configuration a 42mL sphere was moved top to bottom in a radial direction in five separate locations along the chambers length. Unused holes were blocked off and the cord supporting the sphere seals the used holes, but a minor reduction in Q factor was observed due to the fractional leak around the cord-to-hole perimeter. The resultant mapping for the sphere's location effects can be seen in Figure 3.4.31. This mapping shows that the sphere's location has a minimal effect on the resonant frequency for the system unless it is placed near the port entrance.

The non-interference distance of the sphere from the port is determined by the port length correction factor. The length correction factor is a displacement beyond the port, which the moving mass of air within the port extends to. The effect of the sphere either side of the port also affects the resonant frequency, due to it altering the flange effect of the junction between chamber end and the port (See Appendix A, Section 8).

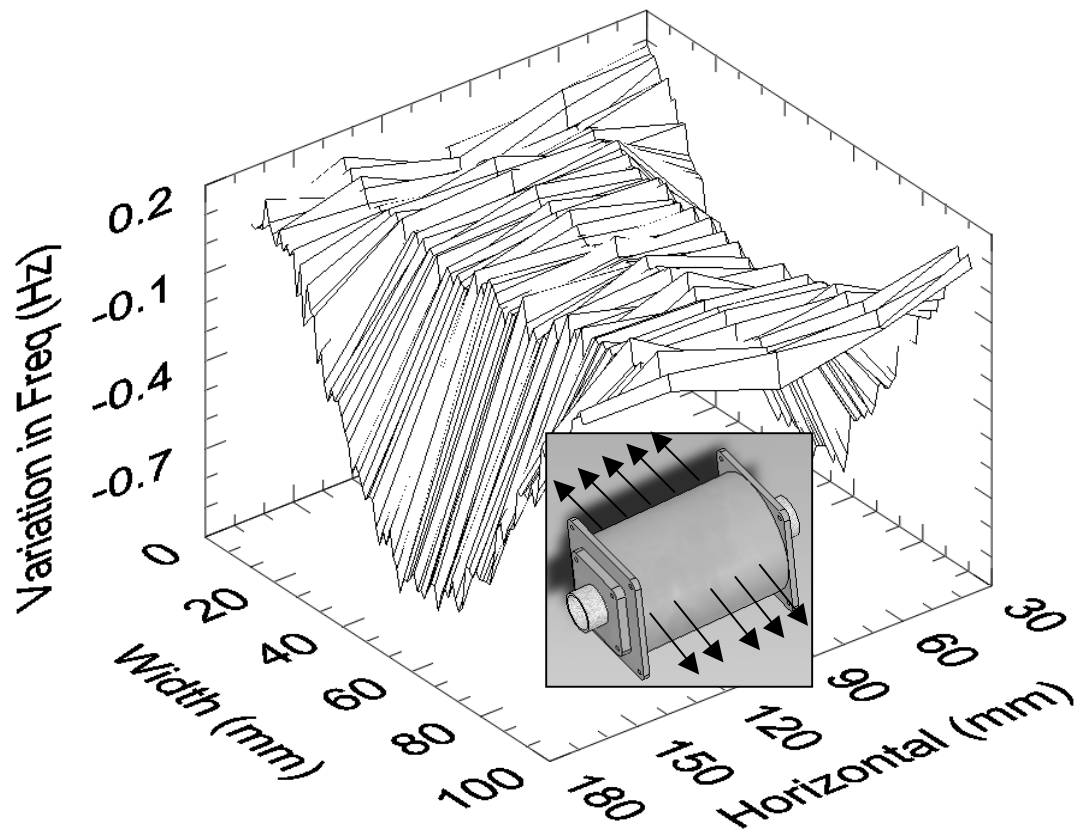


Figure 3.4.31 Frequency chamber mapping using a 42mL aluminium sphere moved in the radial direction in 1mm steps at 5 positions along the chamber's length. The frequency has been normalised and temperature corrected. Also shown is the 3L chamber indicating orientation of mapping, width being radial movement and horizontal being chamber length.

Axial configuration tests, when the sphere was near the port entrance or exit, showed the same behaviour in frequency reduction as was seen in the radial tests, Figure 3.4.32. A flat steady frequency region was apparent for the main length of the chamber where the sphere is outside of the length correction and flange effect zones. This 'flat region' is further expanded as a change in volume plot, Figure 3.4.33, showing the interference effects of the sphere and port extend well into the chamber, contrary to what Figure 3.4.32 suggests. Therefore, the useable range in the chamber for making volume measurements is the 60mm between 115mm and 175mm. The physical internal length of the chamber is 190mm. Hence; the usable zone for acoustic measurement is only approximately $\frac{1}{3}$ of the chamber length.

A large number of outliers were observed in the data where the sphere is in either of the ports. This was due to resonant peak broadening caused by the space around the sphere. A gap of 0.5mm existed around the sphere when in the port which appears as an air leak to the resonant system. This small gap around the ball represents a high viscous force region where the acoustic resistive losses to the system are large. Hence, the gap appears as an air leak, not a secondary port (See Section 3.4.8). In this state, with a port effectively blocked, the resonator reverts to a single port resonator, which explains the large change in observed frequency. The greatly reduced Q factor makes

it difficult for the automated software, using resonant hunting, to ‘lock’ onto the resonant frequency, thus causing the outliers.

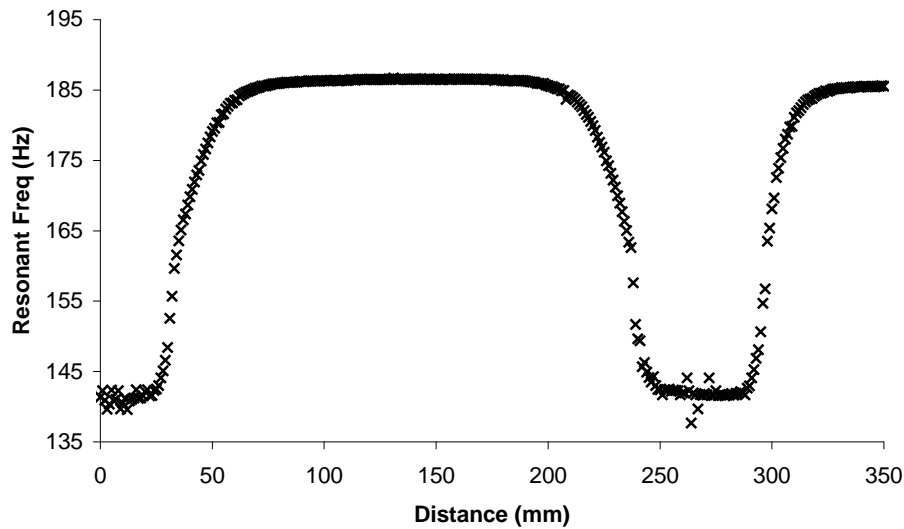


Figure 3.4.32 Frequency chamber mapping using a 42mL aluminium sphere moved in an axial direction in 1mm steps along the chamber’s length. Using a 3L chamber with two 22mm radius, 51mm asymmetric ports.

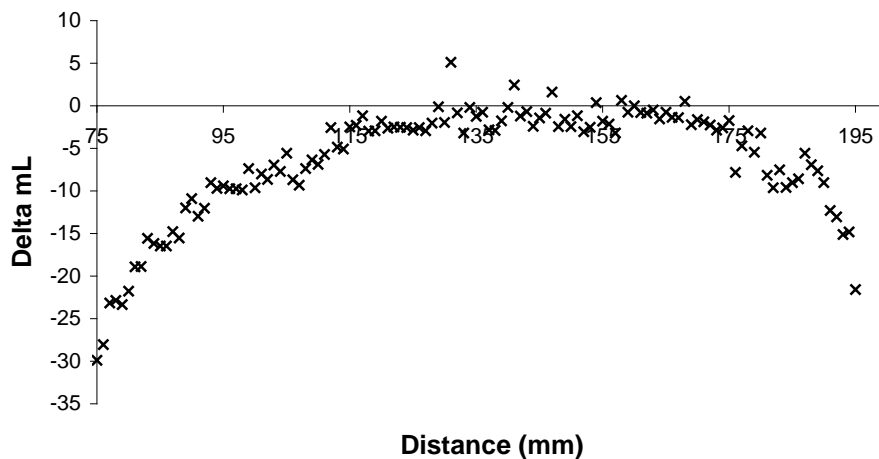


Figure 3.4.33 Enlargement of ‘stable’ region in figure 4.32. Plot shows change in mL from a central value of 3168mL at 145mm displacement. Using a 3L chamber with two 22mm radius, 51mm asymmetric ports.

3.4.10 Controlled decent using a dual-port resonator and resonant hunting

Using the established resonant hunting method, pink noise followed by two chirps, decent speeds through the 3L dual port resonator could not exceeded 1mm/s. The speed could be increased to 2mm/s with an associated reduction in volume measurement accuracy from $\pm 0.1\%$ to $\pm 0.5\%$ of full scale. To achieve this a reduced scanning time and coarser chirp frequency is used. Measurement times for these accuracies are 40 seconds and 20 seconds respectively. The largest spherical object that can be lowered through the dual port resonator is 43mm diameter (42mL), hence the uncertainty for these two measurements accuracies are $\pm 3\text{mL}$ and $\pm 15\text{mL}$ respectively.

These poor results, in terms of sample transit time, prompted the development of rapid volume measurement methods described in Chapter 4. New techniques are developed using both phase shifting and Q profile shifting as ways to reduce measurement times while maintaining accuracy.

3.4.11 Measurement of port flanging effects

Resonator port flanging effects were tested for by using a range of flange sizes mounted to the exterior of the port (Figure 3.3.6, Methods). The flange factor determines the port length extension (See Chapter 2, Section 2.3 and Appendix A, Section 8) and is therefore important in determining the correct constant to use in volume calculations. A maximum flange factor of 1.698 is the theoretical limit for two acoustical point sources in an infinite plane (twice $8/3\pi$). Two sources are considered due to there being both an internal and an external flange effect.

By changing the port to flange ratio the flange effect can be studied, Figure 3.4.34. This shows a distinct lowering of the resonant frequency for both the 3L chamber with 51mm port and the 3L chamber with 170mm port, which is to be expected. Figure 3.4.34 shows there is an upper limit when only the thickness of the port wall exits (3mm). This equates to a flange factor of 1.374 for the 51mm port and 1.375 for the 170mm port. When the largest flanges were used the flange factors increased to 1.589 and 1.690 respectively. In all instances the equipment was at a steady state temperature of (21°C for 51mm port and 20°C for 170mm port), which was necessary in order to isolate the flange effects. The upper value of 1.690 for the 170mm port suggests the flange factor is approaching the theoretical maximum value of 1.698.

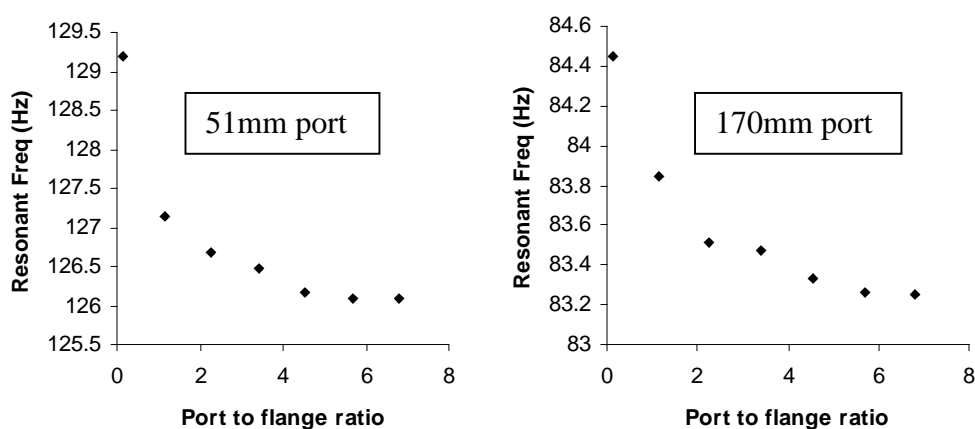


Figure 3.4.34 Effects of various flange sizes on resonant frequency used to evaluate port length extension. Measurements taken with 3L resonator having two different port lengths, 51mm and 170mm.

From the results for the 170mm port, specifically the value 1.690, it can be seen that the internal flange factor must be close to the theoretical value of twice $8/3\pi$. If this is true the external flange factor for the un-flanged port must be approximately 0.526. This result can be compared to the suggested value of 0.6 for an un-flanged port. The combined flange factor value of 1.375 was used in all volume calculations in Chapter 4 but not Chapter 3. Theoretical values for the internal flange factor, between the port and chamber using an alternative method by Kang and Ji (2007), gave values significantly less than those measured and could not be used for objective

comparisons. The Kang and Ji method predicts an internal value of 0.482 and an external value of 0.61 giving a total of 1.092 (See Chapter 2, Section 2.1.3).

3.5 Discussion

3.5.1 Characterising the fabricated resonators

In early testing it was noticed that different environmental configurations changed the behaviour of the resonant system. Small changes such as a door left ajar caused significant changes in resonant amplitudes being detected in the port. This is principally due to secondary behaviour of the environment, which changes the amount of sound energy present at the port of the resonator.

Trials coupling of sound source to resonator were found not to have the high Q factors observed in the uncoupled configuration. Other investigations, such as Selamet, Dickey and Novak (1995), used a coupling method to isolate the system from changes in the environment. A directly coupled system results in a resonant dip rather than a resonant peak. The dip occurring at resonance is a product of cancellation between the driving source (loudspeaker) and the resonator. Difficulties arise in locating the dip's centre, as cancellation is so complete that there is insufficient signal amplitude for the acquisition system to detect. This effect of irresolvable frequency data can be seen in detection limit results, Figure 3.4.1, where there is frequency scattering occurring at signal levels less than -50dB.

In this configuration it is therefore necessary to have a standardised room or enclosure for resonant equipment to be mounted in if the un-coupled Helmholtz volume measurement system is to be used industrially or commercially. Such a set-up might entail an anechoic room or enclosure for the system to reside in that can be temperature controlled. The later developed environmental normalisation technique was able to remove this dependence and is discussed further in Chapter 4.

Testing the resonator in different locations showed the resonant frequency to be insensitive to its position relative to the sound source. This location insensitivity was unexpected as environmental effects had such a large affect on the resonant peak amplitude. The only exception was having the port opening facing the sound source where a slight (0.1Hz) frequency shift occurred. Therefore this configuration should be avoided. The resonant frequency for a given configuration was also insensitive to small changes in the applied sound level between approximately 70 and 90dB.

3.5.2 Repeatability of measurements using resonators

It was often necessary to disassemble the resonator during this investigation. As a result of this disassembly there was an O-ring compression uncertainty in the resonator end plates. This caused a repeatability uncertainty of $\pm 3\text{mL}$, which was the same order of magnitude as that found in non-disassembly calibration tests.

The resonator body is coupled to the resonator end plates via four rods, which compress O-rings between the ends and the chamber. There was insufficient compression available to compress the O-rings completely and hence there were slight variations in the chamber size when running a series of tests requiring disassembly. Therefore, in future versions of this resonator a complete O-ring compression method will be required or a change in chamber design to eliminate this problem.

Consecutive repeat testing of the same samples, spheres and cubes, gave results that indicated high repeatability, within $\pm 1\text{mL}$. The need of a reliable assembly/disassembly method was avoided by using the variable chamber resonator in Chapter 4.

A large discrepancy was noticed between theoretical Q factor predictions using methods developed by Kinsler and Frey (1962) and Blackstock (2000), and those measured for the various resonator configurations. Typically the resonators were designed to have Q factors of over 100 and as high as 500. In reality the highest Q factor measured was around 65. This large difference was due to the acoustic losses in the system, principally viscous and thermal boundary layer effects within the resonator and to a lesser extent radiation resistance from the port. The theoretical Q factor values are derived from radiation resistance losses and not boundary layer losses, hence the significant differences. To rectify this discrepancy, thermal and viscous boundary layer losses would need to be analytically evaluated and incorporated into the existing theoretical Q factor Equation (No.25), Basic Equations. This might be achieved using boundary element modelling.

For a very high Q factor there must be a large amount of energy stored in the system. Such high energies must be contained in the form of a moving mass of air in the port. Normally the rapid pressure changes preclude heat energy transfers. Therefore, the resonance would be predominantly adiabatic. However, if this were true the pressure amplitudes and velocities would continue to increase in the port and the system would soon violate lumped parameter assumptions that treat the chamber and port as two distinct entities.

Within the port there is a secondary boundary layer associated with the region where the system is no longer adiabatic. Near the port surface there is thermal conduction zone, called the thermal boundary layer. This layer is considerably larger (calculated to be 1.54mm) than the viscous boundary layer (calculated to be 0.217mm). With an increase in the pressure amplitude and velocity there must be increases in the viscous and thermal losses caused by the boundary layer within the port (See Appendix A, Section 9). Much like a shock absorber, the quicker the displacement the larger the resisting force. The maximum Q factor is therefore self limiting.

There is the opportunity for further investigation into optimal energy storage in a resonator using non-lumped parameter techniques. If the Q factors could be increased the potential accuracy could likewise be extended, as the resolvability of resonant frequencies increase. The accuracy in determining the resonant frequency determines the uncertainty in any given volume measurement.

A variation of $\pm 3\text{dB}$ in resonant gain was observed using the water calibration data, the variation being due to loudspeaker deficiencies and environmental effects. The average Q factor remained at approximately 60 up to an 85% fill. This supports the argument that Q factor is bounded to an upper limit determined by the viscous boundary layer losses.

The ratio of reactance to resistive impedance may be linked to the boundary layer resistance at large amplitudes. Standard Q factor theory only includes mechanical impedance and not viscous losses. Boundary layer thickness is a function of velocity;

therefore as the amplitude becomes larger the rate of change in pressure also increases. So the pressure velocity will reach a maximum value but the group propagation velocity, speed of sound, remains constant.

3.5.3 Temperature effects

Temperature can have a significant effect on repeatability of frequency measurement, due to changes in the speed of sound with temperature. Throughout testing there were constant changes in temperature occurring. A standard adjustment of $0.6\text{m/s/}^{\circ}\text{C}$ was used throughout the initial parts of this investigation - Chapter 3. A temperature gradient of $0.534\text{ m/s/}^{\circ}\text{C}$, which was capable of giving more accurate results, was used for experimental work in Chapter 4, using an additional β multiplier for c , of 0.91. This adjustment was rechecked by a repeat measurement of the empty chamber volume at the end of each series of measurements, revealing a need for highly accurate temperature measurements.

Discrepancies in the temperature gradient for the speed of sound occurring in the resonator indicated other temperature dependant components within the Helmholtz equation. The speed of sound was derived by standard methods given by Kinsler and Frey (1962), Blackstock (2000) and other standard texts as Equation (No.23), Basic Equations. The speed of sound should change by $0.587\text{m/s/}^{\circ}\text{C}$, over the narrow range of 8°C to 24°C with a linear fit. However, when measured indirectly using the Helmholtz equation for the 3L resonator configuration a value of $0.534\text{m/s/}^{\circ}\text{C}$ was calculated. This showed there was an extra multiplying term β (0.91) that was needed in temperature compensation. β may vary according to the physical constraints of the resonator.

This extra β term in the Helmholtz equation contains components that rely on temperature that were not considered in the initial stages. These include temperature dependence of the port length extension term based on air density. Also small terms that are omitted in deriving the lumped parameter Helmholtz equation as described in Appendix A, Section 2. The viscosity of air in the port can change the behaviour of the boundary layer at the port surface, and hence change the effective cross sectional area of the port (See Appendix A, Section 9). Humidity may also contribute to small changes in resonant behaviour and will need to be monitored in future studies to gauge its effect.

If possible it is preferable to take temperature measurements inside the chamber to give the appropriate compensation factor. In addition, the sample being measured should be at the same temperature as the chamber to avoid temperature gradients occurring that could skew volume measurements. In future studies it is recommended a range of low-mass temperature sensors should be used in the chamber and port to better understand acoustic power dissipation within the resonator. Doing so will enable acoustic thermal heating to be monitored and enable its significance to be evaluated. It may also allow calculations of energy lost to boundary layer effects and those to acoustic radiation.

3.5.4 Calibrating the asymmetric single port resonator

Calibration of the resonant system yielded results having measured frequencies almost indistinguishable from those of prediction. This led to comparisons of volume

deviation rather than absolute values. A repeatable second order trend in over-predicting volume was apparent in water volume measurements.

The reason for this parabolic anomaly is unclear, but could be due to secondary effects caused by assumptions made in generating the Helmholtz equation. Specifically, the small signal approximations made to allow linearisation and the completion of the wave equation (See Appendix A, Section 2). Also, various small angle approximations were made in lumped parameter assumptions and transmission theory. Because measurements were being made to such a high accuracy these previously unimportant small terms may now be significant.

Despite this second order over-prediction it can be compensated for in a correction that can flatten the deviation curve. With this correction the volume predictive capability was within $\pm 0.1\%$ of the volume of the resonant chamber.

The success in the predictive capabilities of this method is in part due to the consistently high Q factor for fill levels up to 2500mL in a 3L chamber. This maintains the resolvability of the resonant peak. Also, the high Q factor is indicative of low energy absorption from the water. At greater fill levels the water approached the interior port and the moving mass of air in the port interfered with the water. This caused the Q factor to decrease rapidly and prevented resonance.

In horizontal water filling the interior port flange, formed by the roof of the chamber, became increasingly obscured. This changed the quantity of flange material in the chamber and hence, directly altered length extension constants used to predict the fill volume, via the Helmholtz equation. Unexpectedly this tended to flatten the over-prediction of volume, displaying a near one-to-one prediction to actual fill up to 500mL. This suggests the flange factor is deviating significantly from $8/3\pi$ (See Chapter 2, Section 2.1.3).

Tests with a solid piston reproduced results seen in the water calibration within the uncertainty of piston position. Likewise Q factor values were also consistent with those observed with water at various fill heights. The piston tests became the forerunner to designing the variable chamber resonator described in Chapter 4.

By customising of the chamber volume to suit the size of the sample the uncertainty in measurement could be kept to a minimum. Therefore, the uncertainty in a volume measurement using a variable chamber resonator would be constant, proportional to the object under test not the size of the chamber. For example, a typical maximum fill is around $1/3$ of the chamber volume, assuming a spherical solid sample and enough clearance above the sample not to interfere with the port. If the current accuracy of $\pm 0.1\%$ of full-scale fill is used then this sample could theoretically be measured to within $\pm 0.3\%$ of its true volume.

3.5.5 Effects of port symmetry

It was expected that the results for a symmetric port configuration would give better predictive results than those of an asymmetric one. The symmetric configuration has two un-flanged ports and as such would be expected to have well defined flange factors, each of approximately 0.6 times the port radius. This benefit was not seen as the amount of scatter in the deviation curve exceeded that seen in the asymmetric port

tests. The larger amounts of scatter might indicate the internal port is violating the lumped parameter assumptions and may need to be analysed as two dimensional boundary layer problem as investigated by Kang and Ji (2008).

The symmetric port configuration is impractical for most measurement applications as the port intrusion into the chamber restricts the available fill space and consequently reduces the potential fill. The port length extension term must also be allowed for which further reduces the available fill space. These poor results suggested the need for investigation into a flanged port exit in an asymmetric configuration (See Section 3.5.11).

3.5.6 Effects of sample irregularities

A marked difference in behaviour of predicted volumes was apparent in the data seen from testing both regular spherical samples and irregular cubic samples. The sample shape to some extent determines the volume over-prediction trends seen in all fill types. Parabolic over-estimation of volume was seen in water data, but an almost exponential increase was observed with the solid samples in the 3L chamber. Some deviation between sample types should be expected if transmission theory is considered, as the propagating pressure wave interferes with each sample type differently (See Appendix A, Section 11).

As a pressure wave emanates from the internal end of the port; it encounters a flat surface, in the case of water filling, which is effectively a high impedance barrier. This causes the bulk of the pressure wave to be reflected back up the chamber. If the emanating pressure wave encounters a regular or irregular solid the pressure wave becomes dispersed and the resulting resonant frequency may in part be a product of chamber size and interference.

In the case of the spherical sample the sound wave is likely to be re-emitted omnidirectionally. In contrast, the angular cubic sample would likely reemit the sound waves as point sources from the edges and corners as well as from its planar surfaces. The angular cubic samples represent a different interference source than spherical ones. Adding to the complexity of the angular sample is the size of any flat surfaces. The larger they are the more efficiently they reradiate the incident sound pressure waves. Studies conducted by Barmatz *et al.* (1983), Leung *et al.* (1982) and Cordero and Mujica (2007) used rigid spheres in a $\frac{1}{2}$ wave resonant cavity and found scattering to affect the resonant frequency. However, the Helmholtz resonator frequency is based on the chamber volume not a standing wave within the chamber. Therefore, the systems are not directly comparable. Changes in frequency due to a solid may be better solved using transmission theory as described in Appendix A, Section 11 or using FEM computer modelling.

Disks of different sizes were used to measure their effect as an acoustic barrier. All disks at some height were able to adversely affect (change by more than the uncertainty in a given measurement) the resonant frequency with dependence proportional to the disks cross sectional area and its proximity to the interior port. The fact that the cross sectional area determines at which height the disk will reduce the resonant frequency suggests this phenomenon is not related to the port length extension term but, is instead associated with an impedance change or acoustic barrier caused by the disk (See Appendix A, Section 11). Leung *et al.* (1982) used various

sized flat disks in their $\frac{1}{2}$ wave resonant cavity to isolate scattering from volume effects. The results of which suggested they were able to partition the cavity causing the largest changes to frequency where pressure velocities were greatest.

For the disks 20mm to 60mm in diameter the resonant frequency was not significantly reduced until the disks were at 85% of the chamber height. This therefore represents the port length extension interference height, beyond which any disk, irrespective of size, will interfere with a moving mass of air in the port during resonance. This trend was also observed in the solids and water calibration tests. In the initial water calibration tests an upper limit of approximately 85% fill was observed when the Q factor significantly reduced above this value.

The angular solids, having many flat and angular reradiating sources, had resonant frequencies consistently lower than the same volume with water filling. The spherical samples fell in between the angular cubic solids and water fill. A complex impedance path occurs with the inclusion of a solid into the resonant chamber. Disks displayed more pronounced frequency shifting than equivalent surface area solids, but this discrepancy is in part due to the secondary cavity created when the disk effectively partitions the chamber.

From these observations two conclusions can be drawn. 1) Samples being measured in a resonant chamber are not expected to alter the resonant frequency if they are kept below 85% of the chamber height and they have a cross sectional area less than 20% of the chamber's cross sectional area, determined by the flange factor. 2) When the sample cross sectional area is greater than 20% of the chamber cross sectional area the resonant frequency is likely to obey resonant theory if the sample is kept in a bounded region. The bounded region can be considered a tapered cone, defined by the sample's cross sectional area and its height. The higher the sample the smaller its cross section must be to be accurately described by the Helmholtz equation.

3.5.7 Measurement on granular materials

A range of granular materials were tested to gauge the effect of collections of particles for bulk measurements using the resonant techniques developed. A distinct trend was seen in predicted volume based on particle size. Larger particles tended to be accurately predicted (marbles 15mm and 25mm). In smaller particles, between 0.7mm and 3mm, under prediction was apparent. This then switched to over prediction in particles of less than 0.3mm.

Samples had a wide range of particle densities from 1.12g/cm^3 for plastic pellets to 2.54g/cm^3 for sand. The trends seen indicate density does not affect the particle size to prediction relationship. It is apparent the sound absorption properties are a function of particle size and geometry, and not particle type. When an incident sound wave encounters the granular bed material it is re-emitted and absorbed by the individual particles. Also occurring is acoustic attenuation due to viscous interstitial effects due to boundary layer dimension being comparable to inter particle space size. As the sound penetrates the bed it is likely the viscous forces will dominate over the inertial ones as calculated in Appendix A, Section 9. This makes the bed acoustically resistive. The smaller the interstitial space the higher the acoustic resistance and the more the energy absorbed in the bed material.

Resonant peak broadening is the result of acoustic absorption within the bed material. As the bed depth increases the larger will be the attenuation of the signal. The reemission of sound from the particle bed is not always at the same frequency as the incoming wave. The result is a broadband noise centred about the resonant frequency, which causes a widening of the resonant peak. This widening makes resonant frequency detection more difficult and compromises the achievable accuracy. The smaller the particles are the more pronounced is the effect. A significant logarithmic relation was found based on Q factor versus particle size. This showed that Q factor is related to particle size. The smaller the particle the more energy is converted from resonance into broadband noise.

The occurrence of sound reemission and absorption limits the maximum fill ratio for the chamber. At a fill level determined by the average bed particle size the level of reemitted sound becomes larger than the resonant frequency amplitude. When this occurs the primary resonant frequency will no longer be detectable. This was apparent in the skewed results from the small ballotini and sand where the prediction values reached a maximum. This was not seen in the larger particles tested, but is expected if the bed depth could be increased. This is an area where further testing could be conducted with a deeper chamber.

There were marked differences in frequencies and sound pressure levels detected in the bed and chamber. A microphone placed beneath the bed material indicated significant attenuation occurring for the particles less than 1mm in diameter. For the small ballotini and the sand samples there was an apparent cut-off depth at which the resonant frequency could no longer be detected. The depth at which this happens is directly related to particle size via the interstitial space size. The relation would need to be determined using a deeper chamber and a range of particles with an average size less than 0.166mm (smallest sample tested, sand).

A useful observation was made based on actual to predicted volume slope information and particle size. There was a near linear drop in slope from parity, as seen in large individual samples, to values of around 0.9 for collections of particles 2mm in diameter. This coincided with theoretical predictions about the Boundary layer distance. Sources such as Blackstock (2000), Beranek (1996) and Fung (1994) suggested the viscous forces should switch behaviour from inertial to viscous dominated at approximately 1mm, the value being dependant on the amplitude and frequency used, as it will change the wave velocity.

It is thought a switch from particle volume to bulk volume measurement occurs as a result of a boundary layer coming into effect for the smaller particle sizes and a given bed depth. Evidence for this behaviour was seen when the small ballotini and sand samples, at low fill ratios, showed under prediction. Predicted volume results then moved rapidly into a linear over prediction volume region, and lastly a region of acoustic absorption by the bed where resonance is completely attenuated. A microphone mounted under the bed material was able to show the different types of resonant behaviour between those in the bed and those in the free space of the chamber and port.

Secondary geometric resonance was often seen in the bed material and port when there was large attenuation caused by the smaller particles. Secondary resonance is a

function of the interior geometry of the chamber and port caused by $\frac{1}{4}$ wave resonance effects, as the dimension becomes a significant proportion of the wavelength. The broadband noise from particle reemissions was able to stimulate these higher resonant frequencies

Bed depth attenuation effects were further confirmed from tests conducted with granular coated disks. Each disk was coated in one of the granular materials tested. Q factor values remained at about 60 irrespective of the coating material. This showed that an irregular roughened surface, independent of particle size, causes only minimal acoustic attenuation.

Volume deviation results using the coated disks gave minimal differences at volumes less than $\frac{1}{3}$ full-scale fill but this increased noticeably by $\frac{2}{3}$ of full-scale fill. The amount of volume deviation from a non-coated disk was independent of particle size. The largest value was for a blank disk, but the smallest was for the plastic pellets despite their being the largest of the granular materials. There may be relationships between granular sample shape, particle size and chamber size, but these were not tested for and remain an area for further investigation of granular materials in a resonant cavity.

The successful results with the coated disks allowed volume measurement of a small amount of the agricultural samples to determine their true particle density. By ensuring only a thin layer of the given sample to be measured was used, no bed depth behaviour would be present in the predictive results. By also using the smallest chamber (1L) the volume accuracy was maintained (within 2%), as each of the granular sample's bulk volume was only 50mL.

Volume measurement accuracy with granular materials was shown to be related to Q factor. As resonant peak broadening occurs the accuracy diminishes. In general terms the accuracy can be divided into three regions. If the Q factor is higher than 50 then volume measurements can be made within $\pm 0.1\%$ full-scale fill. Typically this is only for larger particles ($>15\text{mm}$) or for thin layers of smaller granular material where bed attenuation does not occur. If the Q factor is reduced by acoustic attenuation, to between 30 and 50, accuracy is lessened to approximately $\pm 0.5\%$ of full-scale fill. In bed materials causing high attenuation, where the Q factor is between 10 to 30, only $\pm 1\%$ full-scale fill accuracy can be achieved.

Appropriate volume deviation curve fitting will be required for all granular materials. Each has a linear region of actual-to-predicted volume that departs from the parity line by an amount determined by the average particle size (See Section 3.4.7). For granular materials with a mean size smaller than 0.7mm in diameter there will be a maximum fill level due to acoustic absorption as the bed suppresses resonance with increasing depth. This occurred at about 25% fill factor for sand ($166\mu\text{m}$) and 50% for the small ballotini ($266\mu\text{m}$) using a 3L chamber with a 140mm internal diameter.

3.5.8 Effects of air leaks on resonant frequency and Q factor

Using the holed 3L chamber from the chamber mapping, Section 3.5.9, allowed investigation of air leaks in a Helmholtz resonator. The holed chamber contained ten 0.8mm holes evenly spaced on two sides of the chamber. The holes are there to allow a suspended ball to be moved inside the resonator by feeding a cable through the

chamber wall at different locations. Therefore, a range of leak combinations were investigated that determined the effect of individual leaks and if leak location was important.

The addition of a single air leak compromised the accuracy of resonant measurements. The air leak resulted in large acoustic attenuation. This reduced the Q factor, which in turn lowered the resonant frequency's resolvability. It was found that the resonant frequency was increased by 0.2Hz per leak and the Q factor reduced by $14\text{Log}(n)$, where n is the number of leaks. The placement of the leak in the chamber was shown not to be significant.

In contrast to multiple air leaks, an individual leak having a variable size showed a far greater effect on the resonant frequency. Despite this the behaviour was predictable and a distinct air leak size to resonant frequency second order relationship could be determined. A second order trend was also seen in the Q factor reduction with increasing air leak size. When the air leak size was greater than a threshold size determined by the boundary layer thickness, the air leak started to act as a secondary port. The air leak size at which this occurs is determined by the resonant frequency (See Appendix A, Section 9).

When the boundary layer dominates the effect is to pinch off the air leak causing an acoustic barrier that absorbs energy from the resonant system. The sound velocity through the leak is unable to move at the bulk velocity occurring in the chamber and port. As the leak area is increased the pinch region is less than the area of the hole, thereby allowing a secondary port to form. At this size a rise in the Q factor should occur as the attenuation properties of the leak decline and the leak starts to aid resonant behaviour. This was seen in the results for an air leak diameter over 6mm using the 3L chamber having a 170mm main port.

3.5.9 Effects of sample position on volume measurements

Results from the 42mL sphere placement at different locations within the chamber showed a marked difference in resonance behaviour only occurred when the ball was placed in the immediate vicinity of the port entrance. This result was expected as it was observed in water calibration tests. Adjusting the sphere position enabled a direct frequency mapping around the port entrance. This data showed directly the flange/port length extension zone, which was hemispherical about the port entrance. The ball was moved in 1mm steps and was therefore able to reveal transitional behaviour at varying distances from the port and its internal flange.

This information assisted in controlled drop experiments in proceeding sections. It was necessary to know how the resonant behaviour changed as an object moved through the chamber from one port to the other. Axial drop tests through the chamber, again with 1mm stepping, revealed a high level of detail in transitions from port entrance to exit. This test indicated that the length extension effect of the ports extend a far greater distant into the chamber than theory suggested. This 'extra' extension represents a decay of the bulk air movement protruding from the interior ports. The effect is only slight and is less than the achievable accuracy of the system, but greater than the repeatability. However, for consistency and accuracy it is best practice to make measurements in the centre $1/3$ of the chamber for a dual port resonator.

3.5.10 Controlled decent using a dual-port resonator and resonant hunting

It was possible to make accurate measurements for controlled decent of samples through the chamber. The maximum speed at which accuracy could be maintained was 1mm/s this could be increased to 2mm/s at the expense of doubling the measurement uncertainty. Therefore, using the resonant hunting method is not a practical method for rapid volume determination of moving samples. These results necessitated the development of the Q profile shifting techniques developed in Chapter 4.

3.5.11 Measurement of port flanging effects

A flange factor is the multiplier for the port radius that determines the port length extension. Flange factors were measured and used to improve the accuracy in calculating volumes for the Q profile shifting procedures in Chapter 4. The configuration using the asymmetric un-flanged external port was found to have a flange factor of 1.375. The volume deviation curves used in the resonant hunting method (Chapter 3) did not incorporate this experimentally derived flange factor and used the theoretical value of $(8/3\pi+0.6)a$. The effect of this flange factor error causes a proportional offset in the volume deviation curve, the value being determined by the difference between the two. However, this discrepancy can be compensated for in a calibration correction. Other methods for determining the theoretical flange factor values presented by Kang and Ji (2008) gave results significantly less than those measured and could not be used for objective comparisons (See Chapter 2, Section 2.3).

The agreement in flange factor value for both the un-flanged 51mm port and 170mm port demonstrated the behaviour of the interior and exterior port were the similar irrespective of the port length for the two port tested. It also demonstrated that the flange factor was frequency independent as the two configurations resonated at very different frequencies. The addition of flange material to the external port revealed a steady decrease in resonant frequency with increasing flange size. The maximum flange factors measured were close to the theoretical maximum value of 1.698, thereby showing at roughly 8:1 flange to port ratio the port appears as a point source in an infinite plane. This transition was seen in Figure 3.4.34, Results, as the flange factors became asymptotic with very little change in resonant frequency for increasing flange size.

Chapter 4

New methods in volume determination using Helmholtz resonance

4.1 Introduction and summary

This chapter represents a progression from the previous chapter in which practicality of making volume measurements was tested and proved to be viable. This chapter describes the development of methods for reducing measurement time and ease of use of the Helmholtz resonator volume measurement system.

To allow faster measurement times a number of methods were undertaken to remove the dependence on frequency scanning (chirps) for determining the resonant frequency. The first method employed was phase shifting, where the phase change was monitored before and after object insertion at a set driving frequency. The second, and more successful, was that of Q profile shifting which relies on negligible changes in the Q profile with small changes in chamber volume.

To allow accurate predictive techniques using the Q profile shifting method an environmental normalisation curve system was implemented to remove environmental artefacts from the signal generated by the loudspeaker including acoustic reflections and diffraction. This method was able to generate flat sound pressure levels over the desired frequency range.

Over the course of this investigation three Q profile shifting techniques were developed, each building on experience gained and progressions made in understanding the factors affecting volume measurement. The first used port microphone data, collected from controlled drop experiments, which was then post processed. The second technique was able to use real time data to determine sample volume. The last incorporated environmental data and dynamically created Q profile curves and was able to make more accurate real time volume measurements. All systems incorporated varying levels of temperature compensation for the speed of sound.

Other potential derivations of resonator design were investigated such as an inverted port resonator. This resonator variation would allow access to the resonant chamber without mechanical contacting or interference. The advantage of such a system would be corrosive environments or seal free configurations.

A variable chamber resonator was designed and built to aid in rapid sample volume measurement and chamber customisation. This allowed fast repeatable measurements of a sample with minimal chamber volume uncertainty. The variable chamber resonator was operated with Q profile shifting and environmental normalisation curves.

To assess this technology for potential commercial applications a limited number of tests were conducted on moving samples in which dynamic measurements were made. Measurements on a range of sample types were also undertaken. These consisted of a number of agricultural produce samples and two typical rock types having very different morphologies used to represent minerals testing.

4.2 Equipment and samples

A large part of the equipment used in this section of work is that used in Chapter 3. This includes the Perspex dual port 3L resonator, the pulley apparatus, loudspeaker, Data acquisition system, temperature sensor, microphones and solid samples. New software was developed as necessary. Software algorithms and functional block diagrams are provided in Appendix B. Full drawings of all experimental apparatus are in Appendix E.

4.2.1 Variable chamber resonator (VCR)

A variable chamber volume resonator was designed and created to allow customisation of the resonator dimensions to better suit the sample size. The chamber floor was controlled by a stepper motor linear actuator type SMC LXP B 200, which in turn was controlled by a SMC LC56D actuator controller, Figure 4.2.1. The actuator controller was sent pulse codes via the computer data acquisition system. The positional control was within $\pm 15\mu\text{m}$, as indicated by the linear actuator manufacturer, which equated to a volume uncertainty of $\pm 0.25\text{mL}$. By adjusting the chamber floor position the resonator chamber volume could be adjusted from 3500mL to 1600mL. The volume measurement accuracy is a function of the full-scale fill, or fill fraction. Full drawings of all equipment and software functional block diagrams are given in Appendix E and B respectively.

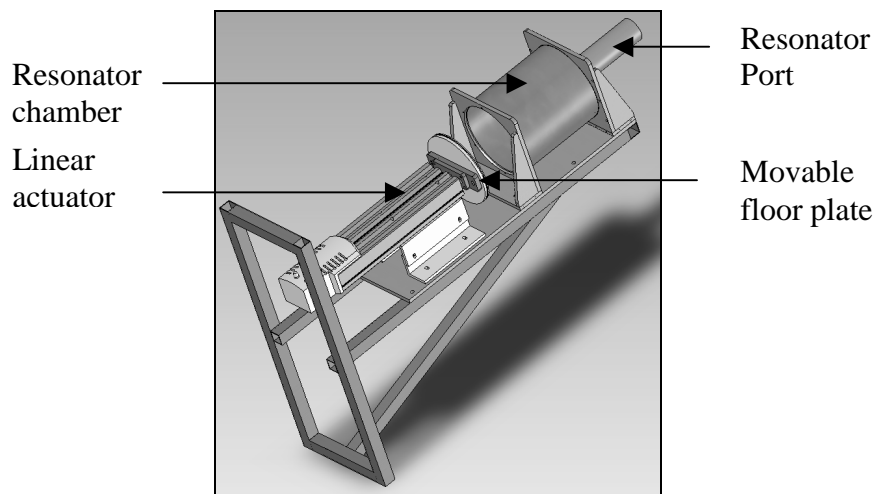


Figure 4.2.1 Variable chamber resonator, 1.6L – 3.5L with 175mm port. Shown are linear actuator placement and movable floor plate allowing sample insertion.

4.2.2 Inverted port resonators

The inverted port resonator consists of a cylindrical chamber and base with a removable concentric insert piece forming the port, Figure 4.2.2. A PCB103A microphone was inserted into the base of the chamber to monitor resonance. Three port pieces were used to test Q factor and resonant frequency. The chamber was made of 50mm diameter aluminium tube with a 3mm wall thickness (44mm internal) and had a length of 145mm. The three port pieces, made from machined 304 stainless steel, were: 41mm diameter with a 50mm length, 41mm diameter with a 25mm length and 35mm diameter with a 50mm length. This gives port to chamber radius ratios of 0.932 and 0.795 for the 41mm and 35mm diameter ports respectively.

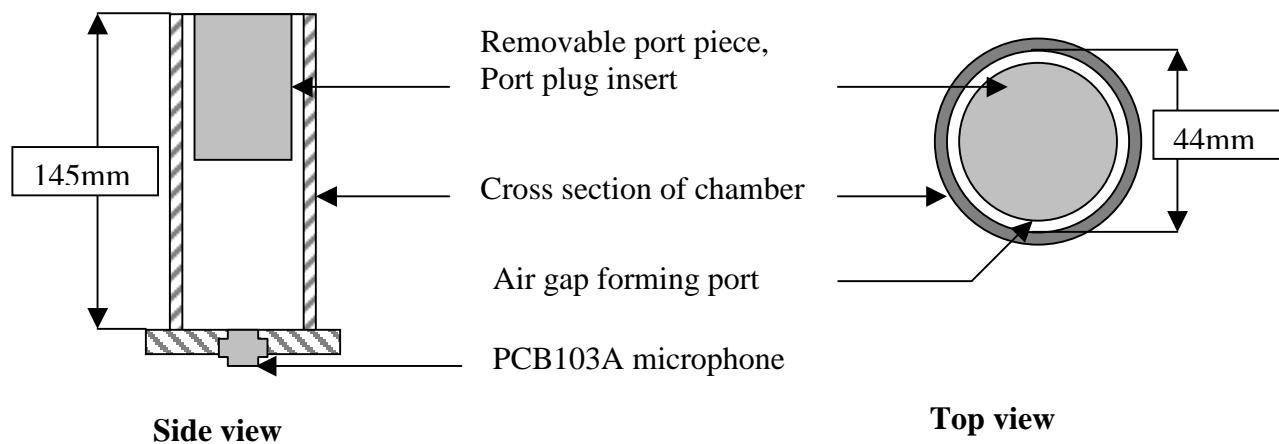


Figure 4.2.2 Inverted port resonator with removable port piece allowing easy access to chamber.

4.2.3 Buoyancy rig

A buoyancy rig was constructed, Figure 4.2.3, to allow accurate objective volume comparison of produce and mineral samples. Volume measurements were by immersion of the produce and mineral samples. Buoyancy volume measurements could be made to within $\pm 0.3\text{mL}$, an order of magnitude better than either the resonant hunting or the Q profile shifting methods. The principle of operation relies on the difference in force for the weight of the sample as measured on the scales and when fully immersed. The sample weight minus its immersed weight will be the volume in cm^3 (mL), dividing by the density of water will give the volume in m^3 (See Appendix D, Section 4 for calibration and Appendix E for mechanical drawings).

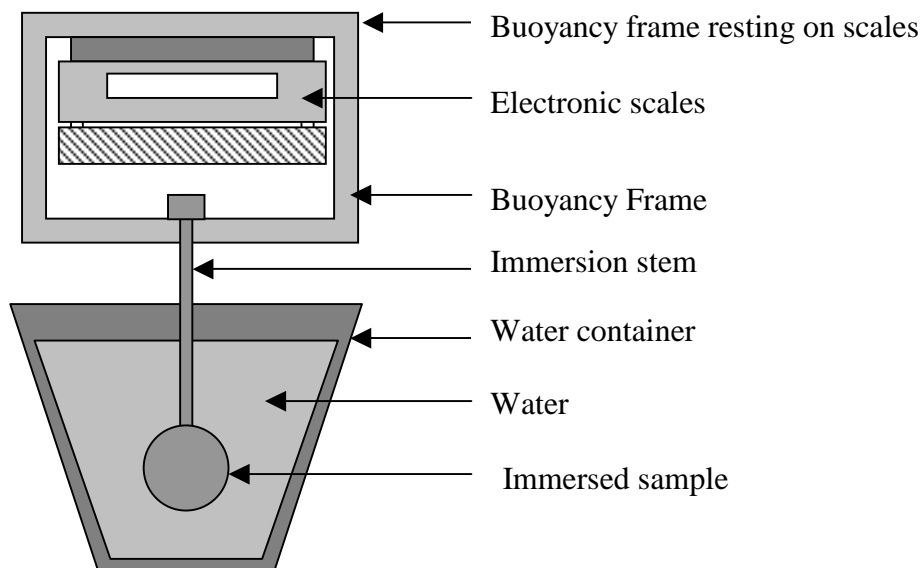


Figure 4.2.3 Buoyancy rig used to either suspend sample or provide forced immersion for samples less dense than water.

4.2.4 Agricultural produce and mineral samples

The following samples were measured using the buoyancy rig from Section 4.2.3, to ascertain their volumes to within $\pm 0.3\text{mL}$.

Sample	Type	Volume (mL)	Mass (g)	Density (kg/m ³)
Potatoes A	Ilam Hardy	232.8	244.9	1052.0
Potatoes B	Ilam Hardy	256.8	269.4	1049.1
Potatoes C	Ilam Hardy	154.2	162.4	1053.2
Potatoes D	Ilam Hardy	143.1	151.3	1057.3
Potatoes E	Ilam Hardy	151.6	160.2	1056.7
Kiwifruit A	Kiwifruit	103.7	107.5	1036.6
Kiwifruit B	Kiwifruit	76.0	78.4	1031.6
Kiwifruit C	Kiwifruit	95.6	99.8	1043.9
Kiwifruit D	Kiwifruit	103.3	107.8	1043.6
Kiwifruit E	Kiwifruit	97.4	100.2	1028.7
Capsicum A	Capsicum	48.1	31.8	661.1
Capsicum B	Capsicum	53.5	34.3	641.1
Capsicum C	Capsicum	50.3	30.4	604.4
Capsicum D	Capsicum	51.5	35.4	687.4
Capsicum E	Capsicum	50.2	32.4	645.4
Orange A	Navel	158.6	151.5	955.2
Orange B	Navel	150.8	144.0	954.9
Orange C	Navel	141.3	133.0	941.3
Orange D	Navel	157.2	141.4	899.5
Orange E	Navel	159.0	147.0	924.5
Egg A	Free range	56.6	62.2	1098.9
Egg B	Free range	55.6	59.7	1073.7
Egg C	Free range	55.3	59.0	1066.9
Egg D	Free range	53.8	58.0	1078.1
Egg E	Free range	65.8	70.1	1065.3
Avocado A	Haas	197.5	197.3	999.0
Avocado B	Haas	178.5	177.1	992.2
Avocado C	Haas	186.9	185.8	994.1
Avocado D	Haas	180.9	180.8	999.4
Lemon A	Lisbon	117.3	106.4	907.1
Lemon B	Lisbon	124.3	112.6	905.9
Lemon C	Lisbon	112.7	101.3	898.8
Lemon D	Lisbon	127.3	114.7	901.0
Lemon E	Lisbon	132.1	121.9	922.8
Greywacke A	Greywacke	82.2	218.5	2658.2
Greywacke B	Greywacke	183.4	493.2	2689.2
Greywacke C	Greywacke	149.7	399.7	2670.0
Greywacke D	Greywacke	99.4	266.6	2682.1
Greywacke E	Greywacke	74.5	199.0	2671.1
Schist A	Schist	52.2	130.9	2507.7
Schist B	Schist	61.0	154.9	2539.3
Schist C	Schist	57.1	144.2	2525.4
Schist D	Schist	101.5	260.6	2567.5
Schist E	Schist	204.6	508.6	2485.8

Table 4.2.1 Various produce and mineral samples used in variable chamber resonator using Q profile shifting.

4.3 Methods

4.3.1 Phase shift technique

A new and alternative method for finding the volume was investigated using frequency phase shift information. A phase shift change occurs in proportion to the difference between the driving frequency and the natural resonant frequency of the system. The closer the driving frequency is to the resonant frequency the larger the phase shift. This is analogous to the phase shift that occurs in resonant electrical circuits.

The phase shift was initially measured using the zero crossing differences between the driving signal and the microphone signal. However, the zero crossing method was not able to give sufficient phase data due to small amounts of microphone signal noise. Zero crossings are locations where the amplitude of the signal passes through zero. To overcome this, complete wave sections of the signal data were analysed and compared to the generated signal to better track phase shifting.

The advantage of a phase shift method is an instantaneous volume measurement. With a phase shift method the driving frequency can be set at the resonant frequency for the empty chamber system. Therefore, by measuring the phase shift change as an object passes through the chamber a phase shift to object size mapping can be made and hence allow for instant volume determination without the need to chirp through a range of frequencies.

4.3.2 Q profile shifting – Controlled decent

A new method of amplitude tracking and Q profile shifting (*QPS*) was also investigated. The new method would be able to determine the instantaneous volume of an object in the chamber using predictive techniques based on characteristics of the resonant peak profile. The resonant system is driven at its natural resonant frequency for an empty chamber. As an object passes through the chamber a microphone signal change will occur, due to the driving frequency no longer matching the empty chamber resonant frequency.

The system will have a resonant frequency based on the object's location and its effect on the geometric properties of the resonator. Important to this process was acquiring a Q profile, which defines the resonant peak, to allow a predicted volume measurement to be made. A Q profile was acquired for an empty chamber in which the frequency is swept over a sufficient range to include the largest frequency shift likely to occur for the largest object to be tested. Also required were accurate temperature measurements as subsequent measurements are likely to be at different temperatures than at the time of the resonant peak profiling. Temperature data is incorporated in the Helmholtz equation for volume calculations.

Assuming there will be negligible changes in the Q profile shape for small changes in chamber volume, the Q profile can be frequency shifted to predict the volume of the sample. The amount of frequency shifting required for the Q profile is determined by the signal change of the port microphone. The greater the signals difference between an empty chamber level and one with a sample, the greater the frequency shifting required.

The Q profile was interpolated using a spline as well as a 5th order polynomial to evaluate which would be a more accurate method for frequency shifting. The spline is an n order polynomial where n is the number of points making up the Q profile. A fifth order polynomial was found to be the lowest order that was capable of accurately interpolating the Q profile over the required frequency range. Q profiles were gathered for three spherical samples to gauge how Q profiles changed with object size. The three spheres volumes were 7mL, 23mL and 42mL.

As an object passes into the top port a significant reduction in cross section of the port occurs and there is a corresponding large microphone signal change. Once an object has passed into the chamber both ports will be free of interference and the resonator will behave in a similar fashion to that of the empty chamber. A reduction in microphone amplitude will occur due to the system no longer resonating at its ideal level, caused by the chamber volume change. By dividing the frequency signal from the microphone into individual cycles, a cycle-by-cycle analysis of the changing microphone amplitude can be made as the object passes through the port and into the chamber. The individual microphone levels are then subjected to a five point running average to minimise outliers and noise.

Using this method three distinct regions can be analysed, the empty chamber amplitude prior to releasing the object, the port interference amplitude as the object passes into and out of the port and the amplitude where the object was in a valid measurement region within the chamber. By comparing the difference in amplitude between the empty chamber and the object in the valid region a ratio difference in signal can be determined. Next a Q profile shift (*QPS*) was made in which the Q profile was frequency shifted in intervals of 0.005Hz until the amplitude of the trailing edge of the curve was at the ratio detected by the microphone (signal ratio between no sample and the sample in the centre of the chamber). The number of increments needed to achieve this ratio will determine the new predicted resonant frequency. For example if 400 steps are required to achieve the ratio change then the new resonant frequency would be $400 \times 0.005\text{Hz}$, plus empty resonant frequency, plus the temperature compensation factor, Figure 4.3.1.

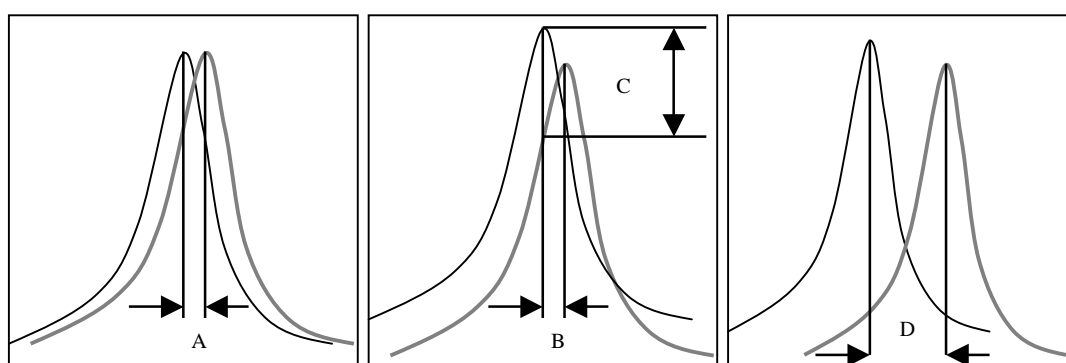


Figure 4.3.1 Software adjustments to the Q profile required to make predictive volume measurements. A is the frequency shift due to temperature change, B the frequency shift associated with a volume change and D the total change in frequency that is used to predict the new resonant frequency. C is the amplitude change proportional to the change in microphone level at the initial resonant frequency.

From the newly determined resonant frequency and temperature information at the time of measurement a volume can be predicted for the object based on the Helmholtz equation for a multi-port resonator.

More formally the mathematical model was constructed and can be described by Equations (4.3.1) to (4.3.4). This uses Equation (No.22), Basic Equations, and linear speed of sound compensation for c . The object volume w is a differential volume; the empty chamber volume minus the one measured containing the object. The first frequency, $freq1_{T2}$, is calculated based on a shift in temperature since the empty chamber frequency scan, $freq1_{T1}$, at the initial temperature (T_{emp1}), Equation (4.3.2). Equation (4.3.3) is the 5th order polynomial approximation of the resonant peak curve i.e. the Q profile. Equation (4.3.4) is the value of the predicted resonant frequency based on polynomial curve, temperature and the number of frequency increments required to reach the ratio of microphone attenuation.

$$w = \left[\frac{(331.4 + 0.534T_{emp2})}{2\pi} \right]^2 \left(\frac{S_p}{l_p'} \right) \left[\left(\frac{1}{freq1_{T2}} \right)^2 - \left(\frac{1}{freq2_{T2}} \right)^2 \right] \quad (4.3.1)$$

$$freq1_{T2} = freq1_{T1} + (T_{emp1} - T_{emp2}) \left(\frac{0.534}{2\pi} \right) \sqrt{\frac{S_p}{V_c l_p'}} \quad (4.3.2)$$

$$dB(freq1_{T1}) = a_1 Dfreq^5 + a_2 Dfreq^4 + a_3 Dfreq^3 + a_4 Dfreq^2 + a_5 Dfreq + a_6 = \Omega(Dfreq) \quad (4.3.3)$$

$$dB(freq_{T2}) = \Omega(Dfreq + \Delta freq + dfreq_{T2-T1}) \quad (4.3.4)$$

where w is the object volume, T_{emp1} and T_{emp2} are the initial and subsequent temperatures respectively, S_p the combined port area, l_p' the length corrected port length, $freq1_{T2}$ and $freq2_{T2}$ the frequency at T_{emp2} before and after object insertion, $freq1_{T1}$ the frequency at T_{emp1} before object insertion, V_c the chamber volume, $dB(freq1_{T1})$ and $dB(freq2_{T2})$ the amplitude in dB at $freq1_{T1}$ and $freq2_{T2}$, $Dfreq$ the driving frequency, $\Delta freq$ the change in frequency required to achieve a percentage change in amplitude seen in lowering the object through the chamber, $dfreq_{T2-T1}$ the change in resonant frequency due to temperature change, a_1 to a_6 the experimentally found coefficients for the fifth order polynomial fit of the Q profile and $\Omega(Dfreq)$ the fifth order meta function dependant on the driving frequency.

4.3.3 Q profile shifting – Free falling sample

For free fall tests two regions of port obstruction occurred. Of interest is the region prior to port entry and that of the valid measurement region within the chamber. Three spheres were used in the freefall experiments, 7mL (23.85mm), 9mL (25.40mm) and 23mL (35.50mm). Sphere sizes larger than the 35.50mm diameter sphere tended to collide with the chamber or cause unacceptable pressure interference in the ports. This was due to the small clearance between sample and port, the port having a diameter of 44mm.

The same methods of recording and analysing data were used as those used in the controlled descent procedure, Chapter 3, Section 3.3.10. The only difference being the removal of a five-point running average on microphone signals. This was performed to give finer detail of microphone amplitude in the decent with compromises in noise level.

A cotton thread suspended the samples to be measured; the thread was then run over the pulleys shown in Figure 3.2.4 (See Chapter 3, Section 3.2.10). As the driving frequency was started the thread was released and suspended the sphere allowed to freefall through the chamber. This was repeated for the other two samples. A control was conducted using a slower descent (50mm/s) to gauge changes in signal level for a controlled drop versus a freefalling sample. The time to traverse the dual port resonator was less than 2 seconds.

4.3.4 Environmental Normalisation Curve (ENC)

Spurious deviations caused by environmental effects such as the loudspeaker, diffraction and reflections, are a constant problem in ascertaining the behaviour of a given resonator configuration (See Appendix D, Section 3). To overcome this a profile scan over the desired frequency range at 0.1Hz stepping intervals was taken at a location appropriate to where the port of the resonator would be without the resonator present. This then provided a benchmark response curve for the sound that would be incident at the mouth of the port.

Using the environmental normalisation curve (*ENC*), a flat output of equal sound pressure level could be produced by the loudspeaker at a given special location. This was achieved by inverting the *ENC* amplitude profile to that measured at a given frequency. The reversed amplitude signal was then used in frequency generation. Alternatively, the *ENC* could be used in normalising *Q* profiles by linear interpolation and superposition. To verify the technique an *ENC* was recorded and then used in a subsequent frequency scan over the same range (at the same temperature). By taking *ENC* over a range of temperatures it was also possible to track how the environment changed with temperature and incorporate this in *QPS* software algorithms.

4.3.5 Continuous Q Profile Shifting technique (QPS)

The previous method developed was further refined and used in continuous measurements with the standard 1L, 2L and 3L chambers with a single port. The software algorithms were also redesigned to incorporate accurate temperature tracking, dynamically shifted *Q* profiles, environmental compensation and linear interpolation rather than the previous polynomial/spline fit. This allowed measurements of a far greater range of volumes and enabled good accuracy over a wider range of temperatures.

The initial *Q* profile scan was similar to that used in the controlled drop with *QPS*. This consisted of pink noise followed by two successive resonant peak scans and a detailed *Q* profile scan. This profile was then used in all the subsequent measurements for the given set of measurements.

A more faithful curve interpretation is possible using linear interpolation of the *Q* profile rather than polynomial curve fitting. This was achieved by initially taking a detailed scan of the *Q* profile, typically 0.1Hz stepping. The *Q* profile is then

superimposed on an environmental normalisation curve (*ENC*) taken of the surroundings at the same location as the port microphone, but with the resonator not present (See Section 4.3.4). The result is a normalised Q profile free from anomalous effects. The environmental curve is frequency shifted in proportion to the difference in temperature (*ENC*) to the Q profile temperature. Hence, only one environmental profile is needed regardless of any subsequent temperature changes.

The normalised Q profile is then subjected to the same linear shifting procedure used in the controlled decent *QPS* procedure (successive frequency stepping to the required degree of microphone signal attenuation). The principal difference is linear interpolation of the shifted profile rather than a numerical calculation based on a polynomial or spline. To make better use of the Q profile, where the gradient is steepest, the driving frequency was selected at a location 1dB less than the peak amplitude (at resonant frequency). This avoided the region at the top of the profile where there was very little change in dB/mL for small samples.

Once the Q profile is acquired, the loudspeaker emits a single tone frequency, which is monitored in the port using the PCB microphone. Continuous volume readings based on microphone signal changes are then displayed. Temperature compensation is dynamically applied by monitoring a Resistance Temperature Device (RTD).

An improved Q factor measurement system was also incorporated. The improved method uses a 3rd order polynomial fit of the data between the lower –3dB frequency and the –1dB upper frequency. This removes any ‘roughness’ in the Q profile, which normally makes high accuracy Q measurements difficult.

Temperature stability tests, Q profile stability tests and calibration plots of varying sample shape were used to confirm the validity of these techniques. Monitoring the predicted volume with changing temperature would test temperature compensation. Inspecting Q profiles at different chamber sizes by including regular solids would test Q profile stability. Granular materials cannot be used with *QPS*. Because of their porous natures the samples have an associated acoustic resistance causing attenuation of the resonant peak. This attenuation is indistinguishable from that caused by the inclusion of a sample.

4.3.6 Inverted port resonators

An experimental trial on inverted port resonators was undertaken to determine the feasibility of using an alternative method of measuring sample volumes in a Helmholtz resonant system. The inverted port resonator consists of a cylindrical chamber and base with a removable concentric insert piece forming the port, Figure 4.2.2. The ability to easily insert and remove the port piece, giving access to the resonator interior, was the primary purpose of testing this configuration. This set up avoids the need for air seals and provides a simple way of accessing the interior of the chamber for volume measurement, which could be highly desirable for commercial applications of this technology.

4.3.7 Variable chamber resonator (VCR)

A variable chamber resonator *VCR* (See Section 4.2.1) was used with Q profile shifting (*QPS*) techniques similar to those described in Section 4.3.5. However, Q

profiles were shifted and overlain with *ENC* data in real time to further refine and speed up volume measurements.

The raw *Q* profile was first stripped of environmental components using the *ENC* data to give a ‘naked’ *Q* profile. This naked profile was then frequency shifted and the corresponding *ENC* data superimposed. A comparison was then made to see if the resultant attenuation at the driving frequency matched that detected by the port microphone. If not, the process was repeated with increasing frequency shifting until either the ratio of attenuation (as measured with and without a sample) was detected or the shifted profile was out of range.

In this way the *QPS* was dynamically dependant on the *ENC* profile at any given frequency. This method is more faithful to the true *Q* profile that would be measured had there been a scan over that frequency range. Correlation between predictive dynamic shifting was compared to actual *Q* profiles to evaluate the success of this method.

A complete set of solids testing and chamber floor positions were carried out to act as comparisons to earlier measurement techniques. Adjusting the chamber floor in 1mm steps was equivalent to water calibration tests conducted in the static Perspex™ resonator. A further use for the *VCR* was to investigate rigid body resonators. The first generation resonators were made of Perspex™ hence; there would be some acoustic loss through the chamber walls associated with the lack of rigidity. In an attempt to reduce rigidity losses the *VCR* was made of thick wall, 304 stainless steel pipe (NPS6 schedule 40). It was hoped that there might be an increase in *Q* factor with the improvement in resonator stiffness. This would give an increase in frequency determination due to a more defined resonant peak and therefore improve accuracy.

4.3.8 Applications – Produce and mineral testing

A number of produce and mineral samples were measured using a variable chamber resonator (*VCR*) and dynamic *Q* profile shifting (*QPS*), Table 4.2.1. This would test the *VCR/QPS* methods suitability for these applications. Samples of agricultural produce included potatoes, kiwifruit, capsicums, oranges, eggs, avocados and lemons. Capsicums were included as they have a large internal void space, which the other produce samples do not. Mineral samples comprised of greywacke and schist. The greywacke was a regular smooth stone with uniform density whereas the schist samples were highly angular.

Five specimens of each sample type were measured, with the exception of the avocados in which only four were measured. Volumes ranged from 50mL to approximately 250mL. Most samples had a narrow size range with the exceptions being potatoes, greywacke and schist. The mineral samples, the kiwifruit, and the orange samples were also measured with the resonant hunting method and the results compared to identify trends between the two systems in measurement applications.

4.4 Results

4.4.1 Phase shift technique

Using phase shifting proved difficult as the phase shift for the objects being tested was very small. For the 42mL spherical ball the phase shift was about 0.002 seconds in the dual port 3L resonator. The uncertainty in this measurement, using zero crossing information, was typically 25%. Hence, for the largest sample tested that could pass freely through the ports, the accuracy was limited to $\pm 10.5\text{mL}$.

By observing larger numbers of wavelengths better resolution was achieved up to about $\pm 3\%$ of the chamber volume. Further work would be required to fully test this method. However due to superior resolution in microphone attenuation occurring, Q profile shifting was deemed a better measurement option. The fastest speed tested at which reliable data could be collected was 80mm/s. The benefit of the phase shift method was its ability to give near instantaneous results. Only preliminary results were gathered for this component and as such were insufficiently detailed for presentation here.

4.4.2 Q profile shifting – Controlled drop

Results from resonant peak profiling with differing sample sizes showed there was a distinct loss in resonant peak amplitude caused by environmental effects, Figure 4.4.1. From previous data using static measurements the Q factor was observed to be nearly constant over small changes in sample volume. It was expected that the resonant amplitude would also remain fairly constant. Figure 4.4.1 shows the resonant peak Q profiles linearly decreased with increasing sample size over this narrow measurement range.

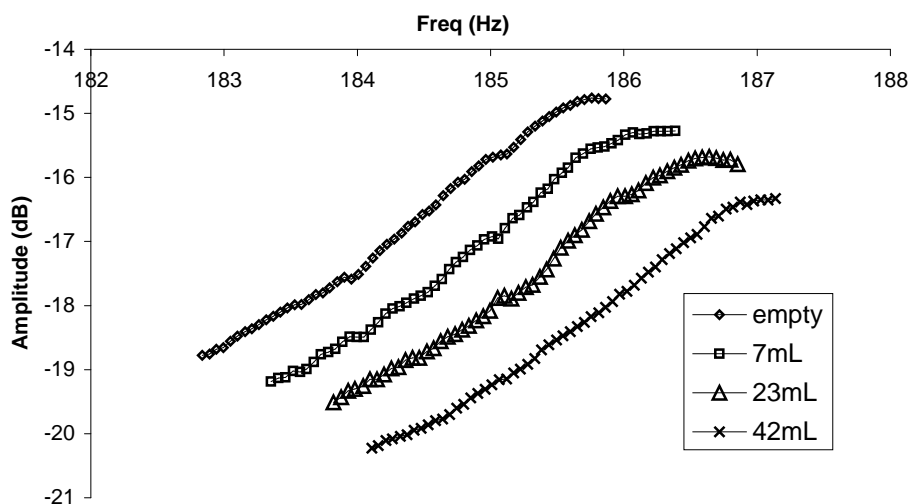


Figure 4.4.1 Q profiles for four chamber configurations, each using a different sized sphere. Using a 3L chamber with two 22mm radius, 51mm asymmetric ports.

A plot of resonant peak decay with increasing sample size revealed a near linear relationship for the small range of samples tested, Figure 4.4.2. This decay value was factored into the Q profile shifting procedure to allow better resonant frequency

prediction in determination of the object within the chamber. Therefore, as the Q profile is incrementally increased, a further amplitude increase is applied to allow for the natural decline in the resonant peak with increasing sample size. The cause of this decline is a combination of loudspeaker frequency efficiency and environmental factors such as sound absorption for the given environment (See Section 4.4.4).

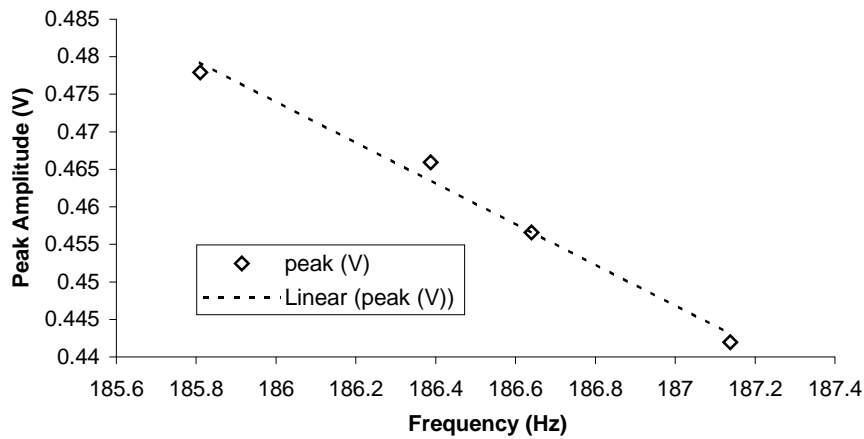


Figure 4.4.2 Resonant peak with increasing sample size for Q profile shifting. Tests used a 3L chamber with two 22mm radius, 51mm asymmetric ports.

The effect of an object passing through the port greatly altered the microphone's instantaneous Root Mean Squared (*RMS*) voltage amplitude, as can be seen in Figure 4.4.3 where large dips are present as the sample passes through the ports. Even with the smallest sample (7mL) a significant amplitude reduction is observed. The dips represent markers that can be used to delineate the chamber region. By taking a measurement centred between the dips a reading at the chamber mid point was acquired. This was then compared to the initial reading and the ratio was then used in Q profile shifting.

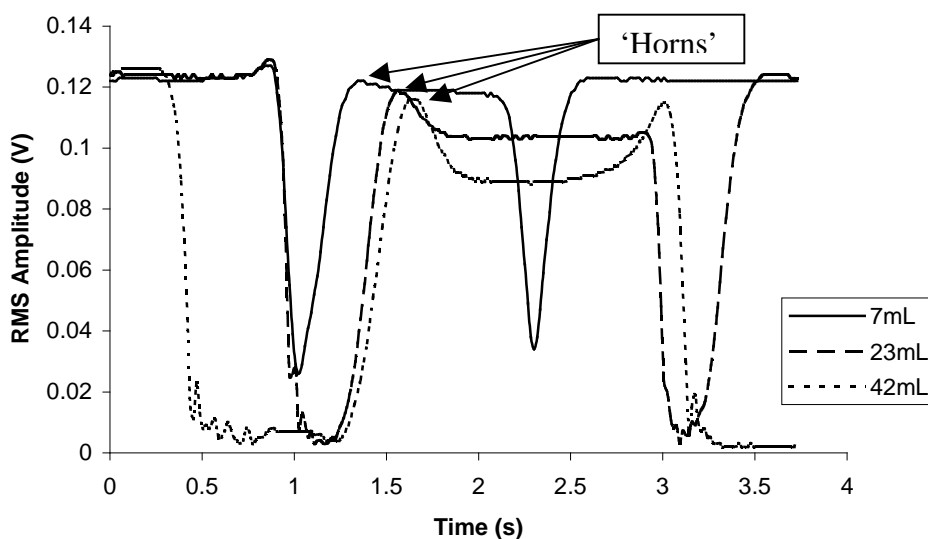


Figure 4.4.3 Reduction in RMS amplitude as samples pass through the chamber at 80mm/s. Transition dips are present as the samples pass through the ports. Using a 3L chamber with two 22mm radius, 51mm asymmetric ports.

The maximum speed at which a sample can descend through the chamber is a function of the port to sample diameter ratio and drop speed. The measurements made in Figure 4.4.3 were at 80mm/s. In Figure 4.4.3 significant ‘horns’ start to appear for the 42mL sample. These horns press into the measurement region. Interference between sample and port give rise to the horns as it is lowered through the port. The tighter fit between the sample and the port the larger the horns.

Using the *RMS* amplitude tracking with Q profile shifting, accuracies of $\pm 0.1\%$ of full-scale fill were achieved and repeatability of $\pm 0.04\%$ of full scale. For the 3L chamber this represents $\pm 3\text{mL}$ and $\pm 1\text{mL}$ respectively. This is similar to the accuracy achieved in static measurements using the resonant hunting method of Chapter 3 ($\pm 3\text{mL}$ accuracy and $\pm 1\text{mL}$ repeatability, assuming no disassembly). Because of restriction in port diameter a large sample range could not be used to verify accuracies of larger samples.

A comparison between a spline vs. a 5th order polynomial fit was made to determine which would be best suited to interpolate data in Q profile shifting over the frequency range of 183Hz to 187Hz. A polynomial of degree 5 was the lowest order capable of accurately reproducing the resonant peak curve.

For an empty chamber the two methods gave almost identical results, Figure 4.4.4. This is in contrast with data collected in an earlier test shown in Figure 4.4.1, which contains a number of ‘kinks’ for the empty chamber. Further testing with samples of 42mL, 23mL and 7mL revealed better consistency was obtained using a 5th order polynomial rather than a spline. A number of repeat Q profiles indicated profile ‘kinks’ were non-repeatable aberrant behaviour associated with environmental effects.

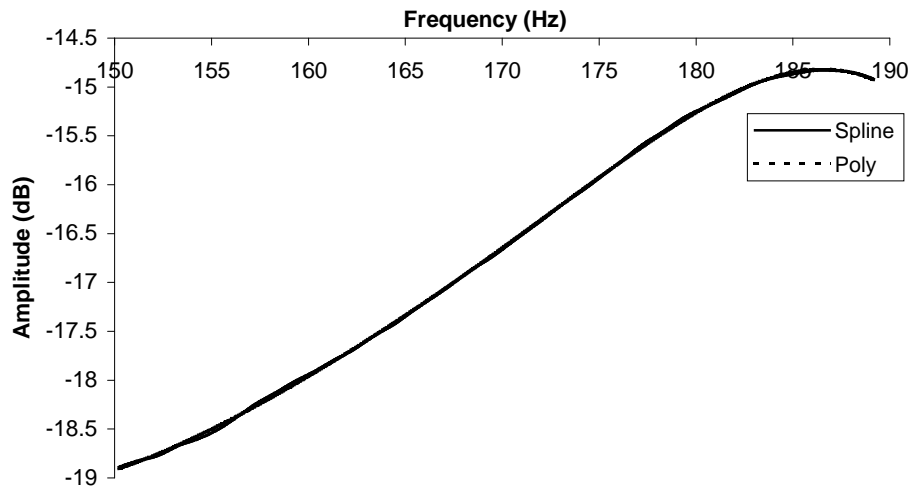


Figure 4.4.4 Comparison between spline fit and 5th order polynomial using an empty chamber. 3L chamber with two 22mm radius, 51mm asymmetric ports.

The volume deviation using a spline tended to be larger when the sample size was small, with deviations of 4mL, 5mL and 5mL for the 42mL, 23mL and 7mL samples respectively. The polynomial fit had a near linear volume deviation of 2mL, 3mL and 2mL for the 3 sample sizes tested. This should be expected, as any aberrant ‘kinks’ in the spline near the top of the Q factor curve should give the biggest deviations.

A changing the decent speed varies the number of microphone data points, thereby limiting the discernable information at the start of the drop and the critical centre region of the chamber. Results for a variable drop speed, Figure 4.4.5, were used to create a chamber map of varying speeds. From this an upper limit of 100mm/s was reached for the 42mL sample due to the lack of available data at the start of the controlled drop and poorly defined data in the centre region. The peak value of the horns and their penetration into the chamber was found to be independent of the drop speed. This suggests that the horns are a function of port to sample diameter ratio only. The chamber length is roughly 300mm, so the transit time through the 3L resonator is this length divided by the descent speed.

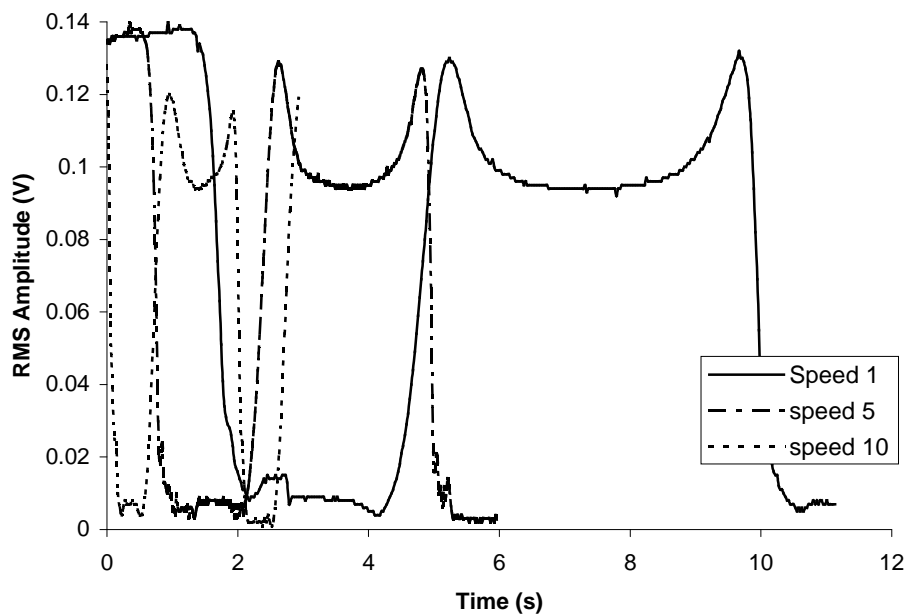


Figure 4.4.5 Changes in descent speed for an aluminium sphere of 42mL. Speeds 1, 5 and 10 are 28mm/s, 50mm/s and 100mm/s respectively. Tests used a 3L chamber with two 22mm radius, 51mm asymmetric ports.

Temperature effects were again found to be very significant at these high accuracies and must be accounted for if temperature stability is to be maintained, as was observed in Chapter 2, Section 3.4.3. By constantly tracking the temperature to within 0.1°C the resultant volume calculations could be kept to within ± 1 mL when repeat measurements were made of the same sample over an 8 °C change in temperature.

4.4.3 Q profile shifting – Free falling sample

In contrast free fall tests were not successful as the number of complete cycles at the driving frequency was inadequate to be representative of the measurement region within the chamber. Comparing the measurement data for the 23mL ball, between a free fall and controlled drop, revealed the plateau signal level was never reached in the free fall test, Figure 4.4.6. A similar pattern was seen in a test conducted with a 9mL ball.

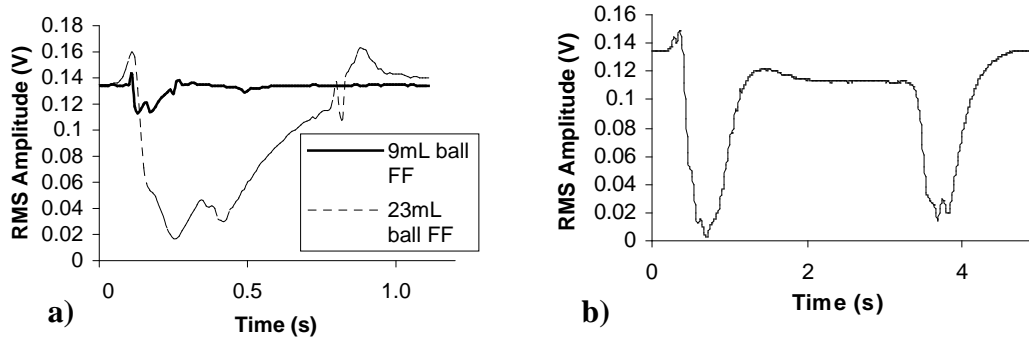


Figure 4.4.6 a) Free fall data for 9mL and 23mL spheres. 9mL sphere measurement at 0.1s and 23mL measurement time at 0.25s b) comparison of slower descent speed at 60mm/s. Tests used a 3L chamber with two 22mm radius, 51mm asymmetric ports.

4.4.4 Environmental normalisation curve (ENC)

Anomalous effects caused by loudspeaker, diffraction and reflection can significantly alter the measured Q profile. This is visible in Figure 4.4.7 where the leading edge of the Q profile is distorted by environmental effects. Using superposition techniques the Q profile can be restored to its true shape. This process was essential in the development of an accurate Q profile shifting methodology described and applied in Section 4.4.5.

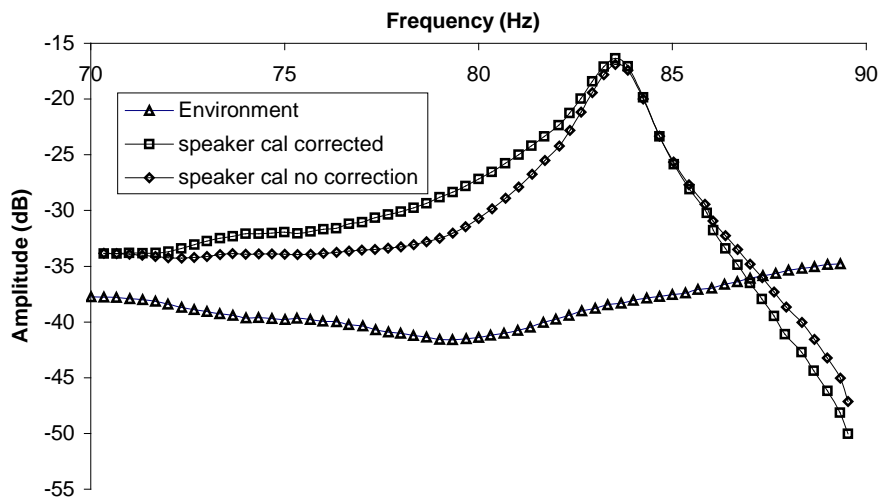


Figure 4.4.7 Corrected Q factor curve using ENC.

As part of the environmental normalisation curve (ENC) verification method an ENC post processed Q profile was directly compared to a dynamic ENC Q profile, Figure 4.4.8. The two Q profiles lie atop each other demonstrating the validity of the ENC process. If differences were seen between the two profiles this would indicate the ENC data was not able to adequately compensate for the loudspeaker, reflection and diffraction effects.

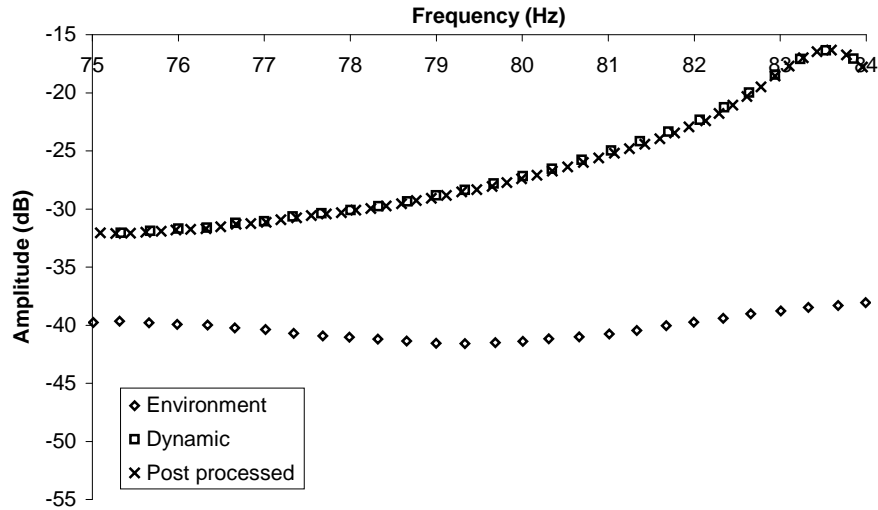


Figure 4.4.8 Comparison of Q factor curve dynamically adjusted with *ENC* data and the same Q factor curve post processed using the *ENC* data.

Environmental effects (Temperature, reflection and diffraction) also have the potential to shift the true resonant frequency. This is dependant on how strongly the system is resonating and the levels of environmental attenuation. Often the resonant peak would coincide with a major environmental peak or dip. For example the resonant frequency of the empty 3L chamber and 170mm long port configuration was approximately 83Hz, which coincided with a region of very poor environmental stability between 60 to 100Hz, Figure 4.4.9.

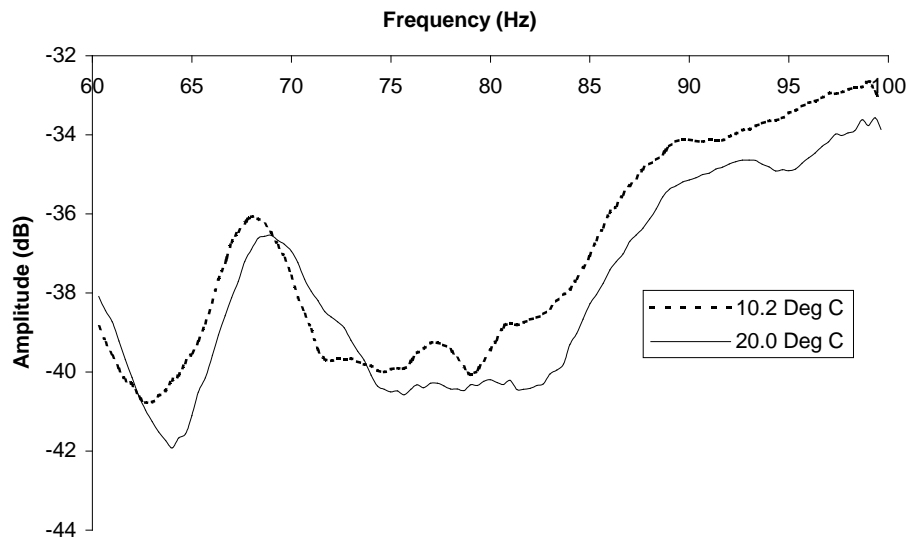


Figure 4.4.9 Stability and linear shifting of environmental profile with changing temperature between 60Hz-100Hz.

Figure 4.4.9 also shows that the environmental curve has small temperature dependence. In this instance there is an average 0.7Hz increase in the profile for an

approximate 10°C rise in temperature. This environmental temperature dependence must also be incorporated in the following procedures using *ENC* data.

To gauge the full array of environmental effects on Q profiles an examination of the resonant peak amplitudes for a range of chamber fill levels using water was undertaken, Figure 4.4.10. The equipment used was the 3L chamber and 51mm long port. An *ENC* is also shown demonstrating that the resonant peak amplitudes follow closely the profile of the *ENC*. Necessitating the use of *ENC* data in conducting Q profile shifting.

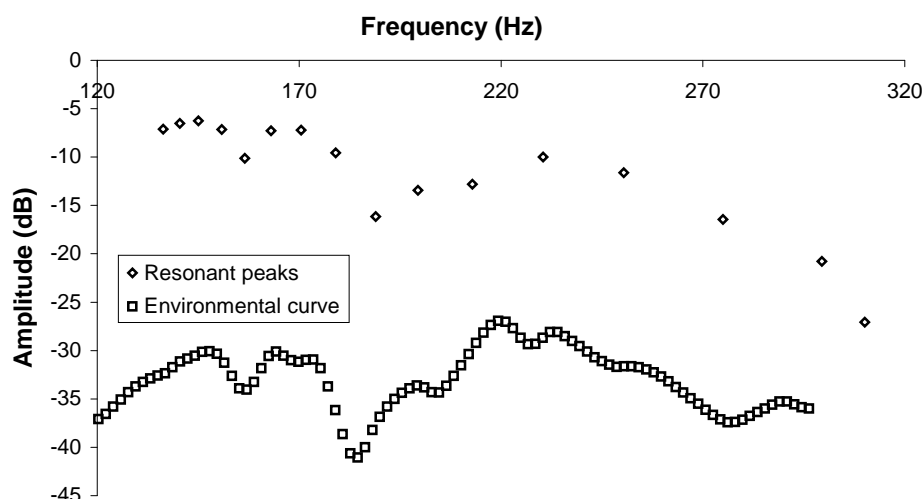


Figure 4.4.10 Resonant peak amplitudes for various chamber fill levels and the *ENC* profile.

When Q profiles were rerecorded incorporating an *ENC* profile, the resonant peak amplitudes still displayed significant variations in height for fill levels greater than approximately 500mL, Figure 4.4.11. The Q profiles were consistent with only minor changes in slope or value up to approximately 1L. As the fill level approached 1L, the Q factor value reduced indicating a steady decline in resonant energy. A flat, corrected profile is also shown in Figure 4.4.11 demonstrating the incident energy at the port was of equal sound pressure level. Therefore, peaks and dips in resonant energy are purely a function of the resonant system. The onset of Q profile broadening at 1L is not in keeping with observations made with the 3L Perspex resonator, which had a consistent Q factor up to 80% chamber fill. The cause of this discrepancy is unknown.

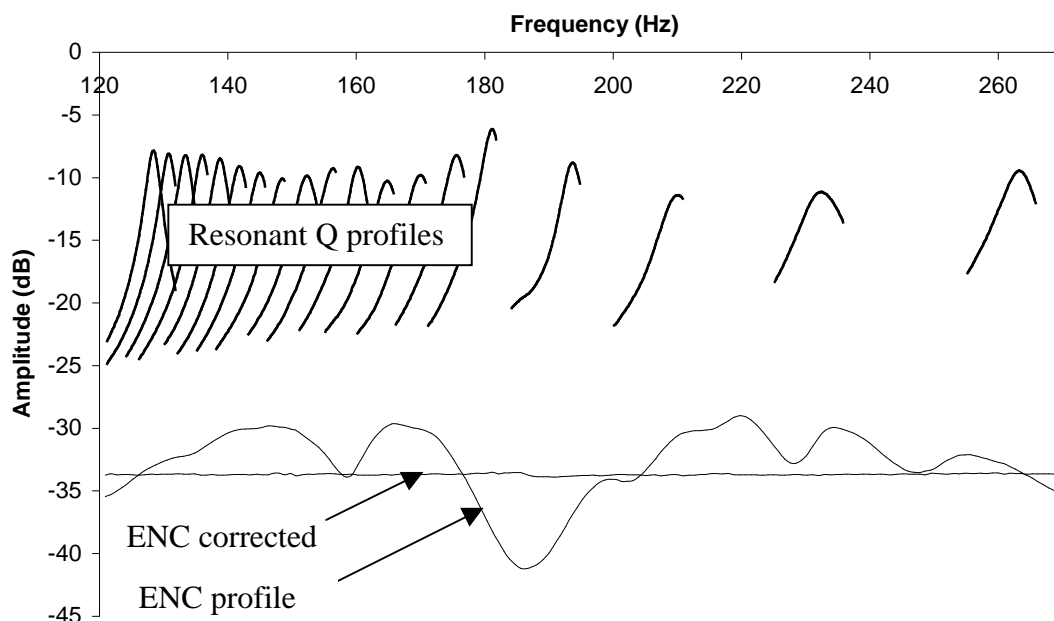


Figure 4.4.11 Q profiles for increasing fill with ENC corrected curves using a 3L chamber and 51mm port with increasing fill level using water.

4.4.5 Continuous Q profile shifting technique

Five successive repeat Q profiles were recorded along with five repeat environmental normalisation curves (*ENC*) to ensure the software and hardware components were capable of replicating results under the same physical conditions. Figure 4.4.12 testifies to the integrity of the software algorithms and hardware used. The deviations from the first trial to the last show negligible change in either Q profiles or *ENC* profiles. The loudspeaker and items in the immediate proximity of the resonator have temperature and humidity associated characteristics and it is these items that are likely to account for differences in *ENC* profiles.

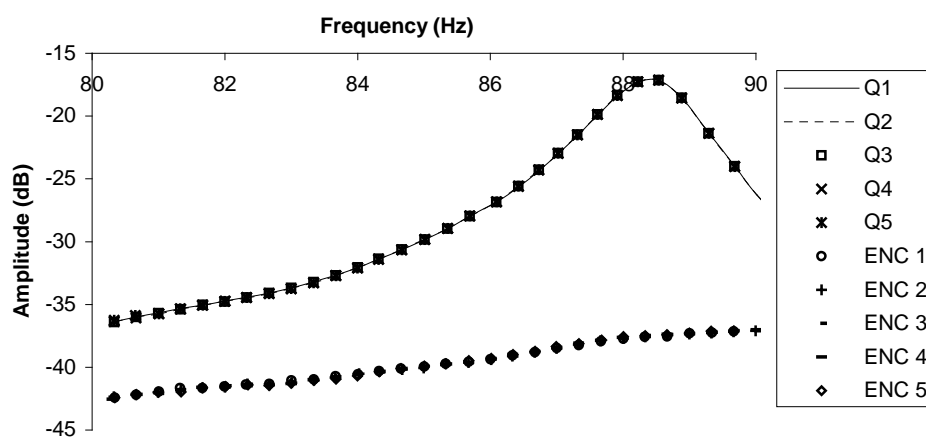


Figure 4.4.12 Five repeat measurements of the Q profile and the environmental curve at 17.0°C showing negligible variation.

The Q profile shifting (*QPS*) technique relies on the Q profile being invariant with temperature. To test this assumption a 3L chamber and 51mm long port configuration was tested with Q profile curves superimposed with temperature compensated *ENC* data. Both an empty chamber and one containing a 278mL steel sphere were tested at two temperatures, Figure 4.4.13. Despite an almost nine degree increase in temperature the results indicate almost identical profiles with negligible deviations in Q profile shape. This result shows the profiles change in frequency with temperature but not shape.

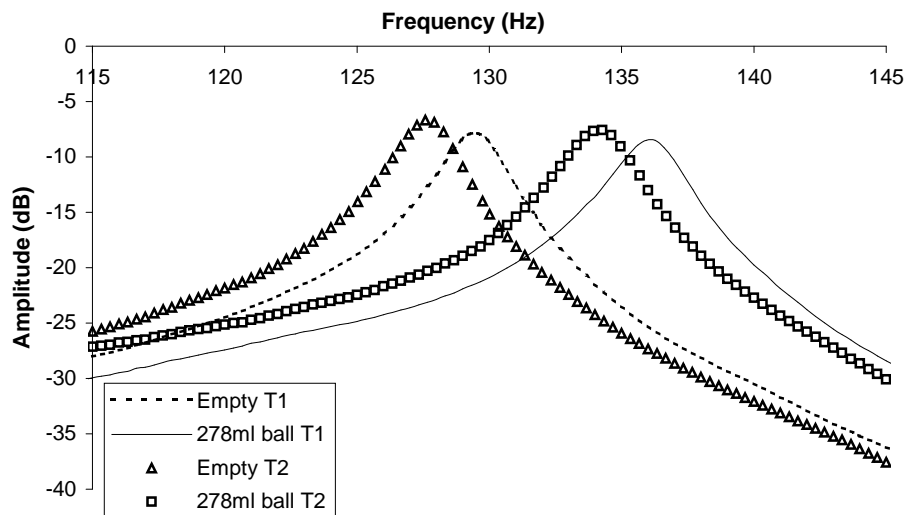


Figure 4.4.13 Temperature stability tests at T1 (21.9°C) and T2 (13.6°C) using a 3L chamber with a 51mm port and a 278mL steel sphere sample.

Amplitude deviation between Q profile curves is approximately ± 1 dB for the two different temperatures with and without a sample displacement of 278mL, Figure 4.4.14. Sound pressure level deviation data was gained by aligning the resonant peaks of the T1 and T2 Q profile curves. The rapid zero crossing at 127Hz and 134Hz represent the alignment frequencies for the empty and sample displaced chamber respectively.

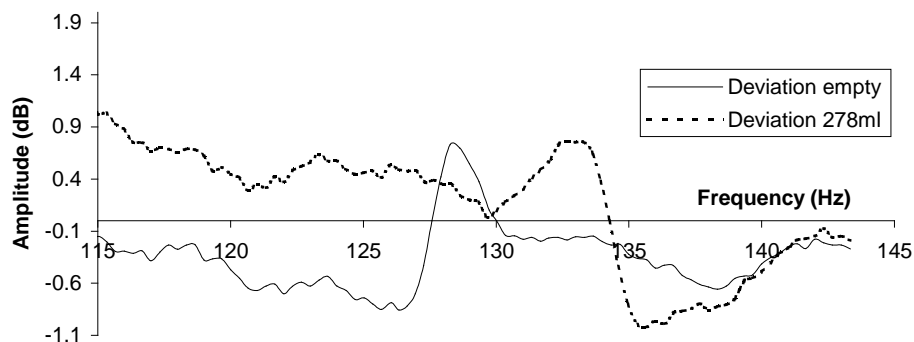


Figure 4.4.14 Temperature stability: Sound pressure level deviation for the empty chamber and for a 278mL spherical displacement sample. Resonator has 3L chamber with 51mm long, 44mm diameter port.

An empty chamber profile has been frequency shifted to overlay one taken when a 278mL steel ball was present to demonstrate the small deviation in Q profile, Figure 4.4.15. The shifted profile having marginal profile divergence results in the need for a calibration curve seen in Figure 4.4.17. The 278mL steel sphere represents one of the largest samples that it was feasible to measure using *QPS*. As profile deviation is a function of sample size, the majority of samples will have profiles with significantly less divergence.

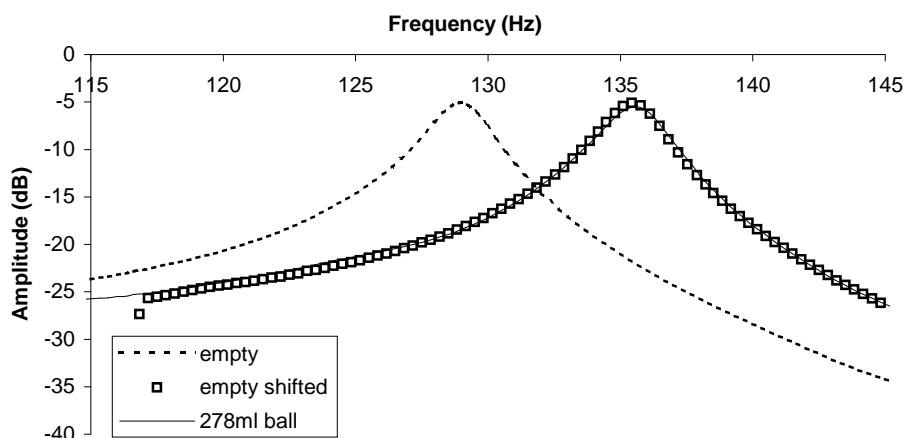


Figure 4.4.15 Q profile stability profiles taken at constant temperature and using 278mL steel sphere sample showing profile insensitivity to volume change. Also shown is a frequency-shifted profile of the empty chamber to allow direct comparison. The chamber was 3L and port 51mm.

The amplitude deviation is maximal either side of the resonant peak reaching values ± 1 dB, Figure 4.4.16. This difference occurs because the Q profile is changing shape and is not symmetrical about the resonant frequency. The asymmetry changes with sample size and shape. Minor variations in the environmental normalisation curve can also exaggerate this effect.

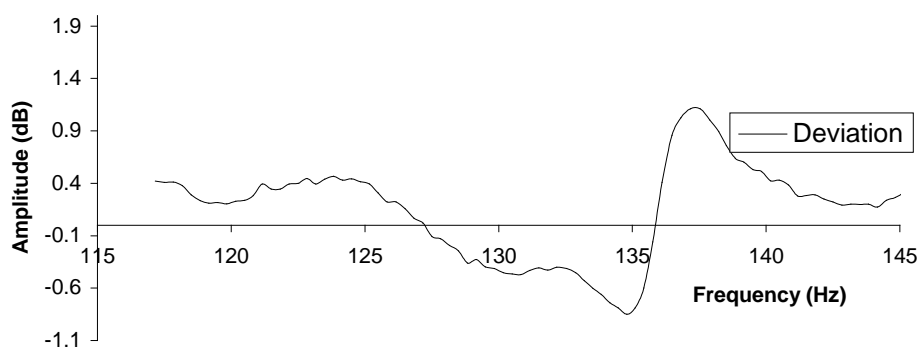


Figure 4.4.16 Q profile stability: associated sound pressure level deviation for a 278mL spherical displacement sample. Resonator has 3L chamber with 51mm long, 44mm diameter port.

Volume measurements were conducted using the improved *QPS* method with a number of spherical, cubic samples and water at varying fill levels. The improved *QPS* method incorporates an empirically derived flange factor (See Chapter 3, Section 3.4.11), a temperature factor (See Chapter 3, Section 3.4.3), linear interpolation and *ENC Q* profile correction using super positioning.

The cost of these enhanced features was a computing bottleneck when performed using a computer having a 2.4GHz Intel CPU. Very large numbers of calculations must be made every second which increases proportionally to the quantity of *Q* profile shifting required, the larger the volume the greater the frequency shifting. Coupled to the calculation times are the thousands of samples being analysed and generated every second by the data acquisition system. This restricted the maximum measurable sample volume to about 300mL in a 3L chamber with a 51mm port.

Despite the limited volume range the continuous *QPS* method was able to measure samples to an accuracy of $\pm 6\text{mL}$ with a repeatability of $\pm 2\text{mL}$ ($\pm 0.2\%$ full scale fill). This is similar to the previous *QPS* method and the traditional frequency scanning method. The dual port *QPS* experiments with controlled drop were limited to sample sizes of approximately 50mL in a 3L chamber.

As with other techniques in this investigation second order curve fitting was required to counter discrepancies between theory and measurement. Comparisons between different sample geometries are given in Figure 4.4.17, all of which can be represented by a second order volume deviation curve. Only small changes are required in second order trends for the range of volumes tested. For small volumes between 0-220mL an averaged second order curve fit is capable of giving accuracies of $\pm 6\text{mL}$ ($\pm 0.2\%$ full-scale fill or $\pm 2\%$ for largest practical sample) irrespective of sample geometry, Figure 4.4.18. For samples larger than 220mL divergent second order corrections make specific curve fitting a necessity.

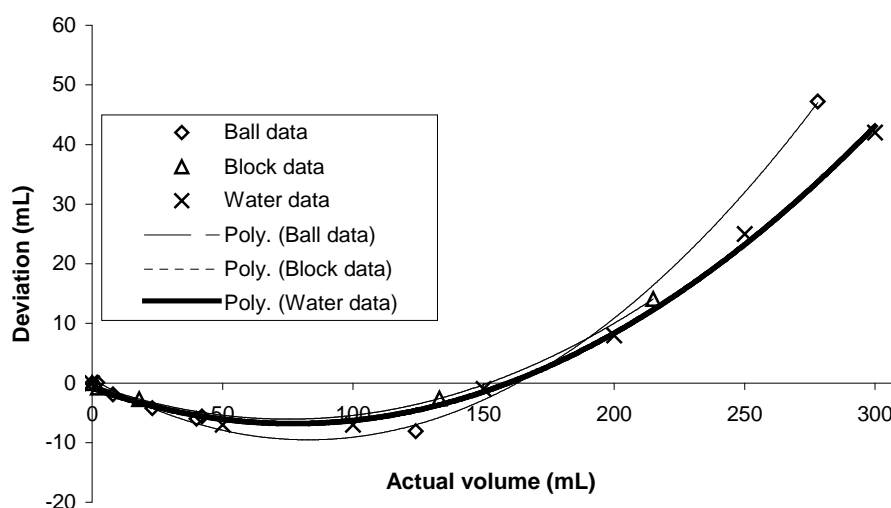


Figure 4.4.17 Volume deviation data and second order polynomial fitted curves for differing sample shape using the continuous *QPS* method. Resonator has 3L chamber with 51mm long, 44mm diameter port.

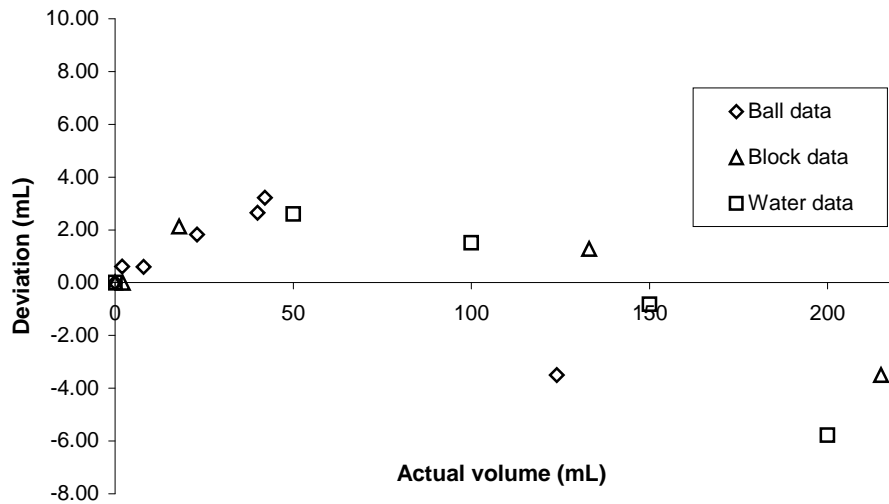


Figure 4.4.18 Continuous QPS deviation volume from true volume using a generic correction factor on water fill, sphere and cube volume. Resonator has 3L chamber with 51mm long, 44mm diameter port.

Similar second order volume deviation trends were also observed when the smaller 1L and 2L chambers (170mm port) were used with this method. Accuracy based on the full-scale chamber volume also remained similar. Accuracy was $\pm 2\text{mL}$ for the 1L chamber with repeatability of $\pm 0.6\text{mL}$. The 2L chamber had an accuracy of $\pm 4\text{mL}$ and a repeatability of $\pm 1\text{mL}$ respectively. This indicates the method is scalable for differing chamber sizes.

The typical time for a measurement to stabilise was about 3 seconds. This is in part due to the investigator causing a temperature gradient to occur when inserting a sample into the chamber. The system requires thermal equilibrium to be achieved to make an accurate volume measurement. Also, the changing location of the investigator disturbs the *ENC* profile. Therefore, not until initial environmental conditions are replicated will measurements be valid.

An improved Q factor measurement system gave repeat Q factor values of ± 1 , whereas previous techniques, using the raw Q profile, were only able to give repeatability of ± 3 . This improved method was also useful in making predictions of the resonant frequency, as it allowed a more precise value to be determined. Normally the peak of the Q factor has a certain 'roughness' associated with *DAQ* amplitude measurement limitations. In configurations with a low a Q factor this method offers improved resonant peak determination as it effectively smoothes the peak of the Q profile.

4.4.6 Inverted port resonators

Q profiles seen in Figure 4.4.19 were gathered using three port insert variations (See Figure 4.2.2) with environmental factors negated using the environmental normalisation technique described in Section 3.3.4. The two inserts with diameters of 41mm showed significant resonant peak broadening indicating substantial viscous losses associated with acoustic resistance in the form of boundary layer effects. As the

port area is similar to the regular resonators used the losses associated with radiation resistance are expected to be comparable. By choosing two contrasting port plug lengths, each resulting in low Q factors of approximately ten demonstrated the losses are definitively boundary layer related and not port length related, Figure 4.4.19. When a port plug of 35mm diameter was implemented the resonant losses were significantly reduced and the Q factor increased to 33.

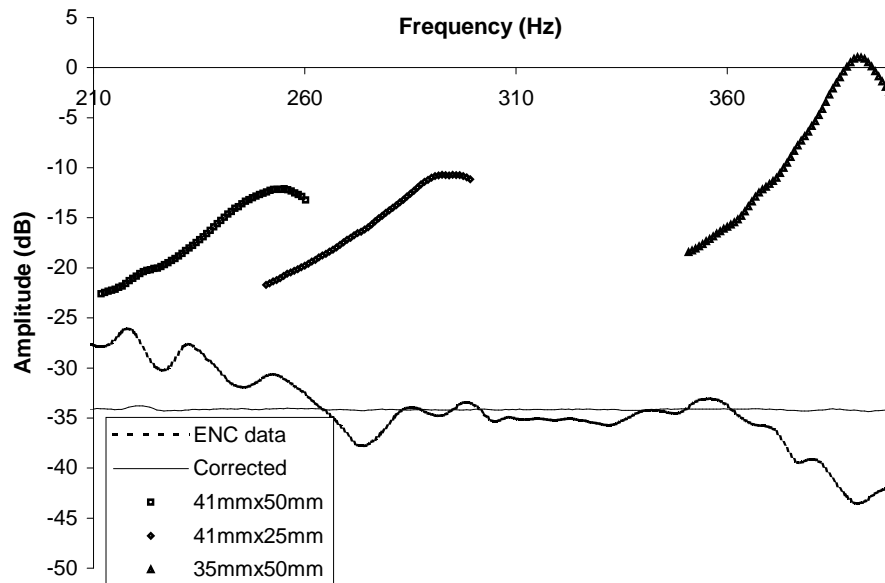


Figure 4.4.19 Environmentally normalization curve, corrected curve and inverted port resonator Q profiles curves with three port insert plug configurations.

Using equations from Appendix A, Section 9 the boundary layer thickness could be assessed for the inverted port inserts. These resulted in values of 20% and 17% boundary layer thickness to port thickness for the 41mm diameter plug insert having lengths 50mm and 25mm respectively (Figure 4.4.20). The boundary layer thickness calculated, reduced to 5% for the 35mm diameter port plug insert. Successful resonant frequency predictions indicate the port area is behaving in a similar fashion to a traditional port. However, the boundary layer penetrates into the port to a far greater degree, interfering with the resonant moving air mass.

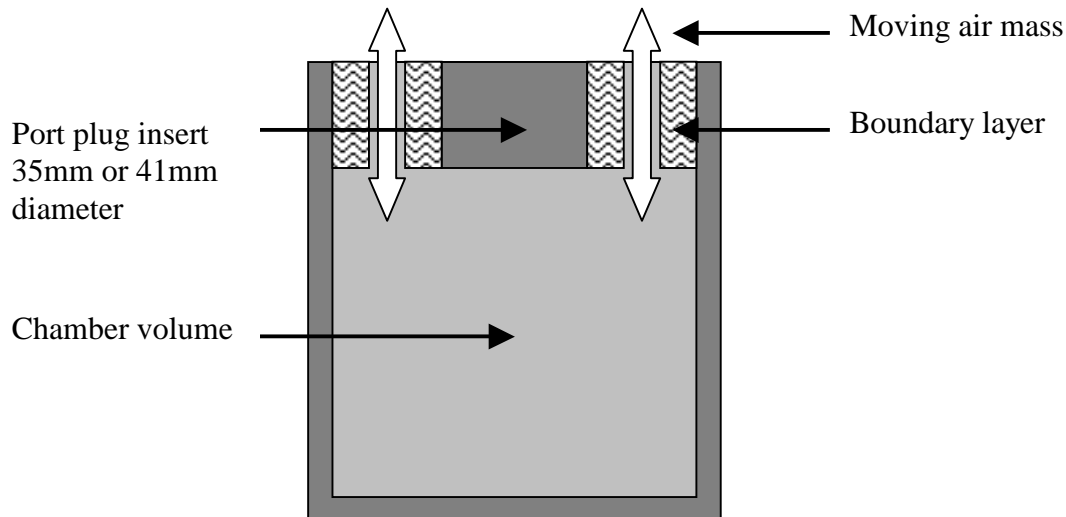


Figure 4.4.20 Boundary layer to port area becomes substantial for the inverted port resonator necessitating a large port area.

The measured resonant frequencies and those found using port radius equivalents were within 1% for the 41mm diameter inserts having lengths of 25mm and 50mm. The 35mm diameter insert predicted value disagreed by more than 3%, despite having a far superior resonant Q factor. The Q factors for the inverted port resonators showed large divergence from the theoretical values in a similar manner to inconsistencies found with the standard resonator configurations. Predicted Q values were between 103-399, but actual values fell well short, ranging from 10-33.

4.4.7 Variable chamber resonator (VCR)

Results for increased Q factor due to resonator rigidity were tested with the variable chamber resonator first numerically and then through Q factor measurements. The effects of chamber rigidity were evaluated as follows. The characteristic impedance ($\rho_0 c_0$) for air is 415kg/m²s (rayls), water 1.48x10⁹rayls, aluminium and Perspex™ ~17 x10⁶rayls and steel 47x10⁶rayls (Blackstock, 2000). Therefore, the impedance of air is 41,000 times less than the most readily coupling material, Perspex. This suggests transmission from one medium to another though the wall materials should be negligible. However, wall diaphragm effects may still be significant.

Measurements of Q factors for the variable chamber resonator (VCR) were not enhanced by an increase in resonator rigidity. The resonator end plates are made from high strength alloy aluminium and the resonator body from thick wall 304 stainless steel (schedule 40). The movable floor of the resonator is 10mm thick aluminium with a 1.7mm O-ring seal. The required force to overcome the linear actuator is in excess of 45N. Despite these improvements in resonator stiffness the Q factor was consistently between 50-60. This is similar to the results for the Perspex™ resonator, indicating very little acoustic losses are occurring through the chamber wall, floor and ceiling.

Calibrations using the improved dynamically shifted Q profiles were still best fitted by second order volume deviation curves similar to those observed in the continuous QPS techniques conducted in Section 4.4.5, Figure 4.4.21. Larger volume divergence was apparent in the fitted curves between the different sample geometries when

compared with those in the continuous *QPS* calibration data. The reason for this difference may be associated with the disparity in resonator geometries, differing base chamber size and port length. Loudspeaker instabilities at frequencies below 100Hz could also cause differences in scatter between the continuous and dynamic *QPS* calibration data.

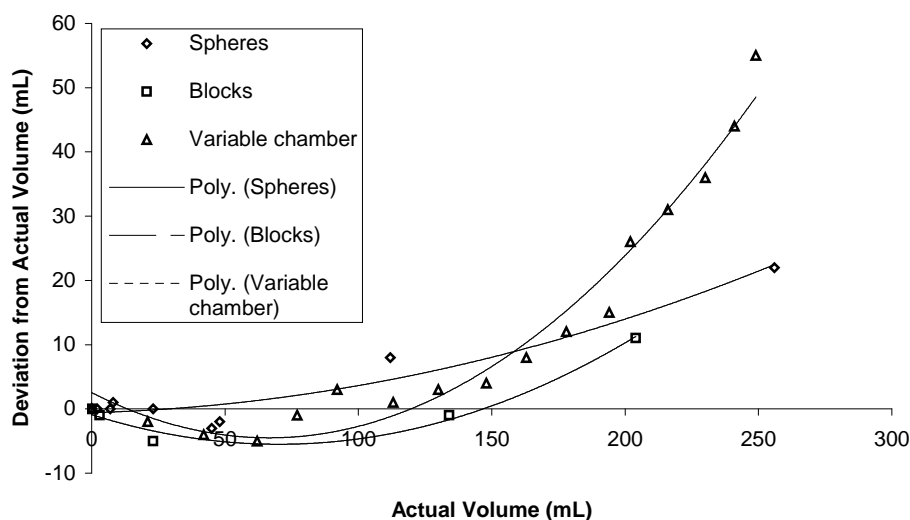


Figure 4.4.21 Deviation volume and second order fitted curves, implemented with *VCR* using *QPS*, when calibrating for a piston, spheres and cubes. *VCR* resonator has 3.5L chamber with 175mm long, 44mm diameter port.

Using a generic second order curve fit the volume accuracy of the *VCR* could be maintained to within $\pm 0.3\%$ ($\pm 10\text{mL}$) of full-scale fill between 0-220mL, Figure 4.4.22. This is a poorer result than the continuous *QPS* procedure. However, this uncertainty could be improved if a shorter port were implemented to raise the frequency range of operation over 100Hz. Loudspeaker instabilities at sub 100Hz frequencies limits the potential accuracy in this configuration.

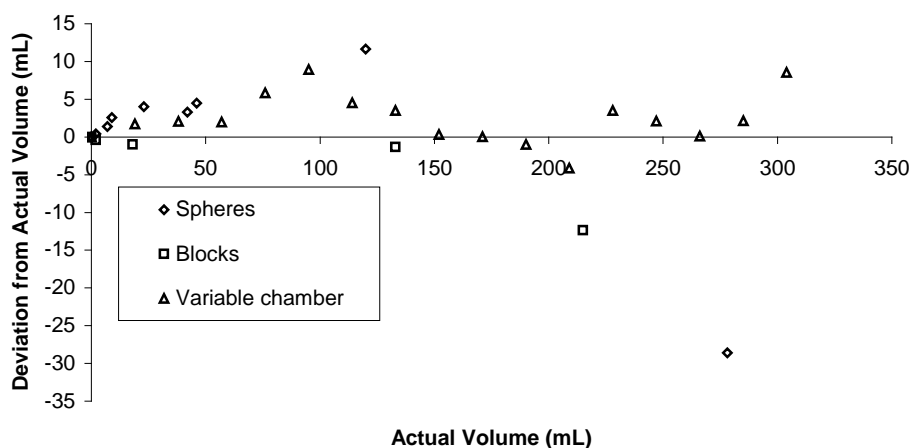


Figure 4.4.22 *VCR* deviation volume from true volume using a generic correction factor on piston, sphere and cube volumes. *VCR* resonator has 3.5L chamber with 175mm long, 44mm diameter port.

Accuracy could be improved to $\pm 0.2\%$ ($\pm 7\text{mL}$) of full-scale fill, Figure 4.4.23, when a specific curve fit for a given sample geometry is implemented. Again, it should be possible to improve this value to $\pm 0.1\%$ by the use of a shorter port to increase the resonant frequency above 100Hz. The large quantity of scatter is most prevalent in the piston driven variable chamber data despite having a volume uncertainty of less than $\pm 0.5\text{mL}$. This suggests data scatter is caused by factors internal to the resonator. This is further confirmed by measurements made in an anechoic chamber (IRL, Lower Hutt, NZ) in which scatter persisted and accuracy could not be improved beyond $\pm 6\text{mL}$ (See Appendix D, Section 3).

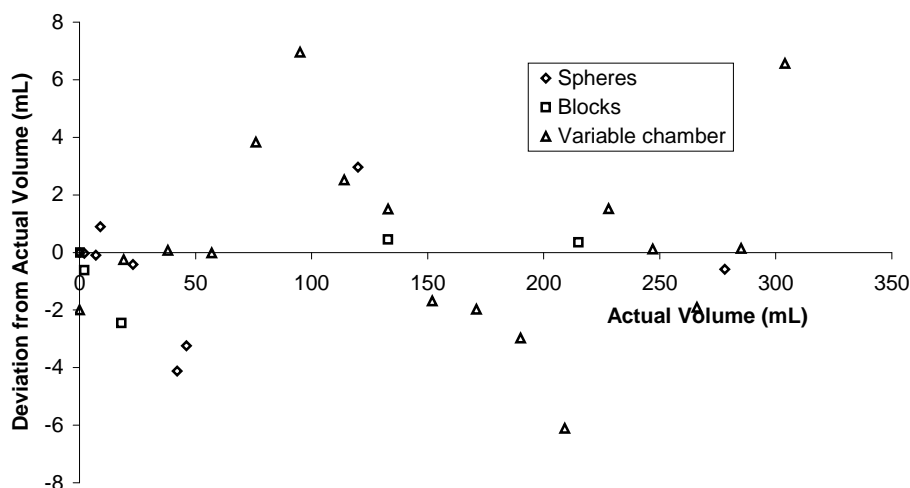


Figure 4.4.23 VCR volume deviation from true volume using a specific second order correction on piston, sphere and cube volumes. Resonator has 3.5L chamber with 175mm long, 44mm diameter port.

By comparing the measured Q profile and a frequency shifted Q profile the accuracy of the dynamic *QPS* technique was tested, Figure 4.4.24. This shows marginal differences in the two profiles. To further resolve deviations Figure 4.4.25 is plotted with a standard deviation of 0.4dB over the given frequency range. Agreement between the measured Q profile and the frequency shifted Q profile was able to confirm the method of dynamic super positioning of the environmental normalisation curve (*ENC*) data onto the ‘naked’ Q profile to adequately predict the Q profile at differing chamber volumes. This reduces the need for special environments for the Helmholtz resonant volume measurement system.

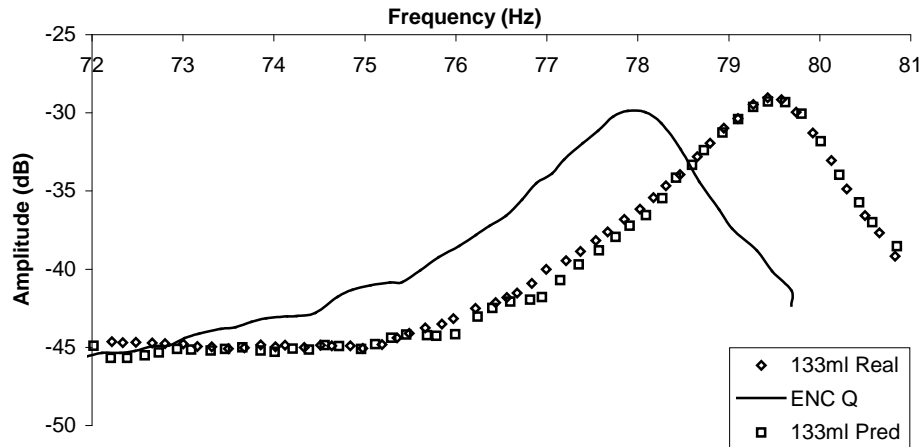


Figure 4.4.24 VCR with dynamic *QPS* of 133mL sample showing original (empty), predicted and measured Q profiles. Resonator has 3.5L chamber with 175mm long, 44mm diameter port.

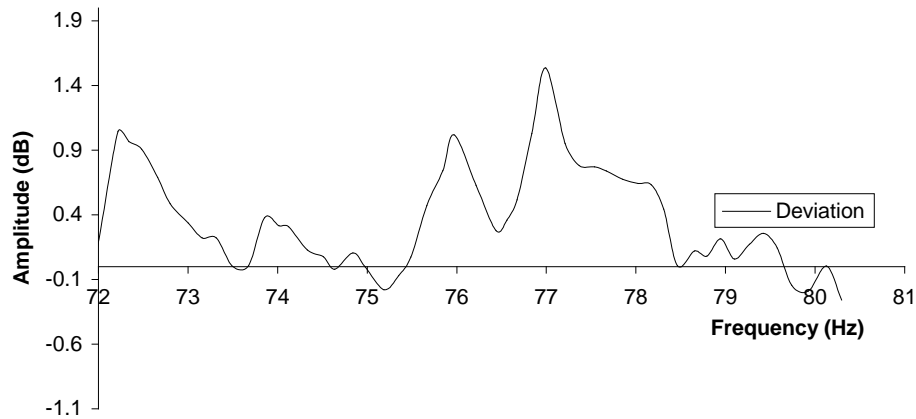


Figure 4.4.25 Plot of amplitude deviation with changing frequency for 133mL sample, predicted and actual Q profiles. Resonator has 3.5L chamber with 175mm long, 44mm diameter port.

As the displacement in the chamber becomes larger the ability of the software algorithms to accurately predict the Q profile reduces as other factors, such as sample geometry, start to affect the resonant behaviour. This effect can be seen in the measured and predicted Q profiles, using *QPS*, for a 215mL cube, Figure 4.4.26. Figure 4.4.27 gives the amplitude deviation plot. The resonant frequency is over-predicted, which is revealed as a rise in the amplitude over the frequency range 76 to 80Hz, Figure 4.4.27. This increases the standard deviation to approximately 0.8dB. As the sample occupies more of the chamber space an increasing impedance occurs in the chamber. The sound wave propagating through the chamber experiences different impedances above and below the sample.

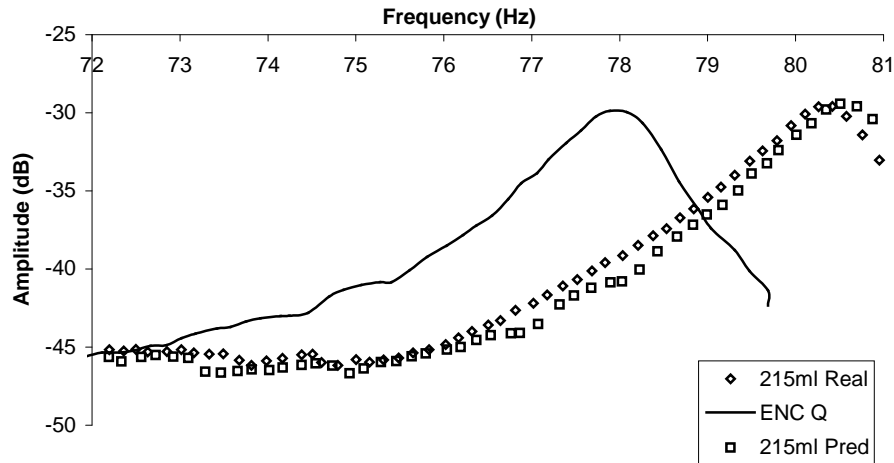


Figure 4.4.26 VCR with dynamic *QPS* of 215mL cube sample showing original (empty), predicted and measured *Q* profiles. VCR resonator has 3.5L chamber with 175mm long, 44mm diameter port.

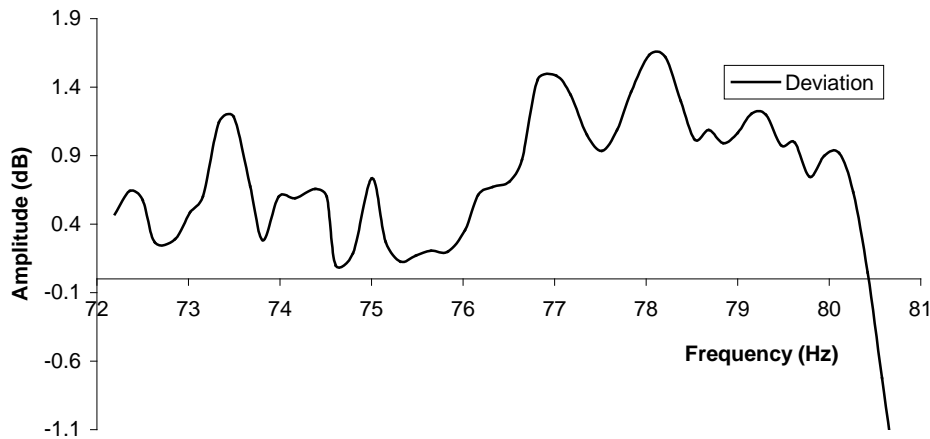


Figure 4.4.27 Plot of amplitude deviation with changing frequency for 215mL cube sample, predicted and actual *Q* profiles. VCR resonator has 3.5L chamber with 175mm long, 44mm diameter port.

4.4.8 Applications – Produce and mineral testing

When testing produce and mineral samples using dynamic *Q* profile shifting (*QPS*), results were generally within $\pm 2\text{mL}$, the only exception being avocados, which were measured to an accuracy of $\pm 3\text{mL}$. Each sample type required an appropriate offset and/or curve fit to allow for their characteristic texture, surface hardness and acoustic diffraction properties. When the sample size variation was less than 20mL from the smallest to largest, only an offset value was required, Figure 4.4.28. A calibration curve was required for samples having a larger range of sizes such as the greywacke, schist and potatoes.

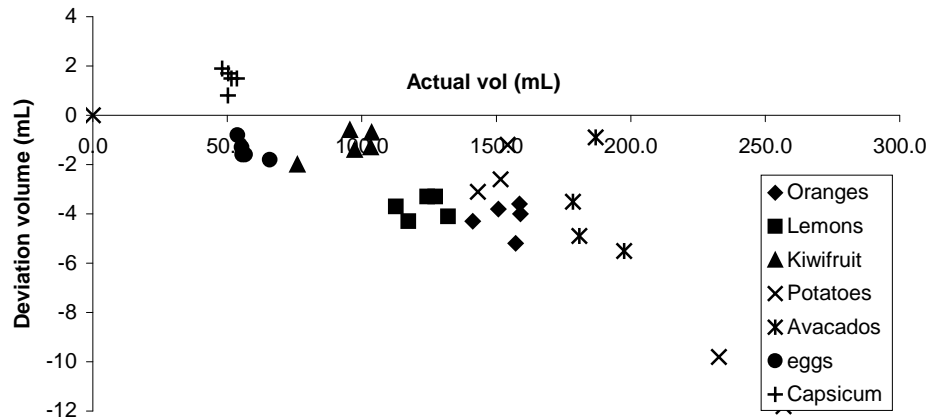


Figure 4.4.28 Produce tests displaying the deviation of the predicted volume from the actual volume. VCR resonator has 3.5L chamber with 175mm long, 44mm diameter port.

Oranges and lemons had comparable behaviour, having similar skin attributes and required a single offset value to measure their volumes to within ± 2 mL, Figure 4.4.28. Kiwifruit having a hairy surface and no pithy skin behaved slightly differently to the citrus samples and required only a small offset value to maintain volume measurements to within 1 mL. Potatoes had a size variation of over 100 mL from smallest to largest and when second order curve fitting was used accuracy was within ± 2 mL. Generally, the softer produce samples tended to have their volume under predicted.

The greywacke and capsicums were the only sample types demonstrating consistent over prediction in volume. Schist samples had volume deviations similar to potato samples, Figures 4.4.28 and 4.4.29. To the authors knowledge there is no published information on acoustic scattering/absorption caused by minerals or agricultural produce, and as such is a further area for investigation. However, it may be anticipated the combination of scattering and elastic properties of the skin/surface will be significant.

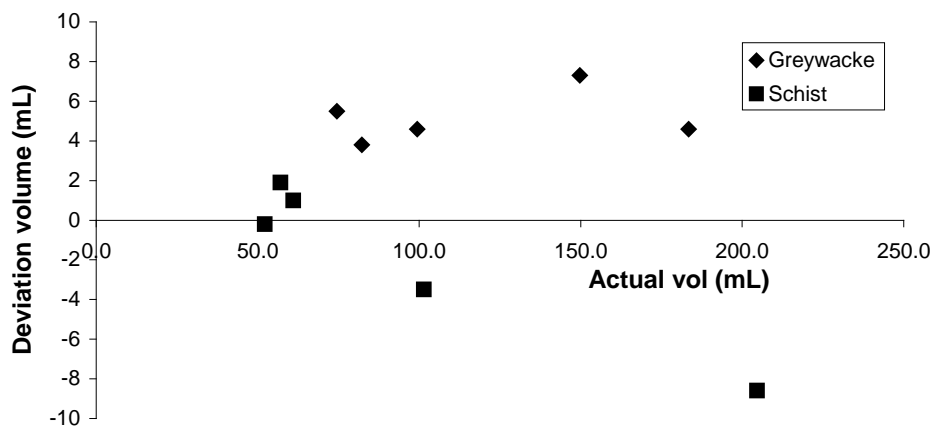


Figure 4.4.29 Mineral tests displaying parabolic deviation of greywacke and linear deviation of schist samples. VCR resonator has 3.5L chamber with 175mm long, 44mm diameter port.

Significant differences were seen between the measurements on the smooth greywacke samples and the schist samples. With appropriate curve fitting both the greywacke and schist samples could be measured to within 1mL over the size ranges tested. The greywacke samples could be characterised by second order over prediction, Figure 4.4.29, whereas the schist sample showed an almost linear under prediction with increasing sample volume.

The mineral, orange and kiwifruit samples were measured again using the resonant hunting method described in Chapter 2. The *VCR* was used in order to give a general comparison between the two volume measurement systems, Figure 4.4.30. The traditional frequency scanning technique was used with a chamber volume of 3.5L, identical to the *QPS* chamber volume. Under prediction was observed for the schist, kiwifruit and orange samples and over prediction for the greywacke samples. These results mimic those gained using *QPS* indicating consistent trends between the two systems. Accuracy using frequency scanning was $\pm 2\text{mL}$ for all the samples when used with appropriate offsets/curve fitting. The measurement accuracy for the frequency scanning method could be increased by selecting a smaller chamber to improve the sample to chamber volume ratio.

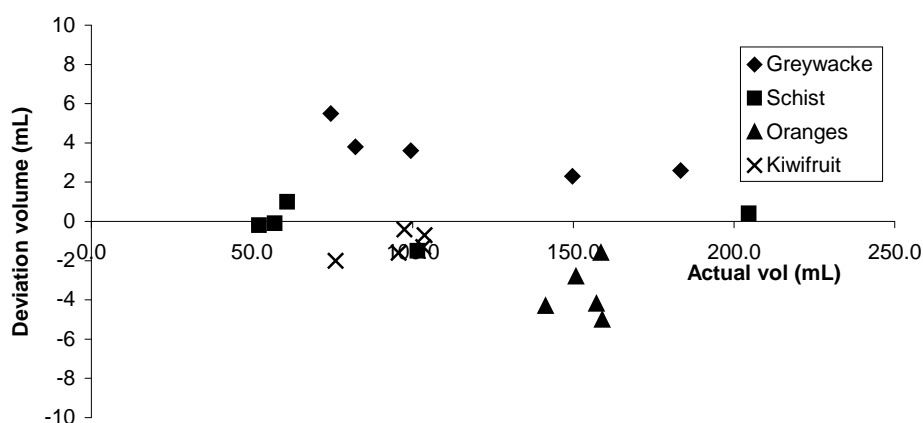


Figure 4.4.30 Comparison of two mineral sample types and two produce sample types as measured in *VCR* with 3.5L chamber volume.

When the variable chamber resonator (*VCR*) chamber volume was reduced to 2L the volume accuracy for the greywacke and schist samples could be maintained to within $\pm 1\text{mL}$, Figure 4.4.31. These results are consistent with trends seen in previous results using the Perspex resonators where accuracy was a function of chamber size. Tests on produce are not presented, as the timeframe was greater than three days between data gathered for tests using the smaller *VCR* chamber size. This time delay between measurements meant the produce sample properties were not necessarily the same as those at the time of earlier testing (i.e. Changes in hardness and density due to maturation). However the greywacke and schist results are indicative of what had been observed in earlier parts of this investigation for a smaller chamber size.

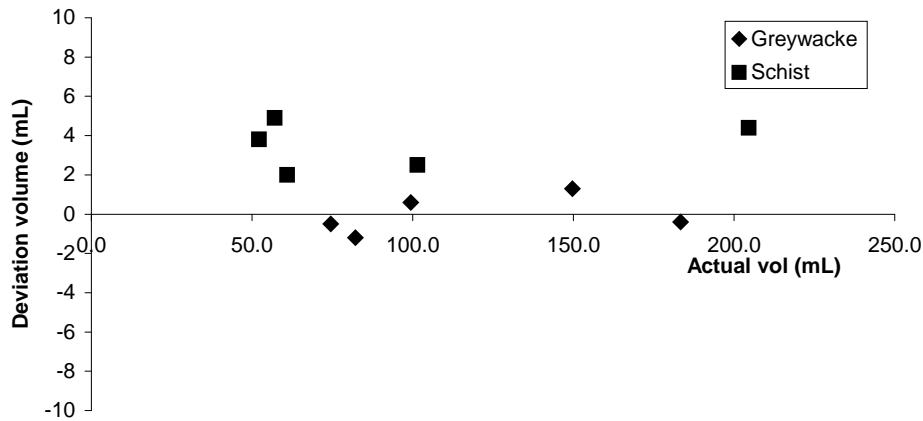


Figure 4.4.31 Greywacke and schist samples as measured in VCR with chamber volume of 2L with low deviation in volume measurement.

In preliminary produce testing four grapefruit volumes were measured using both *QPS* and frequency scanning (results not presented). Of these, one had a significantly different density value, approximately 60g/cm^3 less than the others. Upon cutting open this sample it was found it had a void space of between 2-5% by volume. This result suggests the accuracy of this system may be sufficient to sort samples with hidden void spaces. Produce having an internal cavity, as may occur with capsicums and apples, represents another potential use for either *QPS* or frequency scanning measurements. A puncture between the internal cavity and the external surface will give a highly aberrant volume measurement, resulting in a density error when incorporated with the sample's weight.

Tests with golf ball sized hollow plastic balls with puncture hole sizes of 1mm and 2mm gave volume results of approximately 50% and 10% of their non-punctured volume respectively. This is consistent with part of the internal space being 'visible' to the driving frequency within the chamber. The amount of coupling between the inside of the ball to the outside is a function of the puncture hole diameter. The transition for these samples occurred at the 1-2mm range, which is consistent with observations of boundary layer penetration dependencies (See also Appendix A, Section 9).

4.5 Discussion

4.5.1 Phase shift technique

The phase shift method may prove useful in port chamber configurations with a larger port radius. This would allow an optimisation of port radius to sample diameter. Improved accuracy and a larger phase shift can be gained when there is an appropriately matched object to port ratio. A careful examination of phase shift to object size will be needed. The phase shift for the largest object must be as close to, but less than 90 degrees to make the greatest gains in accurate measurement.

Investigation using larger numbers of repeat frequency sampling was able to improve resolution and accuracy to approximately $\pm 3\%$ full-scale chamber fill. However there was an increase measurement time and despite significant gains in accuracy the Q profile shifting method was able to give far superior results. However, this method remains tenable and represents a potential area for future study.

4.5.2 Q profile shifting – Controlled drop

The microphone amplitude tracking method with Q profile shifting (*QPS*) method proved successful with accuracies and repeatability similar to those gained using the resonant hunting method. Using wider, longer ports, improvements could be made that would allow larger samples to be tested and superior resonant peak amplitude profiles gained.

Tests were made on the time needed in the chamber's central region for a required accuracy as objects traversed the chamber. If the central region is made large then the height of the chamber must increase in size accordingly. The problem of pressure differentials within the chamber then arises when the length of the chamber starts to approach $\frac{1}{4}$ wavelength of the resonant frequency.

Panton and Miller (1975) noted the pressure difference from the top of the chamber to the bottom starts to become significant at as little as $\frac{1}{16}\lambda$, for high accuracy systems. This pressure differential invalidates the use of Helmholtz resonator equations as these equations assume a lumped invariant pressure within the chamber. The methods for non-lumped pressure require the chamber to be calculated as a pressure continuum. Further details can be found in Selamet and Lee (2003) investigating non-linear effects within the chamber.

For small samples, causing only a slight frequency shift, accuracy is compromised due to correspondingly small changes in amplitude about the resonant peak. As the object size increases the changes in microphone amplitude per millilitre become greater and more linear. Therefore, it is more practical to use a driving frequency either higher or lower than the resonant frequency. Consistent volume uncertainties can be achieved if the linear portion of the resonant curve is used to predict new resonant frequencies.

In a similar way, it maybe possible to use a higher driving frequency. For large volume resonators a benefit may be had in using driving frequencies higher than the resonant frequency. For large resonators, in the cubic metre range, resonant frequencies maybe in the 10Hz to 30Hz range, far too low to be practical using

standard loudspeakers. But this may be avoided by using a higher driving frequency, far to the right of the resonant peak.

The maximum usable range of the resonator will be determined by the Q factor. The steeper the Q factor the less the usable range, but the better the resolvability of sample size. Either side of the resonant peak a 'dead' region exists for which the resonator looks like an acoustic barrier to the driving frequency. For this investigation this occurred at signal levels less than -50dB.

Microphone signal data contained large amplitude *horns* for a sample moving through the chamber (See Figure 4.4.5). These were largest for sample that had a cross sectional area close to that of the port area. The size of the *horns* was independent of the descent speed. The likely cause is blocking of the moving mass of air at the port exit, within the chamber, as seen in the chamber mapping experiments of Chapter 3, Section 3.4.9, Figure 3.4.32. It is therefore necessary to have a port area approximately twice the sample's cross sectional area. Doing so will enlarge the centre measurement region, minimise the horns and allow the fastest possible decent speed.

The typical time taken in making a Q profile shifted measurement is approximately three seconds. This is a substantial decrease in the time when compared to more than 40 seconds to make a similarly accurate measurement using the resonant hunting method. However, a restriction in sample size exists; this limits the maximum size of a sample to what can be fitted through the port entrance and exit.

Two alternate methods for measuring volume remain untested, but may be viable. The first using the transition time for the sample to traverse the port and second the change in microphone signal level observed as the object passes through the port. Both these methods rely on the sample being roughly spherical. For each method the relationship would need to be modelled. These two methods may also be suitable for free falling samples.

4.5.3 Q profile shifting – Free falling sample

Free fall measurements using the Q profile shifting method were unsuccessful, but did reveal sufficient differences between samples to warrant future investigation. No plateau region was seen, mid chamber, in the free fall data. This indicated that insufficient repeat cycles were gathered at the driving frequency. It may be possible to modify existing software to reinterpret the profile data, but this would require extensive investigation with careful consideration given to factors likely to affect interaction between sample and port.

A measurement region does exist with a limited number of data points. By performing a numerical integration on the perturbation there may be sufficient data for a volume measurement. Whether this can be further refined could be an area for future investigation. However, refinements in acquisition would need to be conducted to establish its plausibility. Alternatively, a far higher driving frequency may give more cycles in the central region within the chamber. This would have to be considered carefully as higher frequencies cause more significant pressure differentials within the chamber and port.

4.5.4 Environmental normalisation curve (ENC)

In calibrating the microphones (See Appendix D, Section 3) it was possible to calculate pressures in the port and chamber, even though these were not directly relevant to any particular part of the investigation. But, from these calibrations a fifty-fold increase in pressure was measured between the ambient level and the chamber for a Q factor of approximately sixty. This can be contrasted to a pressure increased of only ten in the port at this Q factor.

The PCB103A microphone's calculated sensitivity value is dependant on the reference sound measurement device used and the stability of environmental effects. Using an environmental normalisation curve profile was able to remove deviations caused by loudspeaker, diffraction and reflection, thereby eliminating one of two possible sources of error in sensitivity calculations (the other being the sound meter calibration). When this was undertaken a 1V peak step change in signal level gave 3dB (± 0.1 dB) signal change in measured sound pressure level by both the sound meter and the PCB microphone. This similarity in results between the microphone and the sound meter allowed subsequent experimental procedures to be conducted with objective sound pressure level readings.

Because the resonant system in this investigation is in an open environment it is susceptible to external anomalous effects as mentioned previously, loudspeaker, diffraction and reflection. The usual solution is to couple the resonator to a zero impedance tube (anechoic termination) and loudspeaker combination (Selamet *et al.*, 1995), but this induces problems such as port and tube coupling, which create difficulties greater than an uncoupled system.

Successful negation of the environmental factors was accomplished using an environmental normalisation curve (ENC) in which environmental profiles are superimposed with reverse frequency amplitudes onto Q profiles. This was able to give environmental free Q profiles for resonator configurations. The validity of this method was proved when the driving frequency amplitude was superimposed with the ENC profile and compared to a post-processed Q profile. Both Q profiles were found to be nearly identical, one created dynamically in real time and the other through post-processing.

A non-repeatable ENC region was found over the frequency range 60Hz to 100Hz. Even when the temperature was invariant, repeat ENC profiles were found to change significantly over this frequency range. The loudspeaker is the likely cause, as this range is close to its natural resonant frequency (~ 68 Hz), where the loudspeaker is most unstable. An environmental linear temperature change was also observed. This was only slight (~ 0.07 Hz/ $^{\circ}$ C), but significant in accurately applying an ENC profile to a Q profile. To counter this there are two potential solutions 1) use a loud speaker capable of controlled lower frequencies or 2) implement a shorter port on the VCR to raise the empty resonant frequency. In future work it is likely a shorter port will be used.

Resonant peak amplitude was shown to fluctuate at various chamber fill levels using water. Non-linearities were evident, even when a flat frequency response curve was presented to the resonant system. This limits the predictable behaviour to fill levels of less than $\frac{1}{6}$ full-scale fill. Q factor slope variation started to become significant at $\frac{1}{3}$

full-scale fill. Therefore, the *QPS* method will be restricted by these considerations unless a repeatable and predictable Q factor deviation function can be derived through experimental means.

4.5.5 Continuous Q profile shifting technique

The frequency region below 100Hz was found to be unstable with non-repeatable environmental normalisation curves (*ENC*). This necessitated the use of the 51mm port when conducting the majority of the experimental work using continuous Q profile shifting (*QPS*). The 51mm port with 3L chamber resulted in a resonant frequency of approximately 135Hz. This combination was able to give repeatable results for all the sample types tested.

In early experiments, difficulties using the 170mm port and 3L chamber were encountered due to a small glue fracture between the port and flange holding the port to the chamber. This small crack caused the resonant amplitude to vary by as much as 10%, causing large errors in the data. From the calibration of the microphones it was known the peak pressure inside the chamber increases 50 fold during resonance, which explains why such a small fracture was able to affect the resonant amplitude so significantly. This also reinforces the importance of avoiding any air leaks in a resonant system. Effects of small leaks in the port can be compared to the significant changes to resonant behaviour observed by Peat (2008) in his work on perforated ports.

Real time computing limitations represent a restriction in conducting measurements over a large range of sample volumes. The number of variables to be shifted and the quantity of data acquisition processing becomes very large for samples over 10% full-scale fill. Ideally testing would be conducted on a range of samples, approaching $\frac{1}{5}$ full-scale fill. This is the volume where the Q profile starts to deviate significantly to the empty chamber Q profile. The stability and regularity of Q profile is another restriction in *QPS*. The frequency region either side of the resonant peak, making up the Q profile curve, contains a limited range where the profile is stable and repeatable. The higher the Q factor, the less the available range for Q factor shifting. Therefore, there is a trade off between narrow measurement range with high accuracy or reduced accuracy with broad measurement range.

Previous measurements using the *QPS* method with controlled drop and dual port were only able to measure samples capable of passing through the port. This thereby restricted the maximum sample volume to approximately 2% of full-scale fill. At these small volume sizes the Q profile is only shifted a small amount. Therefore, the environmental factors do not adversely affect the measurement and only temperature effects need be incorporated. Increasing the fill factor to 10% necessitated the use of the more advanced software systems described in the methods relating to this procedure.

For the smaller samples, under 220ml in a 3L chamber, the sample geometry did not adversely affect the accuracy of volume measurement. This indicates the sample's inability to reradiate sound compared to that of the chamber. This observation is reinforced when compared to similar observations made with acoustic barriers in Chapter 3, Section 3.4.6. As the sample volume is increased to over 8% of full-scale fill the sample's surface geometry starts to alter the resonant behaviour, changing the

resonant strength. Between 8-10% specific second order correction curves are needed for the given geometry of the sample type.

The accuracy for the continuous *QPS* method was found to be similar to the resonant hunting method, $\pm 0.2\%$ full-scale fill. This equates to a measurement accuracy of $\pm 6\text{ml}$ with a repeatability of $\pm 2\text{ml}$ using a 3L chamber and 51mm long port. Using temperature compensation, the system was stable over the temperature ranges 8°C to 24°C . When the chamber size was reduced to 1L and 2L the accuracy was likewise scaled, and remained at approximately $\pm 0.2\%$ of full-scale fill. The time to make a measurement is theoretically 1 second, but this is not possible when an operator is required to insert/remove a sample. The thermal variation and the change to the *ENC* caused by the moving presence of the operator makes a three second time delay necessary while equilibrium conditions are restored.

4.5.6 Inverted port resonators

Helmholtz resonance was successfully induced using the inverted port resonator with an appropriately chosen port insert. The inverted port resonator was capable of sufficiently high *Q* factors to make volume measurements, approximately $\pm 1\%$ of full-scale fill. However, the *Q* factor is not high enough to make measurements at comparable accuracies to the standard port resonator used in earlier procedures. But, this new and novel approach may have applications in processes requiring interference free resonator configurations with accessible interiors. Additionally, the resonant frequency can be easily changed by the application of a differing port length piece. It may also be feasible to have the port piece at various depths in the chamber ranging from fully removed to flush insertion. This should yield a variable frequency resonator based on the insertion depth, though *Q* factor is likely to be compromised.

4.5.7 Variable chamber resonator (VCR)

The variable chamber resonator (*VCR*) was able to show that a solid body resonator, having very high acoustic impedance, was not able to produce significantly higher *Q* factors to those of the original Perspex™ body resonators. This suggests very little sound is propagated away through the resonator body for either type of resonator configuration. Therefore, the energy losses are strictly those caused by boundary layer acoustic resistance and radiation resistance from the port. A third source of acoustic resistance can occur from energy absorbed in a porous sample as with the granular materials experiments.

It was unclear why larger divergences were apparent in the curve fit calibrations seen in the dynamic *QPS* used for the *VCR* to those observed in the continuous *QPS* data. Some differences could be associated with the disparity in resonator geometries. The Perspex™ resonator has an internal diameter of 140mm, whereas the *VCR* has an internal diameter of 156mm. There was also a difference in port length, 175mm for the *VCR* and 51mm for the Perspex™ resonator. Results suggest resonators with a higher average frequency are less susceptible to sample geometry. However, transmission theory suggests that a lower average frequency should give less divergence, Blackstock (2000).

In both the dynamic and continuous *QPS* techniques the Helmholtz equation used to derive the frequency is for a chamber having no impedance change associated with the inclusion of a sample. Therefore, it is expected that diffraction from sample edges

and impedance changes, due to the sample cross sectional area, should cause roughly the same divergence in each method. The continuous *QPS* technique had the most divergence for the spheres, whereas for the dynamic *QPS* technique it was the movable piston. The piston behaviour should be identical to changes in volume caused by water filling.

Good agreement between real and predicted Q profiles demonstrated the ability of the dynamic *QPS* technique to accurately create Q profiles for small sample sizes (<5% full-scale fill). As the sample size approached 10% of full-scale fill, significant profile deviations started to occur and there was a need for deviation volume curve fitting for the given sample type. For all samples an increase in the Q profile asymmetry was observed with increasing sample size that made large frequency shifting increasingly less accurate. At these larger fills other factors such as changing higher order harmonics and sample interference patterns start to become more dominant, skewing the resonators properties away from the idealised one used to generate the Helmholtz equation.

Anechoic testing of the *VCR* revealed conclusively instabilities in loudspeaker performance for frequency ranges below 100Hz (See Appendix D, Section 3). This will necessitate the use of a shorter port for future use. A shorter port will raise the frequency range into the stable region between 120Hz to 150Hz. At the time of *VCR* design the sub 100Hz instability was not known to be significant, as it would be negated in *ENC* compensation. Only through extensive testing in the continuous *QPS* procedures was the sub 100Hz region found too variable to compensate for. This led to the shorter 51mm port being used for much of the continuous *QPS*.

4.5.8 Applications – Produce and mineral testing

Close grouping of results for all sample types tested suggest the variable chamber resonator (*VCR*) using dynamic Q profile shifting (*QPS*) is a viable measurement technique, capable of sufficient accuracy to be able to sort a range of sample types to within 1% of their true volume ($\pm 0.2\%$ chamber volume). Measurement times are typically between 2-3 seconds and require temperature stability and measurement accuracy of 0.1°C. Temperature compensation is incorporated in the software algorithms, but sudden fluctuations can cause significant measurement errors.

Differences in sample hardness, geometries and morphologies have a considerable effect on the resonator's behaviour. This was seen in deviation volume trends for the various produce and mineral sample types. The regular grouping and trends between like samples indicates the *VCR* using dynamic *QPS* has potential in applications where rapid, medium accuracy volume determination is required. The lack of existing research in this area makes comparisons and analysis difficult and as such highlights the need for a more in-depth investigation on the acoustic properties of produce and minerals samples within a Helmholtz resonator.

The only other known rigorous studies on the effects of solids in a resonant chamber are those by Leung *et al.* (1982) and Barmatz *et al.* (1983). Both performed tests using solid spheres of different sample materials (plastics, aluminium and steel) in a $\frac{1}{2}$ wave resonant cavity. They noticed no appreciable differences in acoustic behaviour for the different sphere materials. This was to be expected, as the acoustic impedance of most solids is at least fifty thousand times that of air. Therefore, impedance coupling would

be expected to be very poor with most of the acoustic energy reflected off the solid by scattering.

The volume deviation in the Q profile with increasing sample size makes the QPS applicable to small sample to chamber volume ratios where the sample does not unduly alter the chamber dynamics. This in turn limits the achievable accuracy, but may be acceptable where speed of measurement is required. Should more accurate measurements be required the VCR 's volume can be readily changed to suit the sample volume and the resonant hunting method used. The traditional frequency scanning method's accuracy is greatest for large sample to chamber volume ratios. In contrast, the QPS accuracy is inversely proportional to the sample size, the smaller the ratio of sample to chamber, the more accurate the measurement.

Measurement times are typically 30 to 40 seconds using resonant hunting. This can be significantly improved upon if the sample volume is already roughly known. For example if kiwifruit were to be sorted they could be weighed first and their volumes calculated based on a kiwifruit's typical average density. The resonator could then perform a narrow sweep based on a known volume range and temperature. This method could reduce the scanning time to between 10 and 15 seconds, dependent on the density range of the sample type.

Both QPS and frequency scanning techniques are sufficiently sensitive to distinguish hidden void spaces larger than approximately 2% of the sample volume, as might be present in citrus fruits, apples and some mineral samples. It is also able to detect punctured samples, as may occur with capsicums and apples. A puncture was found to give highly aberrant volume measurements due to acoustic resistance between the internal cavity and the exterior. The cause was consistent with calculations for the boundary layer dimensions given the resonator configuration.

Chapter 5

Conclusions and recommendations

5.1 Conclusions

The aims of this investigation were met by the successful measurement of volume for specific liquid, solid and particulate matter to a high accuracy. It was established that the accuracy was a function of the resonator chamber volume, for tested volumes between 1L and 3.5L. Two distinct and new methods were developed for this investigation: 1) the resonant hunting technique and 2) the Q profile shifting technique.

Traditional frequency scanning methods were found to be slow. To improve this, a resonant hunting technique was developed enabling a reduction in measurement times to approximately 40 seconds with an accuracy of $\pm 0.1\%$ of the chamber volume. It was found that acoustic absorption in the chamber bed material reduced the achievable accuracy when measuring the volume of particulates.

A novel approach using Q profile shifting (*QPS*) was tested and found to be successful in volume measurements on liquids and solids. The accuracy for *QPS* was similar to the resonant hunting method. The *QPS* method was further improved using environmental sound level compensation techniques and temperature drift compensation. The *QPS* method was able to reduce measurement times by a factor of ten - approximately 3 seconds - at the expense of reducing the maximum sample-to-chamber fill ratio of less than 15%.

5.1.1 Characterising the fabricated resonators

A resonant hunting algorithm was developed to allow resonant frequencies to be determined more rapidly than traditional frequency sweep methods. A short burst of pink noise (random frequencies at equal power) is applied that allows approximate identification of the resonant frequency. This was followed by two short frequency sweeps (chirps) over a narrow range to locate the resonant frequency to within $\pm 0.005\text{Hz}$. This process reduced measurement time to around 40 seconds.

Environmental acoustics significantly alter the incident sound pressure level at the port of an uncoupled Helmholtz resonator. Therefore, it is recommended to use a dedicated anechoic chamber to house future systems that do not incorporate environmental normalisation curves.

Flange factors for determining the port length extension were found experimentally to be 1.375 for both the asymmetric 170mm port and 51mm port with a radius of 22mm mounted on a 3L chamber. In these instances, for an un-flanged port, the flange factor was frequency and port length independent. Therefore, the un-flanged factor was a function of port radius only. When flanging material was added to the exterior port (to a maximum ratio of approximately 8:1) the flange factor was found to be a function of the port length.

5.1.2 Repeatability of measurements using resonators

Using a standard 3L resonant chamber repeatability of measurement was better than $\pm 1\text{mL}$, provided chamber disassembling is not required. Uncertainty increased to $\pm 3\text{mL}$ when testing objects requiring chamber disassembly. Future resonators need to eliminate assembly/disassembly O-ring compression uncertainties.

Significant discrepancies were found in calculated Q factor values when compared to measured Q factors. It is believed this is due to large thermal and viscous losses occurring at higher sinusoidal velocities at resonance that are not accounted for in standard theoretical Q factor calculations.

5.1.3 Temperature effects

Temperature measurement and compensation is essential for high accuracy measurements. Temperature compensation was in part responsible for the high repeatability of measurements despite temperature changes of up to sixteen degrees Celsius over the course of this investigation.

Using a standard theoretical relationship for the sound of sound based on temperature results in a linear value of 0.587m/s/°C over the temperature range used in this investigation. When this value was indirectly measured by experiment using the Helmholtz equation it was found to be 0.534m/s/°C. The resulting extra temperature correction being a variable β times c . The beta term is responsible for other temperature sensitive variables in the Helmholtz equation. These include the length extension and the small signal approximations that are negated in lumped parameter analysis.

5.1.4 Calibrating the asymmetric single port resonator

Appropriate calibration curve fitting was required when either solid samples or water-filling displacement occurred within the resonant chamber. All chamber displacements caused second order volume deviation in calculations. With second order compensation the Helmholtz resonance equation provides a method for measuring to an accuracy of better than $\pm 0.1\%$ of full-scale fill volume of liquids, solids and granular materials larger than 15mm diameter, placed within a suitably designed chamber.

5.1.5 Effects of port symmetry

A symmetric configuration having two un-flanged port ends had significant scatter in the results when calibration was attempted using water at various fill levels. The un-flanged symmetric resonator was not able to give as accurate results. The limited filling potential and high scatter make the symmetric resonator inappropriate for high accuracy volume measurement.

5.1.6 Effects of sample irregularities

Results from testing spherical and cubic samples in a 3L chamber showed a rapid, almost exponential rise, in over prediction at a threshold sample size. This trend was not seen in the 1L or 2L configurations. Despite this, corrective curve fitting was applied to the deviation volume and an accuracy of $\pm 0.1\%$ of full-scale fill was maintained.

Acoustic barriers were formed using a number of movable flat disks within the resonant chamber. When a disk's area became larger than 20% of the chamber area its surface area was found to significantly alter the resonant frequency. Additionally, changes were also observed in the resonant frequency when any of the disks were within the top 15% of the chamber surface. The height at which the area of a disk affects the resonant frequency was found to be a function of the disk area. Hence, the

larger the area of the disk the lower the height at which it starts to alter the resonant frequency.

The effect on frequency caused by the disks was more pronounced than any of the solids tested, effectively partitioning the chamber. Therefore, the bounded volume inferred from disk height data represents the worst-case impedance effects a sample could have.

5.1.7 Measurement of granular materials

For collections of particles, whose average particle diameters are between 1mm and 15mm, accuracy can be maintained to within $\pm 0.5\%$ of full-scale fill. Particles having sizes larger than 15mm diameter are capable of being measured at accuracies similar to individual solid samples ($\pm 0.1\%$ of full scale fill)

When the measured average particle diameter drops below 1mm the boundary layer effects result in dominant thermal and viscous forces. This limits sound penetration into the bulk material; hence measurements start to become indicative of bulk volume rather than particle volume.

Measurements of particles with diameters less than 1mm also show significant resonant peak broadening. Energy absorption by these small particles limits measurements of fill ratios to less than 50%. Accuracies of approximately $\pm 1\%$ of full-scale volume are achievable in the range where measurements can be made. Appropriate curve fitting is required for all granular materials. The coefficients required are readily found through experiment using the given material.

5.1.8 Effects of air leaks on resonant frequency and Q factor

Air leaks in a Helmholtz resonator cause significant changes to the resonant behaviour. It was found that even a small hole resulted a large reduction in Q factor and caused resonant peak broadening. In instances of multiple air leaks distinct relationships were observed in resonant frequency and Q factor. Resonant frequency increased linearly with increased number of holes whereas Q factor reduced by a logarithmic factor based on hole size and number.

A far more pronounced effect on frequency was observed when a single air leak having a variable size was made the subject of investigation. The larger boundary layer effect for an increase in air-leak size caused the Q factor to drop rapidly from a no leak value of 60 to a minimum of 18 for a 6mm diameter hole. Air-leaks larger than 6mm allowed the air-leak to act as a secondary port. The pinch off in the hole, caused by the boundary layer, was unable to restrict bulk airflow through the hole over a certain diameter.

5.1.9 Effects of sample position on volume measurements

Mapping of the chamber showed that an object placed in the immediate vicinity of the port greatly altered the resonant frequency. This included obscuring any part of the internal flange, which altered the planar point source assumption in volume prediction calculations.

Moving a sample through the chamber lengthwise revealed that the port's moving mass of air penetrates deeply into the chamber, three times greater than the theoretical

length extension suggests. However, this length extension ‘tail’ does not significantly alter volume prediction. Generally though, samples should be placed in the centre of the chamber for volume measurements with a dual port resonator and at the base for a single port resonator.

5.1.10 Controlled decent and free falling sample using a dual-port resonator

Comparable accuracy was achieved for a 3L dual port resonator, when using microphone signal attenuation information with Q profile shifting (*QPS*). This new method makes predictions of resonant frequency based on amplitude changes with temperature compensation. A significant advantage is a near instantaneous volume measurement. Only one calibration curve is needed and all subsequent measurements are made from this. Temperature compensation allowed for temperature stability over changes greater than 10°C. The maximum controlled drop speed was found to be approximately 100mm/s in order to gather sufficient data points for analysis.

Free fall measurements were not possible as there was a general lack of data in the critical region required to interpret either changing frequency or amplitude. Sufficient differences in signal were seen in amplitude variation to warrant future investigation into new methods. Phase shifting information represents another alternative that could yield potentially useful results. However, phase resolution information is not yet adequate.

5.1.11 Environmental normalisation curve (ENC)

An acoustical equalisation procedure was developed to allow removal of unwanted environmental (diffraction/reflection) and loudspeaker components that interfere with Q profile analysis. This method was applied to experimental work in Chapter 4. An Environmental normalisation curve (*ENC*) method was essential to allow measurement of samples larger than 2% of full-scale chamber fill using Q profile Shifting. At over 2% the environmental affects were found to be increasingly non-linear. The *ENC* profile could be post fitted to existing data or used in real time signal generation to produce flat ($\pm 0.4\text{dB}$) frequency response curves.

5.1.12 Continuous Q profile shifting technique

A continuous volume measurement system was developed using Q profile shifting techniques developed earlier and environmental normalisation methods coupled with empirically derived flange factors and temperature factors for the speed of sound. To provide additional accuracy linear interpolation was used on normalised Q profiles having a large number of data points.

The new method allowed samples to be continuously added and removed from a resonant chamber in which dynamic volume measurements could be made. Measurement time was between 1-3 seconds depending on the stability of the environment. Accuracy was similar to the traditional frequency scanning method and remains constant for up or down scaling of the chamber volume. Using temperature information, the system was able to measure volumes without drift over a range of temperatures from 8-24°C.

Q profiles were found to remain sufficiently regular for fill levels up to $\frac{1}{6}$ full-scale fill. The maximum volume fill level was generally restricted to $\frac{1}{10}$ full-scale fill. Q profiles were also found to remain stable over the range of temperatures measured (8-

24°C). Granular materials cannot be used with *QPS*. Because of their porous natures the samples have an associated acoustic resistance causing attenuation of the resonant peak. This attenuation is indistinguishable from that caused by the inclusion of a sample.

5.1.13 Inverted port resonators

A new design of resonator was investigated incorporating an inverted port. Resonant frequency prediction using traditional theory yielded values within 3% of those measured. Q factors were highly compromised by significant boundary layer effects causing acoustic resistance. Despite this the inverted port resonator could be used for medium accuracy volume measurements requiring no seals and easy access of the chamber.

5.1.14 Variable chamber resonator (VCR)

Initial testing with the *VCR* was able to confirm that further stiffening of the resonator body was not able to raise the Q factor of the system above 60. Q factors for a range of chamber volumes were similar to those observed using the Perspex™ body resonator in earlier experiments. Therefore, energy losses to the system were primarily boundary layer acoustic resistance and radiation resistance.

A number of further improvements in the Q profile shifting algorithms were made to better predict the Q profiles when a volume displacement occurred in the resonant chamber. These included rebuilding the Q profile dynamically as the frequency shift was taking place. The success of this procedure was verified when samples up to 5% of full-scale fill were observed to have standard deviations of less than 0.4dB between predicted Q profiles and real, as measured, Q profiles. When the displacement was increased to 10% the standard deviation increased to approximately 0.8dB.

Accuracy for the *VCR* was compromised to $\pm 0.2\%$ ($\pm 7\text{mL}$) of full-scale fill due to instabilities in the sub 100Hz range over which the *VCR* operated. In future work the port will need to be decreased in length to raise the resonant frequency into the stable region above 120Hz. Loudspeaker instabilities were revealed to be the cause in anechoic testing of the *VCR* and loudspeaker.

5.1.15 Applications – Produce and mineral testing

The variable chamber resonator (*VCR*) demonstrated its practical usefulness in being able to accurately size both produce and mineral solids to within 2mL when using dynamic Q profile shifting and a resonator chamber volume of 3.5L. Similar accuracies were observed using standard frequency scanning techniques. Both techniques are sufficiently accurate to detect hidden void spaces larger than 2% of the sample volume and the presence of a puncture in a sample containing an internal cavity (e.g. a holed capsicum).

The resonant hunting method could be employed for mineral and produce sorting by using the *VCR* with an appropriately chosen chamber volume to sample volume ratio and applying a narrow sweep. However, measurement time would still be between 10-15 seconds. The reduction in sweep time from 40-50 seconds to 10-15 seconds can be gained by knowing the sample weight and average density before a volume measurement is performed. This information would allow a localised sweep to be performed.

Volume measurement accuracy can be increased to ± 1 mL when using a suitably sized chamber volume (2L) and the resonant hunting method, as was found for greywacke and schist samples. This represents an accuracy of $\pm 0.05\%$ for samples having a narrow size range ($< 5\%$ chamber volume). This will increase to $\pm 0.1\%$ for larger size ranges ($> 5\%$ chamber volume).

5.2 Recommendations

A number of areas for further investigation have been identified as being important in the volume measurement of liquids, solids and particulate matter. There is little existing literature referring to these problems. Therefore, these will need to be addressed in order to improve the Helmholtz volume resonant measurement system.

5.2.1 Energy in resonance, improving the Q factor

Further investigation into optimal vibration energy storage in a resonator using non-lumped parameter techniques would increase the potential accuracy. If the Q factors could be enhanced the potential accuracy would likewise be extended, as the resolvability of resonant frequencies would be increased. The accuracy in determining the resonant frequency determines the uncertainty in any given volume measurement.

5.2.2 Thermal heating and temperature inside the resonator

Further temperature investigation needs to be conducted to ascertain the acoustic heating that may be taking place within the chamber and port due to the viscous energy dissipation. To enable this a number of small low mass thermistors or thermocouples need to be implemented in the port and chamber. This further investigation could provide additional information on temperature gradient discrepancies calculated in this study. Additionally humidity should be measured to ascertain its effects on frequency at resonance.

5.2.3 Broadband noise from particle reemission of sound

A more complete understanding of maximum fill ratios for different particle sizes could be gained if the bed depth of granular material in the chamber could be increased. The sound reemission from the particle bed limits the maximum fill ratio for the chamber. At a fill level determined by the average bed particle size the level of reemitted sound becomes larger than the driving sound source. It may be possible to make volume measurements based on either energy absorption or increases in broadband noise.

5.2.4 Effects of particle shape when testing granular materials

Achievable measurement accuracies for different particle types could be increased through better data interpretation, as there is likely to be relationships between granular sample shape, particle size and chamber size. Also investigation of powder dilation needs to be undertaken for aerated systems.

5.2.5 Phase shifting method of measuring sample volume

A larger phase shift would give better resolution in measurement. This could be gained by using a wider port with a smaller chamber than was used in this investigation. Also improvements in phase analysis could be made using more cycles and improved algorithms.

5.2.6 Alternate methods for volume measurements of moving samples

Two methods for measuring volume remain untested, but may be viable. The first using the transition time for the sample to traverse the port and second, the change in microphone signal level observed as the object passes through the port. Both these

methods rely on the sample being roughly spherical. These two methods may also be suitable for free falling samples.

By performing a numerical integration on the microphone signal perturbation there may be sufficient data for a volume measurement. However, refinements in data acquisition would need to be conducted to establish its plausibility. Alternatively a far higher driving frequency may give more cycles in the central region within the chamber. This would have to be considered carefully as higher frequencies cause more significant pressure differentials within the chamber and port.

5.2.7 Measurement of surface hardness and structure

Measurement of produce and minerals samples revealed distinct differences in behaviour based on surface texture, morphology and hardness. The role each plays in changing the acoustic impedance within the chamber will need further investigation.

5.2.8 Energy impulse response

An acoustic impulse method may provide an alternative to the sustained excitation methods used in this investigation. Information on the acoustic impedance within the chamber and hence the volume of the object may be revealed by applying a burst of energy at a given frequency and measuring the decay curve.

Appendix A

Mathematics of acoustics

1. The wave equation

The material that follows has been assembled and integrated into a consistent form the following authors: Kinsler and Frey (1962), Blackstock (2000), Boyce and DiPrima (1997) and Fung (1994). It covers the relevant acoustics fundamentals, boundary value solutions and elements of continuum mechanics.

The continuity, conservation of momentum and the isentropic equation of state are the three equations fundamental for deriving the wave equation. A complete solution would also contain the conservation of energy equation, but is unnecessary here because the body forces such as from gravity have almost no effect at the scale under investigation. Two other forces left out due to their small effects are those from viscosity (See Appendix A, Section 11) and those losses caused by flow. Blackstock (2000) states that these forces are many orders of magnitude smaller than those considered.

For a bounded region the density change of that system must be equal to the mass flow in or out of the region, Equation (1.1), continuity condition.

$$\frac{\partial \rho}{\partial t} + \frac{\partial(\rho u)}{\partial x} = 0 \quad (1.1)$$

where ρ is the density, u is the particle velocity x is the particle position and t the time. This may be expanded out to Equation (1.2) or as (1.3) in Eulerian form. The Eulerian or total material form can be derived by noting that $D\rho/Dt = \partial\rho/\partial t + u\partial\rho/\partial x$ or the total density change with time is equal to the relative density change with time plus the particle velocity multiplied by the change in density with position.

$$\frac{\partial \rho}{\partial t} + \rho \frac{\partial u}{\partial x} + u \frac{\partial \rho}{\partial x} = 0 \quad (1.2)$$

$$\frac{D\rho}{Dt} + \rho \frac{\partial u}{\partial x} = 0 \quad (1.3)$$

Similarly for momentum, the rate of increase in momentum of a closed bounded region must equal the total inflow of momentum plus the total forces acting on that region or in its mathematical form, Equation (1.4).

$$\frac{\partial(\rho u)}{\partial t} + \frac{\partial(\rho u^2)}{\partial x} + \frac{\partial p}{\partial x} = 0 \quad (1.4)$$

Expanding out the partial derivatives gives Equation (1.5).

$$u \frac{\partial \rho}{\partial t} + \rho \frac{\partial u}{\partial t} + u \frac{\partial(\rho u)}{\partial x} + \rho u \frac{\partial u}{\partial x} + \frac{\partial p}{\partial x} = 0 \quad (1.5)$$

By observing that the first and third term are in fact the continuity equation a reduction can be made resulting in Equation (1.6) or in its Eulerian form Equation (1.7).

$$\rho \left[\frac{\partial u}{\partial t} + u \frac{\partial u}{\partial x} \right] + \frac{\partial p}{\partial x} = 0 \quad (1.6)$$

$$\rho \frac{Du}{Dt} + \frac{\partial p}{\partial x} = 0 \quad (1.7)$$

Using the differential relationship between the speed of sound, pressure and density $c^2 = dp/d\rho$ for an isotropic system Equation (1.8) can be derived. The speed of sound becomes proportional to the ratio of molar specific heats (γ), the universal gas constant (R_c), the temperature in Kelvin (T_{emp}) and the molecular mass of the air (M).

$$c_0 = \sqrt{\gamma \frac{p_0}{\rho_0}} = \sqrt{\frac{\gamma R_c T_{emp}}{M}} \quad (1.8)$$

A difficulty arises in trying to resolve the continuity, momentum and isentropic equations, as they are non-linear. A linearisation is possible between the three equations by observing that some terms in these equations are orders of magnitude smaller than others; these are often called small signal approximations (Blackstock, 2000) and are given in Equations (1.9).

$$|\delta\rho| \ll \rho_0 \quad \text{Implies} \quad |p| \ll \rho_0 c_0^2 \quad \text{Implies} \quad |u| \ll c_0 \quad (1.9)$$

With the reduction in complexity brought about by small signal assumptions Equations (1.10) to (1.12) result, where $\delta\rho = \rho - \rho_0$ and $\delta p = p - p_0$.

$$\frac{\partial \delta\rho}{\partial t} + \rho_0 \frac{\partial u}{\partial x} = 0 \quad (1.10)$$

$$\rho_0 \frac{\partial u}{\partial t} + \frac{\partial \delta p}{\partial x} = 0 \quad (1.11)$$

$$\delta p = c_0^2 \delta\rho \quad (1.12)$$

Differentiating the isentropic state Equation (1.12) with respect to time gives Equation (1.13). Then substituting Equation (1.13) into the continuity Equation (1.10) and multiplying by c_0^2 gives Equation (1.14). This can then be differentiated with respect to time to give Equation (1.15). Differentiating the momentum Equation (1.11) with respect to position to give Equation (1.16) and combining with Equation (1.15) results in the classical wave Equation defined by pressure, Equation 1.17.

$$\frac{\partial \delta p}{\partial t} = c_0^2 \frac{\partial \delta\rho}{\partial t} \quad (1.13)$$

$$\frac{\partial \delta p}{\partial t} + c_0^2 \rho_0 \frac{\partial u}{\partial x} = 0 \quad (1.14)$$

$$\frac{\partial^2 \delta p}{\partial t^2} + c_0^2 \rho_0 \frac{\partial^2 u}{\partial x \partial t} = 0 \quad (1.15)$$

$$\rho_0 \frac{\partial^2 u}{\partial t \partial x} + \frac{\partial^2 \delta p}{\partial x^2} = 0 \quad (1.16)$$

$$\frac{\partial^2 \delta p}{\partial t^2} - c_0^2 \frac{\partial^2 \delta p}{\partial x^2} = 0 \quad (1.17)$$

A similar method for deriving the wave equation in terms of particle velocity can be used by differentiating Equation (1.13) with respect to position, the momentum Equation (1.11) with respect to time and combining to give Equation (1.18).

$$\frac{\partial^2 u}{\partial t^2} - c_0^2 \frac{\partial^2 u}{\partial x^2} = 0 \quad (1.18)$$

2. Solutions to the wave equation for Helmholtz resonator

The wave equation is expanded upon to make up the oscillatory conditions existing within the resonator. The second term in Equation (1.18) is zero because the resonator's dimensions are small compared to the wavelength, lumped parameters. Therefore, the velocity does not vary with position within the confines of the chamber. Three extra terms are needed to complete the equation. The mechanical spring force generated by the air trapped in the chamber; the acoustical resistance generated by sound radiated away from the system; and the driving force causing oscillation. Hence, the losses from the system must be equal to the driving force plus the force of oscillation.

The forced mechanical oscillator can be rewritten in mathematical form, Equation 2.1, in which the oscillation is described in terms of position. The first term is Newton's second law of $f=ma$, where $a=d^2x/dt^2$. The term $R_m dx/dt$ represents acoustical energy lost to the system through mechanical and radiation resistance. The third term sx is the restorative spring force and $fe^{i\omega t}$ is the complex driving force. In this form the position is a vector quantity but the solution will be solved for the one-dimensional case only. The partial derivative for position becomes a regular derivative, as the velocity is not changing with position.

$$m \frac{d^2 \bar{x}}{dt^2} + R_m \frac{d \bar{x}}{dt} + s \bar{x} = f e^{i\omega t} \quad (2.1)$$

The mass m is the mass of air in the port, which is equal to $\rho_0 l_p s_p$, the air density times the corrected port length times the CSA of the port. R_m the mechanical resistance generated by acoustic radiation resistance and is defined by $(\rho_0 c k^2 s_p^2)/2\pi$ (See Appendix A, Section 6). The stiffness or restoring force s and is equal to $(\rho_0 c^2 s_p^2)/V$ (See Appendix A, Section 10).

Equation (2.1) is a linear, non-homogeneous, second order differential equation with an undetermined coefficient. The general solution is well known to be of the type $x=Ae^{i\omega t}$, where A is complex (Boyce and DiPrima, 1997). Performing the necessary differentiations and substituting gives Equation (2.2), in which A is directly resolvable as Equation (2.3). Therefore x is expected to be of the form Equation (2.4).

$$(-A\omega^2 m + iA\omega R_m + As)e^{i\omega t} = fe^{i\omega t} \quad (2.2)$$

$$A = \frac{f}{(i\omega R_m + (s - \omega^2 m))} \quad (2.3)$$

$$x = \frac{-ife^{i\omega t}}{\omega(R_m + i(\omega m - s/\omega))} \quad (2.4)$$

The term in the denominator is the mechanical impedance Z_m , Equation (2.5), and contains the real mechanical resistance (R_m) and the imaginary mechanical reactance (X_m). The mechanical reactance is equal to $\omega m - s/\omega$. As a consequence the natural relationship between reactance and resistance can be written as Equation (2.6), the phase angle ϕ between X_m and R_m .

$$Z_m = \sqrt{(R_m^2 + X_m^2)} \quad (2.5)$$

$$Z_m = Z_m e^{i\phi}$$

$$\phi = \text{ArcTan}\left(\frac{X_m}{R_m}\right) \quad (2.6)$$

Therefore, the position can be written in terms of the forcing function, the angular frequency and the mechanical impedance, Equation (2.7). The first derivative of Equation 2.7 with respect to time will give the velocity, Equation (2.8). Equations (2.7a) and (2.8a) are given for the real components.

$$x = \frac{-ife^{i\omega t - \phi}}{\omega Z_m} \quad (2.7)$$

$$x = \frac{f \sin(\omega t - \phi)}{\omega Z_m} \quad (2.7a)$$

$$U_s = \frac{fe^{i\omega t - \phi}}{Z_m} \quad (2.8)$$

$$U_s = \frac{f \cos(\omega t - \phi)}{Z_m} \quad (2.8a)$$

From these relations it can be seen that the maximal position will be $f/\omega Z_m$ and the maximum velocity f/Z_m .

For a resonant system the frequency of oscillation is determined at the point where the reactance vanishes, $X_m=0$ or when $\omega m-s/\omega=0$. Using the definitions for m and s from Equation (2.1), Equation (2.9) can be formed and simplified into Equation (2.10), the classical Helmholtz equation.

$$\omega \rho_0 s_p l_p = \frac{c^2 \rho_0 s_p^2}{\omega V} \quad (2.9)$$

$$\omega = 2\pi f_{req} = c \sqrt{\frac{s_p}{V l_p}} \quad (2.10)$$

3. Mechanical Power and Q factor for a resonator

The instantaneous power (W_{inst}) for a resonator is the product of the real components of the driving forcing ($f \cos(\omega t)$) and the velocity ($f \cos(\omega t - \phi)/Z_m$) resulting in Equation (3.1).

$$W_{inst} = \frac{f^2}{Z_m} \cos(\omega t) \cos(\omega t - \phi) \quad (3.1)$$

The average power will be the power delivered over one complete cycle (T). This is therefore the integral of W_{inst} over T , resulting in Equation (3.2). Noting that $Z_m/R_m = \cos \phi$ from the trigonometric implication Equation (2.6), an alternative form is also shown.

$$W_{avg} = \frac{\int_0^T W_{inst} dt}{T} = \frac{f^2}{2Z_m} \cos \phi = \frac{f^2 R_m}{2Z_m^2} \quad (3.2)$$

The Q factor for a resonant system is then defined by the narrowness of the resonant peak. The narrowness is a direct function of the mechanical resistance, the smaller the mechanical resistance the sharper the peak. So in designing a Helmholtz resonator with a high Q factor the resistance due to viscous losses in the port and acoustic radiation need to be kept as small as possible (See Appendix A, Section 7 and 9).

Mathematically the Q factor is the region bounded by the half power points either side of the resonant frequency. If the resonant frequency is ω and the half power frequencies ω_L and ω_H for low and high respectively, then the Q factor can be represented by Equation (3.3).

$$Q = \frac{\omega}{(\omega_H - \omega_L)} \quad (3.3)$$

At the half power point, Equation (2.5), the mechanical reactance must be equal to the mechanical resistance. Therefore, $X_m = \pm R_m$ and X_m being $\omega m - s/\omega$, Equations (3.4a)

and (3.4b) must be true. Combining Equations (3.4a) and (3.4b) and eliminating s_p gives Equation (3.5).

$$R_m = \omega_H m - \frac{s_p}{\omega_H} \quad (3.4a)$$

$$-R_m = \omega_L m - \frac{s_p}{\omega_L} \quad (3.4b)$$

$$Q = \frac{\omega m}{R_m} \quad (3.5)$$

From Section 6, the mechanical radiation resistance is equal to $(\rho_0 c k^2 s_p^2)/2\pi$ and the mass of air in the port, $\rho_0 l_p s_p$. Therefore, the Q factor for a Helmholtz resonator can be defined by Equation (3.6). Alternatively, ω can be replaced by the classical Helmholtz Equation (2.10).

$$Q = \frac{2\pi l_p}{\omega s_p} = 2\pi \sqrt{\frac{l_p^3 V}{s_p^3}} \quad (3.6)$$

4. Mechanical piston radiator

The sound emitted from the end of the port can be likened to a piston radiator. This behaviour is annexed to transmission of sound within the port (See Appendix A, Section 11) to allow the derivation of radiation impedance in Section 7.

A fundamental platform on which to derive the pressure function for a radiating piston needs to be established to allow an analysis of the piston radiator. The first step is to consider sound pressure and velocity of a spherical radiating surface. A piston moving in a planar surface behaves like a spherical emitting surface so long as $ka \ll 1$ or the wavelength is considerably greater than the radius of the emitting source. This assumption will be used extensively in the following calculations and is true for this investigation.

If a sphere is oscillating with a fundamental velocity amplitude of U_0 then the specific velocity, U_s , of the sphere's surface can be described as $U_s = U_0 \cos(\omega t)$. However, it is more convenient to describe the specific velocity in complex form ($U_s = U_0 e^{i\omega t}$) to allow easy integration in later stages. For the purposes of this investigation the piston will never be in the situation where the piston velocity is greater than the particle velocity of the medium. The particle velocity can be describe by Equation (4.1) in which A is some complex constant and Z_s is the specific impedance of the radiating source of radius a . Equation (4.1) is a general time dependent/position independent solution to the wave Equation (1.23)

$$U_s = \frac{\bar{A}}{a Z_s} e^{\omega t - ka} \quad (4.1)$$

The specific impedance is derived from the solution to the spherical wave equation and is given by Equation (4.2). The angle θ refers to the phase difference between the pressure and the velocity. As the port is open to the atmosphere the phase difference is equal to $\pi/2$. Knowing that $ka \ll 1$ the small angle approximation can then be applied to the exponential term, Equation (4.2a). The small angle approximation can also be used in the denominator of Equation (4.2) where the square root can be effectively removed, Equation (4.2b). Using approximations of Equations (4.2a) and (4.2b), Equation (4.3) can be formed from (4.2).

$$\bar{Z}_s = \frac{\rho_0 c k a}{\sqrt{(1 + k^2 a^2)}} e^{i\theta} \quad (4.2)$$

$$e^{i(\pi/2 + ka)} = \cos(\frac{\pi}{2} + ka) + i \sin(\frac{\pi}{2} + ka) \approx (ka + i) \quad (4.2a)$$

$$\sqrt{(1 + k^2 a^2)} \approx (1 + k^2 a^2) \quad (4.2b)$$

$$\bar{Z}_s = \frac{\rho_0 c k a}{(1 + k^2 a^2)} (ka + i) \quad (4.3)$$

As the particle velocity is equal to the specific velocity U_s , Equation (4.4) can be formed from Equation (4.1). Therefore, the complex constant A must be equal to $U_0 \bar{Z}_s a e^{ika}$. Substituting the specific impedance into Equation (4.4) and solving for A gives Equation (4.5). Again using the small angle approximation of $ka \ll 1$ in the exponential term, Equation (4.5a) leads to Equation (4.6). After cancelling, A can be defined by the primary velocity (U_0) and the radius of the piston (a) Equation (4.7).

$$U_0 e^{i\alpha x} = \frac{\bar{A}}{a \bar{Z}_s} e^{i(\alpha x - ka)} \quad (4.4)$$

$$\bar{A} = \frac{a^2 \rho_0 c k U_0 (ka + i)}{(1 + k^2 a^2)} e^{ika} \quad (4.5)$$

$$e^{ika} = \cos(ka) + i \sin(ka) \approx (1 + ika) \quad (4.5a)$$

$$\bar{A} = \frac{a^2 \rho_0 c k U_0 (ka + i)(1 + ika)}{(1 + k^2 a^2)} \quad (4.6)$$

$$\bar{A} = i a^2 \rho_0 c k U_0 \quad (4.7)$$

The time dependant pressure and velocity for a spherical wave is defined by Equations (4.8) and (4.9). Using the value for A from previous calculation it is now possible to completely define p and u for spherical waves at a distance r .

$$\bar{p} = \frac{\bar{A}}{r} e^{i(\omega t - kr)} = \frac{ia^2 \rho_0 ck U_0}{r} e^{i(\omega t - kr)} \quad (4.8)$$

$$\bar{U}_s = \frac{\bar{A}}{r Z_s} e^{i(\omega t - kr)} = \frac{ia^2 \rho_0 ck U_0}{r Z_s} e^{i(\omega t - kr)} \quad (4.9)$$

The strength Q of the source can be defined as the integral of the dot product of specific velocity (U_s) and the surface element (ds) or $Q = \int U_s \cdot ds$. The strength (Q) will be the surface area multiplied by the specific velocity if the specific velocity is perpendicular to the radiating surface. For a spherical radiator this is $4\pi a^2 U_0$, and $2\pi a^2 U_0$ for a $\frac{1}{2}$ sphere. Using the definition for source strength of a $\frac{1}{2}$ sphere radiator, an equation for the intensity and power can be defined using fundamental Equations (4.8) and (4.9), basic Equations. The result is Equations (4.10) and (4.11) respectively.

$$I = \frac{\rho_0 c}{8} \left(\frac{kQ_s}{\pi a} \right)^2 \quad (4.10)$$

$$W = \frac{\rho_0 c (kQ_s)^2}{4\pi} \quad (4.11)$$

With the definitions of a spherical and $\frac{1}{2}$ spherical radiator complete it is now possible to analyse the pressure at a distance R from a surface element on the piston, Figure 4.1. The differential Equation (4.12) can be constructed using the definition for the pressure in Equation (4.8) and the source strength to assess the infinitesimal change in pressure caused by a surface element on the piston radiator at distance R .

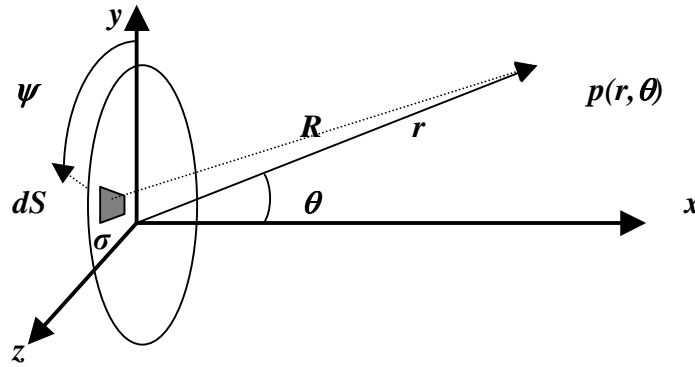


Figure 4.1 Pressure at distance R from surface element caused by a piston radiator.

$$d\bar{p} = \frac{i\rho_0 ck U_0}{2\pi R} e^{i(\omega t - kR)} d\bar{s} \quad (4.12)$$

The distance R can be defined by Equation (4.13). A reduction in complexity is required due to the complexity in continuing to integrate Equation (4.12) with such an exponential term. By using a farfield approximation the difference between r and R is minimal and the phase difference caused by two adjacent surface elements is a

function of the angle and not the distance. The farfield describes the area where the pressure and velocity from a source is effectively even for a given radius and angular region.

A power series expansion of Equation (4.13) is given by Equation (4.14). Only the first two terms are required in the farfield as the first confirms that R is approximately equal to r and the second gives the phase relationship between surface elements. Equation (4.12) can now be rewritten as Equation (4.15) with r in the denominator for the amplitude component and the first two terms from Equation (4.14) in the exponential term to describe the phase relationship.

$$R = \sqrt{(r^2 + \sigma^2 - 2r\sigma\sin\theta\cos\psi)} \quad (4.13)$$

$$R = r - \sigma\sin\theta\cos\psi + \dots\text{etc} \quad (4.14)$$

$$d\bar{p} = \frac{i\rho_0 ckU_0}{2\pi r} e^{i(\alpha t - kr)} e^{ik\sigma\sin\theta\cos\psi} d\bar{s} \quad (4.15)$$

The surface element $d\bar{s}$ is implicitly defined as $\sigma d\sigma d\psi$, using this and integrating both sides of Equation (4.15), Equation (4.16) is formed. Using a standard Bessel function integral, Equation (4.17), the first integral for $d\psi$ can be solved. The second integral is now defined, in which it is possible to use the Bessel identity $xJ_1(x) = \int xJ_0(x)dx$. In the integral defined by Equation (4.18), $x = k\sigma\sin\theta$, therefore $dx = k\sin\theta d\sigma$. Making the necessary substitutions and substituting a for a^2/a gives the general solution, Equation (4.19). The last term in the square bracket is the decay rate from a source and will be used to define the pressure and intensity distributions.

$$\bar{p} = \frac{i\rho_0 ckU_0}{2\pi r} e^{i(\alpha t - kr)} \int_0^a \sigma d\sigma \int_0^{2\pi} e^{ik\sigma\sin\theta\cos\psi} d\psi \quad (4.16)$$

$$2\pi J_0(x) = \int_0^{2\pi} e^{ix\cos\psi} d\psi \quad (4.17)$$

$$2\pi \int_0^a \sigma J_0(k\sigma\sin\theta) d\sigma = 2\pi a^2 \left[\frac{J_1(ka\sin\theta)}{ka\sin\theta} \right] \quad (4.18)$$

$$\bar{p} = \frac{i\rho_0 ckU_0 a^2}{2r} e^{i(\alpha t - kr)} \left[\frac{2J_1(ka\sin\theta)}{ka\sin\theta} \right] \quad (4.19)$$

The component outside the square brackets of Equation (4.19) is the pressure for a hemispherical oscillator defined in Equation (4.8), the only difference being the Bessel directivity component. Therefore, small piston radiators on a planar surface behave as a hemispherical source.

5. Directivity of a piston source

As stated previously, the term in the square brackets of Equations (4.19) defines the directivity of a piston source. At θ equal to zero, the axis pointing directly out from the source, the pressure is largest. The line of equal pressure then decays away by the

amount determined by the first order Bessel relationship. Figure 5.1 shows the pressure decay as a function of x where x is an angular interval. The points of zero crossing are defined by a numerical solution as $ka \sin \theta = 3.83$. Hence, if ka is small and never approaches 3.83 the piston source appears as a hemispherical radiator. If ka is greater or equal to 3.83 then irregular lobes appear like those calculated for the 8-inch speaker source in Appendix C, Section 4.

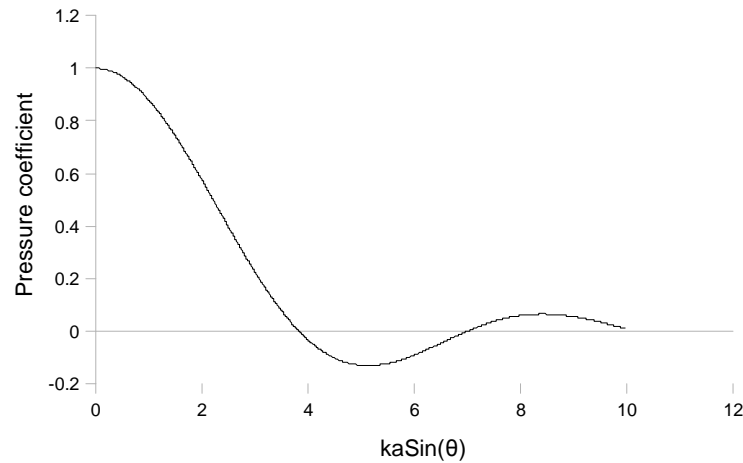


Figure 5.1 Pressure decay from axial direction extending over x , where x is defined as $ka \sin(\theta)$.

Even lobes are 180 degrees out phase with odd lobes, assuming the primary lobe is odd. Also the side lobes are considerably smaller in pressure amplitude than the primary lobe. For a $\frac{1}{2}$ pressure side lobe the intensity is expected to be a quarter, as the intensity is proportional to the pressure squared. The number of lobes will increase and the sound from the piston will become increasingly more directional as the wavelength decreases and becomes comparable with the radius of the piston. This fact is most obvious in Hi-fi systems; the bass from the woofer tends to be omnipresent whereas the high frequencies from the tweeters are highly directional.

The directivity can be analysed in respect to angle where the width of the beam is defined as the $\frac{1}{2}$ power points (-3dB) either side of the main axis of radiation. For this to be true the directivity component must be equal to $1/\sqrt{2}$, Equation (5.1). The analytical solution to Equation (5.1) solving for θ is given by Equation (5.2). Note: the angle is multiplied by two as the directivity function accounts for only the clockwise region from the centre axis, i.e. one $\frac{1}{2}$ power point, the angle between the two $\frac{1}{2}$ power points is therefore twice this.

$$\frac{1}{\sqrt{2}} = \left[\frac{2J_1(ka \sin \theta)}{ka \sin \theta} \right] \quad (5.1)$$

$$\theta_{-3dB} = 2 \text{ArcSin}(1.616 / ka) \quad (5.2)$$

6. Pressure at the piston source

For a radiating piston it is important to know not just the pressure in the farfield and velocity but also the pressure and velocity at the piston source. This allows the calculation of the radiation impedance occurring at the mouth of the port. The calculation for the pressure over the surface of the piston can be conducted in much

the same way as for the piston at a distance R . The difference is any small element ds experiences the force from a remote element ds' and vice versa. This entails a doubling of the integrations required. The first set of integrations is to solve the pressure across the piston and the second set to determine the force generated.

Figure 6.1 shows the piston surface with two arbitrary surface elements ds and ds' separated from the horizontal by an angle θ , the radius of ds' is given by b . To resolve the pressure integral, Equation (4.8) must be solved for R in which R is now the distance between surface elements, Equation (6.1). The surface element ds at a distance R and at an angle θ from the surface element ds' can be written as $ds = R dR d\theta$. The length of R can vary between $0 - 2b \cos \theta$ so this sets the limits of the integral over dR . The angle θ between the horizontal and ds can vary between $-\pi/2$ and $\pi/2$, this sets the limits for the second integral over $d\theta$.

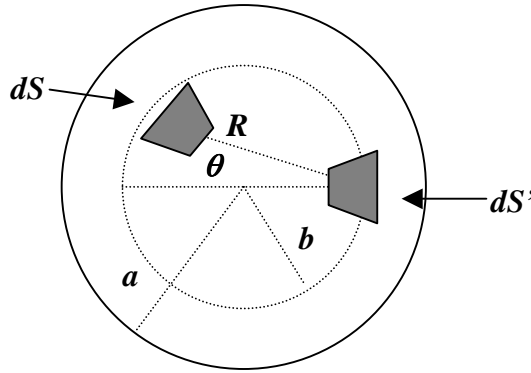


Figure 6.1 Piston face occupied by two arbitrary surface elements ds and ds' and their geometric relations

$$p = \frac{i\rho_0 c k U_0}{2\pi} e^{i\omega t} \int_{-\pi/2}^{\pi/2} d\theta \int_0^{2b \cos \theta} \frac{e^{i(-kR)}}{R} R dR \quad (6.1)$$

The solution to the first integral is given by Equation (6.2) and this now gives rise to the second integral in the form of Equation (6.3), the solution to which can be found by rewriting the integral in its Eulerian complex equivalent, Equation (6.4). Note: the integral must be performed over the region $0 - \pi/2$ and the final solution doubled to allow integral evaluation. The solution can then be found using standard Bessel integrals, the zero order Bessel function and the zero order Struve function. The Struve function is the complex counterpart of the Bessel function. The final form of the pressure at the surface of the radiator is given by Equation (6.7).

$$\frac{1 - e^{-ikb \cos \theta}}{ik} = \int_0^{2b \cos \theta} e^{i(-kR)} dR \quad (6.2)$$

$$p = \frac{\rho_0 c U_0}{2} e^{i\omega t} \left[1 - \frac{2}{\pi} \int_0^{\pi/2} e^{-i2kb \cos \theta} d\theta \right] \quad (6.3)$$

$$p = \frac{\rho_0 c U_0}{2} e^{i\omega t} \left[1 - \frac{2}{\pi} \int_0^{\pi/2} \cos(2kb \cos \theta) d\theta + i \frac{2}{\pi} \int_0^{\pi/2} \sin(2kb \cos \theta) d\theta \right]$$

(6.4)

$$J_0(2kb) = \frac{1}{\pi} \int_0^{\pi/2} \cos(2kb \cos \theta) d\theta \quad (6.5)$$

$$iK_0(2kb) = i \frac{1}{\pi} \int_0^{\pi/2} \sin(2kb \cos \theta) d\theta \quad (6.6)$$

$$p = \frac{\rho_0 c U_0}{2} e^{i\alpha t} [1 - J_0(2kb) + iK_0(2kb)] \quad (6.7)$$

The force exerted by the piston is the integral of pressure generated by all the surface elements. As mentioned previously, for any two surface elements ds and ds' , ds exerts a force on ds' and vice versa, hence the force requires a multiplier of two. The force integral can now be written as Equation (6.8). The radius b is allowed to extend from $0 - a$ and the angle ψ from $0 - 2\pi$. Evaluating left hand integral first gives Equation (6.9) with the addition of a 2π term. Use of the Bessel identity $xJ_1(x) = \int xJ_0(x)dx$ allows the resolution of the Bessel and Struve integrals. The force, Equation (6.10), can now be shown to be derived from the specific velocity ($U_s = U_0 e^{i\omega t}$) and a complex radiation impedance term, Equation (6.11). The real (R_r) and imaginary (X_r) part of the radiation impedance (Z_r) is given in Equations (6.12) and (6.13) respectively. Equations (6.12a) and (6.13a) are given for small values of ka .

$$f = \rho_0 c U_0 e^{i\alpha t} \int_0^{2\pi} d\psi \int_0^a b [1 - J_0(2kb) + iK_0(2kb)] db \quad (6.8)$$

$$f = 2\pi \rho_0 c U_0 e^{i\alpha t} \int_0^a [b - bJ_0(2kb) + ibK_0(2kb)] db \quad (6.9)$$

$$f = a^2 \pi \rho_0 c U_0 e^{i\alpha t} \left[1 - \frac{2J_1(2ka)}{2ka} + \frac{i2K_1(2ka)}{2ka} \right] \quad (6.10)$$

$$Z_r = \frac{f}{U_s} = a^2 \pi \rho_0 c \left[1 - \frac{2J_1(2ka)}{2ka} + \frac{i2K_1(2ka)}{2ka} \right] \quad (6.11)$$

$$R_r = a^2 \pi \rho_0 c \left[1 - \frac{2J_1(2ka)}{2ka} \right] \quad (6.12)$$

$$R_r = a^2 \pi \rho_0 c \frac{[2ka]^2}{8} = \frac{\rho_0 c (s_p k)^2}{2\pi} \quad (6.12a)$$

$$X_r = a^2 \pi \rho_0 c \left[\frac{i2K_1(2ka)}{2ka} \right] \quad (6.13)$$

$$X_r = \frac{8}{3} a^3 \rho_0 c k \quad (6.13a)$$

7. Radiation impedance

The radiation impedance has been defined by Equation (6.11) and as stated contains a real and imaginary component. Figure 7.1 shows the relative magnitude of the resistive and reactive components with increasing value of ka . For $ka < 1$ the reactive component dominates but as the piston becomes a significant part of the wavelength the resistive component is larger. The resistive and reactive components are equal for $ka \approx 2.8$. The first four terms of the power series expansion of the Bessel and Struve functions are also given, demonstrating their validity for $ka < 2.5$. For $ka < 1$ the resistive and reactive components can be approximated by $R_r \approx x^2/8$ and $X_r \approx 4x/3\pi$.

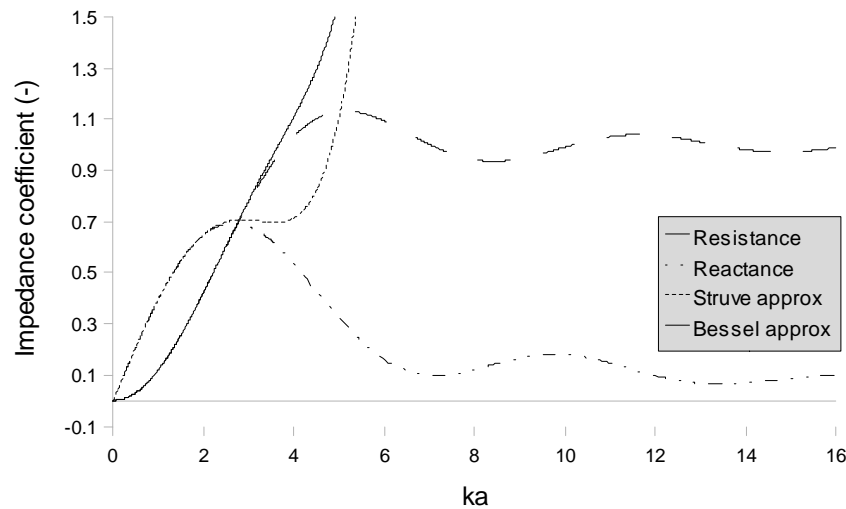


Figure 7.1 The Resistive and reactive coefficients for increasing ka and the first four term approximations for the Bessel and Struve functions.

The force in Equation (6.8) to (6.10) will be negative when considered in the complete definition of the wave equation as the radiation impedance is a restrictive force and acts to oppose the driving force. Adding (6.10) to Equation (2.1) it is now possible to account for the radiation resistance in the form of Equation (7.1). The solution to Equation (7.1) is the same as that for the wave Equation (2.1) and is given by Equation (7.2). The mechanical impedance (Z_m) has already been shown to be the denominator in Equation (7.2), from Section 2. Simplifying Equation (7.2) and solving for U_0 gives Equation (7.3).

$$m \frac{d^2 \bar{x}}{dt^2} + R_m \frac{d\bar{x}}{dt} + s\bar{x} = \bar{f}e^{i\omega t} - \bar{Z}_r U_0 e^{i\omega t} = e^{i\omega t} (\bar{f} - \bar{Z}_r U_0) \quad (7.1)$$

$$U_s = \frac{e^{i\omega t} (\bar{f} - \bar{Z}_r U_0)}{(R_m + i(\omega m - s/\omega))} \quad (7.2)$$

$$U_0 = \frac{\bar{f}}{\bar{Z}_m + \bar{Z}_r} \quad (7.3)$$

Equation (7.3) is identical in form to the mechanical impedance definition of $Z_m = f/U_0$. The total impedance now consists of that caused by mechanical losses in the

port and sound emitted in the form of radiation away from the port. The radiation impedance has the same units as the mechanical impedance (N.m/s) and hence can be added to that of the established mechanical impedance. The effect of the radiation reactance is to add a virtual mass to the mass of air already moving in the port. The additional mass of air is given by a frequency dependant relationship, Equation (7.4), where the angular frequency can be changed for its wave number equivalent ($\omega = kc$). Because ka is small in this investigation the first term in the Struve function expansion can be used for the radiation reactance, $8ka/3\pi$.

$$m_r = \frac{X_r}{\omega} = a^2 \pi \rho_0 c \cdot \frac{8ka}{3\pi} \cdot \frac{1}{kc} = \frac{8}{3} a^3 \rho_0 \quad (7.4)$$

This mass of air must be equal to the mass of air contained in a cylinder of cross sectional area equal to the port cross sectional area ($\rho_0 \Delta l \pi a^2$). Hence, the equivalence Equation (7.5) can be generated that can then be solved for the change in length component Δl . The resulting Equation (7.6) is the extra effective length generated by the radiation reactance that must be added to the physical length of the port. It is important to note that this is for a flanged port as all calculations have assumed a radiating piston in a planar surface.

$$\rho_0 \Delta l \pi a^2 = \frac{8}{3} a^3 \rho_0 \quad (7.5)$$

$$\Delta l = \frac{8a}{3\pi} \quad (7.6)$$

The power transmitted from the end of the port is defined in the usual way for an oscillating radiator as $\frac{1}{2} R_r U_0^2$. The small value of ka means the first term approximation can be used from the radiation resistance Bessel function ($x^2/8$). The result is Equation (7.7).

$$W = \frac{(2ka)^2}{8} \cdot a^2 \pi \rho_0 c \cdot \frac{1}{2} U_0^2 = \frac{s_p \rho_0 c (U_0 k)^2}{4\pi} \quad (7.7)$$

8. Flanged and un-flanged ports

The pressure wave travelling up the port 'sees' an effective impedance of zero where the wave front is no longer bounded by the confines of the port. In standard transmission theory this usually indicates that the wave is reflected and retransmitted back down the port. This is not the case; a small fraction of the sound is radiated away. The radiation reactance and resistance are shown in figure 7.1 and at small values of ka it can be seen that the reactance term dominates. Hence, it is expected that only a small proportion of the sound be transmitted away by a real component of resistance. It is this fact that also determines the efficiency of a piston of radius a to transmit a given frequency of wavelength λ . Accordingly efficient reproduction of low frequencies is impossible for a small piston.

Using the radiation impedance it is possible to calculate its equivalent acoustic impedance Z_a . Acoustic impedance is also defined as the radiation impedance over the surface area squared ($Z_a = Z_r / s_p^2$). The radiation impedance is proportional to the

surface area (s_p) the characteristic impedance ($\rho_0 c$) and $R_r + X_r$ from Equations (6.12) and (6.13). Combining these gives Equation (8.1), from which it is evident that a small value of ka will cause the second term, the reactive component, to dominate. The effective mass of air can be calculated and the length extension again shown to be equal to $8a/3\pi$, in a similar way to Section 7.

$$\bar{Z}_a = \frac{\bar{Z}_r}{s_p^2} = s_p \rho_0 c (R_r + X_r) = \frac{\rho_0 c k}{a} \left[\frac{ka}{8\pi} + \frac{ia}{s_p^2} \left(\frac{8a}{3\pi} \right) \right] \quad (8.1)$$

An analysis of the un-flanged port end is considerably more difficult than its flanged counterpart and is yet to be solved satisfactorily. This is due to the way the plane wave emerges from the port end. In the flanged configuration the sound wave in the port transitions from a plane wave to a spherical wave upon emerging from the port. This change in wave type is accompanied by a complex change in velocity profiles around the sharp edged rim of the port and the value of $8a/3\pi$ is an upper limit rather than a precise value. This result is therefore found using a step change in the wave type rather than a continuum.

In the un-flanged port there are two sharp edge boundaries caused by internal and external port edges. In addition there is no planar surface (flange) for the spherical wave to radiate off. Neither Rayleigh (1896) nor Blackstock (2000) have attempted to analytically solve this complex boundary layer problem as velocity approaches infinity at the inner and outer edges of the port. Both authors suggest an experimental value of between 0.6 and 0.61.

9. Mechanical resistance caused by boundary layer

To establish the mechanical resistance (R_m) caused by the air in the port, the air moving against the surface of the port needs to be evaluated. In acoustical calculations the air is usually considered to be an inviscid fluid (viscosity of zero). This is due to the air's very low viscosity ($\mu=1.78 \times 10^{-5} \text{Ns/m}^2$ at *STP*). At low viscosities the air effectively slips over most surfaces with little shear force occurring between the solid boundary and the air. Therefore, very little frictional losses occur.

A series of calculations is required to quantify the viscous shear forces causing mechanical resistance to steady airflow. It is possible to evaluate the turbulence occurring in the port using the Reynolds number (R_N). The Reynolds number is described by Equation (9.1) and is a dimensionless value that determines the ratio of inertial to viscous forces. It is evident that the low value of viscosity for air in the denominator will cause a large resultant Reynolds number.

$$R_N = \frac{\rho U_0 2a}{\mu} \quad (9.1)$$

A Reynolds number of 2788 is calculated using the typical dimensions for this investigation, a port radius (a) of 0.022m, velocity (U_0) the transverse pressure velocity of 1.88m/s, at 100Hz and 90dB using Equation (2.8a), and an air density (ρ) of 1.2kg/m^3 . Fung (1994) states that with the best available equipment turbulence cannot generally be prevented in systems having a Reynolds number of greater than

40,000 and typically starts at about 10,000. Consequently, the airflow in this work can be considered laminar.

The region adjacent to where two mediums meet is called the boundary layer. It is physically impossible to have two materials in contact and have differing velocities; this is called the no-slip condition. Solutions to continuity equation for a viscous fluid (Blackstock, 2000) show that the boundary layer (no-slip) region typically manifests itself as a parabolic velocity function linking the bulk flow to zero flow at the solid boundary (Figure 9.1).

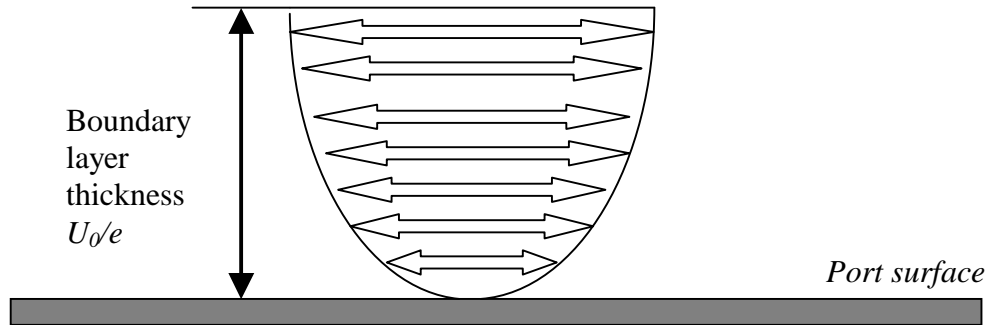


Figure 9.1 Velocity profile from internal port surface boundary. Arrows indicate velocity direction and magnitude. The boundary grows linearly with length.

Two important boundary layer effects exist for an oscillatory plane wave in a tube, one for viscosity and one for thermal losses. Unlike a steady state boundary layer thickness, which increases with distance, an oscillatory pressure wave has a constant thickness defined as U_0/e and is uniform along the surface length. The combinations of viscous and thermal boundary layers form the total boundary layer thickness.

The boundary layer thickness associated with viscosity is defined by the kinematic viscosity (ν) $\nu = \mu/\rho$, and the angular frequency (ω) given by Equation (9.2) (Blackstock, 2000). For a 100Hz frequency in a port the expected viscous boundary layer is 0.217mm. This is consistent with findings by Beranek (1996), in which he suggests a lower limit of 4mm and an upper limit of 66mm for the radius of the port, at 150Hz. The lower limit of the port radius is determined by the viscous properties and the upper limit by the dimensions of the port becoming comparable to the wavelength, given by the equations $0.05/\sqrt{freq}$ and $10/freq$ respectively.

$$BL_{vis} = \sqrt{\frac{2\mu}{\omega\rho}} = \sqrt{\frac{2\nu}{\omega}} \quad (9.2)$$

The thermal boundary layer occurs at a transition from adiabatic behaviour of sound in air to that of isothermal near the port surface (Blackstock, 2000). The moving air, close to the port surface, conducts heat away and represents an additional loss of acoustic energy in the port. The thermal mass of the port, aluminium, is far greater than the air and as such remains at a stable temperature. The energy in the form of sound, changing pressure, is very small and any proportion of this absorbed by the port will cause negligible heating.

The thermal boundary layer can be described by Equation (9.3) (Blackstock, 2000), where Y is the thermal conductivity of air (0.026 W/m.K), C_p the specific heat of air at constant pressure (29.11 J/mol.K). By Using the Prandtl number, relating viscosity and conductivity, given by Equation (9.4), the thermal boundary layer equation can be simplified to a function of the viscous boundary layer. Using the previous viscous boundary layer value of 0.217mm this results in a thermal boundary layer of 1.54mm, considerably larger than the viscous boundary layer.

$$BL_{therm} = \sqrt{\frac{2Y}{\rho\omega C_p}} = \frac{BL_{vis}}{\sqrt{P_r}} \quad (9.3)$$

$$P_r = \frac{\mu C_p}{Y} \quad (9.4)$$

For this reason the boundary layer losses are associated with the frequency and not the sound pressure level. So as the amplitude in the port increases it is expected that the thermal and viscous losses should remain constant. The exception to this is at very high sound pressure levels (Ingard, 1953).

To ascertain the effects of temperature on the Reynolds number a numerical analysis can be undertaken by considering changes to the air viscosity with temperature. Fung derives an air viscosity described by Equation (9.5), where v_{rms} is the root mean squared molecular velocity give by Equation (9.6). Using the ideal gas law the density ρ can be rewritten as Equation (9.7) and the mean free path L_{mfp} as Equation (9.8), Equations (9.6) to (9.8) provided by Halliday *et al.*, 1997. R_c is the universal gas constant, M_{mol} the molar mass, P the nominal pressure, m the mass of air, n the number of moles, N the number of molecules and V the volume of air.

The effect of temperature on density and the mean free path tend to counteract each other leaving only the molecular velocity dependence. Therefore, the air viscosity is proportional to the temperature squared and will have negligible effects over a narrow temperature range as was used in this investigation (8-24°C).

$$\mu = \frac{1}{3} \rho v_{rms} L_{mfp} \quad (9.5)$$

$$v_{rms} = \sqrt{\frac{3R_c T_{emp}}{M}} \quad (9.6)$$

$$\rho = \frac{Pm}{nR_c T_{emp}} \quad (9.7)$$

$$L_{mfp} = \frac{1}{\sqrt{2}\pi 2a(N/V)} \quad (9.8)$$

Therefore the losses in the port caused by the viscous and thermal boundary layer are significant and dominant over those caused by radiation in the form of sound.

Changes in viscosity for the narrow temperature range will have negligible effects on these parameters.

To calculate the radiation losses it is necessary to calculate the sound transmission effects within the port. These include the incident, transmitted and the reflected components. The equations describing these effects can be divided into those in which the dimension of the system are a significant proportion of the wavelength and those that are not. For this investigation the dimensions are considerably smaller than the wavelengths used ($ka < 1$). Further details on the power transmitted from the port can be found in Section 7.

10. Mechanical stiffness caused by an orifice

The mechanical stiffness is the effect of the port on the resonator's ability to pass a moving mass of air in and out of that port. The excess pressure change associated with the change in density caused by the moving mass of air in the port can be represented by Equation (10.1). If the densities are replaced by mass over volume and the mass then cancelled, as there is conservation of mass throughout, Equation (10.2) is derived. In the port $dV = xs_p$, the small change in particle position multiplied by the cross sectional area of the port will be equal to the change in volume, Equation (10.3). Multiplying the pressure by the cross sectional area gives the associated force caused by the stiffness, Equation (10.4). The terms inside the brackets of Equation (10.4) are the stiffness coefficients.

$$p = \rho_0 c^2 \delta \rho / \rho_0 \quad (10.1)$$

$$p = \rho_0 c^2 dV / V \quad (10.2)$$

$$p = (\rho_0 c^2 s_p / V) x \quad (10.3)$$

$$f = (\rho_0 c^2 s_p^2 / V) x \quad (10.4)$$

11. Acoustic transmission effects

Transmission effects must be calculated for any propagated wave encountering a change of system. This includes a medium change or a physical constraint change, both which will be shown to equate to an impedance change. Transmission effects include incident, transmitted and reflected components and are usually complex in nature. The distribution of energy between these three paths will be entirely dependant on the impedance paths as seen by the propagating wave.

The characteristic impedance for any medium is defined as the product of speed of sound through that medium and its density ($Z = \rho_0 c$). From this information the pressures may be calculated for incidence, reflection and transmission. The incident pressure is denoted by p^+ , reflected by p^- and transmitted by p^t . The coefficients of reflection and transmission can be defined as the ratios of these respective pressures. Equations (11.1) and (11.2) define the reflected and transmitted coefficients.

$$R_{reflect} = \frac{p^-}{p^+} \quad (11.1)$$

$$T_{transmit} = \frac{p^t}{p^+} \quad (11.2)$$

For conservation of energy the incident and the reflected pressure must sum to the transmitted pressure, Equation (11.3). Dividing (11.3) by p^+ gives $T_{transmit}=I+R_{reflect}$, the relationship between transmission and reflection. Conservation of energy also requires the particle velocities to balance. Equation (11.4) states that the sum of the incident and reflected particle velocities must equal the transmitted velocity. The superscripts refer to the usual incident, reflected and transmitted particle velocities.

$$p^+ + p^- = p^t \quad (11.3)$$

$$U_s^+ + U_s^- = U_s^t \quad (11.4)$$

Equation (11.3) can be divided through by the characteristic impedance for the mediums each of the waves is propagating through resulting in Equation (11.5). The incident and reflected propagate through Z_1 and the transmitted through Z_2 . Equation (11.5) is then divided through by p^+ and appropriate substitution of the reflected and transmitted coefficients gives Equation (11.6). Solving for $R_{reflect}$ and $T_{transmit}$ respectively gives Equations (11.7) and (11.8), the reflection and transmission coefficients in terms of the impedance for the two mediums.

$$\frac{p^+}{Z_1} + \frac{p^-}{Z_1} = \frac{p^t}{Z_2} \quad (11.5)$$

$$\frac{1}{Z_1} + \frac{R_{reflect}}{Z_1} = \frac{T_{transmit}}{Z_2} \quad (11.6)$$

$$R_{reflect} = \frac{(Z_2 - Z_1)}{(Z_2 + Z_1)} \quad (11.7)$$

$$T_{transmit} = \frac{2Z_2}{(Z_2 + Z_1)} \quad (11.8)$$

From Equations (11.7) and (11.8) it can be seen that the pressure phase relationship between incident and transmitted waves is always the same irrespective of the impedance change. Whereas the pressure phase relationship for the reflected wave is not always the same. Larger secondary impedances retain the incident pressure phase, as $Z_2 - Z_1$ is positive. If $Z_2 - Z_1$ is negative the reflected wave is out of phase by 180 degrees.

It is often more important to know the power that is incident, reflected and transmitted rather than the pressure. By using Equation (8), Basic equations, for the intensity, new reflection and transmission coefficients for the power can be derived ς and τ respectively. The intensities can be used directly as all the surface areas in these instances are identical and therefore cancel. Equations (11.9) and (11.10) show the derivation and reduction. Conservation of energy is obeyed as $\varsigma + \tau = I$.

$$\zeta = \frac{W^-}{W^+} = \frac{I^-}{I^+} = \frac{\left(\frac{p^-}{Z_1}\right)^2}{\left(\frac{p^+}{Z_1}\right)^2} = R_{reflect}^2 = \frac{(Z_2 - Z_1)^2}{(Z_2 + Z_1)^2} \quad (11.9)$$

$$\tau = \frac{W^t}{W^+} = \frac{I^t}{I^+} = \frac{\left(\frac{p^t}{Z_2}\right)^2}{\left(\frac{p^+}{Z_1}\right)^2} = T_{transmit}^2 \frac{Z_1}{Z_2} = \frac{4Z_2Z_1}{(Z_2 + Z_1)^2} \quad (11.10)$$

If the impedance of the second medium is very large, approaching ∞ , the reflected coefficient $R_{reflect}$ approaches 1 and no pressure is transmitted as it is all reflected. If the second impedance is very small, $R_{reflect}$ approaches -1 , a complete out of phase reflection and again no pressure is transmitted into the second medium. When Z_1 equals Z_2 complete transmission occurs and no pressure or energy is reflected back. This represents complete acoustic coupling.

A complete description of the impedance will also include the complex forms of pressure velocity and impedance. It is normal for most of these variables to be frequency dependent and contain reactive components in addition to the purely resistive one. The specific pressure can be defined by some complex oscillatory primary pressure such that $p(x,t) = P(x)e^{i\omega t}$, which must be a part solution to the position independent wave equation, Equation (1.17). Differentiating p twice with respect to time gives Equation (11.11). Placing this into the general wave equation for pressure gives Equation (11.12), where P is a function of x , this is the Helmholtz equation for a one-dimensional system.

$$\frac{d^2(Pe^{i\omega t})}{dt^2} = -k^2 P e^{i\omega t} \quad (11.11)$$

$$\frac{\partial^2 P}{\partial x^2} + k^2 P = 0 \quad (11.12)$$

The solution to Equation (11.12) is that of a standard elliptic partial differential equation and can be solved by separation of variables. The solution of which is given by, Equation (11.13). As the specific velocity is the pressure over the specific impedance U_s can be represented by Equation (11.14). The subscript 1 indicates the primary medium; subscript 2 will be used for the secondary medium. Figure 11.1 shows the general representation of an impedance change for a given driving source. Note: the alpha term is the outward travelling wave as it decreases with distance x and the beta term is the inward travelling wave as it decreases with decreasing distance x . The inward and outward pressure wave are P^+ and P^- respectively where $P^+ = \alpha e^{-ikx}$ and $P^- = \beta e^{ikx}$.

$$P(x) = \alpha e^{-ikx} + \beta e^{ikx} \quad (11.13)$$

$$U_s = \frac{\alpha}{Z_{s1}} e^{-ikx} - \frac{\beta}{Z_{s1}} e^{ikx} \quad (11.14)$$

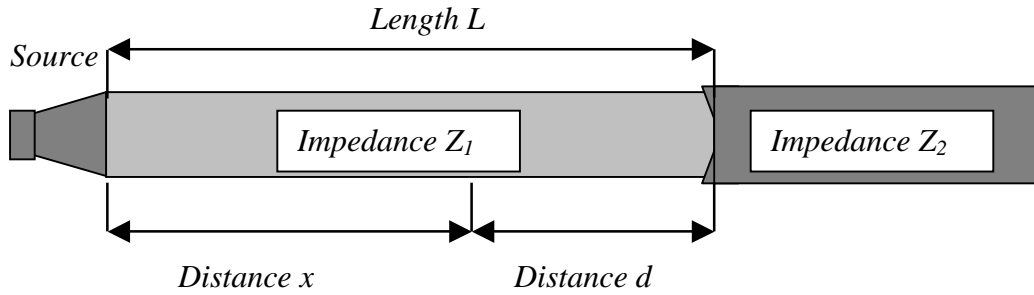


Figure 11.1 Sound source driving into impedance Z_1 which then changes to impedance Z_2 . The distance $d=L-x$ for considering pressure and velocity as a function of the distance from the impedance change.

It is more convenient to know the distance from the medium change than from the source, defined as $d=L-x$. With this in mind Equation (11.13) and (11.14) can be rewritten as Equations (11.15) and (11.16) respectively. The beta term in Equation (11.15) can be multiplied by P^+/P^+ and the pressure reflection coefficient R inserted for P^-/P^+ . Similarly the beta term can be replaced in Equation (11.16).

$$P(d) = \alpha e^{-ikL} e^{ikd} + \beta e^{ikL} e^{-ikd} = P^+ (e^{ikd} + R_{\text{reflect}} e^{-ikd}) \quad (11.15)$$

$$U_s = \frac{\alpha}{Z_{s1}} e^{-ikL} e^{ikd} - \frac{\beta}{Z_{s1}} e^{ikL} e^{-ikd} = \frac{P^+}{Z_{s1}} (e^{ikd} - R_{\text{reflect}} e^{-ikd}) \quad (11.16)$$

$$U_s = U_s^+ (e^{ikd} - R_{\text{reflect}} e^{-ikd}) \quad (11.16a)$$

Equations (11.15) and (11.16) are now defined in terms of the distance from the impedance boundary and both P and U_s are functions of d . Therefore, an impedance as a function of d can be generated, Equation (11.17). At the boundary where $d=0$ the exponential terms vanish and the impedance of the secondary medium can be defined by Equation (11.18), solving for R_{reflect} gives Equation (11.7).

$$Z_s(d) = Z_{s1} \frac{(e^{ikd} + R_{\text{reflect}} e^{-ikd})}{(e^{ikd} - R_{\text{reflect}} e^{-ikd})} \quad (11.17)$$

$$Z_{s2} = Z_{s1} \frac{(1 + R_{\text{reflect}})}{(1 - R_{\text{reflect}})} \quad (11.18)$$

So long as Z_{s1} is not equal to Z_{s2} a standing wave pattern will be generated and is usually defined by the standing wave ratio (SWR). The SWR is the ratio of maximum pressure to minimum pressure ($\text{SWR} = P_{\text{max}}/P_{\text{min}}$). The pressure at any given location is given by Equation 11.15, where the maximum possible pressure is $(1 + R_{\text{reflect}})$ and the minimum $(1 - R_{\text{reflect}})$. Therefore, the SWR can be defined in terms of R_{reflect} , Equation

(11.19) or $R_{reflect}$ in terms of SWR , Equation (11.20). The absolute value for $R_{reflect}$ is used as only the magnitude of the SWR ratio need be considered.

$$SWR = \frac{(1 + |R_{reflect}|)}{(1 - |R_{reflect}|)} \quad (11.19)$$

$$|R_{reflect}| = \frac{(SWR - 1)}{(SWR + 1)} \quad (11.20)$$

Two important transmission cases exist for the Helmholtz resonator, a pressure release tube, port, and a rigid termination, chamber. Both these need to be evaluated to examine the pressure, velocity and impedance occurring in each. The port is terminated into free space so has a reflective coefficient of -1 . The chamber is terminated in a solid end and hence has a reflective coefficient of 1 .

The solution for an open port can be derived using the existing transmission equations. Using Equation (11.15) and combining with the definition for pressure given by $p(x,t) = P(x)e^{i\omega t}$, noting that is $R_{reflect} = -1$ and $d=L-x$, gives Equation (11.21). Expanding out the exponential terms and cancelling gives Equation (11.22). At $x=0$ Equations (11.23) and (11.24) must be true. These can be combined to derive an expression for P^+ , Equation (11.25). A complete interpretation for the pressure can now be formed into Equation (11.26).

$$P(x,t) = P^+ (e^{ik(L-x)} - e^{-ik(L-x)})e^{i\omega t} \quad (11.21)$$

$$P(x,t) = P^+ 2i \sin(k(L-x))e^{i\omega t} \quad (11.22)$$

$$p(0,t) = P_0 e^{i\omega t} \quad (11.23)$$

$$P(0,t) = P^+ 2i \sin(kL)e^{i\omega t} \quad (11.24)$$

$$P^+ = \frac{P_0}{2i \sin(kL)} \quad (11.25)$$

$$P(x,t) = \frac{P_0 \sin(k(L-x))}{\sin(kL)} e^{i\omega t} \quad (11.26)$$

A similar analysis of the velocity is possible starting with Equation (11.16a) in which the substitution $d=L-x$ is made resulting in Equation (11.27). Cancelling the complex trigonometric terms expanded from the complex exponentials gives Equation (11.28). Using the definition for the velocity at $x=0$, Equation (11.29) and combining with (11.28) at $x=0$ leads to Equation (11.30). Equation (11.30) can be placed into (11.28) to form the complete mathematical description of velocity, Equation (11.31).

$$U_s = U_s^+ (e^{ik(L-x)} + e^{-ik(L-x)}) \quad (11.27)$$

$$U_s(x,t) = U_s^+ 2\cos(k(L-x))e^{i\omega t} \quad (11.28)$$

$$U_s(0,t) = U_0 e^{i\omega t} \quad (11.29)$$

$$U_s^+ = \frac{U_0}{2\cos(kL)} \quad (11.30)$$

$$U_s(x,t) = \frac{U_0 \cos(k(L-x))}{\cos(kL)} e^{i\omega t} \quad (11.31)$$

The velocity may also be solved using the small signal form of the conservation of momentum, Equation (11.16). By noting that the first derivative of the pressure with respect to position must equal the first derivative of velocity with respect to time. Using Equation (11.31) this can be expressed by Equation (11.32). Therefore, the integral of Equation (11.32) with respect to time must be the velocity in terms of the primary pressure, Equation (11.33). Substituting in $k=2\pi/\lambda$ and $\omega=2\pi$ and appropriate cancellation then allows a further substitution of the characteristic impedance ($\rho_0 c = Z_1$, from $c = \lambda \text{freq}$). Finally arriving at the specific velocity, Equation (11.34).

$$\frac{d}{dx} \frac{1}{\rho_0} \left[\frac{P_0 \sin(k(L-x))}{\sin(kL)} e^{i\omega t} \right] = \frac{-k P_0 \cos(k(L-x))}{\rho_0 \sin(kL)} e^{i\omega t} \quad (11.32)$$

$$\frac{-k}{\rho_0} \int \left[\frac{P_0 \cos(k(L-x))}{\sin(kL)} e^{i\omega t} \right] dt = \frac{ik P_0 \cos(k(L-x))}{\rho_0 \omega \sin(kL)} e^{i\omega t} \quad (11.33)$$

$$U_s(x,t) = \frac{i P_0 \cos(k(L-x))}{Z_1 \sin(kL)} e^{i\omega t} \quad (11.34)$$

The specific impedance can be calculated by dividing Equations (11.26) by (11.34), the specific pressure over the specific velocity. The result is Equation (11.35), which can be further simplified by changing $L-x$ for d , Equation (11.35a). It may be noted that the impedance is no longer time dependant.

$$Z_{s1}(x) = i Z_1 \tan(k(L-x)) \quad (11.35)$$

$$Z_{s1}(d) = i Z_1 \tan(kd) \quad (11.35a)$$

The specific pressure, velocity and impedance can be calculated in an identical fashion for the rigid termination occurring inside the chamber ($R_{\text{reflect}} = 1$). The time dependant pressure and velocities are given by Equations (11.36) and (11.37) respectively. The time independent impedance is given by Equation (11.38).

$$P(x,t) = \frac{-i Z_1 U_0 \cos(k(L-x))}{\sin(kL)} e^{i\omega t} \quad (11.36)$$

$$U_s(x,t) = \frac{U_0 \sin(k(L-x))}{\sin(kL)} e^{i\omega t} \quad (11.37)$$

$$Z_{s1}(d) = -iZ_1 \cot(kd) \quad (11.38)$$

12. Lumped parameters

If the chamber and port are small compared to the wavelengths that are driving the system and are causing the primary resonance then the system can be broken into its lumped components. This is true for all the exploratory work conducted in this investigation.

The Helmholtz resonator can be approached in terms of the lumped components making up the port and the chamber. The impedance of the port is that of a short open cavity and the chamber a mass spring system. Therefore, by considering the sum of the impedances for the combined system the resonator system can be solved. It must be noted for a resonant system to oscillate, the reactance component of the impedance must be zero at the frequency of oscillation.

For a short open cavity, which is effectively what the port is, the specific impedance is given by Equation (12.1), derived from Section 11 for an open tube. For $k(l_p + \Delta l) \ll 1$ the small angle approximation can be used and tangent function ignored giving Equation (12.2). Using the definition for the characteristic impedance and converting the impedance from that of radiation to acoustic impedance (See Basic Equations (No.5) and (No.6), Equation (12.3) is formed. The sound losses to the environment caused by the radiation impedance are then added using the acoustic impedance of Equation (6.12a). Therefore, the total acoustic impedance generated by the port is given by Equation (12.4).

$$Z_s^{in} = iZ \tan(k(l_p + \Delta l)) \quad (12.1)$$

$$Z_s^{in} = iZ(k(l_p + \Delta l)) \quad (12.2)$$

$$Z_a^{in} = \frac{i\omega\rho_0}{s_p}(l_p + \Delta l) \quad (12.3)$$

$$Z_a^{in} = \frac{i\omega\rho_0}{s_p}(l_p + \Delta l) + \frac{\rho_0 c k^2}{2\pi} \quad (12.4)$$

The acoustic impedance generated by the chamber is then added as an additional lumped component to that of the port. The chamber appears as a closed volume acted upon by a radiating piston source and hence can be represented by Equation (12.5). The specific input impedance to the chamber can be rewritten in the form of Equation (12.6) using the small angle approximation for the tangent function, which is valid for $kl_c \ll 1$ (l_c is the chamber length), and the definition for the characteristic impedance. To find the acoustic impedance the specific impedance is divided by surface area of the port, s_p . The volume V can then be substituted for the product $l_c s_p$ allowing Equation (12.7) to be formed.

$$Z_s^{in} = \frac{-iZ}{\tan(kl_c)} \quad (12.5)$$

$$Z_s^{in} = -\frac{i\rho_0 c^2}{\omega l_c} \quad (12.6)$$

$$Z_a^{in} = -\frac{i\rho_0 c^2}{\omega V} \quad (12.7)$$

The total acoustic impedance can now be equated and as previously stated the reactance at resonance is zero. Hence, Equation (12.8) can be formed and reduced to Equation (12.9); the second term effectively vanishes at the resonant frequency. The classical Helmholtz resonator equation results with appropriate cancelling and rearranging, Equation (12.10).

$$Z_a^{in} = \frac{i\omega\rho_0}{s_p}(l_p + \Delta l) + \frac{\rho_0 c k^2}{2\pi} - \frac{i\rho_0 c^2}{\omega V} \quad (12.8)$$

$$\frac{i\rho_0 c^2}{\omega V} = \frac{i\omega\rho_0}{s_p}(l_p + \Delta l) \quad (12.9)$$

$$\omega = 2\pi f_{req} = c \sqrt{\frac{s_p}{V(l_p + \Delta l)}} \quad (12.10)$$

13. Diffraction from edge effects

A detailed analysis of diffraction is not included. There are a number of assumptions needed to solve even the simplest diffraction cases. This fact renders the results inadequate for the frequencies and dimensions used in this investigation. Even when such assumptions are used the results are only valid in the farfield and only for high frequencies. The general Helmholtz-Kirchhoff integral needs to be solved for pressure in three spatial dimensions and the time dimension, an exercise that would be a detailed investigation unto itself (See Blackstock (2000) for an introduction to diffraction).

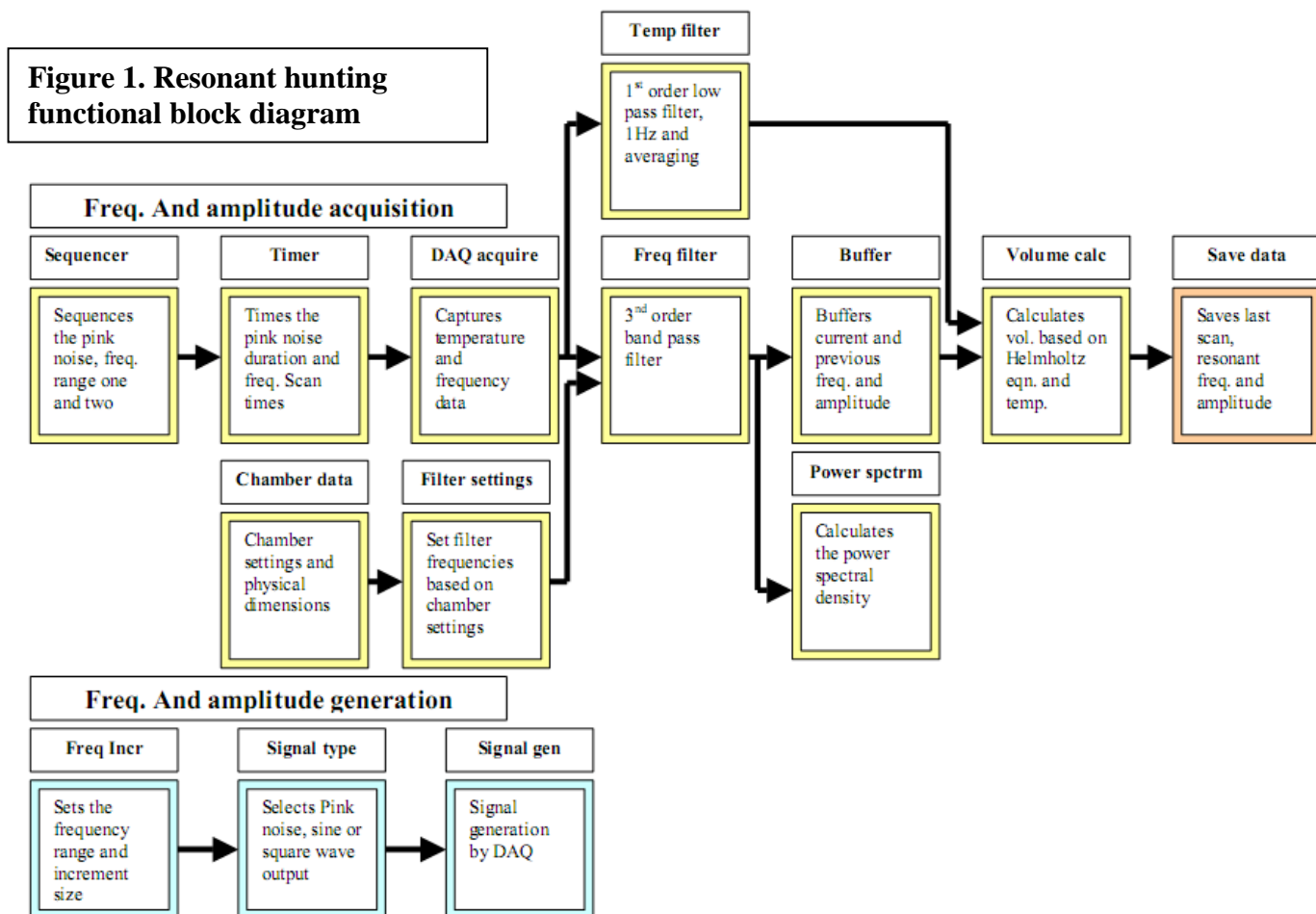
To solve the Helmholtz-Kirchhoff integral the pressure normal to any given diffraction source must be known advance. An empirical method would provide the most efficient way of analysing the diffraction occurring in complex shapes such as the interior and exterior area of the port. Avoidance of excess sources of diffraction is advantageous. In this investigation the microphone is within the port and hence does not 'see' the direct effects of diffraction taking place at the port entrance and exit. The microphone is affected by the indirect pressure variations occurring outside of the port. These 'fringing' effects will cause small secondary variation within the port as the interference can be considered a secondary impedance source to the openings. These secondary sources are far smaller than the primary ones caused by radiation impedances, which are a more significant loss to the system.

Appendix B

Software descriptions and functional block diagrams

1. Resonant hunting

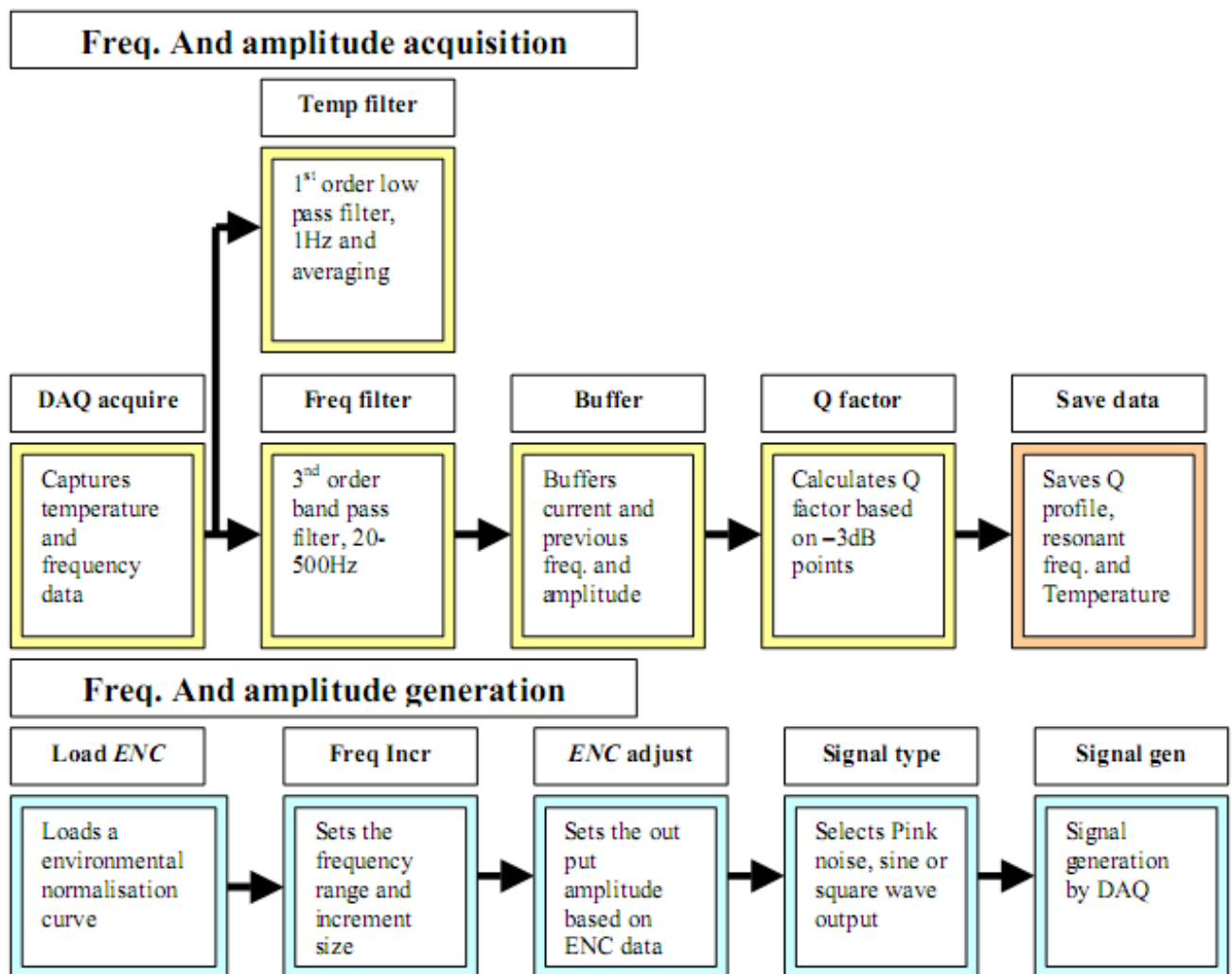
Chamber, port dimension and IIR software filters are set. Timers set duration for pink noise (10 seconds) followed by two frequency sweeps (0.1Hz stepping and 0.005Hz stepping). The first sweep is 2Hz wide and the second 0.1Hz. The acquisition captures frequency data (FFT) and temperature data (RTD) at 40,000 samples per second. Amplitude data is converted to dB using 1V signal as a reference value. An IIR 3rd order band pass filter is applied to frequency data to remove unwanted pink noise frequencies. An IIR 1st order low pass filter is applied to temperature data to remove thermal noise. A buffer joins continuous frequency data together to build a profile of the resonant peak. The maximum amplitude value is used to calculate the chamber volume. Simultaneously a power spectrum is displayed to allow the user to determine if resonance has been correctly identified. Once a volume has been calculated the user can save the frequency, amplitude, volume and temperature data. A function block diagram of this process is given in Figure 1.



2. Broad frequency scanner

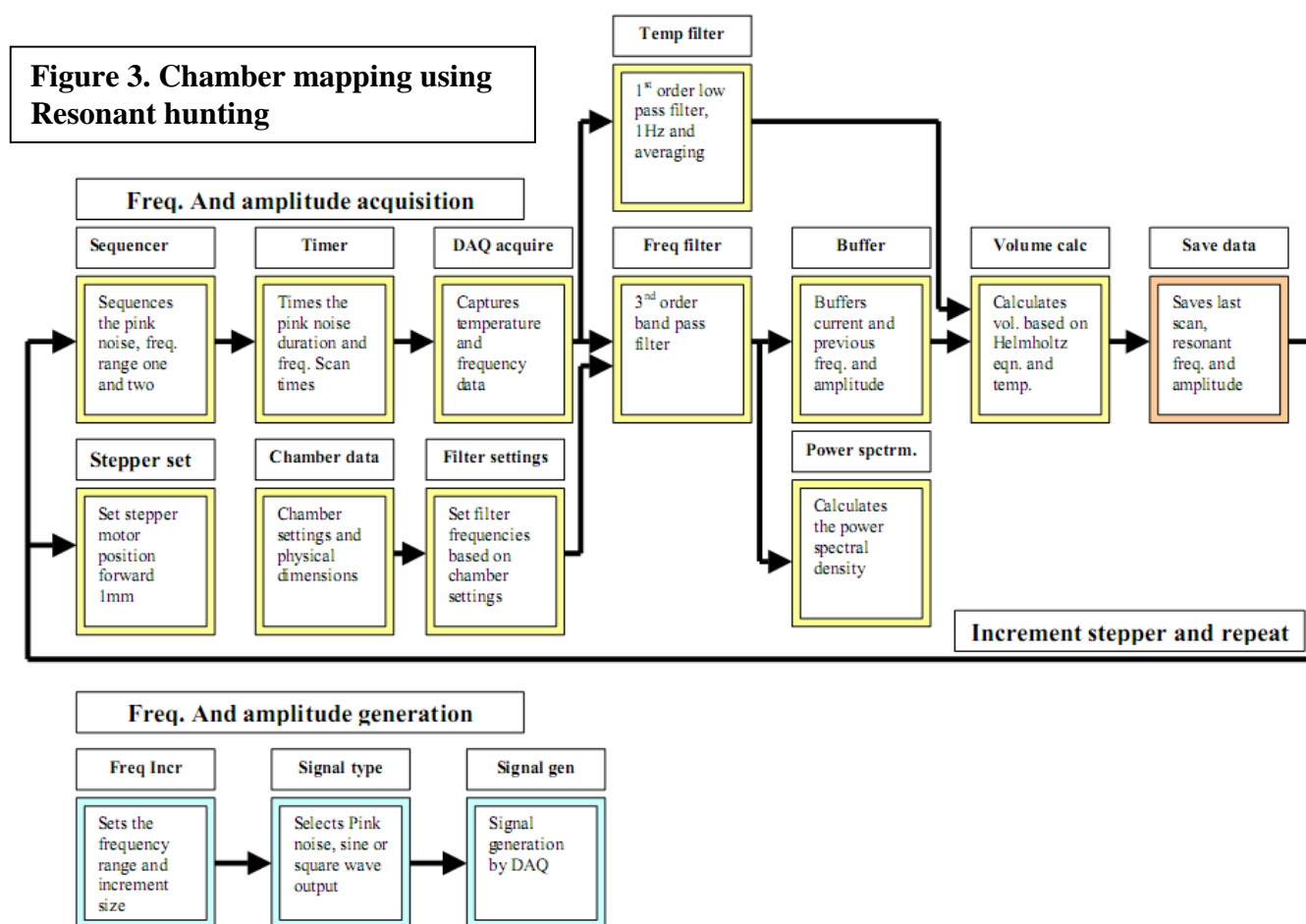
Frequency range and IIR software filters are set. ENC profile is loaded for the frequency range to be scanned. The acquisition captures frequency data (FFT) and temperature data (RTD) at 40,000 samples per second. Amplitude data is converted to dB using 1V signal as a reference value. An IIR 3rd order band pass filter is applied to frequency data to remove noise frequencies. An IIR 1st order low pass filter is applied to temperature data to remove thermal noise. A buffer joins continuous frequency data together to build a profile over the frequency range. The maximum amplitude and Q factor values are displayed. Simultaneously a power spectrum is displayed to allow the user to determine if resonance is occurring. The user can save the frequency, amplitude, Q factor and temperature data. A function block diagram of this process is given in Figure 2.

Figure 2. Broad frequency scanner functional block diagram



3. Chamber mapping using resonant hunting

Chamber, port dimension and IIR software filters are set. The user sets the initial height for the sample volume to start at and the distance for it to travel. Timers set duration for pink noise (10 seconds) followed by two frequency sweeps (0.1Hz stepping and 0.005Hz stepping). The first sweep is 2Hz wide and the second 0.1Hz. The acquisition captures frequency data (FFT) and temperature data (RTD) at 40,000 samples per second. Amplitude data is converted to dB using 1V signal as a reference value. An IIR 3rd order band pass filter is applied to frequency data to remove unwanted pink noise frequencies. An IIR 1st order low pass filter is applied to temperature data to remove thermal noise. A buffer joins continuous frequency data together to build a profile of the resonant peak. The maximum amplitude value is used to calculate the chamber volume. Simultaneously a power spectrum is displayed to allow the user to determine if resonance has been correctly identified. Once a volume has been calculated the frequency, amplitude, volume and temperature data are saved. The stepper motor is incremented 1mm and the process repeated until the maximum distance for the sample to travel is achieved. A function block diagram of this process is given in Figure 3.

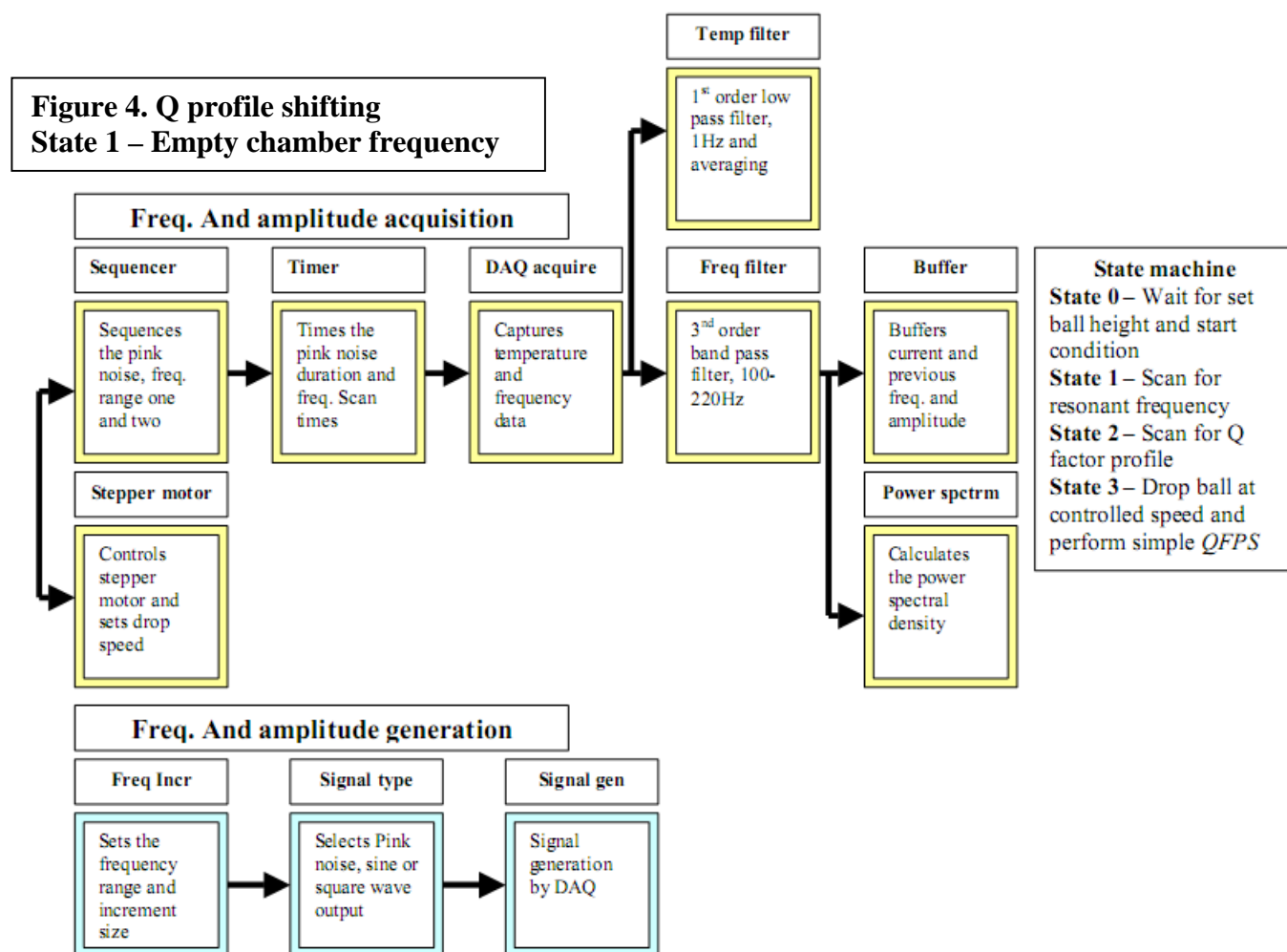


4. Q profile shifting

A four state software system was implemented in the Q profile shifting technique (Figures 4-6). The initialise state 0 is the setting of the sample to be used in controlled drops. State 1 - Find the resonant frequency via resonant hunting. State 2 - Acquiring a Q profile for the empty chamber. State 3 - Perform a controlled drop and analyse microphone amplitude data to allow Q profile shifting.

State 1 – Resonant hunting on empty chamber

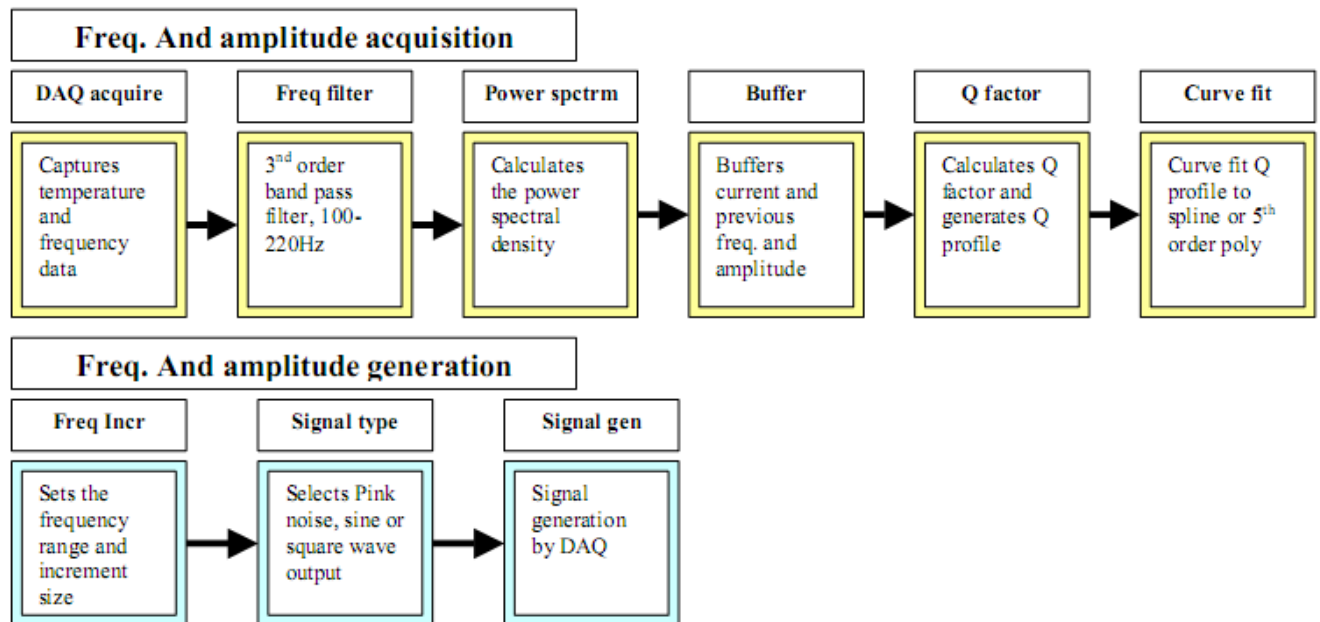
Chamber, port dimension and IIR software filters are set. The user sets the initial height for the sample volume to start at, drop speed and the distance for it to travel. Timers set duration for pink noise (10 seconds) followed by two frequency sweeps (0.1Hz stepping and 0.005Hz stepping). The first sweep is 2Hz wide and the second 0.1Hz. The acquisition captures frequency data (FFT) and temperature data (RTD) at 40,000 samples per second. Amplitude data is converted to dB using 1V signal as a reference value. An IIR 3rd order band pass filter is applied to frequency data to remove unwanted pink noise frequencies. An IIR 1st order low pass filter is applied to temperature data to remove thermal noise. A buffer joins continuous frequency data together to identify the resonant peak. Simultaneously a power spectrum is displayed to allow the user to determine if resonance has been correctly identified. A function block diagram of this process is given in Figure 4.



State 2 – Generate Q profile

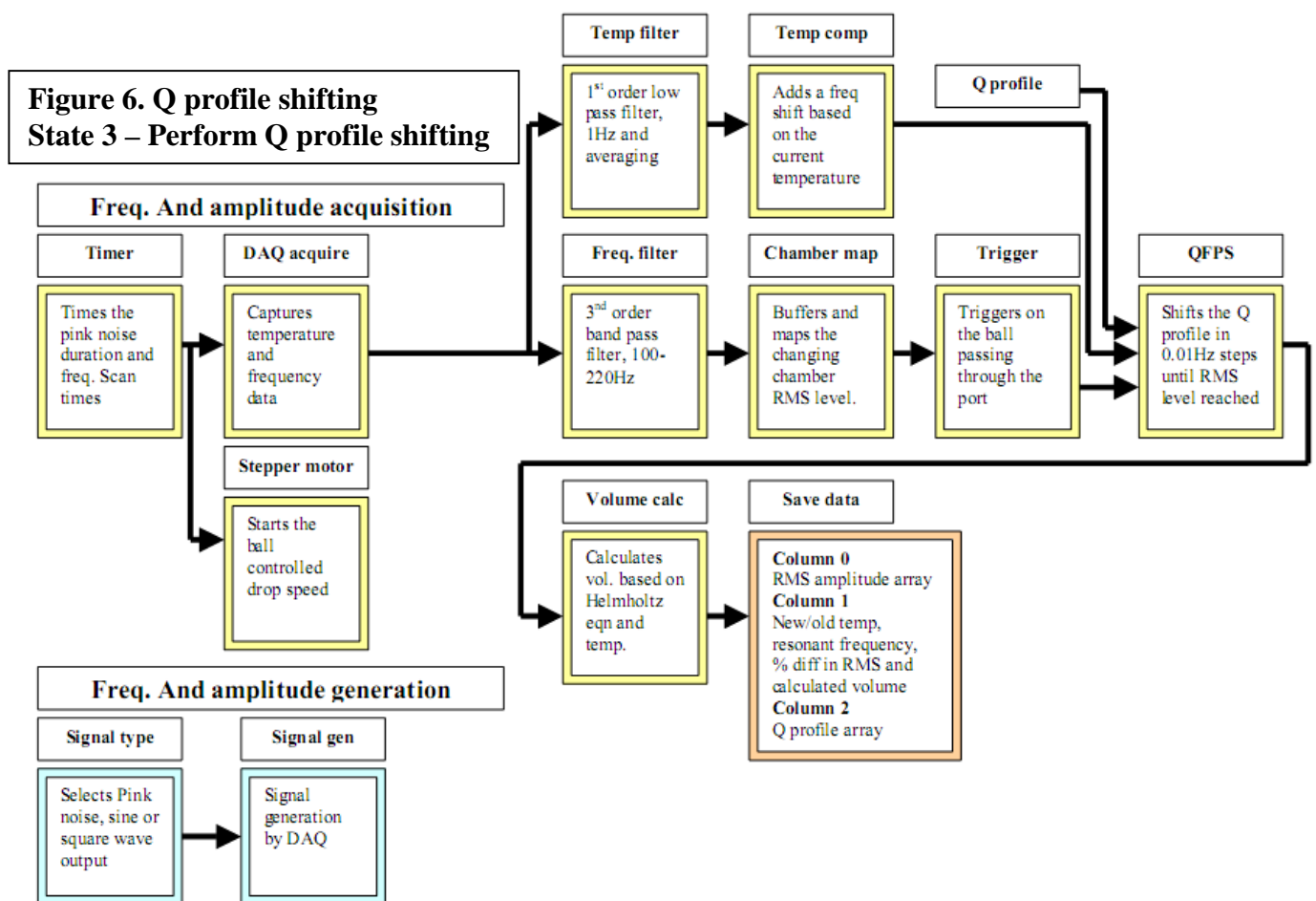
A continuous frequency sweep (0.01Hz stepping) is performed based on the resonant frequency identified in state 1 (10Hz prior to 1Hz post). The acquisition captures frequency data (FFT) and temperature data (RTD) at 40,000 samples per second. Amplitude data is converted to dB using 1V signal as a reference value. An IIR 3rd order band pass filter is applied to frequency data to remove unwanted pink noise frequencies. An IIR 1st order low pass filter is applied to temperature data to remove thermal noise. A buffer joins continuous frequency data together to identify the resonant peak. Simultaneously a power spectrum is displayed to allow the user to determine if resonance has been correctly identified. Q factor is calculated and a 5th order polynomial or spline is fitted to the resonant peak profile (Q profile). A function block diagram of this process is given in Figure 5.

Figure 5. Q profile shifting
State 2 – Generate Q profile



State 3 – Perform Q profile shifting

A single frequency is output to the loudspeaker based on the resonant frequency detected for the empty chamber. The acquisition captures frequency data (FFT) and temperature data (RTD) at 40,000 samples per second. Amplitude data is converted to dB using 1V signal as a reference value. An IIR 3rd order band pass filter is applied to frequency data to remove unwanted noise frequencies. An IIR 1st order low pass filter is applied to temperature data to remove thermal noise. A buffer joins continuous microphone amplitude data together to identify when the sample is in the centre of the chamber. Q profile shifting is performed to match attenuation to that observed for the empty chamber and the chamber containing the sample. A volume is calculated using the Helmholtz equation based on the predicted new resonant frequency. Microphone levels during the drop, Q factor, temperature at start and finish and the Q profile are saved. A function block diagram of this process is given in Figure 6.

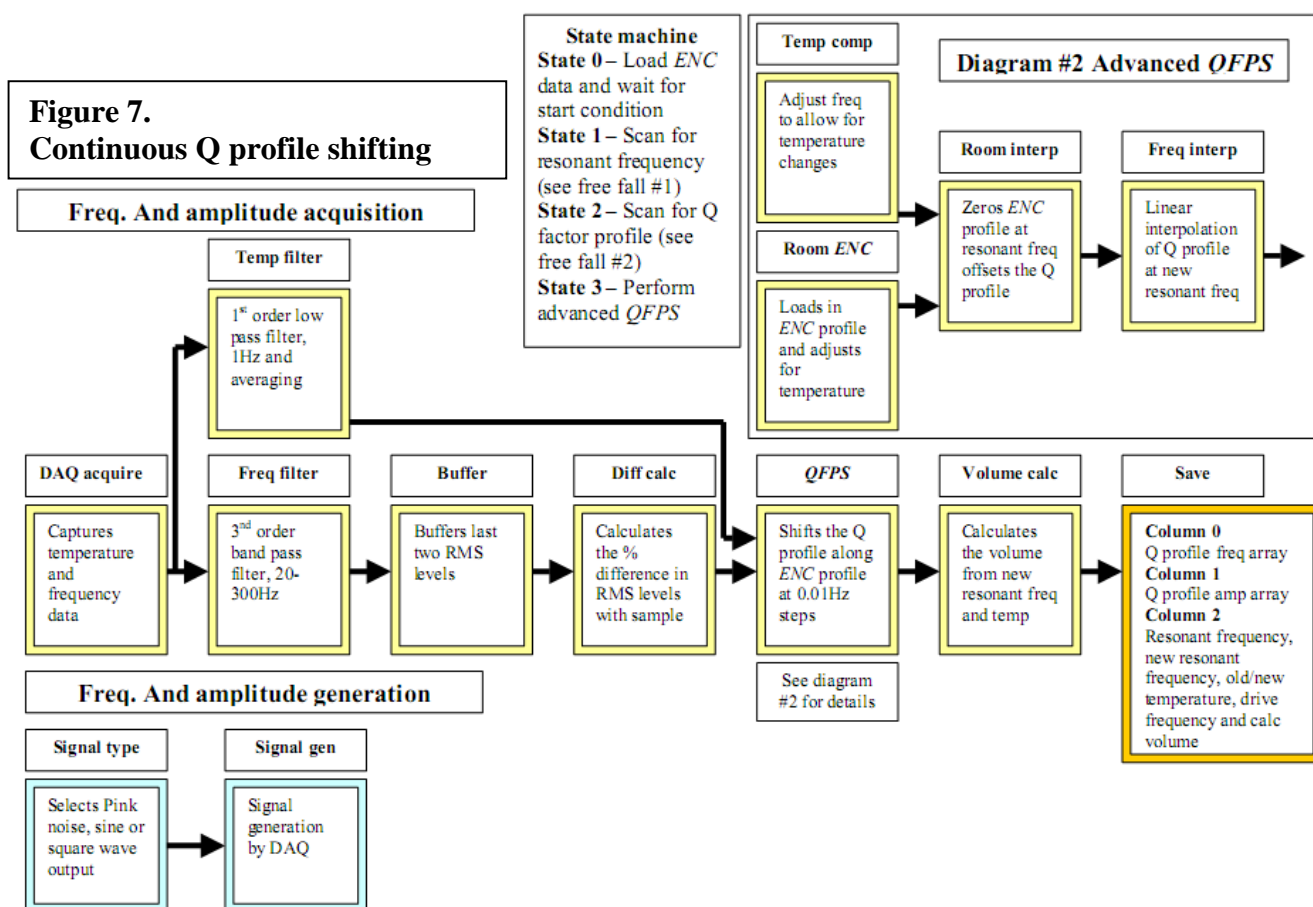


5. Continuous Q profile shifting

A four state software system was implemented for the continuous Q profile shifting technique. States 1 and 2 are identical to those used for the previous Q profile shifting, Section 4. State 0 - Load an *ENC* profile to be used in subsequent measurements. State 1 - Find the resonant frequency via resonant hunting (Figure 4, Section 4). State 2 - Acquiring a Q profile for the empty chamber (Figure 5, Section 4). State 3 - Perform continuous Q profile shifting.

State 3 – Continuous Q profile shifting

A single frequency is output to the loudspeaker based on the resonant frequency detected for the empty chamber. The acquisition captures frequency data (FFT) and temperature data (RTD) at 40,000 samples per second. Amplitude data is converted to dB using 1V signal as a reference value. An IIR 3rd order band pass filter is applied to frequency data to remove unwanted noise frequencies. An IIR 1st order low pass filter is applied to temperature data to remove thermal noise. A buffer joins the last two microphone acquisitions and averages them. The percentage difference in level from an empty chamber and the one containing the sample is evaluated. The *ENC* data is used to create a corrected Q profile. The corrected Q profile is frequency shifted to match attenuation to that observed for the empty chamber and the chamber containing the sample. Linear interpolation is used to evaluate the Q profile as it is shifted. A volume is calculated using the Helmholtz equation based on the predicted new resonant frequency. Temperature at start and finish, Q profiles (raw and *ENC* corrected), the drive frequency, predicted resonant frequency and predicted volume are saved. A function block diagram of this process is given in Figure 7.

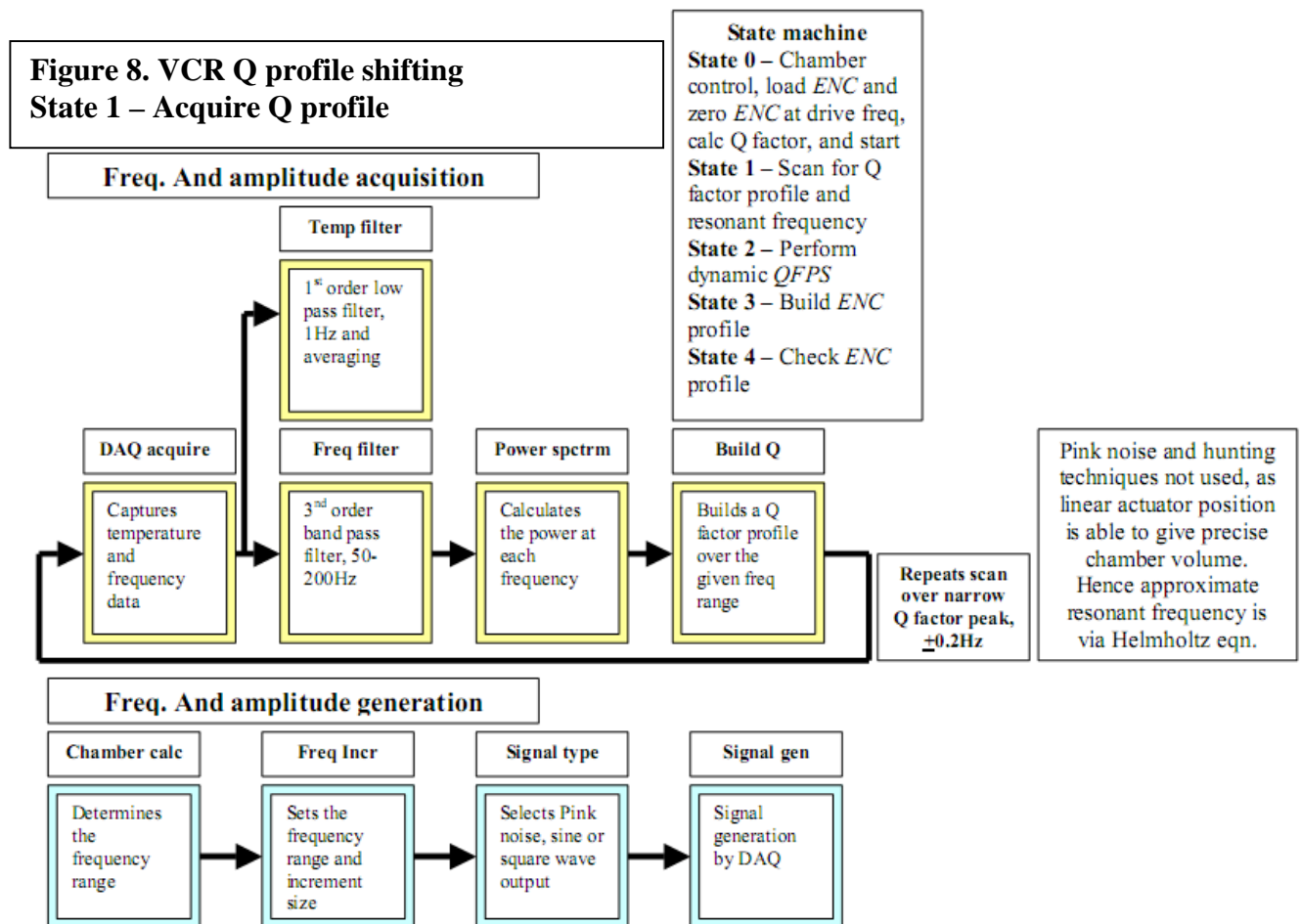


6. VCR Q profile shifting

A five state software system was implemented for the continuous Q profile shifting technique. State 0 - Load an *ENC* profile to be used in subsequent measurements and offset it based on the amplitude at the driving frequency of the empty chamber. State 1 - Acquiring a Q profile for the empty chamber. State 2 - Perform a dynamic Q factor profile shift. State 3 - Create an *ENC* profile. State 4 - Check an *ENC* profile. The VCR floor can be raised and lowered via software control. The position will determine the interior chamber volume.

State 1 – Acquire Q profile

Using the chamber volume information an approximate resonant frequency can be calculated based on the Helmholtz equation. This removes the need for a pink noise burst to identifying the resonant frequency. A two-sweep frequency scan is then performed as described in Section 1 to identify the resonant frequency to within 0.01Hz. Amplitude data is converted to dB using microphone calibration data described in Appendix D, Section 3. An IIR 3rd order band pass filter is applied to frequency data to remove unwanted noise frequencies. An IIR 1st order low pass filter is applied to temperature data to remove thermal noise. A frequency scan is then performed over a range to allow for a 15% change in chamber volume. A buffer joins continuous frequency data together. Simultaneously a power spectrum is displayed to allow the user to determine if resonance has been correctly identified. A function block diagram of this process is given in Figure 8.



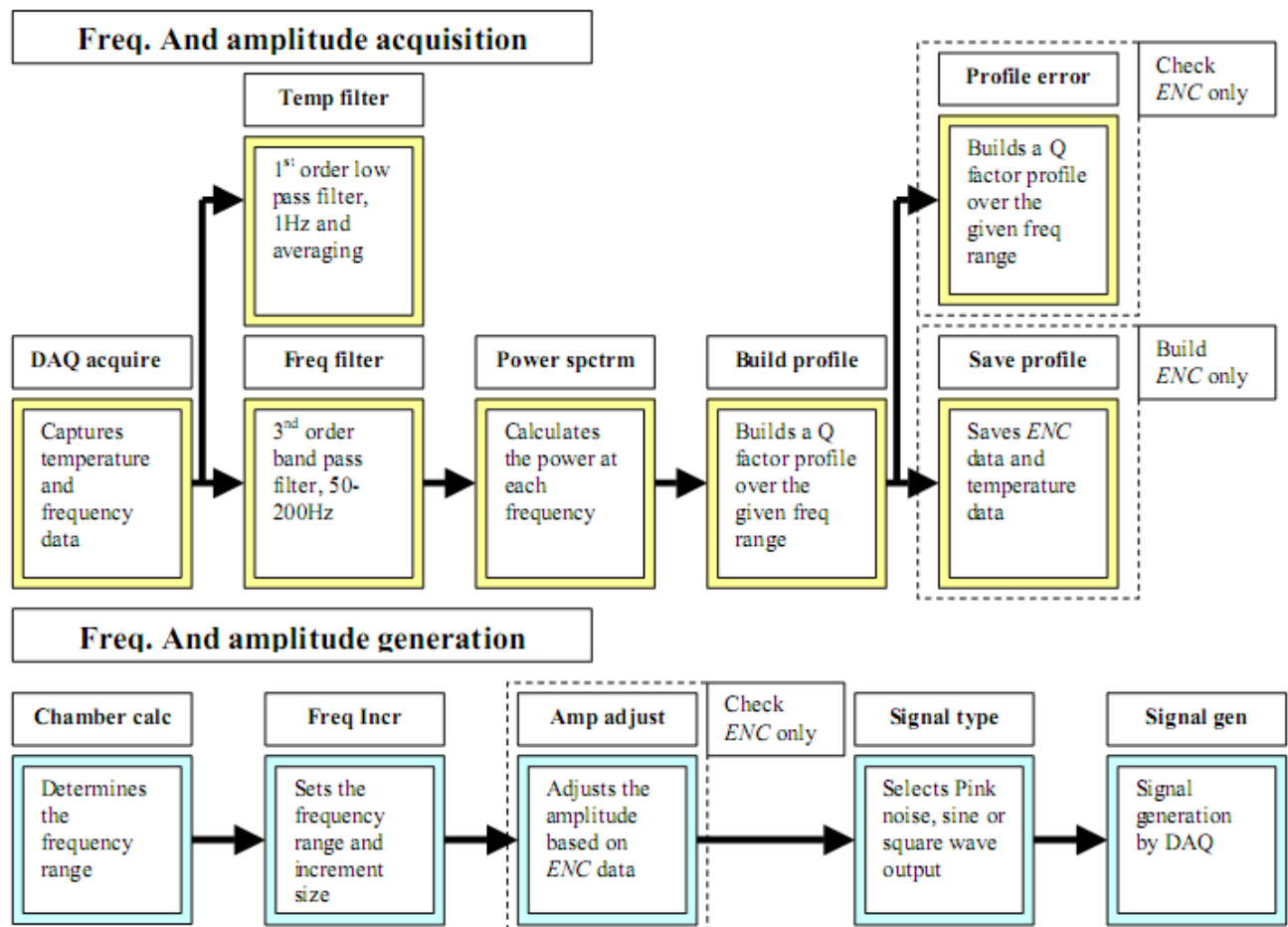
A single frequency is output to the loudspeaker based on the resonant frequency detected for the empty chamber. The acquisition captures frequency data (FFT) and temperature data (RTD) at 40,000 samples per second. The percentage difference in level from an empty chamber and the one containing the sample is evaluated. The *ENC* data is used to create a corrected Q profile. The corrected Q profile is frequency-shifted 0.01Hz and a comparison made with the attenuation observed for the empty chamber and the chamber containing the sample. If the attenuation is not equal the process is repeated. Each time the Raw Q profile is overlain with *ENC* data. Linear interpolation is used to evaluate the Q profile as it is shifted. A volume is calculated using the Helmholtz equation based on the predicted new resonant frequency. *ENC* data, Temperature at start and finish, Q profiles (raw and *ENC* corrected), the drive frequency, predicted resonant frequency and predicted volume are saved. A function block diagram of this process is given in Figure 9.



State 3 and 4 – Create and check an ENC profile

A second microphone adjacent the port measures SPL with the Helmholtz resonator port blocked. A continuous frequency sweep (0.01Hz stepping) is performed over a frequency range to allow for a change in chamber volume of 15%. The acquisition captures frequency data (FFT) and temperature data (RTD) at 40,000 samples per second. Amplitude data is converted to dB using microphone calibration data described in Appendix D, Section 3. An IIR 3rd order band pass filter is applied to frequency data to remove unwanted noise frequencies. An IIR 1st order low pass filter is applied to temperature data to remove thermal noise. A buffer joins continuous frequency data together. Frequency, amplitudes and temperature are saved to disk. To check the *ENC* profile the same frequency sweep is performed only the amplitudes have been reversed based on an average SPL for the initial *ENC* frequency sweep. A maximum and minimum deviation is given in dB to ascertain whether the *ENC* profile is still valid. Figure 10 shows the functional block diagram for this process.

Figure 10. ENC profile creation and checking



Appendix C

Loudspeaker Parameters

1. Loudspeaker design considerations

The process of loudspeaker enclosure design is as complex as the procedures for developing the resonator and any other specialised area in acoustics. It can be said that there are a number of similarities between the two fields, but for the most part they are treated quite separately.

Small (1972) stated that the real beginnings of loudspeaker and enclosure design started in the 1950's with a switch from what is now considered the primitive low compliance designs to more modern high compliance ones. This principally refers to the compliance of the loudspeaker cone (diaphragm) or its stiffness and 'throw'.

It was important in this investigation to have a known referenced sound source with which to generate incident plane waves. Papers by Thiele (1971 and 1973) and Small (1972 and 1973) provided excellent details for analysis of loudspeakers and enclosures. What follows is a summary of their work, supported by similar findings of Beranek (1996).

The chosen enclosure was a sealed air suspension, infinite baffle designs as considered by Small, Thiele and Beranek (1996). For the traditional moving coil loudspeaker there are two main enclosures those of the vented (ported) types and those of the sealed infinite baffle. The sealed air suspension type of enclosure is designed to damp all rare projected sound and provide a mass loading for the high compliance loudspeaker.

Vented types use the Helmholtz resonator effect to extend the low frequency response of a loudspeaker beyond what it is normally capable of. It does this by providing an extra radiating piston in the form of the port. The port then resonates at the tuned frequency just below the natural resonant frequency of the enclosure to provide a secondary sound source. At all other frequencies the port appears as a high or low impedance path depending on frequency.

2. Loudspeaker enclosure design

Keeping the driver within its limitations is most important in enclosure design. To achieve this the small signal parameters values must be measured. These values will immediately reveal the true characteristics of the loudspeaker, i.e. whether it is of a high or low compliance type and therefore whether it is best suited to an air suspension, open baffle or ported configuration. Additional information can be gathered on the power handling capacity and the reference efficiency to fine-tune the enclosure.

Most importantly the resonant frequency of the loudspeaker in free space must be considerably lower than that of the system. For an air suspension type of enclosure the ratio of suspension to enclosure compliance must be at least three. Additionally the resonant frequency in free space must be half the resonant frequency of the loudspeaker in the enclosure. The acoustic compliance volume of the loudspeaker must be bigger than the volume of the enclosure. Lastly, filling is usually beneficial to

the performance, but is best considered in reference to the overall system performance.

3. Noise cancellation and echo suppression

The creation of an equal-potential sound source across a range of frequencies is a particular problem in this investigation for creating aberration free resonant Q profile curves. The primary reason is loudspeaker non-linearities, echoes, diffraction sources and reflections. Recording studios and digital communications applications in the cellular phone industry have actively pursued the problem of flat frequency response and perceived signal levels.

For cellular phones the main concern is background noise and echo reduction (Scalart and Benamar, 1996) for the recording industry and audio enthusiast it is to recreate a flat frequency response from their sound system (Everest, 2001). To this end digital signal processors are used to provide delays and filtering to the base signal in an attempt to compensate for the variety of anomalous effects described. In this investigation external noise does not pose a problem but loudspeaker deficiencies, diffraction, reflection and echo do.

The problem for the recording industry and audio enthusiasts is to create compensation for these effects in a general way that is independent of listening position. To achieve this often multiple microphone correlation and signal convolution is performed (Everest, 2001). For this investigation the various components are statically located and advanced digital signal processor algorithms are therefore not required.

By reducing the amount of reflection in a given environment a reduction in the dependence on negative phase corrections can be made. Everest suggests such measures include rubber supported glass and sound absorbing/diffracting panels. These methods are forms of passive noise control and are to be differentiated from active ones taking place electronically/digitally.

Everest has identified diffraction from loudspeaker and baffling edges contribute as much as $\pm 5\text{dB}$ to the perceived sound level at the microphone location. This is caused by constructive and destructive interference. Again, to remove dependencies on the active control these diffraction sources can be significantly reduced by flush mounting the loudspeaker and removing baffling corners by rounding or addition of absorbing material.

Echoes are generated from walls and other surfaces that reradiate sound from the primary source and those caused by diffraction. The effect of these can be 'combing' of the sound level at the microphone. Combing is the constructive and destructive interference pattern that manifests itself as a series of notches in the frequency spectrum. These notches can change frequency with any slight changes in the environment. To reduce the influence of the environment, passive control needs to be implemented as much as possible. As any active noise control in the form of negative feedback used to cancel reflection and diffraction can be negated by slight shifts in the notch frequencies.

4. Loudspeaker lobes and interference

Figures 4.1a – 4.1d are calculated polar plots for an 8-inch full range speaker between 100Hz and 5kHz. They show the narrowing of the primary lobe and appearance of secondary lobes with increasing frequency (More complete details of the piston type radiator can be found in Appendix A, Section 5). For frequencies lower than 1kHz the primary lobe is wide enough to be considered an omni directional source. The resonator was tested in off axis positions, as well as on axis located in front of the speaker.

It should be noted that side lobes, those not on the primary axis, will have alternating negative and positive phase relationships with the primary lobe. This stems from Bessel functions being solutions to the pressure wave equation emanating from the loudspeaker. Lobe transitions are zero crossings and hence there is expected to be regions of zero sound intensity. This phenomena should only occur at frequencies where $ka\sin\theta \ll 1$, i.e. when the wave length is smaller than the speaker diameter, where k is the wave number ($1/\lambda$), ' a ' the sound source diameter and θ the off centre angle in radians).

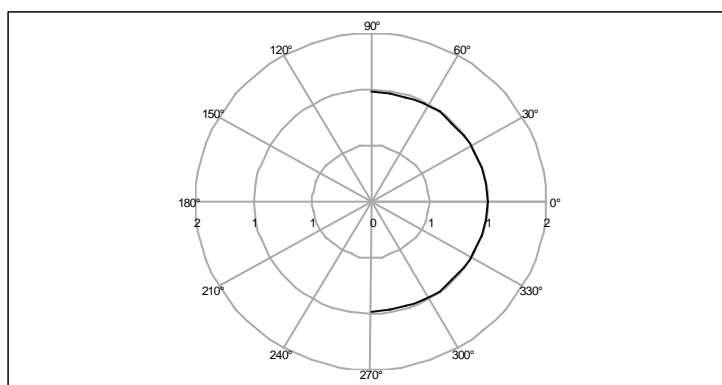


Figure 4.1a Polar plot of sound intensity for an 8" speaker at 100Hz

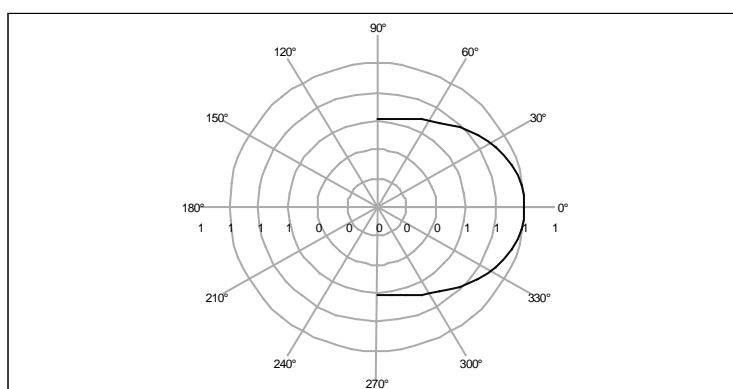


Figure 4.1b Polar plot of sound intensity for an 8" speaker at 500Hz

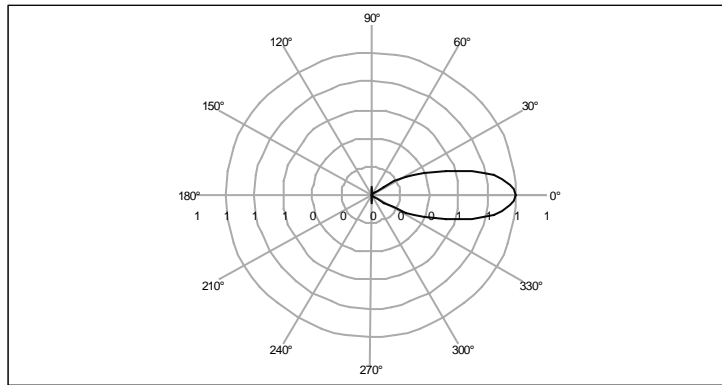


Figure 4.1c Polar plot of sound intensity for an 8" speaker at 1kHz

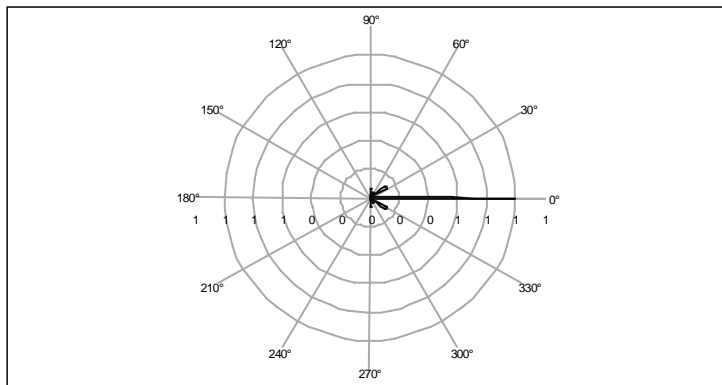


Figure 4.1d Polar plot of sound intensity for an 8" speaker at 5kHz

It is important the sound source is at a distance where fringe effects caused by edges directly adjacent to the loudspeaker are not likely to be present at the port. Fringe effects are usually present in the immediate vicinity around the driver, within one driver diameter of a secondary radiating edge.

Figure 4.2 illustrates the reradiating effects (diffraction/fringing) that edges have on the primary sound source (Blackstock, 2000). Reradiated sound is out of phase and can cause both constructive and destructive interference. At distances greater than the lowest wavelength, regions of positive and negative attenuation occur at angles corresponding to overlap.

Only certain frequencies produce lobes that extend over the radiating surface, Figures 4.1a – 4.1d. The radiating surface can be considered the 90 - 270 degree axes that the loudspeaker is mounted.

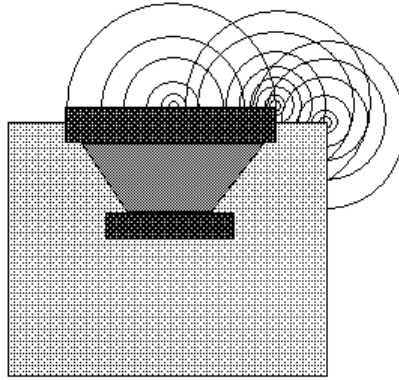


Figure 4.2 **Interference caused by reradiating by sharp edges within proximity of sound source (fringing).**

Interference effects from reflections are similar to those created by edge diffraction as seen in Figure 4.2. Therefore, the sound source should be physically remote from any immediate reflecting surfaces, such as walls or plane objects. As accuracy is the ultimate goal of this investigation, these small details may prove to be significant.

Appendix D

Calibrations

1. Density measurements of marbles used in granular testing

A representative sample of twenty marbles used in procedure 7, both large and small, were measured using Mitutoyo slide callipers ($\pm 0.01\text{mm}$) and again using the buoyancy rig developed for produce and mineral tests. Both the large and small marbles were first rolled across a flat surface to ensure they were sufficiently regular; then their diameter was measured. From the diameter measurements a total volume could be established. Marble glass density was calculated from the total weight for the marbles as measured using a set of Mettler PE6000 scales.

Buoyancy was also used as a comparative method for determining the marble glass density. The precise volume of all small and large marbles was calculated by combining the submerged and un-submerged weights of each collection. From this and their collective weights the marble glass density was calculated.

Results for the slide calliper measured glass density were 2.503g/mL and 2.500g/mL for the large and small marbles respectively. Buoyancy glass density results were 2.522g/mL and 2.518g/mL respectively. The values derived from buoyancy testing should be more accurate as it was not possible to measure precise marble diameters due to their spheroidal (diameters had up to 3% eccentricity) rather than spherical manufacture.

2. Calibration of variable chamber resonator, SMC LXPB200 linear actuator

The SMC LXPB200 linear actuator movement was measured via a set of Mitutoyo slide callipers with a stated accuracy of $\pm 0.01\text{mm}$. The linear actuator was moved at 1mm step intervals as measured from the actuator body to the actuator plate, Figure 2.1. The range of movement was from 109.71mm to 124.74mm equating to a $0\text{--}300\text{mL}$ volume sample range when using the variable chamber resonator (VCR). The step accuracy was found to be $\pm 0.02\text{mm}$; the specified accuracy of the SMC LXPB200 linear actuator was $\pm 0.03\text{mm}$.

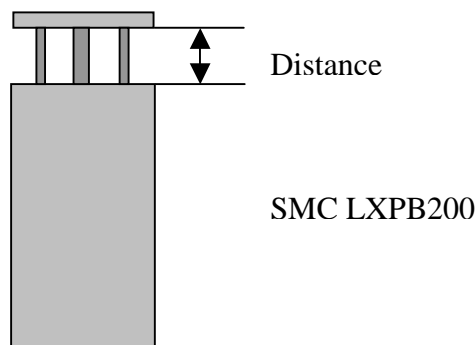


Figure 2.1 The SMC LXPB200 linear actuator diagram showing where calibration measurements were taken.

Taking ten repeat measurements of extension from 6.50mm to 116.50mm provided checks on the repeatability of the actuator movement. The repeat accuracy was

$\pm 0.015\text{mm}$. This shows the repeatability accuracy is greater than linear stepwise movement accuracy. Measurements of incremental stepping and repeat positioning are both better than the stated data sheet for the SMC LXPB200. The volume inaccuracy associated with a 0.02mm error is 0.2mL , which is better than the *VCR* volume measurement accuracy by a factor of ten.

Both a dry and thin water film layer method was used to ensure there were no air leaks occurring at the boundary between piston O-ring and the chamber bore. The *VCR* piston position was actuated between 100mm to 115mm dry and the Q factor and temperature recorded. This was then repeated with a 50mL thin film of water covering the piston. The water would act as a barrier to any potential air gaps that may exist. The dry and wet Q factors should be significantly different if any leaks were present in the dry tests. Results showed Q factors between wet and dry mirrored each other with incremental stepping of the piston position, Figure 2.2, suggesting no air leaks for the *VCR*'s normal operation.

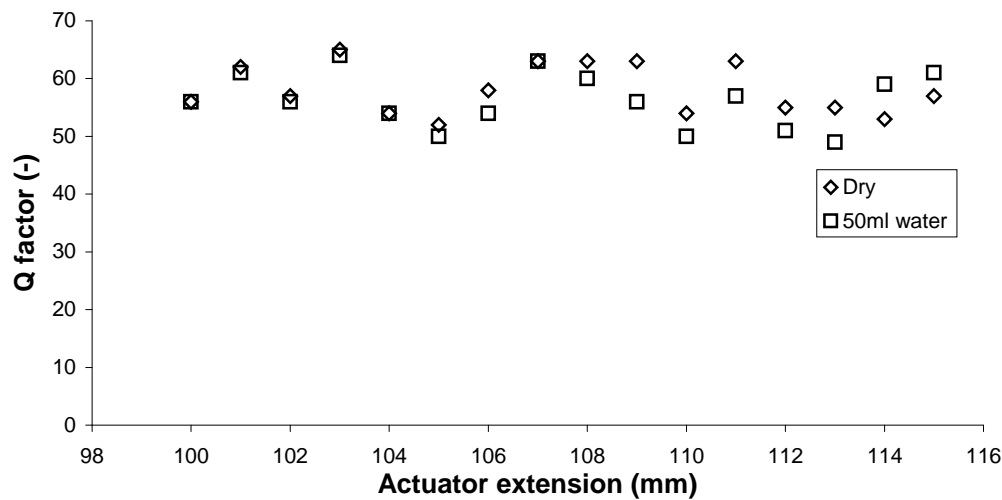


Figure 2.2 Q factor tests of *VCR* when dry and with a 50mL thin water film covering the piston.

3. Anechoic chamber calibration of microphone and loudspeaker

An anechoic chamber was used to calibrate the PCB 103A microphones and *Realistic* sound meter at IRL, Lower Hutt, NZ. The reference was a calibrated *Quest* 2400 sound meter and 1kHz noise source of 93.6dB . Calibration was conducted at 16.2°C as measured by a calibrated *Hart Scientific* RTD temperature meter model 1502A.

A broad frequency sweep from $50 - 300\text{Hz}$ was conducted to gauge the influence of the loudspeaker in terms of linearity (Figure 3.1). Anechoic testing revealed the loudspeaker to within $\pm 0.5\text{dB}$ over the range $90\text{Hz} - 200\text{Hz}$ and $\pm 4\text{dB}$ between $50\text{Hz} - 300\text{Hz}$. Measurements were made with a PCB103A microphone. Two other plots are given in Figure 3.1 as position 1 and position 2. These are the plots for the usual measurement environment during the experimental component of this investigation. These show the influence of reflection and refraction and also the need for environmental normalisation curves (*ENC*). The pronounced step in the anechoic data below 90Hz made measurements in this region difficult as described in the *QPS* procedures.

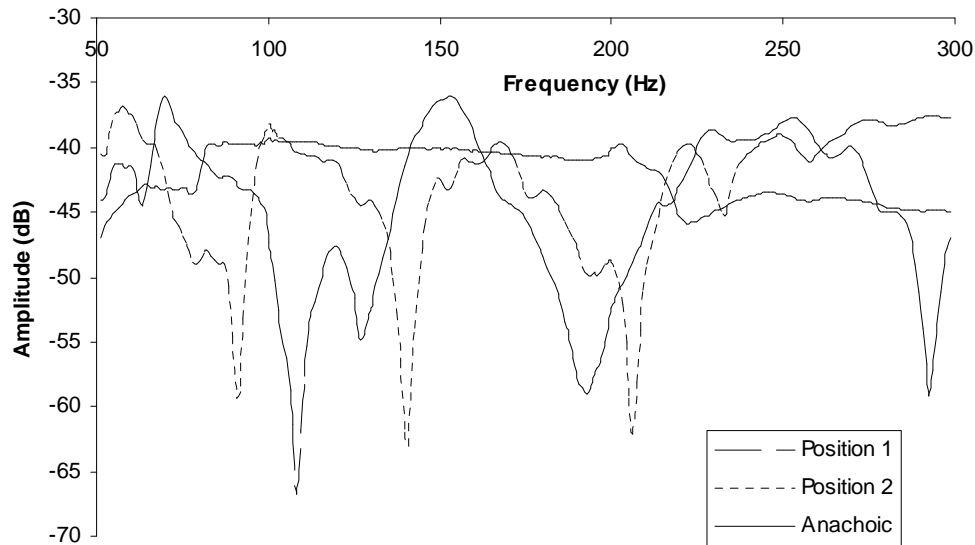


Figure 3.1 Broad frequency sweep of anechoic chamber and two positions used in non-anechoic environment. Measurements made with PCB 103A microphone mounted 30 degree off axis at 0.5m. Position 2 taken atop of VCR resonator with port plug 50 degrees off axis at 0.5m.

In all tests the PCB 103A microphone and *Realistic* sound meter data was offset to coincide with the calibrated *Quest* meter. This allowed direct comparison of sensitivity. Objective tests with a calibrated noise source showed the *Realistic* sound meter was 2.3dB low on its display and 9dB low on its analogue output at 77Hz.

To gauge the response time and sensitivity of the PCB microphone, *Realistic* sound meter and *Quest* sound meter, all three were subjected to a broad frequency sweep between 50Hz – 300Hz, Figure 3.2. Results showed only marginal differences in sensitivity and response, Figure 3.3 is given to further highlight any differences between the *Realistic* and *Quest* sound meter from that of the PCB microphone. Both the *Realistic* and *Quest* meters have similar deviations. This discrepancy from the PCB microphone may be attributed to the weighting C filter built into the two sound meters.

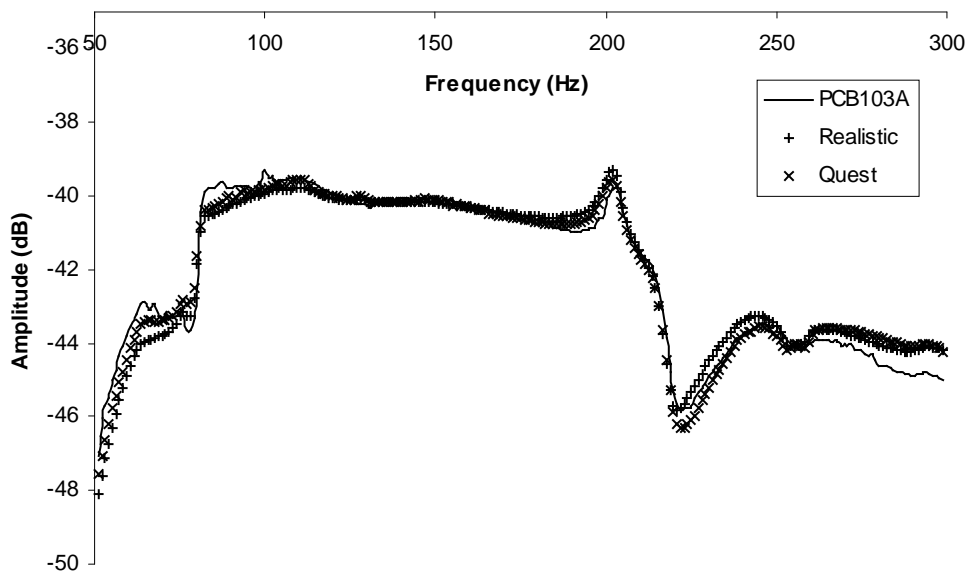


Figure 3.2 Broad frequency sweep comparison between PCB 103A microphone, *Realistic* sound meter and *Quest* sound meter taken in anechoic chamber. Fast sweep, 2Hz/sec

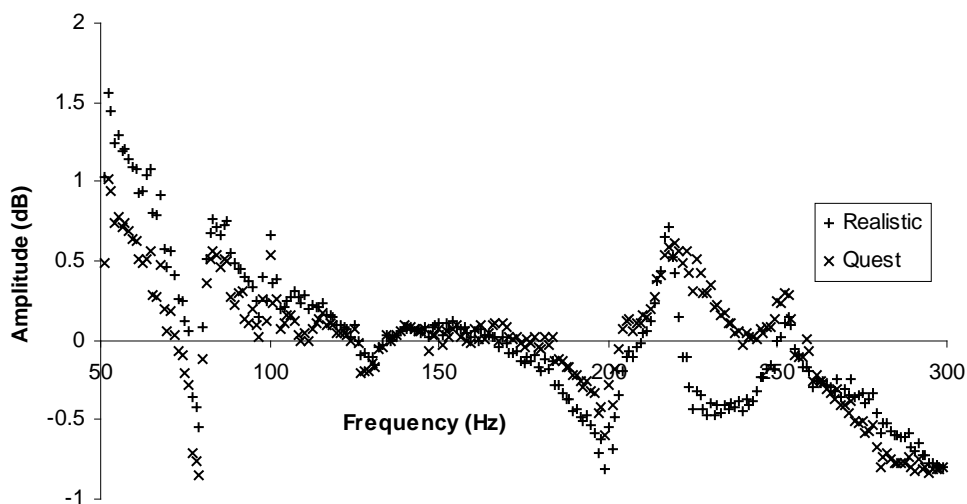


Figure 3.3 Broad frequency sweep deviation from the PCB 103A microphone for the *Realistic* sound meter and *Quest* sound meter taken in anechoic chamber. Fast sweep, 2Hz/sec

When a narrow sweep over 65Hz – 95Hz was made the deviation between the PCB microphone and the sound meter was negligible. This indicates the sweep speed is significant in comparing the devices, Figure 3.4. As mentioned, the weighting filter may be responsible for deviations seen in the broad frequency sweep. There was a ± 0.2 dB difference detected when comparing the deviation of the microphone to the sound meters, Figure 3.5. At the frequency of 77Hz there was less than 0.1dB difference and hence this frequency was chosen to calibrate the PCB 103A microphone.

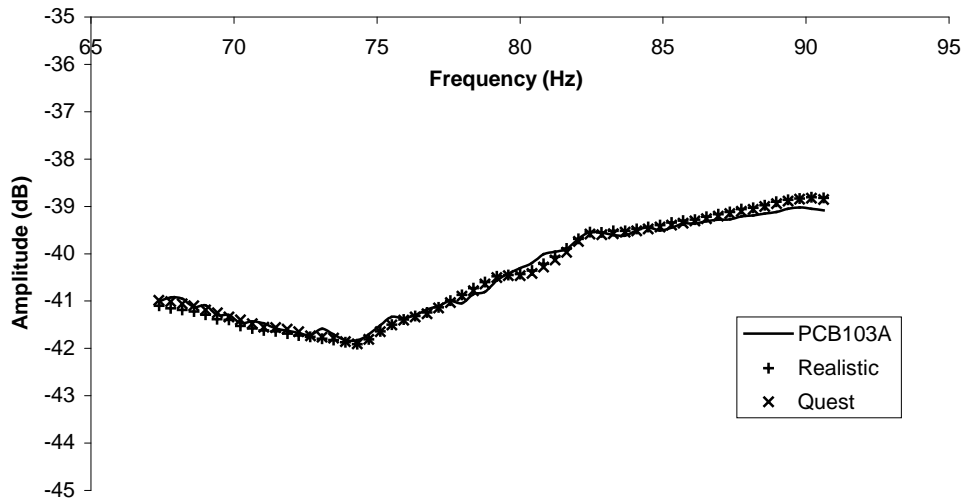


Figure 3.4 Narrow frequency sweep comparison between PCB 103A microphone, *Realistic* sound meter and *Quest* sound meter taken in anechoic chamber. Slow sweep, 0.2Hz/sec

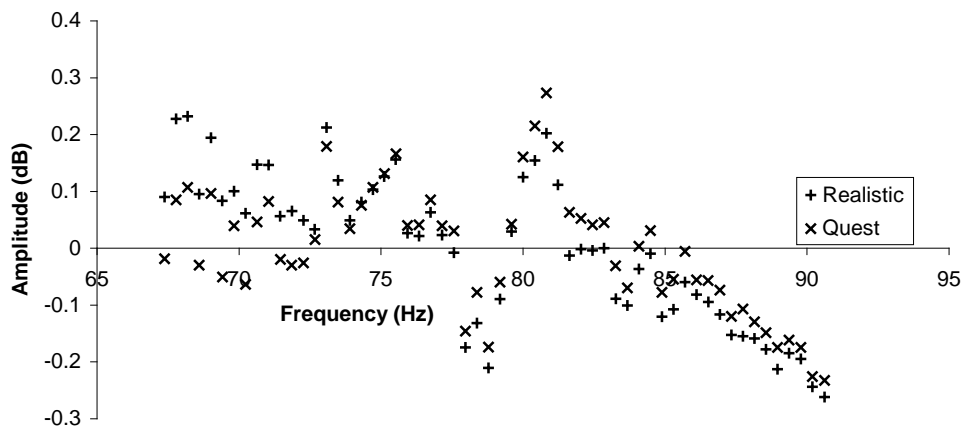


Figure 3.5 Narrow frequency sweep deviation comparison between *Realistic* sound meter and *Quest* sound meter taken in anechoic chamber. Slow sweep, 0.2Hz/sec

The PCB103A microphone calibration was conducted using the Realistic sound meter. Both the microphone and the sound meter were subjected to two signal levels over a frequency range from 50Hz to 200Hz, Figure 3.6. The signal differential was an average of 3dB for both the PCB microphones and the sound meter. This indicated they each had the same differential sensitivity. When the output was normalised using the environmental normalisation procedure, Chapter 4, the output from the loudspeaker was recorded at a steady 86.3dB \pm 0.1dB. By taking this as the objective sound level the PCB signal could be offset and correctly calibrated for its sensitivity.

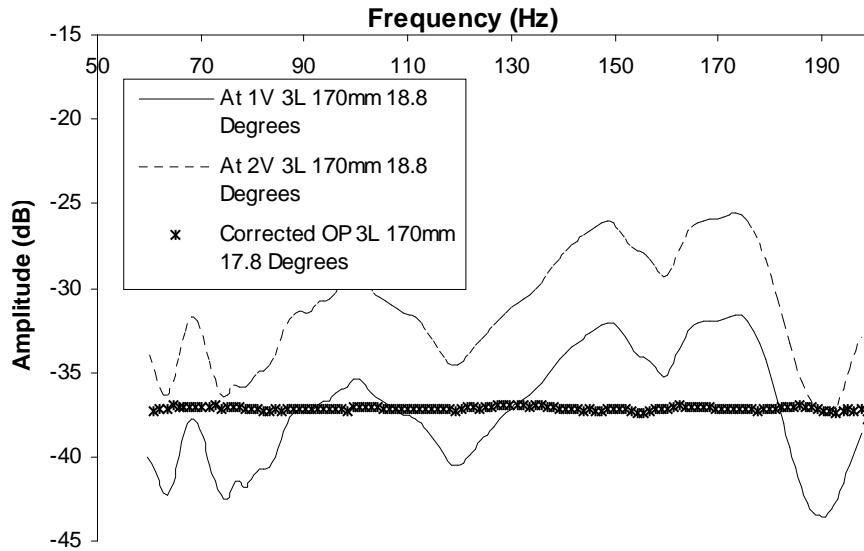


Figure 3.6 Calibration tests using 1Vpp and 2Vpp signals generated by DAQ, demonstrating a 3dB change in level as measured in the port. Also shown is a corrected output profile using *ENC* data at -37dB.

The output was compared for both the sound meter and the PCB microphone to confirm the similarity in sensitivity over a nominal range of 70Hz to 110Hz, Figure 3.7. The outputs of both were offset to allow direct comparisons. No resonator was present; therefore the output was representative of the loudspeaker and environmental effects. The average sound pressure level in this instance was 90dB.

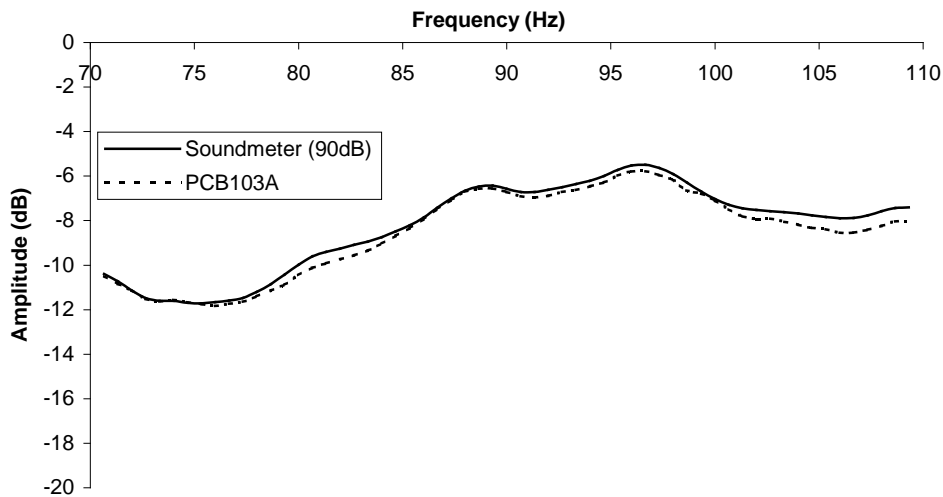


Figure 3.7 Output from the Realistic sound meter and PCB 103A microphone in experimental environment. Amplitude is referenced to a 90dB level (0dB = 90dB).

The sound pressure level in dB is given by Equation (No.13), Basic Equations. By rearrangement the source pressure can be made the subject, Equation (3.1), and hence

the sensitivity in volts per kilopascal ($V_{\text{RMS}}/\text{kPa}$) can be determined. By noting that the PCB microphones are used on the x100 setting, Equation (3.2) can be formed which gives the PCB103A's sensitivity. This calculation is dependant on the reference sound level meter's output (86.3dB).

$$P = 2 \times 10^{-5} \exp\left(\frac{SPL}{20}\right) \quad (3.1)$$

$$\text{Sensitivity} = \frac{1000V}{100P} = \frac{10V}{P} \quad (3.2)$$

where V is the *RMS* signal voltage measured from the PCB microphone under test (8.404mV_{RMS}) and P is the pressure in Pascal of the reference source (86.3dB = 413.07mPa). The 1000 multiplier in the numerator is due to the sensitivity being in kPa and the one hundred term in the divider in the denominator to the x100 setting of the PCB amplifier. The sensitivity of the PCB103A microphone was calculated to be 203.5mV/kPa (-6% from stated datasheet sensitivity, PCB 103A microphones are $\pm 15\%$ their nominal listed value).

A *VCR* calibration using variable piston position was undertaken in the anechoic chamber to gain a better understanding of how the instability at sub 100Hz frequencies affect the accuracy in *QPS* techniques. The amount of scatter seen is not significantly less than that observed in the *VCR*'s normal non-linear environment, Figure 3.8. The reduction in scatter after specific curve fitting is reduced from $\pm 7\text{mL}$ to $\pm 5\text{mL}$.

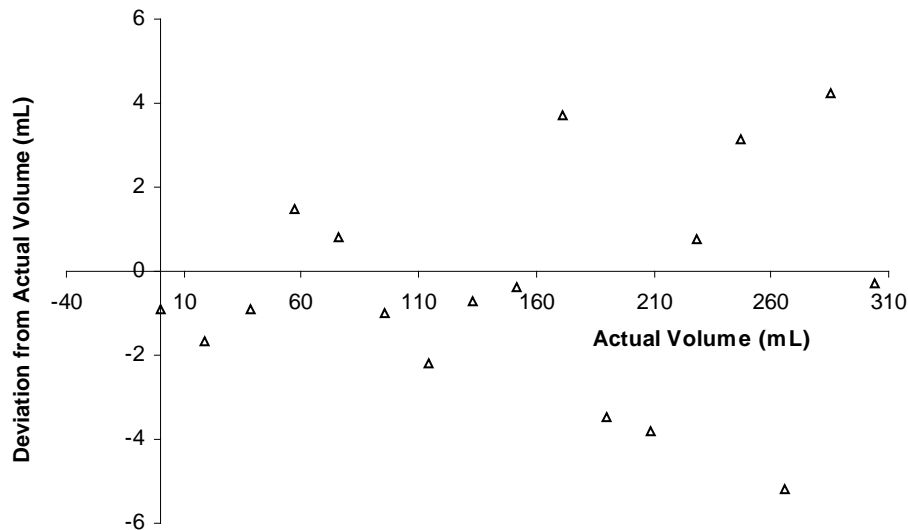


Figure 3.8 Anechoic chamber *VCR* volume deviation from true volume using a specific correction factor on piston volumes. Resonator has 3.5L chamber with 175mm long, 44mm diameter port.

4. Buoyancy uncertainty due to balance deflection

A small uncertainty in volume determination is possible due to movement in the Mettler PE600 scales used. If the scale's measurement plate deflects significantly it

will insert a proportional amount of the immersion stem (used to suspend samples) into the water container and cause an error in the buoyancy weight of the sample. To quantify this uncertainty two steel blocks were placed either side of the scales and a steel rule placed edge on between the blocks. A range of sample weights were placed on the scales (0-3.5kg) and the deflection measured from the top of the steel rule to the scale's measurement plate, Figure 4.1.

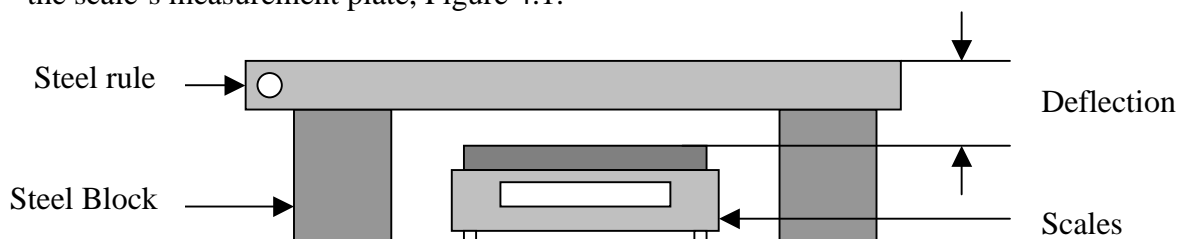


Figure 4.1 Scale deflection tests for establishing buoyancy uncertainty due to the immersion stem.

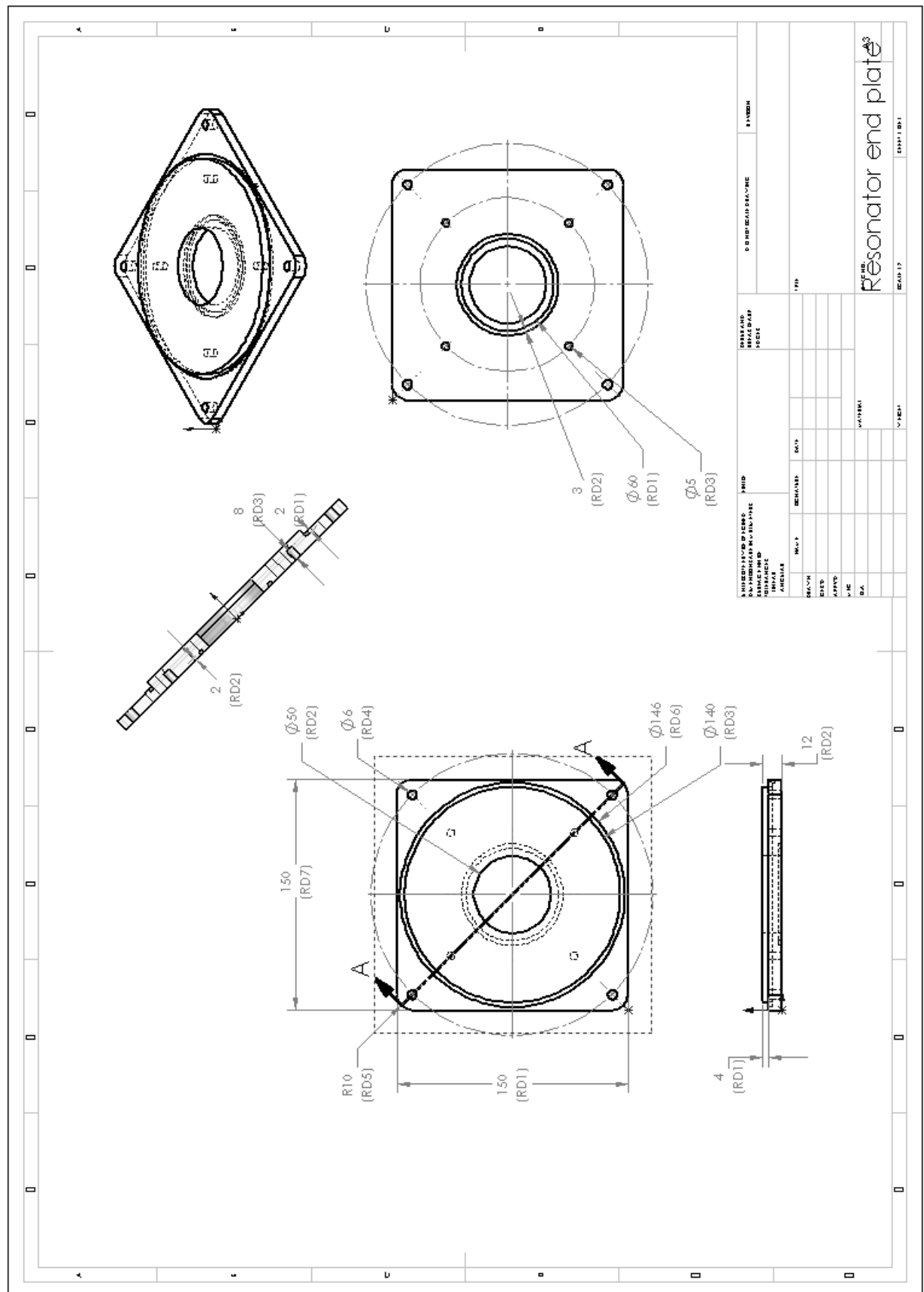
Deflection tests revealed changes in height due to weight were linear for sample weights under 500g and proportional to 0.0002mm/g. For samples over 500g the deflection became parabolic with a defining proportionality of $y = -4 \times 10^{-8} x^2 + 0.0004x$, where x is the sample weight and y the deflection in mm. Most of the produce and mineral testing samples were less than 500g in weight. The immersion stem is 5.6mm in diameter this gives it an immersion volume of 0.0246mL/mm of deflection. Coupled with the deflection coefficient of 0.0002mm/g for the scales this equates to approximately 4.9×10^{-6} mL/g. This result is many orders of magnitude smaller than the measurement uncertainty in volume by weight. Hence, scale deflection is negligible in buoyancy volume measurements.

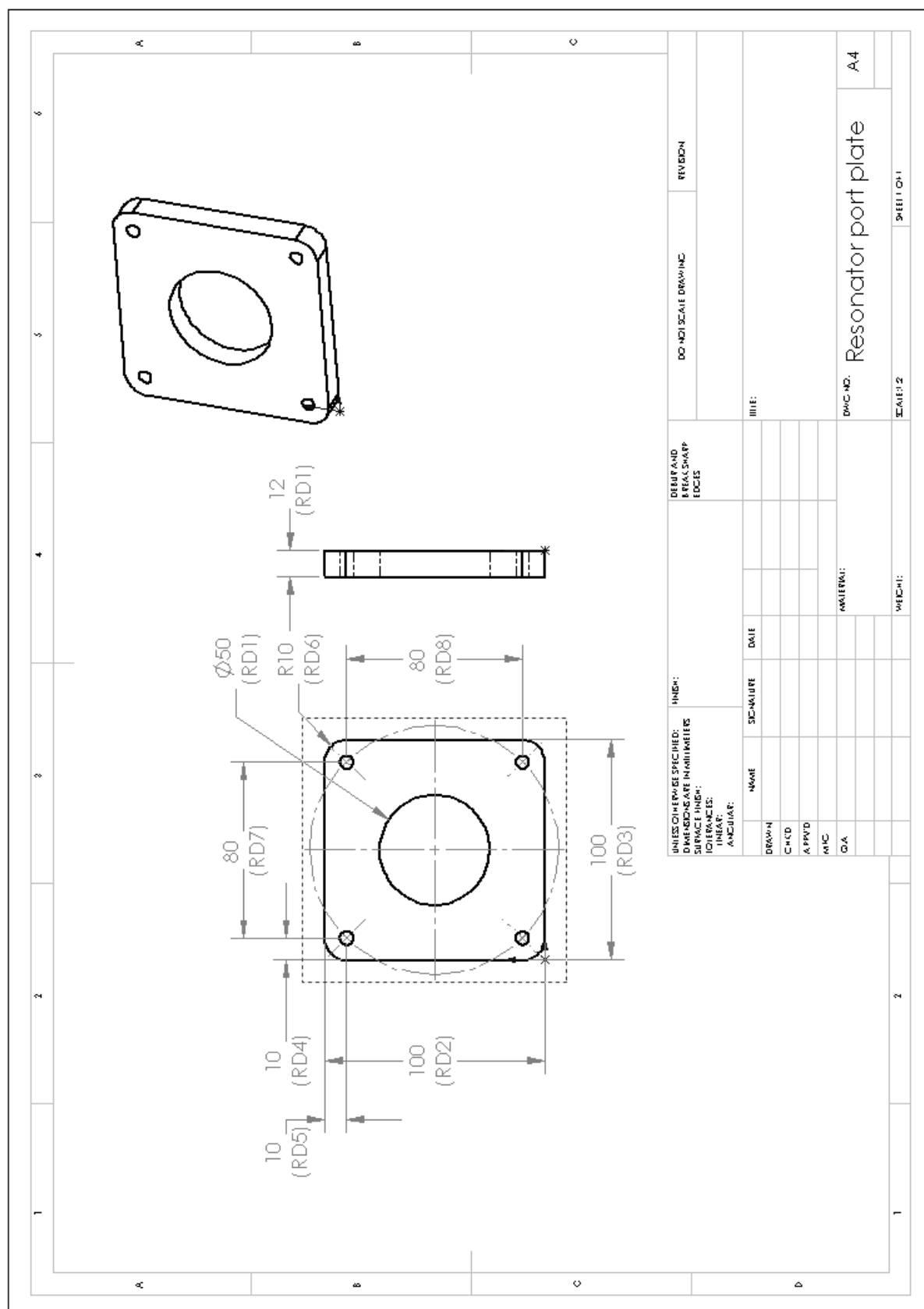
The water container for buoyancy volume determination had a diameter of 260mm; this gave it a height change of 53mL/mm caused by a sample volume change. The immersion stem had a volume height change of 0.0246mL/mm, this meant the error associated with an increase in water height due to sample submersion was 4.64×10^{-4} mL per millilitre of the sample volume. The largest sample measured using the buoyancy method was 410mL, therefore, it had an error of 0.2mL. This is the same order of uncertainty as the sample's weight measurement. For the majority of samples (<200mL) the error due to an increase in water height is significantly less, less than 0.1mL. Therefore the buoyancy method should be accurate to ± 0.2 mL for samples under 500mL.

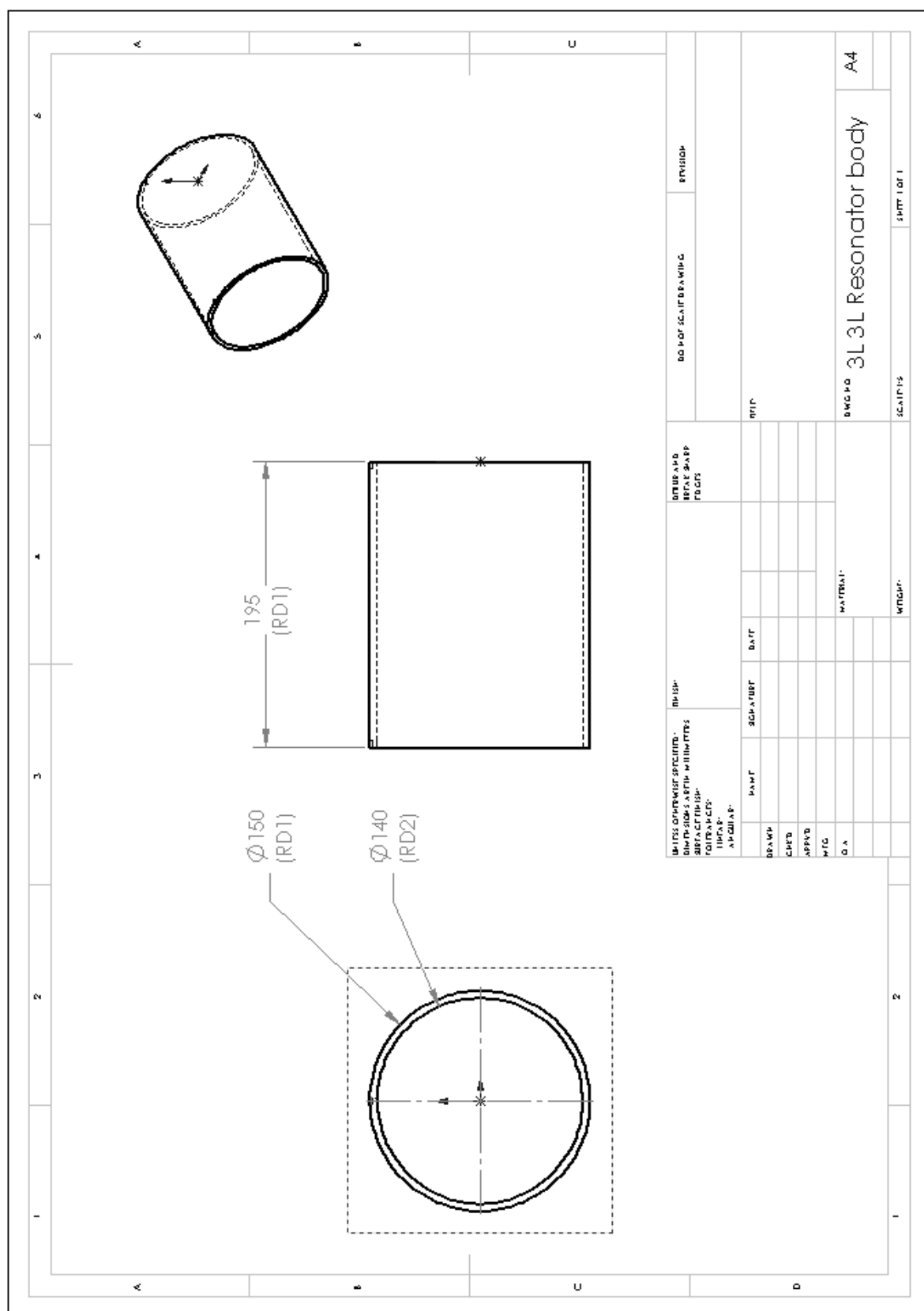
Appendix E

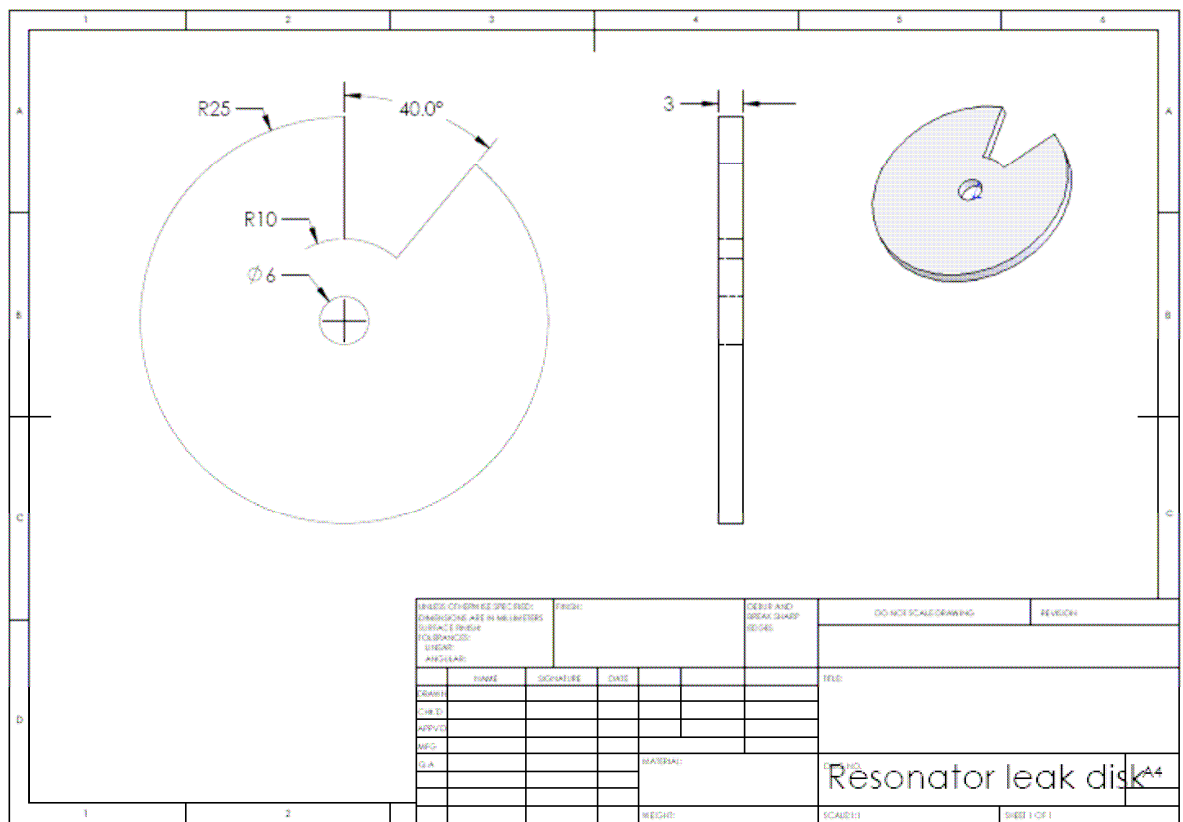
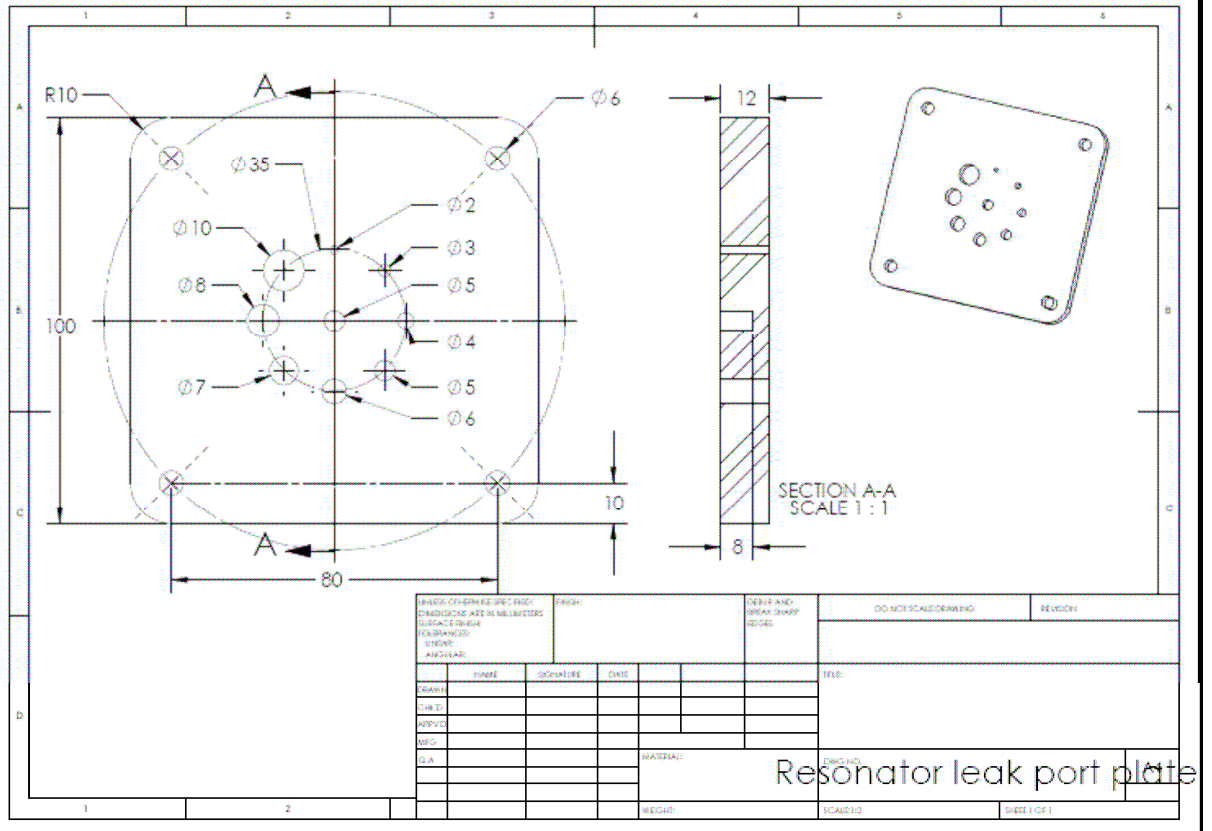
Working drawings and data sheets

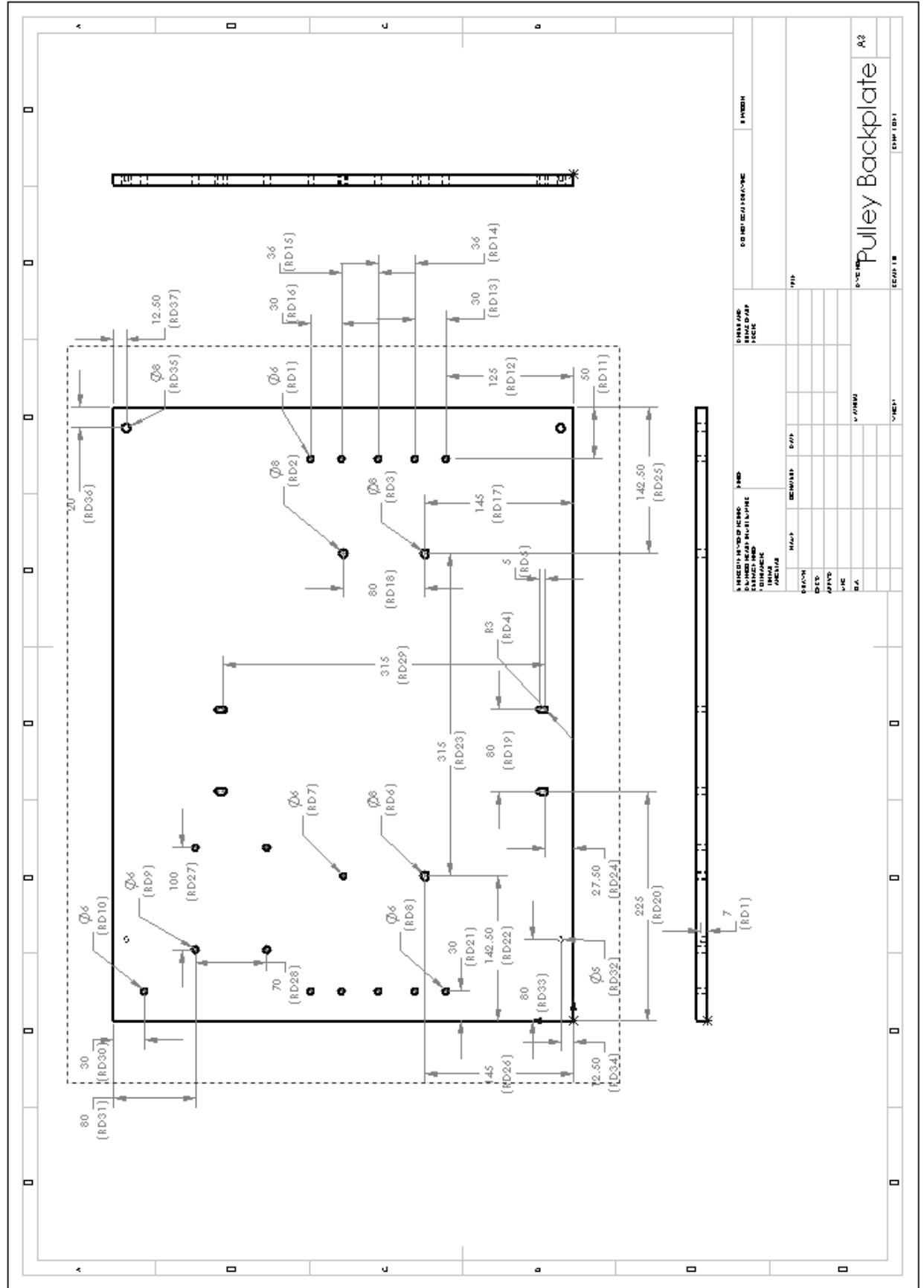
Drawings for primary Helmholtz resonator:

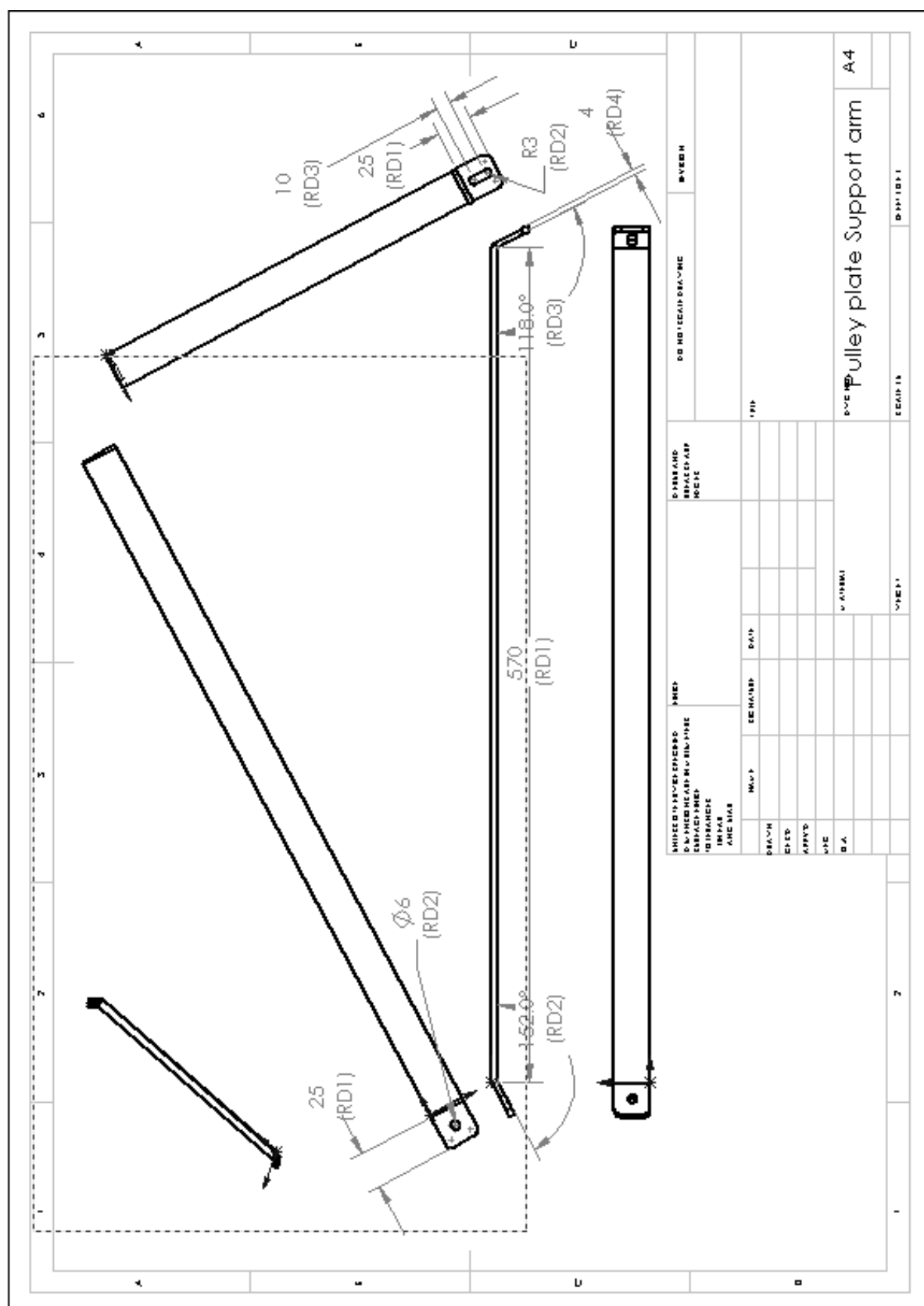


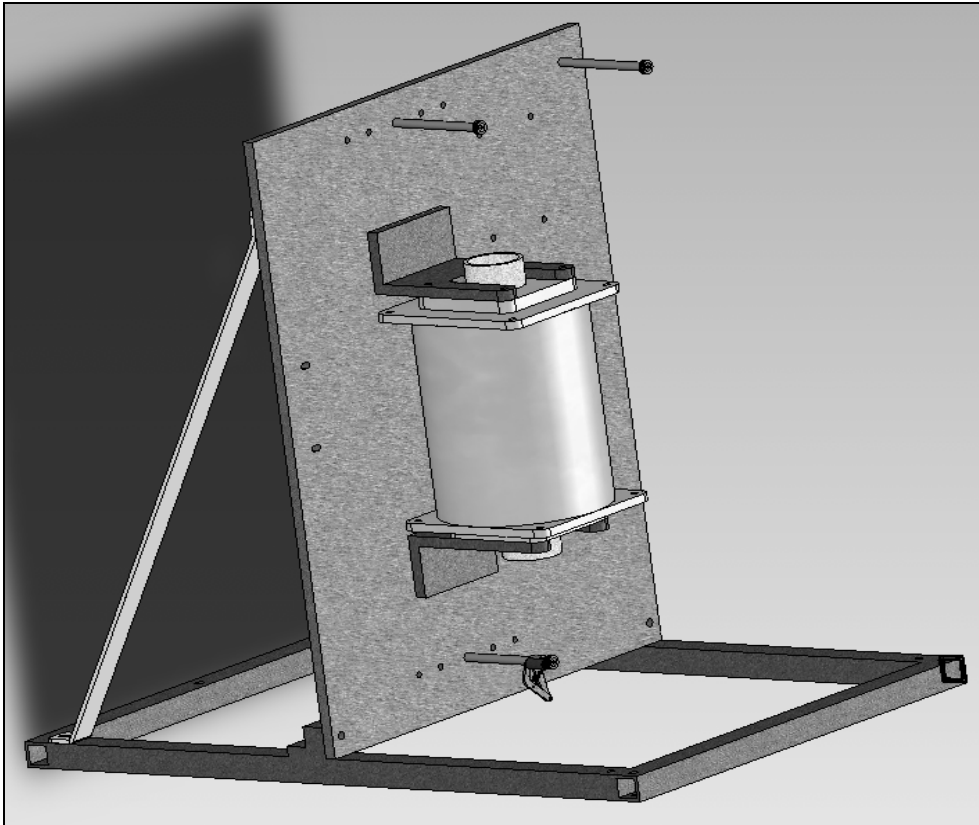




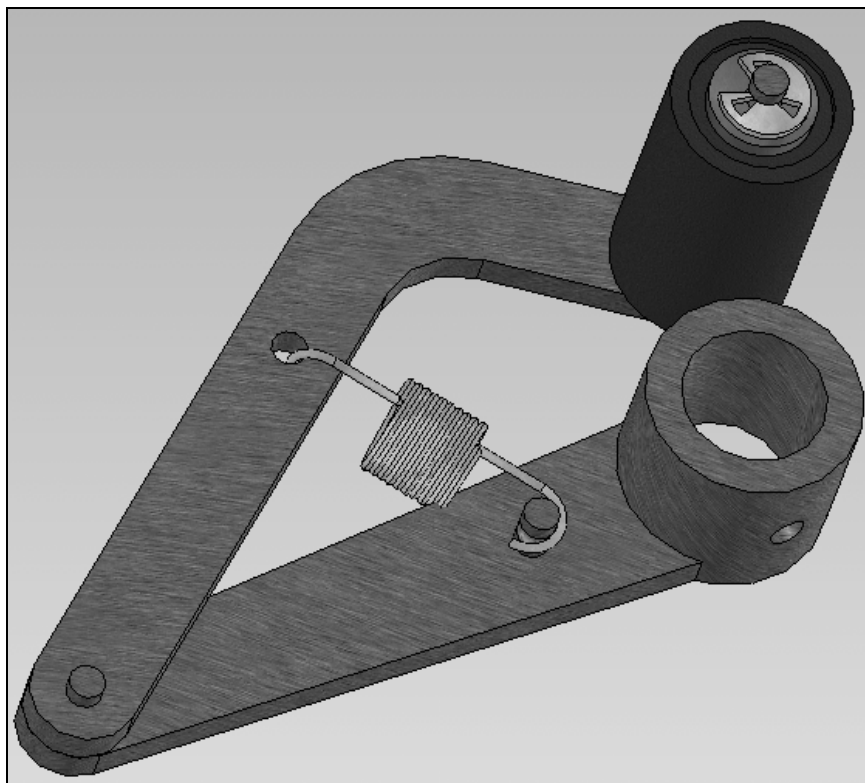






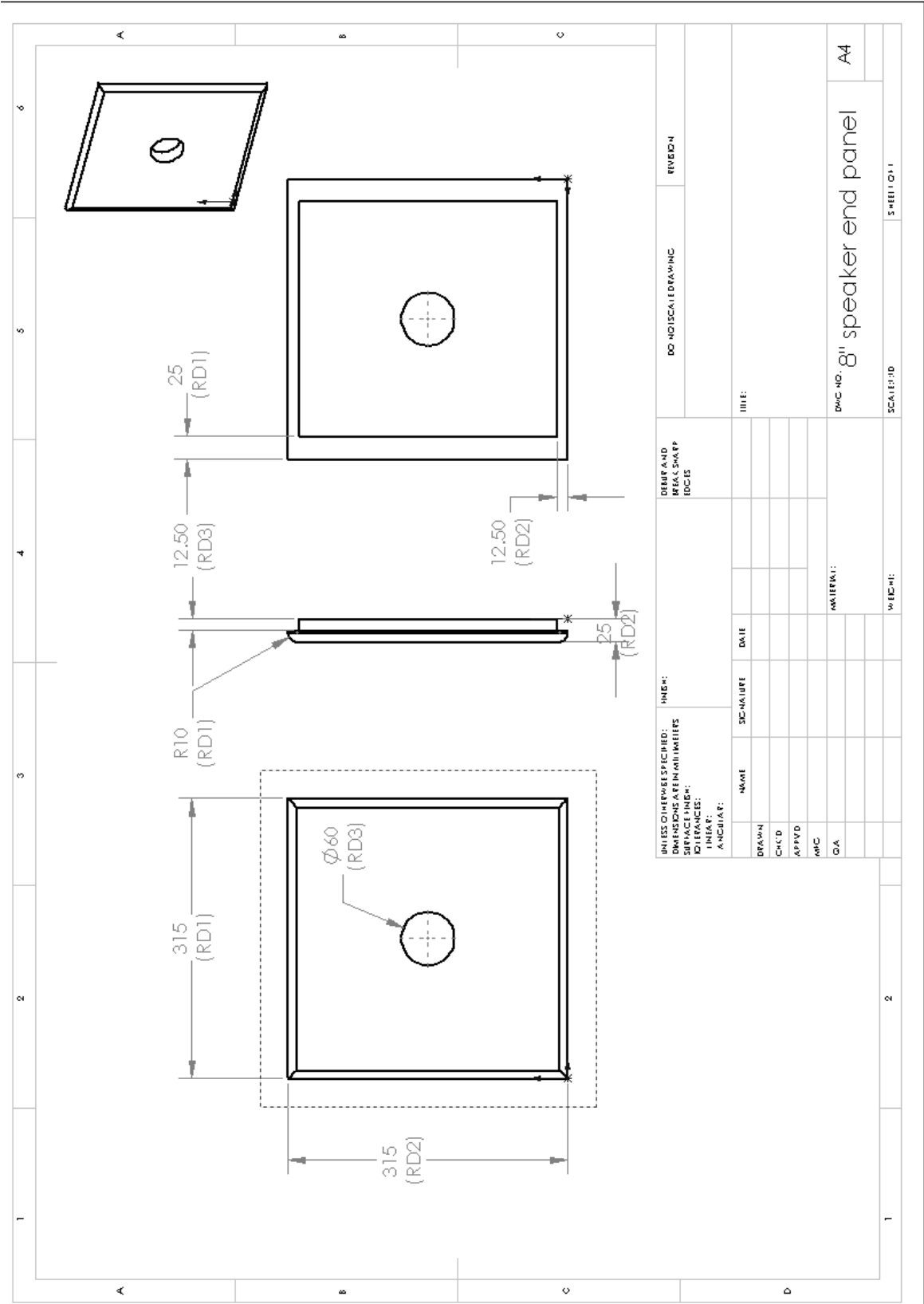


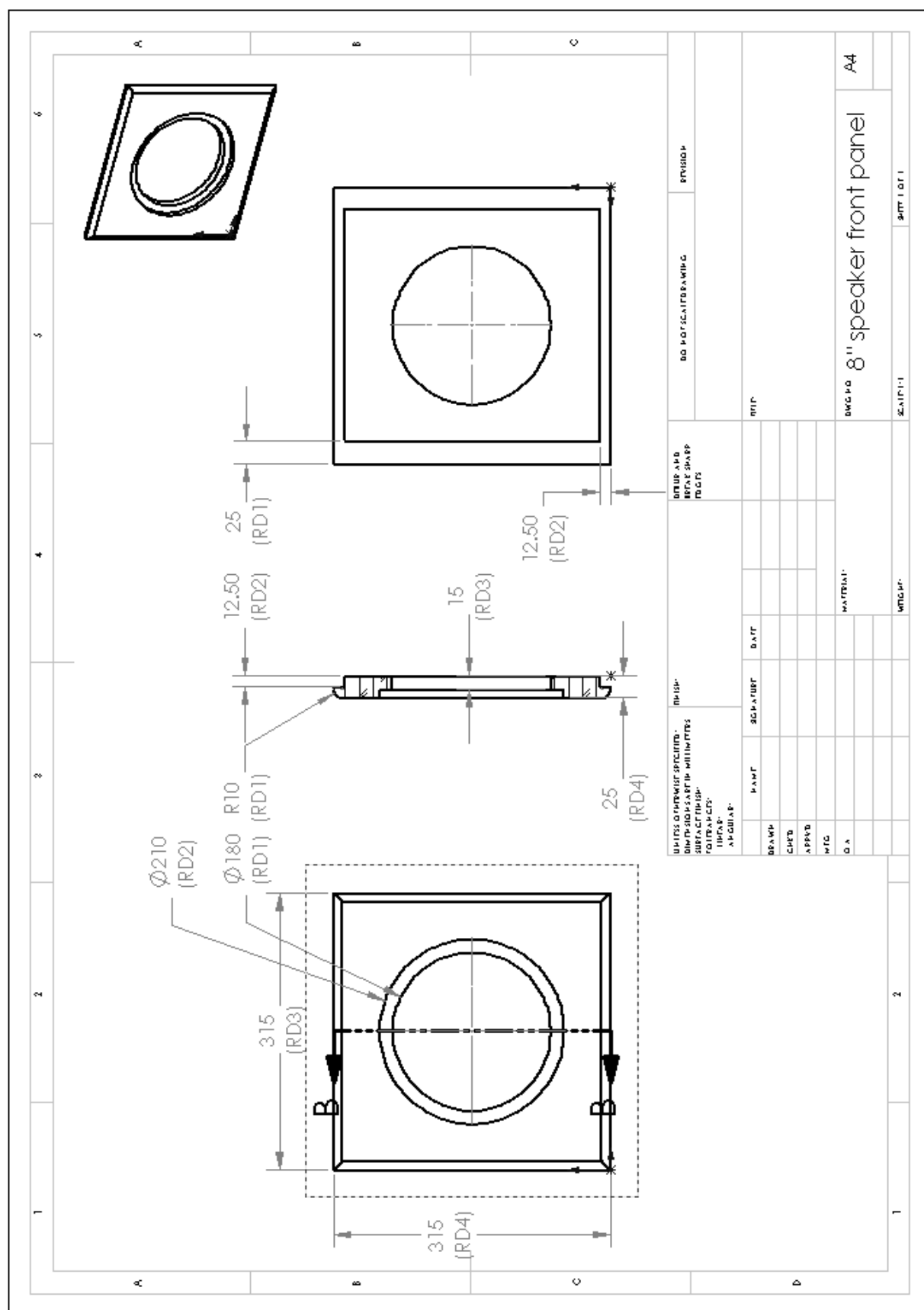
Complete Helmholtz resonator assembly with dual ports and pulley back plate assembly

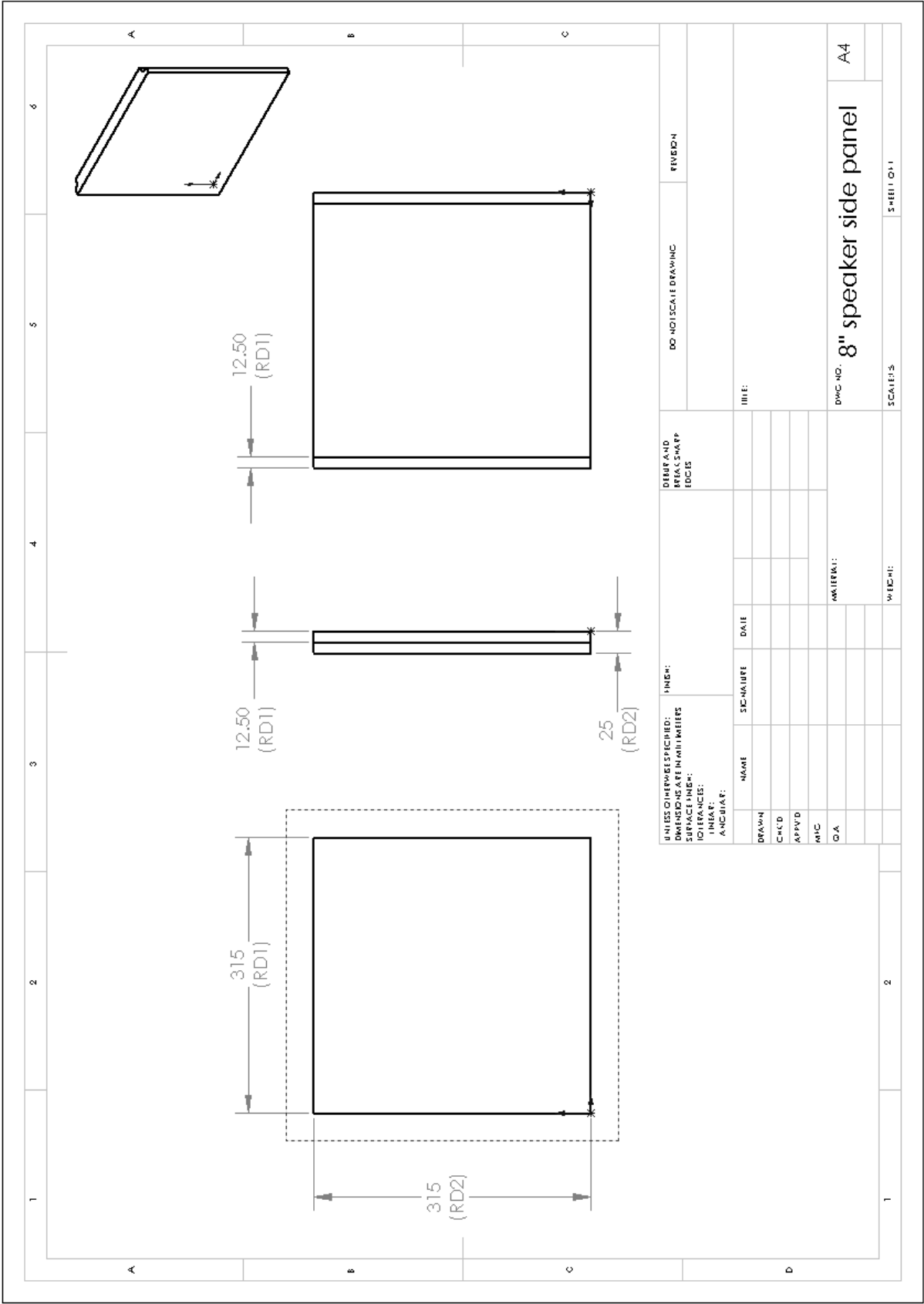


Pinch roller assembly

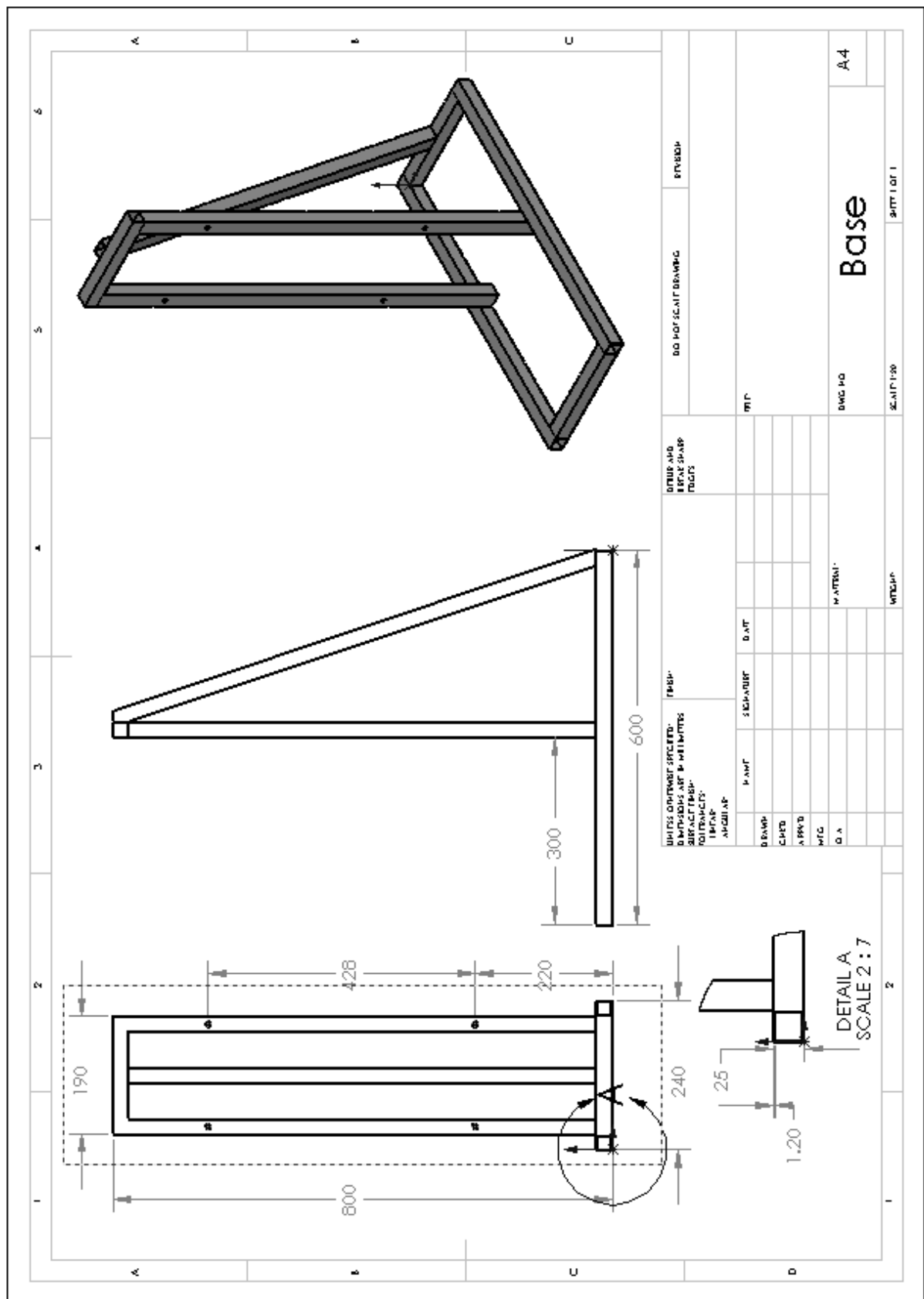
Speaker enclosure drawings:

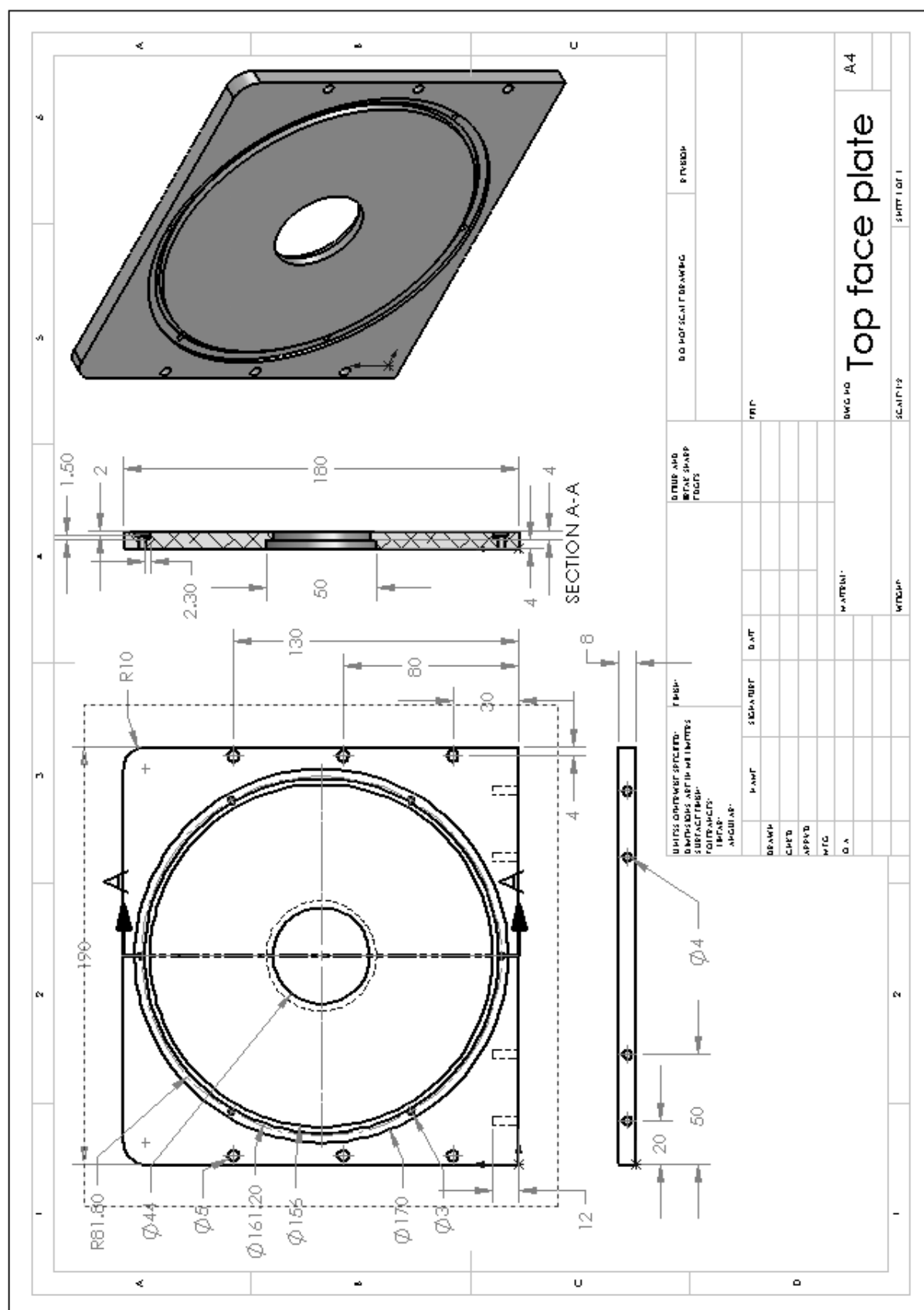


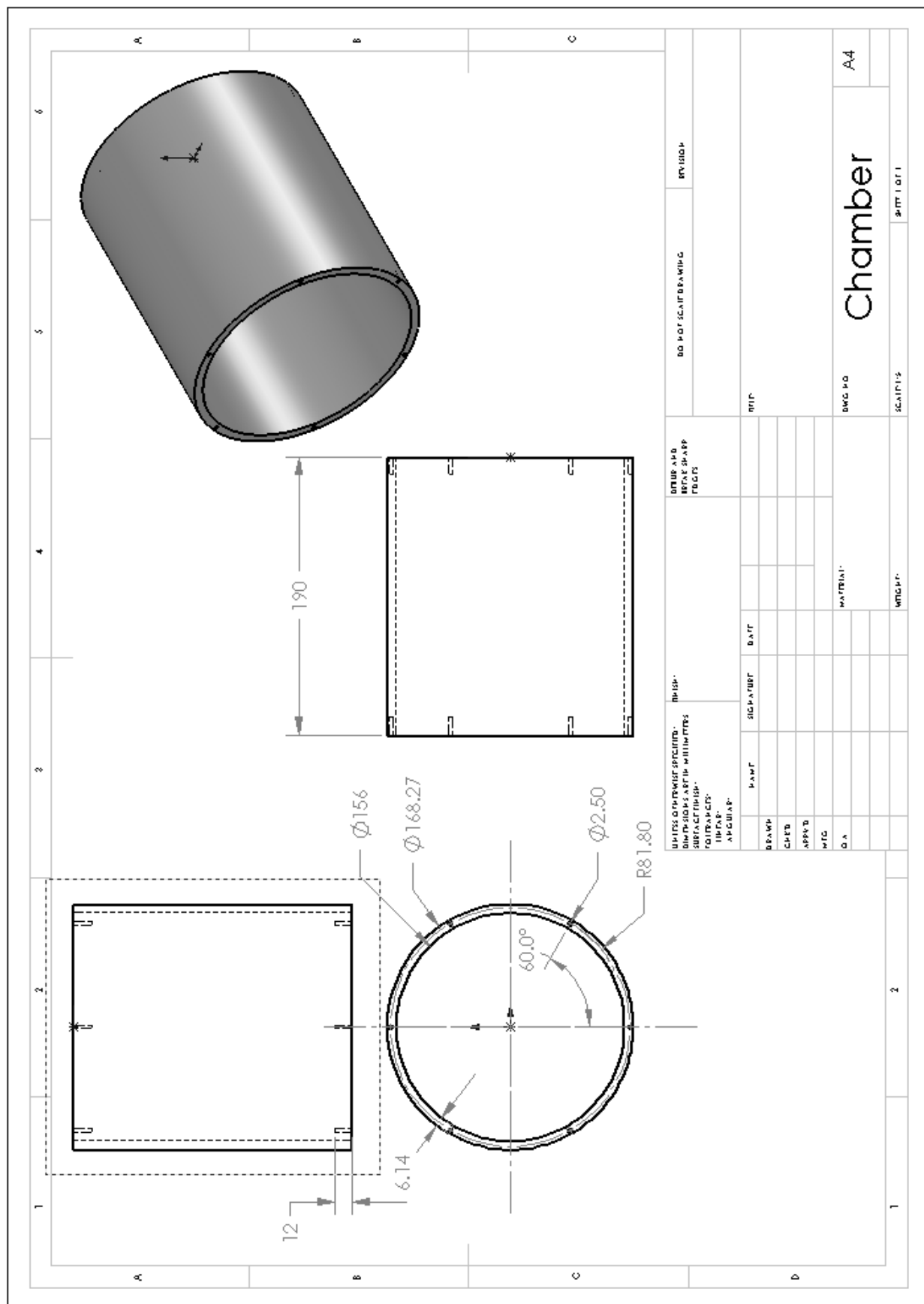


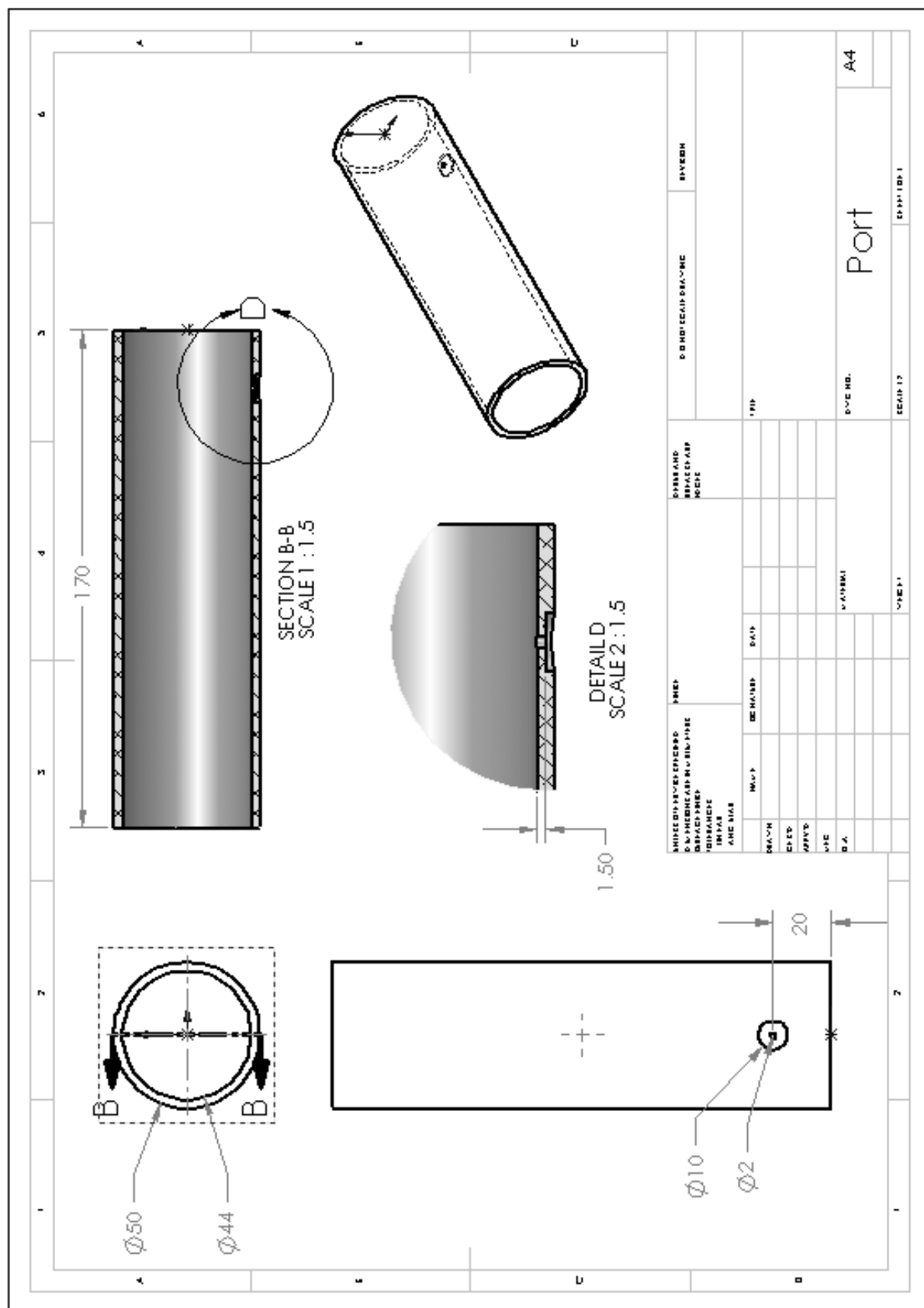


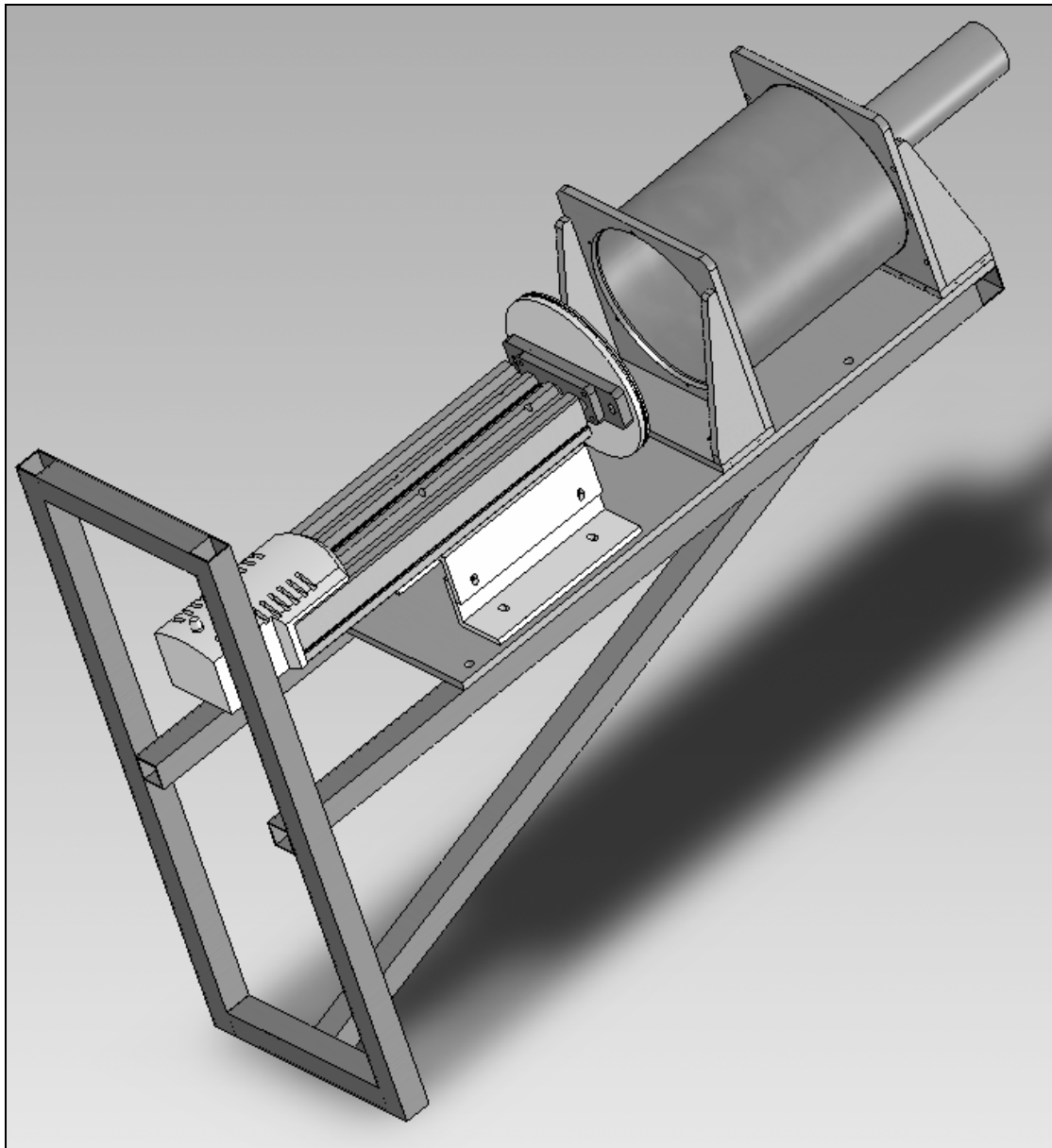
Drawings for variable chamber resonator:





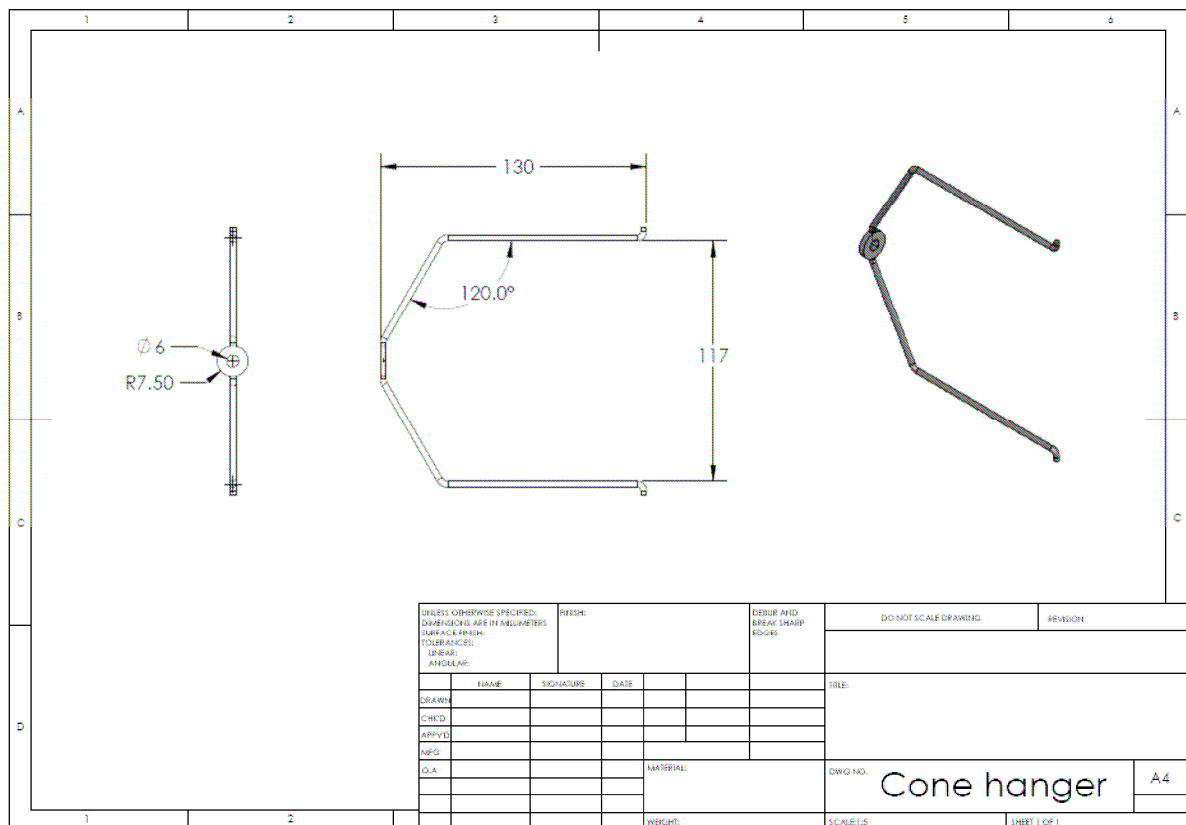
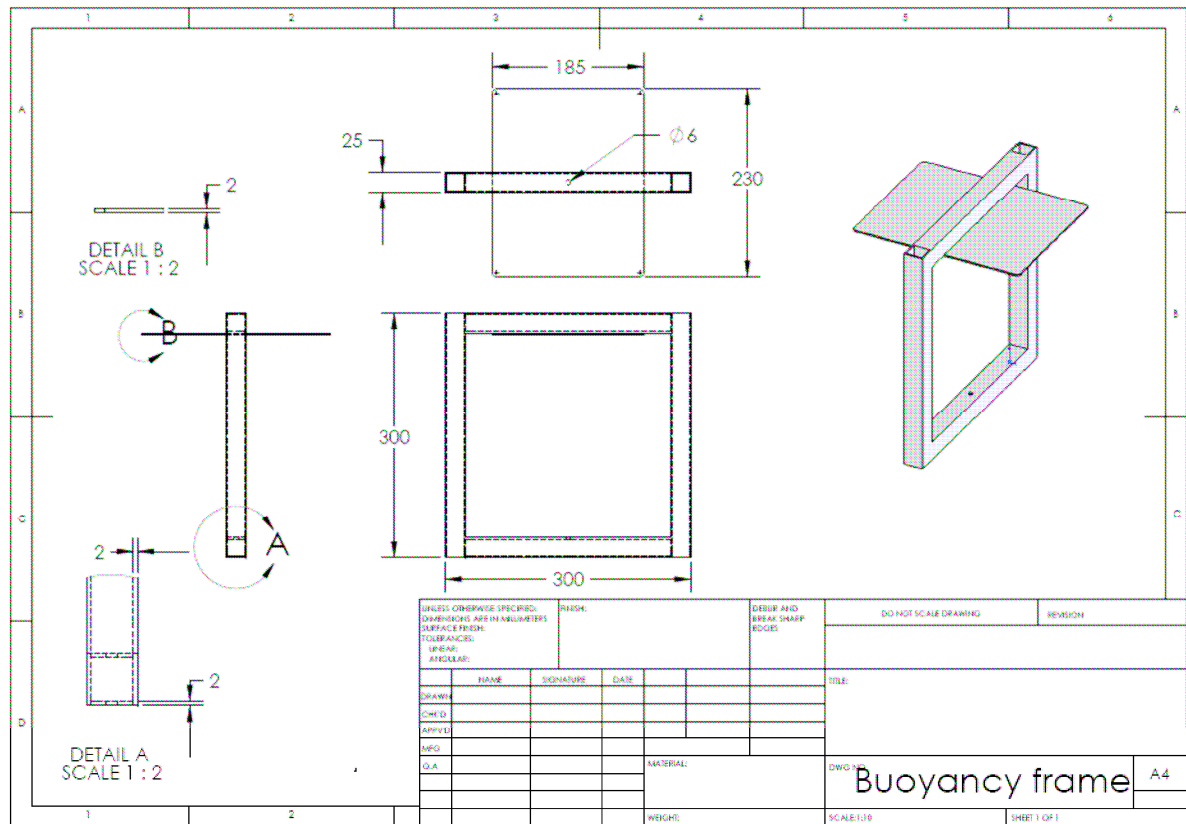







Complete Assembly of variable chamber resonator

Drawings for volume buoyancy rig:



Data sheets

Model Number 103A	ICP® PRESSURE SENSOR SPECIFICATIONS				Revision: K ECN #: 8684
DYNAMIC PERFORMANCE					
Dynamic Range (for +3V output)	psi [dB]	2 [177]			
Useful Overrange	psi [kPa]	-2 to +6 [-13.8 to +41.4]			
Maximum Pressure	psi [kPa]	25 [172]			
Resolution	psi [dB]	0.00002 [78]			
Resonant Frequency	kHz	≥13			
Rise Time	μ sec	≤25			
Low Frequency Response (-5%)	Hz	5			
Linearity	% FS	≤2	[1]		
ENVIRONMENTAL					
Acceleration Sensitivity	psi/g [kPa/m/s ²]	≤0.0005 [≤0.00035]			
Operating Temperature Range	°F [°C]	-100 to +175 [-73 to +79]			
Temperature Coefficient of Sensitivity	%/°F [%/°C]	≤0.03 [≤0.054]			
Maximum Flash Temperature	°F [°C]	1,000 [538]			
Maximum Shock	g pk [m/s ² pk]	1,000 [9 807]			
ELECTRICAL					
Sensitivity	mV/psi [mV/kPa]	1,500 [217.5]	[2]		
Output Polarity (positive pressure)		Positive			
Discharge Time Constant (at room temp)	sec	≥0.1			
Excitation Voltage Required	+ VDC	11 to 30			
Excitation Constant Current Required	mA	2 to 20			
Output Impedance	ohms	≤100			
Output Bias Voltage	+ VDC	3 to 8			
MECHANICAL					
Sensing Element	material	Ceramic			
Case	material	Invar			
Diaphragm	material	Invar			
Sealing	type	Epoxy			
Connector	type	Coaxial Pigtail			
Weight	oz [grams]	0.08 [2.3]			
<div> <div> OPTIONAL VERSIONS Optional versions have identical specifications and accessories as listed for the standard model except where noted by the letter prefixes below. More than one option may be used. </div> <div> <input type="checkbox"/> M Metric Mounting Threads Supplied Accessories: Model 060A24 Clamp Nut </div> </div>					
<div> NOTES: [1] Zero based best straight line. [2] Unless otherwise specified, sensitivities are ±15%. </div>					
<div> <div>  </div> <div> SUPPLIED ACCESSORIES: Model 061A04 Clamp </div> </div>					
<div> <div> <small>In the interest of constant product improvement, we reserve the right to change specifications without notice.</small> </div> <div> <small>ICPI® is a registered trademark of PCB Piezotronics, Inc. Form DD035 Rev.C 2/28/98</small> </div> </div>					
Drawn:	Engineer:	Sales:	Approved:	Spec Number:	
Date:	Date:	Date:	Date:	103-1010-80	

Driver name		8 inch Polycone	
Enter the values in the shaded boxes. Values in bold are calculated			
Calculate Qms, Qes and Qts			
Source voltage at amplifier terminals	Vs	930.00	mV
Source DC resistance	Rs	10.00	Ohms
Speaker voice coil DC resistance	Re	6.50	Ohms
Adjust F to at least 2 octaves above resonance. Check that varying frequency causes little or no change in voltage. Compare voltage reading with Vref - they should be within 10%.			
Voltage across Rs	Vref	563.64	mV
Source current	Is	56.36	Amps
Voltage across Rs at resonance	Vm	105.40	mV
Resonance frequency	Fs	37.00	Hertz
Speaker impedance at resonance (Rm)	Rm	78.24	Ohms
Current flow at resonance	Im	10.54	mA
-6dB current	Ir	24.37	mA
r0	r0	5.35	
-6dB voltage	Vr	243.74	mV
Carefully adjust frequency until Vr is observed across Rs, above and below resonance. Enter the frequencies.			
Frequency above Fs for stated voltage	Fh	46.00	Hertz
Frequency below Fs for stated voltage	Fl	30.00	Hertz
Fs sanity check (should equal Fs)		37.15	Hertz
Mechanical Q	Qms	5.35	
Electrical Q	Qes	0.48	
Total Q of driver	Qts	0.44	
Calculate Vas			
Box Volume	Vb	22.29	Litres
Cone Volume	Vc	0.83	Litres
Resonance in box	Fb	65.00	Hertz
	Vas	48.23	Litres
Cone Volume Calculations			
Cutout diameter		185.00	mm
Baffle thickness		15.00	mm
Cone Diameter		152.00	mm
Dustcap Diameter		64.00	mm
Average cone depth		25.00	mm
Approximate cone volume		0.83	Litres
Reference Data			
Use this information to create an equivalent circuit of the driver's resonant circuit.			
Capacitance		320.66	uF
Inductance		57.70	mH
Parallel resistor		71.74	Ohms

References

- Agnew J.M., Leonard J.J., Feddes J., Feng H., 2003, *A modified air pycnometer for compost air volume and density determination*, Can. Biosyst. Eng., Volume 45, pp. 27–35(8).
- Alster M., 1972, *Improved calculations of resonant frequencies of Helmholtz resonators*, Journal of sound and vibration, volume 24, part 1, pp. 63-85.
- Barmatz M., Allen J.L. and Gaspar M., 1983, *Experimental investigation of the scattering effects of a sphere in a cylindrical resonant chamber*, Acoustical Society of America, volume 73, No. 3, pp. 725-732.
- Beranek L. L., 1996, *Acoustics*, Acoustical Society of America through American Institute of Physics, Inc., New York.
- Blackstock D. T., 2000, *Fundamentals of physical acoustics*, John Wiley & Sons, Inc., New York.
- Boyce W. E. and DiPrima R. C., 1997, *Elementary differential equations and boundary value problems*, John Wiley & Sons, Inc., New York.
- Chanaud R.C., 1997, *Effect of geometry on the resonant frequency of Helmholtz resonators, part II*, Journal of sound and vibration, volume 204, part 5, pp. 829-834.
- Chanaud R.C., 1993, *Effect of geometry on the resonant frequency of Helmholtz resonators*, Journal of sound and vibration, volume 178, part 3, pp. 337-348.
- Cordero M.L. and Mujica N., 2007, *Resonant frequency shifts induced by a large spherical object in an air-filled acoustic cavity*, Acoustical Society of America, volume 121, No. 6, pp. 244-250.
- De Bedout J. M., Franchek M. A., Bernhard R. J., Mongeau L., 1996, *Adaptive-passive noise control with self-tuning Helmholtz resonators*, Journal of sound and vibration, volume 202, pp. 109-123.
- Everest F., 2001, *Master handbook of acoustics*, McGraw-Hill, New York.
- Fung Y. C., 1994, *A first course in continuum mechanics*, third edition, Prentice Hall, Inc., Englewood Cliffs, New Jersey.
- Ganghua Y., Deyu L., Li Cheng, 2008, *Effects of internal resistance of a Helmholtz resonator on acoustic energy reduction in enclosures*, Acoustical Society of America, volume 124, No. 6, pp. 3534-3543.
- Halliday D., Resnick R. and Walker J., 1997, *Fundamentals of physics*, fifth edition, John Wiley and sons Inc., USA.

Helmholtz H., 1877, *On the sensations of tone as a physiological basis for the theory of music*, translated by Alexander J. E., Kessinger Publishing, USA, 2005.

Ingard U., 1953, *On the theory and design of acoustic resonators*, Acoustical Society of America, volume 25, No. 6.

Iwase T., 2007, *Observation of acoustic particle velocity around neck of Helmholtz resonator*, The acoustical society of Japan, volume 29, No. 3, pp. 238-241.

Johnson Jr. V. E., 1995, *Device for determining the volume of objects using a chamber with two resonators to compensate for temperature and humidity effects*, United States Patent, PN. 5385069.

Kang Z. X., Ji Z. L., 2007, *Acoustic length correction of duct extension into a cylindrical chamber*, Journal of sound and vibration, volume 310, pp. 782-791.

Kinsler L.E and Frey A. R., 1962, *Fundamentals of acoustics, second edition*, John Wiley & Sons, Inc., New York, London.

Leung E., Lee C. P., Jacobi N. and Wang T.G., 1982, *Resonant frequency shift of an acoustic chamber containing a rigid shere*, Acoustical Society of America, volume 72, No. 2, pp. 615-620.

Lide, D. R. (Ed.), 1990), *CRC Handbook of Chemistry and Physics* (70th Edn.). Boca Raton (FL), CRC Press.

Nakano A., Torikata Y., Yamashita T., Sakamoto T., Futya Y., Tateno A., Nishizu T., 2006, *Liquid volume measurement with a closed Helmholtz resonator under micro-gravity conditions*, Cryogenics, volume 46, pp. 126-131.

Nishizu T., Ikeda Y., Torikata Y., Manmoto Y., Umehara S., Mizukami T., 2001, *Automatic, continuous food volume measurement with a Helmholtz resonator*, CIGR J Sci R& D, pp. 1–10.

Oppenheimer J.R., Martin A.G., Walker L.P., 1997, *Measurements of air-filled porosity in unsaturated organic matrices using a pycnometer*, Bioresource Technology, Volume 59, Number 2, pp. 241-247(7).

Panton L., Miller J. M., 1975, *Resonant frequencies of cylindrical Helmholtz resonators*, Acoustical Society of America, volume 57, No. 6, Part2.

Peat, K. S., 2008, *End correction at the interface between a plain and a perforated pipe*, Journal of sound and vibration, volume 319, pp. 1097-1106.

Rayleigh J. W. S., 1945, *The theory of sound, volume two*, Dover Publications, Inc., New York.

Scalart P., Benamar A., 1996, *A system for speech enhancement in the context of hands free radiotelephony with combined noise reduction and acoustic echo cancellation*, Speech communication, Volume 20, pp. 203-214.

Selamet A., and Lee I., 2003, *Helmholtz resonators with extended neck*, Acoustical Society of America, volume 113, No. 4, Part1.

Selamet A., Dickey N. S. and Novak J. M., 1995, *Theoretical, computational and experimental investigation of Helmholtz resonators with fixed volume: lumped versus distributed analysis*, Journal of sound and vibration, volume 187, part 2, pp. 358-367.

Shmulevich I., Galili N. and Howarth M.S., 2003, *Non-destructive dynamic testing of apples for firmness evaluation*, Postharvest Biology and Technology, In print.

Silva F., Guillemain Ph., Kergomard J., Mallaroni B., Norris A.N., 2008, *Approximation formulae for the acoustic radiation impedance of a cylindrical pipe*, Journal of sound and vibration, volume 322, pp. 255-263.

Small, R.H., 1972, *Direct-Radiator Loudspeaker System Analysis*, Journal Audio Eng. Soc., volume 20, pp. 383-395.

Small, R.H., 1972 and 1973, *Closed-Box Loudspeaker Systems*, Journal Audio Eng. Soc., volume 20, pp. 798-808, volume 21, pp. 11-18.

Small, R.H., 1973, *Vented-Box Loudspeaker Systems*, Journal Audio Eng. Soc., volume 21, pp. 363-372, pp. 438-444, pp. 549-554, pp. 635-639.

Sugiyama J., Al-Haq M., and Tsuta M., 2005 *Application of portable acoustic firmness tester for fruits*, Proceedings, Information and Technology for Sustainable Fruit and Vegetable Production, Montpellier – France.

Tamari S. and Aguilar-Chávez A., 2004, *Optimum design of gas pycnometers for determining the volume of solid particles*, Proceedings, CENAM Symposium, Center for Metrology of Mexico.

Tamari S., 2004, *Optimum design of the constant-volume gas pycnometer for determining the volume of solid particles*, Measurement Science and Technology, Volume 15, Number 3, pp. 549-558.

Tang S. K., 2003, *On Helmholtz resonators with tapered necks*, Journal of sound and vibration, volume 279, pp. 1085-1096.

Thiele, A.N., 1971, *Loudspeakers in Vented Boxes, Parts I and II*, Journal Audio Eng. Soc., volume 19, pp. 382-392, pp. 471-483.

Web Links:

Dessy R. and Dessy L., 2001, *The clay pot that sings*, retrieved July 2008 from <http://www.recorderhomepage.net/ocarina.pdf>

http://physics.kenyon.edu/EarlyApparatus/Rudolf_Koenig_Apparatus/Helmholtz_Resonator/Helmholtz_Resonator.html, retrieved May 2008.